

The Potential of Large Eddy Simulation for the Modeling of Wall Bounded Flows

Eugene de Villiers

Thermofluids Section
Department of Mechanical Engineering
Imperial College of Science, Technology and Medicine

25th July 2006

Abstract

Large Eddy Simulation (LES) has shown great promise in the calculation of traditionally difficult turbulent cases, such as unsteady and recirculating flows and for aeroacoustic applications. Unfortunately, this added accuracy, (though much less expensive than *Direct Numerical Simulations* (DNS)) comes at a considerable computational cost increase when compared to the conventional *Reynolds Average* (RANS) approach. Although it is by no means the only factor leading to this increased cost, the way in which LES interacts with wall boundaries has been identified as the major contributor to this problem. In an attempt to address this issue, many turbulence researchers have investigated the requirements and effects of simplifying the aforementioned interaction, which has to date met with varying degrees of success.

The current work aims to contribute to this effort, with the main goal of ascertaining whether LES can effectively be used in the near term to model aerodynamic flows of the type associated with automobiles. In addition to providing more accurate aerodynamic results, such a methodology should also allow the calculation of aero-acoustic noise for the problem under investigation. Large grid sizes necessitated by well resolved aerodynamic simulations of such high Reynolds number flows make them generally unfeasible given current CPU speeds. This project attempts to address this issue in two ways: firstly, through the application of approximate wall treatments and secondly through improved mesh distribution.

Several such wall treatments are investigated and the most promising are implemented for further testing. In addition, embedded mesh refinement is employed to resolve flow

regions of interest, while still maintaining a reasonable overall grid size. Very good agreement between experimental data and computational results is observes for all test cases although requirements in terms of wall treatments and turbulence modelling differ. Significantly, large eddy simulation is shown to be an efficient tool for the prediction of aero-acoustic noise sources and other unsteady flow phenomena.

Acknowledgements

I wish to express my gratitude to my supervisor, Prof. David Gosman, for the incredible amount he has taught me during the course of this thesis. It has been an exceedingly rewarding experience.

I would like to thank Henry Weller, not only for developing and making FOAM available, but also for his feedback and many fruitfull discussions on all matters CFD related. Thanks also to Dr. Hrv Jasak, co-developer of FOAM, who kindly offered to proof read my thesis. To everyone else with whom I shared Room 600: your collaboration and companionship has been invaluable in completing this work.

To my wife Liesl I am eternally grateful for the many years of patience and unfailing support. Dr. Michael Wessels, your encouragement and friendship is thankfully acknowledged. Finally, to the project sponsor DaimlerChrysler: thank you for making it all possible.

Eugene de Villiers

July 2006

Contents

Abstract	i
Acknowledgements	ii
List of Figures	viii
List of Tables	xiv
Nomenclature	xvii
1 Introduction	1
1.1 Simulating Turbulence	2
1.2 Research Objectives	5
1.3 Thesis Outline	6
1.3.1 Methodology	6
1.3.2 Validation and Test Cases	7
1.3.3 Accomplishments	9
2 Turbulent Boundary Layers	13
2.1 Turbulence Basics	13
2.2 Vortex Identification	18
2.2.1 Vortex Eduction Methods	19
2.2.2 Comparison	24
2.3 The Near-wall Turbulence Cycle	25
2.3.1 The Streak Instability Cycle	27

2.3.2	Extent of the Near-wall Cycle	34
2.4	Core Flow Interaction	38
2.4.1	Inverse Energy Cascade	38
2.4.2	Effects of Pressure Gradient	44
2.5	Modelling Requirements	53
3	LES Principles and Modelling	59
3.1	Governing Equations	59
3.2	Sub-grid Scale Modelling	64
3.2.1	Algebraic Models	64
3.2.2	Differential Sub-grid Models	66
3.2.3	Scale Similarity and Linear Combination (mixed) Models	68
3.2.4	Dynamic Models	70
3.2.5	SGS Model Choice	74
3.3	Wall Treatments	74
3.3.1	Equilibrium Stress Models	75
3.3.2	Two-layer Models	83
3.3.3	Detached Eddy Simulation (DES)	87
3.3.4	Structural Support Models	94
3.3.5	Local Mesh Refinement	98
3.3.6	Choice of Wall Treatment	100
4	Computational Methodology	103
4.1	Governing Equations	103
4.2	Discretisation Practices	106
4.2.1	Domain Discretisation	106
4.2.2	Spatial Discretisation	106
4.2.3	Time Integration	113
4.2.4	Navier-Stokes Discretisation	115
4.3	Modelling Implementation	121
4.3.1	One-equation Turbulent Energy Model	121

4.3.2	Spalart-Allmaras	125
4.4	Boundary Conditions	127
4.4.1	Basic Boundary Conditions	127
4.4.2	Turbulent Wall Properties	130
4.4.3	Turbulent Inlets	133
4.5	Errors and Mesh Refinement	138
4.5.1	Errors in LES	138
4.5.2	Refinement Indicators	153
5	Basic Test Cases	161
5.1	Plane Channel Flow	161
5.1.1	Computational Setup and Reference Details	162
5.1.2	Channel Flow Initialization	163
5.1.3	Model Comparison	167
5.1.4	Mesh Resolution	170
5.1.5	Summary	178
5.2	Asymmetric Plane Diffuser	179
5.2.1	Computational Setup and Reference Details	180
5.2.2	RANS Diffuser Results	182
5.2.3	LES of the Diffuser	188
5.2.4	Spalart-Allmaras DES Model	202
5.2.5	Local Mesh Refinement	208
5.2.6	Summary	215
6	Side Mirror	217
6.1	Side Mirror A	220
6.1.1	Computational Setup and Reference Details	220
6.1.2	Flow Features and Dynamics	227
6.1.3	Static Pressure	237
6.1.4	Pressure Spectra	242
6.1.5	Length Scale Reduction	258

6.1.6	Summary	264
6.2	Side Mirror B	265
6.2.1	Experimental Data	265
6.2.2	Computational Setup and Reference Details	267
6.2.3	Flow Features and Dynamics	272
6.2.4	Surface Flow Patterns	277
6.2.5	Static Pressure	281
6.2.6	Pressure Spectra	284
6.2.7	Mean Velocity and Reynolds Stress	296
6.2.8	Summary	313
7	Conclusions and Suggestions	315
7.1	Summary of Primary Results	315
7.2	Proposals for Future Work	320
7.3	Closing Comments	323
A	Mirror Animations	325
B	Probe locations	331

List of Figures

1.1	Plane channel flow calculation domain.	8
1.2	Diagrammatic representation of the asymmetric plane diffuser flow and calculation domain.	9
1.3	Idealised side mirror geometry.	10
2.1	Flow topologies	16
2.2	Turbulence in a mixing layer	17
2.3	Three dimensional incompressible flow topologies.	23
2.4	Low speed streaks and attendant vortices.	28
2.5	Streak base flow.	29
2.6	The streak instability mechanism.	30
2.7	Streamwise vortex formation.	31
2.8	Streamwise vortex tilting.	32
2.9	Near-wall educed coherent structures and associated events.	33
2.10	Internal shear layers and arch vortices.	34
2.11	Boundary layer velocity profile.	35
2.12	Damping of near-wall fluctuations.	36
2.13	Explicitly filtered channel.	37
2.14	Turbulent energy balance.	40
2.15	The two energy cascades in the near-wall inertial layer.	42
2.16	The double cone eddy.	43
2.17	Adverse pressure gradient velocity profiles.	45
2.18	Wall limiting behaviour of u'_{rms}/u_τ in an APG.	46

List of Figures

2.19 DNS of APG induced separation of a flat plate boundary layer.	47
2.20 Turbulence intensity trace in an APG boundary layer.	48
2.21 Contour plot of two-point correlation of wall-pressure fluctuations.	49
2.22 Mean streamlines of APG driven separation of a flat plate boundary layer. .	50
2.23 Contours of two point correlation of streamwise velocity fluctuations. . . .	51
2.24 APG driven separation of a flat plate boundary layer.	52
2.25 Schematic representation of coherent structures in a boundary layer.	54
3.1 One-dimensional representation of an arbitrary filter function.	61
3.2 Filter functions.	62
3.3 Filtering of a test function in Fourier space.	62
3.4 Wall function implementation.	75
3.5 Typical two-layer model implementation.	85
3.6 Typical distribution of DES turbulence zones for flow over a bluff body. . .	89
4.1 Control volume for finite volume discretisation.	107
4.2 Face interpolation.	108
4.3 Decomposition of the face area vector due to non-orthogonality using the “over-relaxed” approach.	112
4.4 PISO solution procedure	120
4.5 Shape of variable profile for $0 < \tilde{\phi}_C < \beta_m$	122
4.6 Variation of \tilde{d} with wall distance, d, and cell size.	127
4.7 A control volume adjacent to a boundary.	128
4.8 Variation of transported turbulent quantities in RANS of a channel flow. .	134
4.9 Inlet boundaries for the plane diffuser.	137
4.10 The effect of top-hat filter size on smallest eddies a) Implicit filter b) Ex- plicit filter $\Delta = 2h$	140
4.11 Face skewness error.	141
4.12 Filtering of a parabolic function.	148
4.13 Change in filter size at a) the wall b) sudden mesh refinement.	150
4.14 Effect of local refinement on transported SGS properties.	151

4.15	Distribution of a smoothed SGS turbulent length scale on a one-dimensional mesh.	152
4.16	Transported SGS viscosity in the presence of local refinement with turbulent length-scale smoothing.	152
4.17	Discrepancy between the interpolated and extrapolated face values.	156
5.1	Schematic representation of the problem domain for the channel flow simulations.	162
5.2	Initial velocity magnitude contours for a steady bulk channel flow with an imposed perturbation scheme, $y^+ = 20$. Streamwise velocity (left) and spanwise velocity (right)	165
5.3	Transition to turbulence: Velocity magnitude and vortex cores in a plane channel at different times after imposed perturbations, $y^+ = 20$	166
5.4	Channel flow model comparison.	168
5.5	Channel flow resolution sensitivity.	172
5.6	Channel flow streaks and vortices.	174
5.7	Spectrum of the total resolved turbulent energy at different wall normal displacements.	176
5.8	Computational domain for the asymmetric plane diffuser.	182
5.9	Velocity distribution for RANS diffuser.	183
5.10	Shear stress distribution for RANS diffuser.	184
5.11	Normal stress distribution for RANS diffuser.	185
5.12	RANS diffuser wall statistics.	188
5.13	Effect of inlet boundary on LES diffuser wall statistics.	190
5.14	LES instantaneous velocity magnitude in the diffuser.	191
5.15	LES instantaneous turbulent properties in the diffuser.	193
5.16	Vortex cores around the separation point.	195
5.17	Velocity distribution for LES diffuser.	198
5.18	Total turbulent shear stress distribution for LES diffuser.	199
5.19	Total normal stress distribution for LES diffuser.	200
5.20	LES diffuser wall statistics.	202

5.21 Effect of modifications on the DES length scale distribution in the diffuser.	204
5.22 Result comparison for Spalart-Allmaras Detached Eddy Model.	205
5.23 Diffuser SGS turbulent viscosity.	206
5.24 Spalart-Allmaras DES diffuser wall statistics.	207
5.25 Ratio of SGS to total turbulent energy.	209
5.26 Normalised residual error in unrefined diffusers.	210
5.27 Zones of refinement.	211
5.28 Refined diffuser turbulence distribution.	213
5.29 Normalised residual error in refined diffusers.	214
5.30 Diffuser with embedded refinement wall statistics.	215
6.1 Side mirror: experimental setup Case A.	217
6.2 Side mirror: experimental setup Case B.	218
6.3 Mirror A experiment (reproduced from Siegert <i>et al.</i> [141]).	221
6.4 Problem domain and boundary conditions for side mirror A.	222
6.5 Coarse mesh for mirror Case A,	224
6.6 Mirror A coarse surface mesh	225
6.7 Centre-line velocity distribution	228
6.8 Base plate parallel velocity ($z = 1.5$ cm)	230
6.9 Bow vortex	234
6.10 Mean turbulence intensity	236
6.11 Mean pressure on the mirror surface	238
6.12 Static pressure probe locations.	240
6.13 Mean pressure probes	241
6.14 Mean pressure distribution on the base plate	241
6.15 Mean sound pressure level on the mirror front face.	245
6.16 Spectra of SPL at selected points on the mirror front face.	248
6.17 Mean sound pressure level on the mirror rear face.	250
6.18 Spectra of SPL at selected points on the rear of the mirror.	251
6.19 Mean sound pressure level in the mirror wake.	254
6.20 SPL spectra in the mirror wake.	255

6.21 SPL spectra in the mirror wake.	256
6.22 Flow features on the mirror front face.	259
6.23 Reducing the turbulent length scale on the mirror front face.	260
6.24 Mean subgrid-scale viscosity adjacent to the mirror front surface.	261
6.25 Velocity magnitude in surface adjacent cells	262
6.26 Comparison of SPL spectra for reduced front face length scale calculations.	263
6.27 Diagram of Imperial College closed windtunnel (courtesy of [31]).	266
6.28 Frontal view of Imperial College experimental rig [31].	267
6.29 Case B calculation domain.	269
6.30 Inlet velocity distribution for case B.	270
6.31 Computational mesh for case B.	271
6.32 Overview of mean flow features, streaklines and velocity magnitude.	273
6.33 Comparison of scaled velocity magnitudes for mirror cases A and B	275
6.34 Comparison of instantaneous vortex cores	276
6.35 Surface flow features on the mirror base plate.	279
6.36 Surface flow features in the recirculation zone.	280
6.37 Surface flow features in front of the mirror.	280
6.38 Surface flow features on the mirror front face.	281
6.39 Mean surface pressure.	282
6.40 Static pressure probes on the mirror surface.	283
6.41 Sound pressure level for surface sources on mirror B.	285
6.42 Probe locations on the mirror base plate, Case B.	286
6.43 Point SPL spectra on and around the mirror.	288
6.44 Point spectra in the near shear layer.	291
6.45 Point spectra in the far shear layer.	292
6.46 Point spectra across the shear layer.	294
6.47 Point spectra on the wake centreline.	295
6.48 LDA measurement plane in front of the mirror.	297
6.49 Comparison of calculated bow vortex with LDA vectors.	298

6.50 Comparison of experimental and calculated velocity components in front of the mirror.	299
6.51 LDA measurement plane beside the mirror.	300
6.52 Calculated velocity components and streamline on the side measurement plane.	301
6.53 Comparison of experimental and calculated velocity components beside the mirror.	303
6.54 Side plane location of the bow vortex core, measured (black lines) and positive contours of $Q_{\nabla \mathbf{U}}$ for BSA3.	303
6.55 Measurement line for LDA of the recirculation extent.	304
6.56 Extent of the predicted recirculation zone on the plane $X/R = 0.1$	304
6.57 Streamwise velocity component in the recirculation zone.	305
6.58 LDA measurement locations across the wake.	305
6.59 Streaklines and streamwise velocity magnitude in the $Z/R = 0.9$ plane.	306
6.60 Comparison of streamwise velocity component for LDA and case BSA3 across the recirculation zone.	307
6.61 LDA measurement position in the wake symmetry plane.	308
6.62 Velocity on the symmetry plane.	309
6.63 Streamwise velocity in the mirror symmetry plane.	310
6.64 Streamwise normal stress component, T_{xx}	311
6.65 Comparison of streamwise normal stresses in the mirror symmetry plane.	312
A.1 Deviatoric surface pressure on the mirror base plate	326
A.2 Isosurface of deviatoric pressure $p' = 100$, side view.	326
A.3 Isosurface of deviatoric pressure $p' = 100$, top view.	327
A.4 SPL contours on a moving cutting plane	328
A.5 Velocity contours on a moving baseplate-normal cutting plane	328
A.6 Velocity contours and vectors on a cutting plane moving across the mirror	329

List of Tables

5.1	Relative wall shear stresses for different near-wall turbulence treatments	170
5.2	Channel flow mesh densities	171
5.3	Relative wall shear stresses for different mesh resolutions	171
5.4	Relative wall shear stresses for Spalart-Allmaras DES model on different mesh resolutions	178
5.5	Grid spacings in wall units, and directional cell counts used in the simulations.	189
B.1	Static pressure probe locations	332
B.2	Dynamic probe locations	333

List of Tables

Nomenclature

Normal symbols represent scalar quantities and boldface symbols represent vector and tensor quantities. Generally boldface Roman symbols represent vector and boldface Greek symbols represent tensor quantities, but this rule is not adhered to religiously. Dimensions and units are given in terms of the relevant SI subset, i.e. mass (M) in kg, length (L) in meters (m) and time (t) in seconds (s).

Roman Symbols

Symbol	Description	Dimensions	Units
a_0	Speed of sound	L/t	m/s
\mathbf{a}	Acceleration	L/t^2	m/s^2
A, \mathbf{A}	Surface area magnitude and vector	L^2	m^2
A^+	Damping constant		
C	Constant coefficient		
C_f	Friction coefficient		
D	Damping function		
\mathbb{D}	Tensor discriminant		
d	Diameter	L	m
\mathbf{d}	Displacement or cell center vector	L	m
\tilde{d}	DES length scale	L	m
E	Wall function constant		
\mathbb{E}	Energy density	L^2/t^2	m^2/s^2
e	Error		
F	Face flux	L^3/t	m^3/s
f	Generic flow variable		
f	Frequency	t^{-1}	s^{-1}
g_b	Fixed gradient (boundary condition)		
h	Height, channel half width	L	m
\mathbf{I}	Unit tensor		

Nomenclature

K	Turbulent energy	L^2/t^2	m^2/s^2
\mathbf{k}	Non-orthogonality vector	L	m
k	Wave number	$1/L$	m^{-1}
k_d	Dissipation wave number	L	m
k_i	Integral wave number	L	m
\mathbf{L}	Correlation tensor		
L	Reference length	L	m
l	Length or length scale	L	m
\mathbf{N}	Neighbouring cell centroid position	L	m
N, n	Total number, number variable		
\mathbf{n}	Unit normal vector	L	m
\mathbf{P}	Cell centroid position	L	m
p, P	Pressure, ensemble average pressure	M/Lt^2	Pa
\mathbb{P}	First tensor invariant		
\mathbb{Q}	Second tensor invariant		
\mathbb{R}	Third tensor invariant (Determinant)		
\mathbf{R}	Mean resolved Reynolds stress	L^2/t^2	m^2/s^2
\mathbf{S}	Rate of strain tensor	t^{-1}	s^{-1}
S	Source term		
\mathbf{T}	Mean total Reynolds stress	L^2/t^2	m^2/s^2
t	Time	t	s
\mathbf{u}, \mathbf{U}	Velocity instantaneous and ensemble average	L/t	m/s
u, v, w	Velocity components	L/t	m/s
u_τ	Shear velocity, $\sqrt{\tau_w/\rho}$	L/t	m/s
V	Volume	L^3	m^3
\mathbf{W}	Anti-symmetric part of $\nabla \mathbf{U}$	$t^{-1} s^{-1}$	
\mathbf{x}	General spatial coordinate	L	m
x, y, z	Coordinate components	L	m
y_w	Wall distance	L	m

Greek Symbols

α	Generic parameter		
β	Generic parameter		
δ_b	Boundary layer thickness	L	m
Δ	Filter size, mesh related length scale	L	m
Δ_s	Streamwise displacement	L	m
η	Kolmagorov dissipation scale	L	m
ϵ	Turbulent energy dissipation	L^2/t^3	J/kg s
γ	Scaling coefficient		
Γ	Diffusivity coefficient		
κ	Von Karman constant		
λ	Tensor eigen value		
λ	Wave length	L	m
ν	Kinematic viscosity	M^2/t	m^2/s
ϕ	Generic scalar quantity		
ψ	Spatial energy flux	L^3/t^3	m^3/s^3
ρ	Density	M/L^3	kg/m^3
σ	Mean sub-grid scale stress magnitude	L^2/t^2	m^2/s^2
ς	Standard deviation		
$\tau, \boldsymbol{\tau}$	Stress magnitude and tensor	M/Lt^2	kg/ms^2
θ	Momentum thickness	L	m
ω	Vorticity	t^{-1}	s^{-1}

Subscripts

\parallel	Parallel
0	First off-the-wall grid point
$1, 2, 3$	Direction or position indices
b	Bulk, freestream
c	Centre
d	Dissipation
DES	Detached eddy simulation
et	Eddy turnover
f	Face based quantity
ft	Flow through
GS	Resolved scale
i	Spatial or summation index
rms	Root of the mean squares
s	Displacement property
SGS	Sub-grid scale
τ	Shear based
t	Turbulent
w	Wall or wall-derived property
x, y, z	Direction indicators

Superscripts

$+$	Wall units
$'$	Fluctuating component
$''$	Deviatoric component
e	Inertial property
T	Transpose

Oversymbols

- Filtered
- \sim Test filter

Dimensionless Groups

CFL	Courant number	$\frac{F_f \Delta t}{ \mathbf{A} \mathbf{d} }$
P^+	Pressure gradient parameter	$\nu \frac{dP}{dx} \frac{1}{u_\tau^2}$
Re	Reynolds number	$\frac{ \mathbf{u} L}{\nu}$
Re_τ	Shear velocity based Reynolds number	$\frac{u_\tau h}{\nu}$
Re_θ	Momentum thickness based Reynolds number	$\frac{U_b \theta}{\nu}$
St	Strouhal number	$\frac{fd}{U}$
U^+	Shear normalised velocity magnitude	$\frac{U}{u_\tau}$
y^+	Wall unit normalised wall distance	$\frac{yu_\tau}{\nu}$

Nomenclature

Chapter 1

Introduction

Turbulence, the pseudo-random and apparently unpredictable state of a fluid, is one of the most challenging problems in fluid dynamics. Turbulent flows show a marked increase in mixing and friction and the prediction of these phenomena is of great importance in practical engineering applications. Consequently, numerous scientists have invested a great deal of effort in the observation, description and understanding of turbulent flows. One of the first attempts at quantifying turbulence was made by Reynolds [131], who showed that the flow regime changes from its orderly laminar state to a turbulent one, when a critical parameter (Reynolds' number) is exceeded. Another important discovery was that turbulent flows incorporate a hierarchy of eddies or whirls, which range from large scales to very small in size. Energy is transferred between these scales, generally from the larger to the smaller, until finally the smallest scales are dissipated into heat by molecular viscosity. This energy cascade theory was formulated into physical laws for the various scales present in turbulent flow by the Russian scientist Kolmogorov [83].

The study of turbulent flows can be divided into three main categories: analytical theory, physical experiments and numerical simulations. The analytical approach to turbulence has faltered against the complexity of the problem that is stochastic and strongly nonlinear in nature and is consequently of limited use as a general tool. Experimental fluid dynamic research has always been of great significance. It still remains the benchmark for the validation of new models and for the foreseeable future will continue to be of fundamental importance in the field. Also, the advent of new measuring techniques

1. Introduction

that allow single- and multi-point sampling of flow characteristics, such as Laser-Doppler velocimeters and multiple wire anemometers, have significantly increased the utility and range of experimental measurements.

Numerical simulation has become evermore popular in the last few decades. From a practical viewpoint, computational fluid dynamics is a lot more flexible and cost effective than experimental methods. It has the advantage that any flow quantity may be sampled at any point in the field and instantaneous field values may be obtained for the whole domain. For engineering applications, numerical simulations of turbulent flows have one major drawback: their inability to guarantee accuracy under all conditions. Even though simulation techniques have become well established as a means of studying turbulent flows, the results of simulations are currently best presented in combination with experimental data, to confirm validity. (Methods that are exceptions and guarantee greater general accuracy exist, but are staggeringly expensive.) Consequently, the development of a cost effective, generally accurate simulation method is probably the main focus of research in computational fluid dynamics.

1.1 Simulating Turbulence

The starting point for the numerical modelling of turbulent flows is formed by the Navier-Stokes equations, which represent conservation of mass and momentum. The most straightforward approach to the solution of turbulence is **Direct Numerical Simulation** (DNS), which directly solves the Navier-Stokes equations by discretisation and numerical algorithms. DNS attempts to solve all scales of motion in the fluid, from the largest coherent structures to the smallest dissipating eddies, without any averaging or smoothing of the solution field, *i.e.* DNS fully resolves the flow. As a consequence, there are no turbulent modelling assumptions or empirical correlations included in the solution and the only difference between the simulation and its experimental equivalent should be errors introduced by numerical approximations. For a sufficiently fine mesh and an error-minimising numerical scheme DNS can be considered exact, delivering an accurate three-dimensional, time-dependent solution.

Small scales in turbulent flow are generated by inertial forces and dissipated by viscous forces. The viscous forces are relatively small if the Reynolds number is high, which leads to the formation of a relatively large proportion of small scales. To capture all of the dissipation, the grid size must be no larger than the viscously determined Kolmogorov scale, $\eta = (\nu^3/\epsilon)^{1/4}$. In addition, the grid domain must be large enough to encompass the largest turbulence scales (and the flow domain). For a uniform grid, this relates to at least L/η grid points in each direction (where L is the integral scale or domain length). Practically, since this number of points must be employed in all three dimensions and the time step is related to the grid size, this means that the cost of the simulation is proportional to the Reynolds number cubed [7]. Secondly, highly accurate, high-order (expensive) discretisation schemes have to be used to limit dispersion and dissipation errors. For these reasons and given the current state of computational capacity, DNS is largely limited to simple geometries (flat plate, homogeneous turbulence, channel) at relatively low Reynolds numbers.

In order to reduce the amount of scales to be resolved, an averaging operator may be applied to the Navier-Stokes equations. The classical averaging method is the ensemble average, which produces the **R**eynolds **A**verage **N**avier-**S**tokes equations (RANS). From a practical point of view, this is equivalent to an infinite set of experiments being sampled at the same time, the average of all the flow fields representing the ensemble average. For a time independent and/or non-cyclic flow, ensemble averaging will produce the same result as time averaging. The RANS equations for an incompressible turbulent velocity field are given by:

$$\frac{\partial \mathbf{U}}{\partial t} + \nabla \cdot (\mathbf{U} \mathbf{U}) = -\frac{1}{\rho} \nabla P + \nabla \cdot \left[\nu (\nabla \mathbf{U} + (\nabla \mathbf{U})^T) \right] - \frac{1}{\rho} \nabla \cdot \boldsymbol{\tau}, \quad (1.1)$$

where uppercase denotes averaged quantities. The averaging of the non-linear terms introduces new unknowns into the equation in the form of the Reynolds stress tensor, $\boldsymbol{\tau}$. This stress tensor represents the effects of all turbulent fluctuations and has to be modeled to close the system. A large number of turbulence models are available, from simple algebraic [129] to the commonly used $K - \epsilon$ models [87], to full Reynolds stress closures [61].

In contrast to DNS, this computational technique can currently be employed to solve

1. Introduction

flows in complex geometries and at high Reynolds numbers, making it the method of choice in engineering practice. Unfortunately, the RANS approach suffers from one principal shortcoming: the turbulence model must represent a very wide range of scales. While the small scales tend to depend mainly on viscosity and are somewhat universal, the larger structures are affected strongly by the boundary conditions. This means, for example, that models that are designed for channel simulation, will perform poorly when used to calculate separating or free shear flows. It does not seem possible to model the effects of the large scales of turbulence in the same way in flows that are very different. It is this lack of consistency that has led to interest in new approaches, such as large eddy simulation.

Having described the methods that bracket it, we now introduce the principal subject of the project, **Large Eddy Simulation (LES)**. LES does not resolve the full range of turbulent scales (as DNS does), but it captures a much larger range of scales than the Reynolds average equations. As an analogy, one can think of LES as a compromise between DNS and RANS; direct simulation being applied to the large scales, while the small scales are averaged out and their effect modeled. This approach appears to be justified because the large eddies contain most of the energy, do most of the transporting of conserved properties and vary most from case to case. In contrast, the smaller eddies are believed to be more universal (largely independent of the boundary conditions) and therefore easier to model.

Since the contribution of the small-scale turbulence to the resolved flow field is small, the errors introduced by their modelling should also be small. In addition, the resolved scales carry much more information than the mean flow predicted by the RANS approach. LES is therefore potentially much more accurate than RANS and when compared to DNS, its demand on computer resources is considerably smaller, since the smallest scales need not be resolved. In addition, LES surface time-pressure histories have proven to be ideal for predicting low Mach number aero-acoustic noise sources, an important consideration in automotive design and other fields. Given all these factors, the steady increase in computing resources and the advancing development of the technique, LES promises to take a prominent role in design environments of the near future.

1.2 Research Objectives

Since large scale turbulent structures are inherently three-dimensional and time-dependent, LES, which captures these structures, must also be so. This and the increased resolution requirements, make LES somewhat more expensive than traditional steady-state RANS simulations. In addition, all facets of LES are highly dependent on the Reynolds number when it comes to modelling near-wall regions. The dimensions of significant flow features in this zone, scale as a function of the inverse of the Reynolds number [7]. Thus in LES calculations of moderate to high Reynolds number flows, the boundary layer region typically contains more than 50% of the domain's total grid points. To date these factors have limited the widespread application of LES to basic flows and test cases.

Keeping these limitations in mind, the broad objective of the project was defined as the assessment and development of LES as a tool for general wall bounded flow calculations. In terms of specific applications, the required emphasis was on flow regimes relevant to external automotive aerodynamics. In order to meet these requirements, it was realized early on that the cost of simulating the turbulent boundary layer had to be significantly reduced. To this end, the implementation of economical near-wall treatments was proposed as one of the main routes to attaining these goals. Several such wall treatments have been developed in recent years (see [10, 20, 116, 126, 136, 163]). Although most offer some form of improvement in efficiency compared to well resolved LES, few of them have been extensively tested in engineering relevant flows. A large portion of this work is therefore devoted to the investigation of the suitability of selected wall treatments for the simulation of cases of the aforementioned type.

An additional field of investigation is computational aero-acoustics, predicting the noise produced by aerodynamic interactions. Advances in air, ground and space transportation have sparked fresh growth in the area, with the minimisation of aerodynamic noise around passenger vehicles being a big impetus for increased sophistication of aero-acoustics calculations in the automotive industry. LES has a massive advantage over more traditional RANS-derived methods of sound prediction [9], in that the actual sources of noise can be directly calculated from the time- and space-resolved flow field. Thus while

1. Introduction

averaged methods must attempt to reconstruct the sound spectra from one point statistics and assumed distributions, direct methods like LES can provide the spectra explicitly. The actual sound sources come in three varieties: mono-pole sources, which account for sound produced by oscillators like microphones; dipole sources which act like two adjacent monopole sources that are 180° out of phase and the more complicated quadrapole sources which are produced by unsteady Reynolds stresses. In automotive applications most of the aerodynamic noise is caused by dipole sources [35], which are produced by rapid pressure oscillations caused by turbulent interactions on the vehicle's surface. Reproducing these fluctuations numerically and comparing their characteristics with experiment, allows assessment of LES' capabilities and effectiveness as an aero-acoustic noise source predictor. In addition these investigations will allow quantification of the methodological requirements of the approach.

1.3 Thesis Outline

The thesis is divided into two parts based on subject matter. The first deals with the theories, derivations and methodologies employed as part of the investigation. These chapters also include the relevant literature surveys. The second section focuses on the validation and characterisation of the proposed approaches using a series of test cases. Overviews are presented below along with some salient points raised by each section.

1.3.1 Methodology

The first subject of investigation, is the characteristics of turbulence and in particular turbulent boundary layers. By drawing from the works of authors in the fields of turbulence theory, vortex dynamics and direct simulation, a cohesive picture of the turbulent boundary layer is produced. Understanding the dynamics and large scale properties of boundary layers is central to determining the requirements of a near-wall treatments in the LES approach.

Using these requirements as a basis, Chapter 3 focuses on evaluating the characteristics of existing treatments of near-wall flows and their suitability for use in aerodynamic/aero-

acoustic LES methods. Several categories of wall treatments are introduced and scrutinised along with past examples of their usage. Some possible modifications to these are proposed and the ramifications and relative merits of the different methodologies are discussed. Other sections of this chapter introduce the derivation of the LES governing equations and give an overview of the concepts and approaches to **Sub-Grid Scale** (SGS) modelling, leading finally to the choices of sub-grid scale models and wall treatments used during the current investigation.

Discretisation practices and other numerical concerns are presented in the next chapter (4). Also addressed is the issue of errors in LES. The different sources of errors in the LES methodology are identified, and some practices are introduced that ameliorate their impact. This is followed by a more in-depth look at the usage and validity of embedded mesh refinement. Specifically, several classes of mesh refinement indicator are identified. Mesh refinements techniques are adapted for LES and new approaches are proposed that take advantage of the unique properties of this methodology (e.g. prediction of turbulence spectra). The mesh refinement section is concluded by addressing the problem of embedded refinement boundaries. Such boundaries necessitate rapid change in cell size which invalidates some of the LES modelling assumptions and could also potentially introduce significant numerical error. The concept of turbulent length scale smoothing is advanced as a partial counter to this problem and a simple implementation is detailed.

1.3.2 Validation and Test Cases

The second portion of the thesis deals primarily with the validation of the various models and numerical practices through their application to pertinent test cases.

The first calculations were performed on the canonical fully developed turbulent plane channel flow shown in fig.1.1. This case is widely used in LES for first step validation of new SGS models and wall treatments, due to its geometric simplicity. Other advantages include the fact that it is computationally undemanding at low Re , has well defined boundary conditions and a plethora of DNS and experimental results for comparison.

Unfortunately, the simplicity of the domain and the accompanying fully developed flow is of limited utility for the rigorous validation of the wall treatments envisioned for

1. Introduction

use in more complex higher Reynolds number flows.

It still presents a relatively inexpensive benchmark test and method for error checking and provides first-hand experience and insight into the turbulent dynamics of a well documented flow. The easily discretised domain also makes it the ideal platform for investigating the effects of mesh density on the boundary layer's turbulent statistics and dynamics.

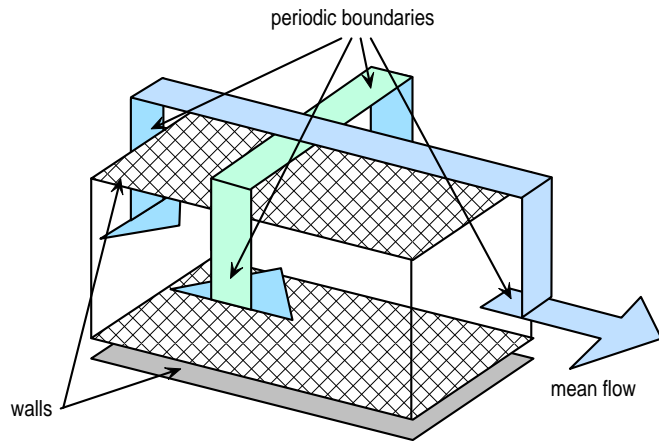


Figure 1.1: Plane channel flow calculation domain.

One of the oft advertised advantages of LES is its ability to predict relatively difficult problems, such as pressure-driven separation, with improved accuracy compared to traditional RANS methods. The asymmetric plane diffuser, the second test case illustrated in fig.1.2, represents just such a flow. Coupled with well defined boundary conditions and good experimental data, it makes an ideal validation case for LES. The comparatively low Reynolds number ($Re_b = 18000$) also makes it relatively inexpensive to compute, allowing greater latitude for experimentation that would be the case for a more demanding flow. The combination of the above factors makes the diffuser flow the perfect platform to investigate the various influences of SGS and wall modelling, grid resolution and local mesh refinement.

One of the original goals of the project was to simulate a full automobile-like shape at operational Reynolds numbers using LES. It quickly became apparent that this would not be feasible given the available computer resources. Audible noise generated through

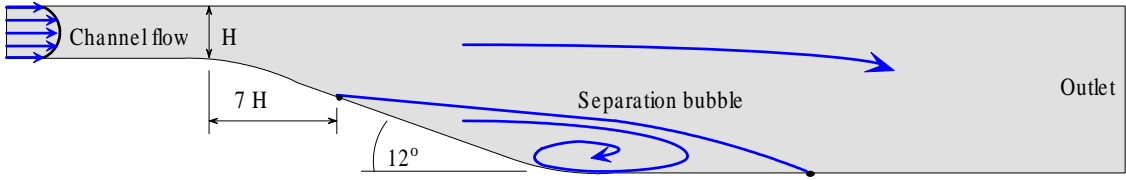


Figure 1.2: Diagrammatic representation of the asymmetric plane diffuser flow and calculation domain.

aerodynamic interaction only becomes significant at vehicle velocities in excess of 20 m/s. For a typical automobile, this is equivalent to a bulk Reynolds number of the order of 10^7 . Although the DES approach significantly reduces the number of grid points, aero-acoustic considerations require that pressure frequencies of several kHz must be resolved, resulting in (optimistic) estimates for the final mesh size in excess of 100 million cells. Coupling this to approximate time step requirements ($\Delta t = 10^{-5}$ s, $\Delta T \approx 2$ s, no. time steps = 2×10^5) leads to a computation that is within the realms of possibility, but not truly practical for an investigative study.

The wall-mounted side mirror test case, depicted in fig.1.3 represents a compromise between expediency and relevance. It consists of a half-cylinder topped by a quarter sphere of the same diameter mounted on a flat plate, which while providing a well defined and easily meshed geometry, still produces all the major flow features of the oft-studied [141][115] external car rear-view mirror. Successful simulation of the aero-dynamics and aero-acoustics on and around this idealized side mirror will lend considerable support to LES' ability to simulate these properties in a range of practical engineering flows. In addition, the wealth of experimental data, allows this case to act as a comprehensive test of the methodologies discussed and developed in earlier sections.

1.3.3 Accomplishments

The work closes with a summary of salient points and a discussion of significant results obtained during the validation and test cases. These include:

- The effect of mesh resolution on boundary layers dynamics.

1. Introduction

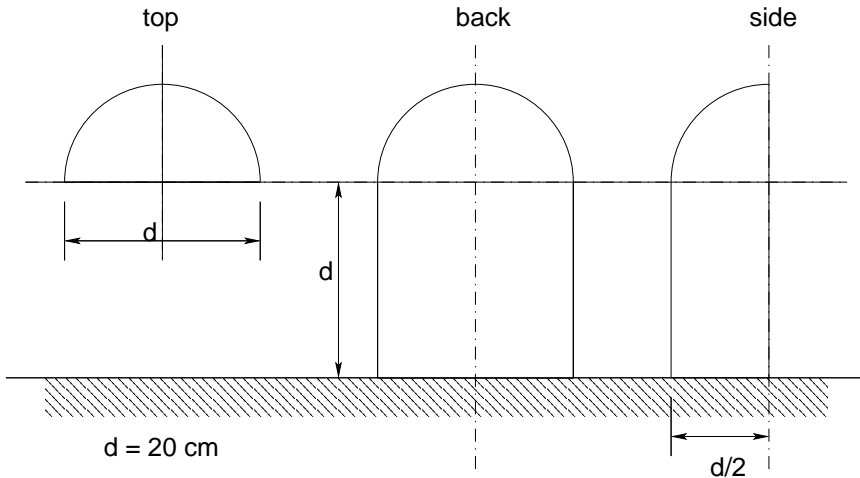


Figure 1.3: Idealised side mirror geometry.

- The impact of poor resolution on the performance of different wall treatments.
- Comparison of RANS and LES results for pressure-driven separating flow.
- The sensitivity of LES of separating flows to mesh resolution and local mesh refinement.
- Demonstration of error based mesh refinement techniques for LES.
- Aerodynamic and aero-acoustic noise source comparisons for two side mirror experimental data sets.
- The effects of wall treatments and mesh resolution on aero-acoustic noise source prediction.

Owing to these and other results, the main contributions of this thesis are identified as:

- Synopsis of the characteristics and dynamics of the near-wall turbulent cycle.
- Comprehensive survey of existing LES wall treatments and their relation to near-wall turbulence.
- Implementation and validation of two wall treatment approaches: DES and under-resolved LES for a variety of flow regimes.

- Development of effective inlet conditions for LES.
- Establishment of LES meshing requirements and practices with an emphasis on the effects of embedded refinement and mesh induced errors.
- Demonstration of LES as a broad spectrum aero-acoustic noise source predictor and superior aero-dynamic simulation methodology.
- Methodological guidelines for LES calculations from a cost-benefit perspective.

This thesis attempts to bring improved understanding and computational practices to the fields of turbulence and LES. While several questions related to the main topic were posed and answered, many significant problems yet remain. The last contribution of this study is to re-examine some of these questions and suggest routes for the future research and development of LES.

1. Introduction

Chapter 2

Turbulent Boundary Layers

One of the main contributing factors to the high cost of LES is the resolution requirements of the small-scale motions in the boundary layer. In order to successfully model and reduce the cost of simulating this region, the required properties of a near-wall treatment must first be ascertained. These properties are dictated by the interaction of the boundary layer with the core flow. Thus a better understanding of the underlying flow physics of the near-wall region, and especially the modes of interaction between this and the core region, becomes desirable.

One of the basic precepts of LES is that the smallest scales of turbulent motion can generally be modeled as an added dissipation without much loss of accuracy in the overall solution. The reasoning behind this assumption and how and when it becomes invalid forms the topic of our introductory section, which will lead us naturally to the study of more complicated boundary layer dynamics.

2.1 Turbulence Basics

Trying to define fluid turbulence without being pedantic can be challenging. Generally, it is described as “*an irregular motion in rotational flows that obeys the constraints of probability*” (Hinze [55]). There is much disagreement on what exactly constitutes the phenomenon however, never mind understanding its complexities. Fortunately, very little of this ongoing debate is directly relevant to this investigation, allowing us to sidestep

2. Turbulent Boundary Layers

the more difficult questions entirely. For our purposes, we define turbulence following the lead of Lesieur [90]:

- Firstly, turbulence flow must be chaotic in the sense that a small initial differences will be amplified and eventually lead to completely uncorrelated fields. This implies that the deterministic prediction of a turbulent flow is practically impossible.
- Secondly, turbulence should be able to mix any transported quantity (including momentum) much more rapidly than molecular diffusion alone.
- Finally, the scales at which this mixing occurs should include a wide range of spatial wave lengths.

Even this definition is rather vague and descriptive, although both the second and third points have direct implication for the computational treatment of turbulent flows, as shall be discussed later. Nevertheless, the principal physical features of these flows are now well determined, allowing a qualitative understanding of their behaviour under most engineering relevant conditions.

Where does turbulence come from? It has been repeatedly shown that turbulence can only develop and persist in rotational flow, *i.e.* in the presence of shear. Such velocity gradients provide the energy differential that transforms small initial perturbations into larger scale motions, through various instability growth mechanisms. The process becomes possible when inertial forces exceed the influence of viscous effects, so that the small perturbations are no longer damped by the molecular viscosity (*i.e.* at large Reynolds numbers). The larger motions then generally degenerate into the finer, more random structures that we know as turbulence. Determining the details of instability mechanisms is an ongoing investigation employing both analytical and numerical tools. To date, some of the growth in perturbations have been explained within the framework of linear stability theory, mainly in the initial stages of their development. A small portion of this will be covered in a later section with reference to boundary layers.

Another turbulent process that is still only vaguely understood is the breakdown of the larger coherent structures into “noisy” eddies. The phenomena is much less amenable to theoretical treatment, and is currently classified only as “*breakdown through series*

of successive instabilities” [90]. In contrast to the more structured parent vortices that sometimes display predictable and/or cyclical behaviour, these entities are completely three dimensional, pseudo-random and tend to be independent of the parent’s formation mechanism. Surprisingly, the scale distribution of these eddies agrees very well with the phenomenological predictions of Kolmogorov [83]. Kolmogorov’s theory assumes that the turbulent energy content of isotropic (invariant under rotation) turbulence is dependent on only the rate of energy dissipation, ϵ , at which the smallest scales of turbulence convert motion into heat and the wavenumber, k , (proportional to the inverse of the eddy lengthscale). This implies, that provided the length scale at which the turbulence energy is injected into the system is sufficiently far removed from that at which the energy dissipates into heat, that the character of the turbulence will be independent of both the large forcing scales and molecular viscosity. A remarkable conjecture, but one that has been found experimentally to hold true for a wide range of flows, from the atmosphere [26] to jets [51]. This also implies that the turbulence tends to behave in an isotropic fashion, a fact that has much bearing on the practicalities of LES.

Kolmogorov’s law is expressed graphically as a line of constant slope in fig.2.1 representing turbulent energy spectrum, which can be derived using dimensional analysis:

$$\mathbb{E}(k) = C_k \epsilon^{2/3} k^{-5/3}, \quad (2.1)$$

where C_k is a universal constant, experimentally determined to be of the order of 1.5. Broadly speaking, the idealised spectrum can be subdivided into several sections:

- The energy-containing, or integral scales, k_i ; these include unstable motions of permanent character, but also more importantly the scales at which turbulent energy is (generally speaking) introduced to the system. These large eddies contain by far the most turbulent kinetic energy.
- A second section contains the transitive scales, more commonly known as the inertial sub-range. These are the scales that obey Kolmogorov’s law, *i.e.* they are independent of the forcing scales, yet are dominated by inertial forces rather than viscosity. In addition, these scales contain and dissipate very little turbulent energy. Their main action is the transfer of energy from the large scales to the very small.

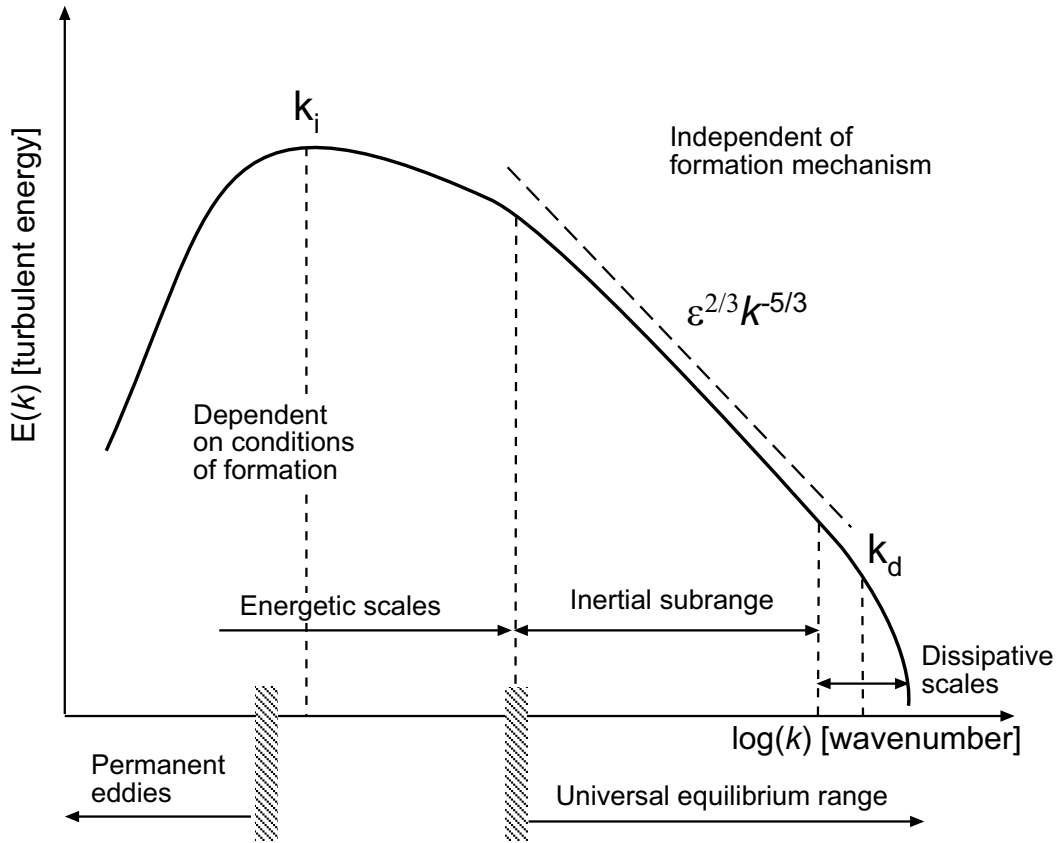


Figure 2.1: Three dimensional incompressible flow topologies (adapted from Hinze [55]).

- The final part of the energy spectrum is the dissipative range. These are scales of motion smaller than the Kolmogorov scale, $k_d \propto (\epsilon/\nu^3)^{1/4}$, the length at which viscous effects start to strongly damp the turbulent motion. The end of the curve is characterised by a rapid, almost exponential dropoff in energy content, which also accounts for the bulk of energy dissipation within the turbulent cascade. Together with the inertial subrange, the dissipative scales constitute what is known as the universal equilibrium range, because the turbulence is considered to be fully developed and free from the disruptive influence of boundaries and other forcing effects.

Despite its prevalence, this shape of the turbulent energy spectrum is far from universal. For example, if energy is added to the system close to the dissipative scales an inertial subrange will not be able to develop. Also, large scale intermittency and other unsteady

phenomena can disrupt and/or modify the distribution of the inertial range [174].

The conversion of bulk fluid kinetic energy into turbulent energy can be divided into two broad categories, both of which involve the existence of a mean shear field. The first is free-shear flows such as mixing layers, jets and wakes and the second is wall-bounded flows such as boundary layers, pipes and channels. In free-shear flows the growth of instabilities is coupled to an inflectional velocity profile and is essentially an inviscid process [173]. These kind of instabilities generally develop into large unsteady quasi two-dimensional vortices through processes like Kelvin-Helmholtz waves in mixing layers (fig.2.2) or Karman vortices in wakes. Sometimes the large vortices can roll up into even larger structures due to vorticity conservation and their two-dimensional nature. Simultaneously however, the vortices degenerate into smaller eddies through the cascade process described earlier. It is important to note that for free-shear flows the most energetic rate-controlling structures are large. This implies that for equilibrium conditions the small scales will generally tend to obey Kolmogorov's law, making them amenable to statistical treatment.

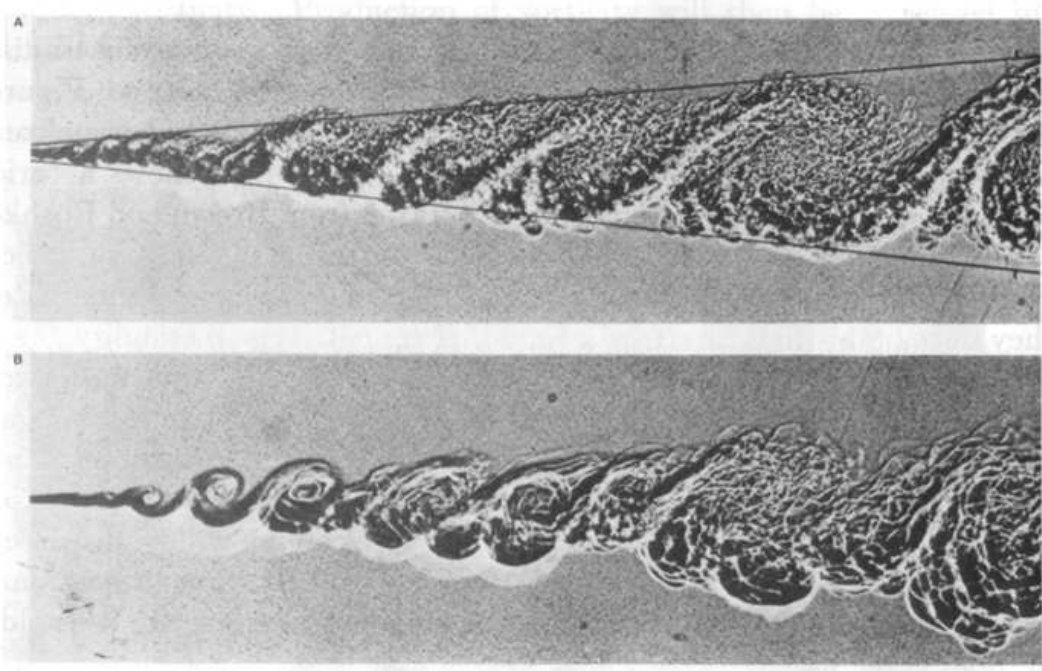


Figure 2.2: Turbulence in a mixing layer. The Reynolds number in the top slide is twice that in the bottom one. (from Brown and Roshko [17]).

Wall-bounded flows, on the other hand, do not allow the inviscid growth of linear instabilities. Instead, the limiting influence of a solid boundary on the scales of motion means that primary instabilities develop through a viscous process, that may or may not induce inviscid secondary instabilities. The presence of the wall also poses a physical limit to the growth of the instabilities, so that the resulting vortices are restricted in scale to some fraction of the distance to the surface. This means that the energetic eddies close to the wall are small, turbulent energy is added at high wavenumbers and a classical inertial range is unlikely to exist. Moreover, experiments have shown (see for example Kim *et al.* [82]) that the energetic near-wall eddies are just as anisotropic and inhomogeneous as the large vortices in free-shear flows, although their shape and dynamics differ markedly. The implications of this for simulation purposes is twofold:

- Firstly, since turbulent energy is introduced into the system at small scales near the surface, there must be some mechanism in the flow allowing its transport to larger scales away from the wall
- and secondly, the anisotropy of the small scales means that models based on assumptions of isotropy will fail to accurately predict their actions.

The rest of this chapter deals primarily with the issues of anisotropy and transport of energy away from the wall and how this impacts attempts to model turbulent wall-bounded flows. The approach taken focuses on the coherent structures in this region and the dynamics that produce the characteristic boundary layer phenomena. First however, the building blocks of turbulence, vortices are introduced and visualisation methods investigated.

2.2 Vortex Identification

Turbulence is not just random noise, but includes spatially coherent, temporally evolving vortical motions (more popularly known as **Coherent Structures (CS)**). Since incoherent turbulence decays much quicker than coherent structures [71], the latter have a much greater influence on transported turbulent characteristics. The study of the behaviour of

these structures is known as vortex dynamics and focuses on the evolution and interaction of coherent structures with each other and the background turbulence. In recent years vortex dynamics has begun to shed some light on the processes that govern the coherent structures in near-wall turbulence [71, 75, 76, 137] and produced a better understanding of their general contribution to the flow.

Before continuing the review of the current theories on near-wall coherent structure dynamics, we must first answer the question: "*What is a vortex?*" Over the years there has been a lot of debate concerning the exact definition of a vortex, especially in wall bounded turbulent flows. The main problem being that most of the earlier eduction methods and definitions allowed for some ambiguity and/or "false positives" in the identification of a vortex. To highlight this problem a few examples of these "inadequate" schemes may be considered.

2.2.1 Vortex Eduction Methods

One of the first definitions of a vortex was given by Lamb [86] as a vortex tube whose surface consists of vortex lines. The existence of a vortex tube does not however guarantee the presence of a vortex, since, for instance, a laminar pipe flow can contain vortex tubes, but exhibits no vortex characteristics. An investigation of currently used vortex indicators by Jeong and Hussain [70] reveals shortcomings in several of the more intuitive approaches, reproduced here in brief:

- *Local pressure minimum* - Since vortices contain a balance of low pressure forces and centrifugal forces, they tend to have a pressure minimum along their axis of circulation. It has been shown by Robinson [133] using a DNS database, that this method can capture vortical structures in a turbulent boundary layer. However, the cutoff pressure level can not be reliably set to capture all the coherent structures in a flow. Jeong and Hussain [70] identify several conditions where the pressure minimum criterion will falsely indicate the presence of vortices. They also note that there is an inherent scale difference between vortex cores and the associated pressure criterion, that when coupled with the above-mentioned pressure level problem, makes the

2. Turbulent Boundary Layers

demarcation of vortices using an iso-pressure surface difficult.

- *Streamlines* - First proposed by Lugt [97], stream or path-lines can be used to detect vortices by requiring that they describe a closed or spiral path. The first drawback of these methods is that they are not Galilean invariant. Thus a vortex might be detected in one reference frame but not in another moving at a different relative speed. In practice this means these methods will obscure two or more vortices moving at different speeds and will fail completely in a turbulent flow where there are many vortices all being advected at dissimilar speeds. The path-line method, also has the added drawback that the stable life of the vortical structure may be shorter than the time it takes a particle to describe a complete rotation of the vortex core. Thus vortices with a high rate of deformation will remain unnoticed.
- *Vorticity magnitude* - One of the most widely used methods for educing coherent structures and representing vortex cores [13, 60, 107] is the vorticity magnitude, defined as

$$\omega = |\nabla \times \mathbf{U}| \quad (2.2)$$

Which has been used with a fair amount of success in free shear flows. However, it may not be suitable in wall shear flows, since ω does not identify vortex cores if the background shear is of comparable magnitude to the vorticity magnitude inside the vortex. It has also been shown [72, 97] that the maximum vorticity magnitude in wall-bounded flows always occurs at the wall surface. Therefore, since a vortex core cannot coincide with the wall, ω is not a suitable measure for identifying vortices in a boundary layer.

In response, Jeong and Hussain[70] proposed two requirements for the objective definition of a vortex core (at least one of which is failed by each of the above eduction methods),

- Vortex cores must have net vorticity and net circulation, so that potential vortices are excluded.
- The geometry of the vortex core should be Galilean invariant.

Recently, three different such Galilean-invariant definitions of a vortex, using the properties of the velocity gradient tensor ($\nabla\mathbf{U}$), have been proposed [29, 58, 70, 104]. A short description and a listing of comparative merits of each follows.

Complex Eigenvalues of $\nabla\mathbf{U}$

Chong *et al.* [29] use the eigenvalues of the velocity gradient tensor to derive a local classification of the various streamline patterns that occur in three dimensional flow. The classification uses a moving coordinate transformation in which the frame of reference remains attached to a given particle in the flow, with the result that structural features of the flow are precisely defined and frame-independent. They propose that a vortex core is defined as a region with complex eigenvalues of $\nabla\mathbf{U}$, which in turn implies that the streamlines relative to the point velocity are closed or have a spiral pattern if the criteria are met. The eigenvalues of $\nabla\mathbf{U}$ satisfy the characteristic equation

$$\lambda^3 - \mathbb{P}\lambda^2 + \mathbb{Q}\lambda - \mathbb{R} = 0. \quad (2.3)$$

Here the first invariant $\mathbb{P} \equiv \nabla \cdot \mathbf{U} = 0$ for incompressible flows, \mathbb{R} the third invariant is equal to the determinant of $\nabla\mathbf{U}$ and second invariant \mathbb{Q} is given by

$$\mathbb{Q} \equiv \frac{1}{2} (||\mathbf{W}||^2 - ||\mathbf{S}||^2), \quad (2.4)$$

where \mathbf{W} is defined as the antisymmetric part of the velocity gradient tensor and \mathbf{S} is the local rate of strain tensor thus,

$$\mathbf{W} = \frac{1}{2} (\nabla\mathbf{u} - (\nabla\mathbf{u})^T), \quad (2.5)$$

$$||\mathbf{W}|| = (\mathbf{W}:\mathbf{W})^{1/2}, \quad (2.6)$$

$$\mathbf{S} = \frac{1}{2} (\nabla\mathbf{u} + (\nabla\mathbf{u})^T), \quad (2.7)$$

$$||\mathbf{S}|| = (\mathbf{S}:\mathbf{S})^{1/2}. \quad (2.8)$$

For the eigenvalues in eq.2.3 to be complex, the discriminant (\mathbb{D}) must be positive, *i.e.*

$$\mathbb{D} = \left(\frac{1}{3}\mathbb{Q}\right)^3 + \left(\frac{1}{2}\mathbb{R}\right)^2 > 0. \quad (2.9)$$

A more concise explanation of the physical significance of these terms can be seen in fig.2.3. When $\mathbb{D} > 0$, two of the eigenvalues will be complex and one real and the flow will

be characterised by swirling and axial motion around the point, labeled as a focus. The exact direction of this motion is governed by the third invariant \mathbb{R} . If \mathbb{R} is positive the fluid moves away from the centre in the plane of the spiral and toward it along the axis because of the incompressibility condition (upper right quadrant fig.2.3), while if \mathbb{R} is negative the motion is reversed. In either case, the swirling motion is indicative of coherent structures and can be used to identify flow features as such. If the discriminant is negative on the other hand, all the eigenvalues are real and the point will experience non-swirling radial inflow (or outflow depending on the sign of \mathbb{R}) and a corresponding mass conserving axial flow. Also, the first term on the right hand side of eq.2.4 is proportional to the total entropy, while the second is proportional to the kinetic energy dissipation rate. Since both these quantities are always positive, large positive \mathbb{Q} indicate regions where the rate of strain is dominated by the rate of rotation (and *vice versa*).

It must be emphasised that both the velocity gradient tensor and its invariant are constant in any inertial frame of reference and thus Galilean invariant, so that this definition conforms to the previously mentioned requirements.

Positive Second Invariant of $\nabla\mathbf{U}$

The second eduction method, by Hunt *et al.* [58], defines an eddy as a region where the second invariant \mathbb{Q} of $\nabla\mathbf{U}$ (from eq.2.4) is greater than zero. They also require that the local pressure be lower than the ambient value, which is not explicitly guaranteed by the $\mathbb{Q} > 0$ condition, but was found to be true in most cases. It can be seen from fig.2.3 that the $\mathbb{Q} > 0$ condition is more restrictive than the $\mathbb{D} > 0$, so that any area that is identified as a vortex by the former will also be acknowledged by the latter (the reverse is not necessarily true).

Second Largest Eigenvalue of $\mathbf{W}\cdot\mathbf{W} + \mathbf{S}\cdot\mathbf{S}$, $\lambda_2 < 0$

The last method for identifying vortex cores was proposed by Jeong and Hussain [70]. Their definition stems from the premise that vortex cores contain a local pressure minimum. Two effects are identified that cause the inconsistencies in previously used pressure based detection schemes:

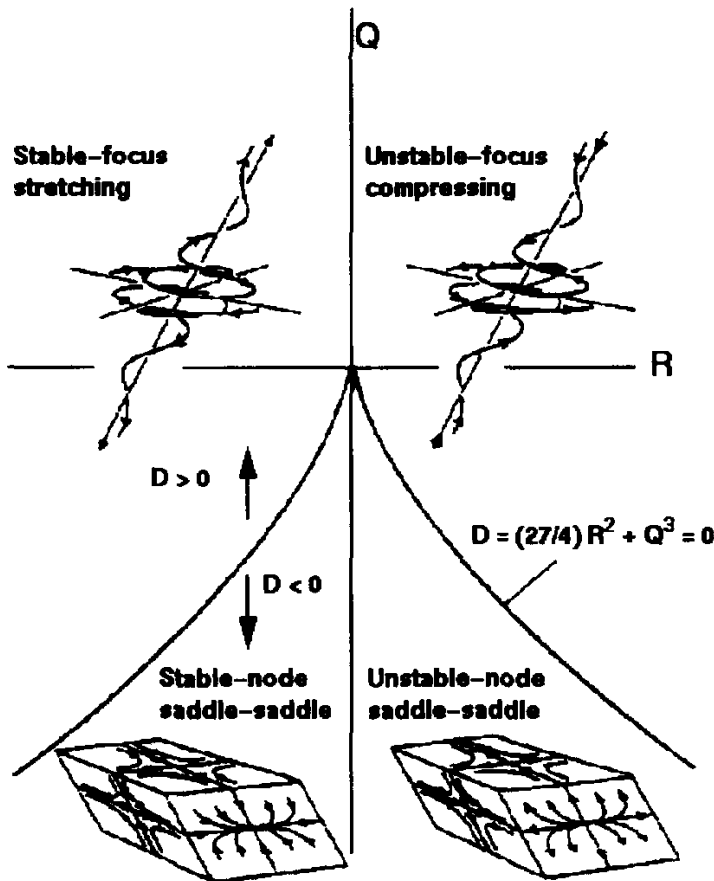


Figure 2.3: Three dimensional incompressible flow topologies (reproduced from Soria et al. [145]).

- Unsteady straining, which can create a pressure minimum without a swirling or vortical motion.
- Viscous effects, which can eliminate a pressure minimum where vortices do in fact exist.

An improved indication for the presence of a vortex can thus be gained by excluding the influence of these factors. Now recall that the second partial derivative (or Hessian) of a scalar function is positive definite in the region of a minimum, negative near a maximum and indefinite at a saddle point. This methodology is applied to the pressure field to find

the local pressure extremes, by taking the gradient of the Navier-Stokes equations

$$\nabla \frac{\partial \mathbf{u}}{\partial t} + \nabla \nabla \cdot (\mathbf{u} \mathbf{u}) = -\nabla \left(\frac{1}{\rho} \nabla p \right) + \nabla \nabla \cdot [\nu (\nabla \mathbf{u} + \nabla \mathbf{u}^T)]. \quad (2.10)$$

Recalling the definitions of \mathbf{S} (eq.2.5) and \mathbf{W} (eq.2.7), the acceleration gradient on the left hand side of eq.2.10 can be decomposed into a symmetric and antisymmetric part as follows:

$$\underbrace{\left[\frac{D\mathbf{S}}{Dt} + \mathbf{W} \cdot \mathbf{W} + \mathbf{S} \cdot \mathbf{S} \right]}_{symmetric} + \underbrace{\left[\frac{D\mathbf{W}}{Dt} + \mathbf{W} \cdot \mathbf{S} + \mathbf{S} \cdot \mathbf{W} \right]}_{antisymmetric}. \quad (2.11)$$

Setting the antisymmetric part of eq.2.11 equal to the antisymmetric part of the viscosity term in eq.2.10 returns the vorticity transport equation. The remaining symmetric part of eq.2.10 can now be written as,

$$\frac{D\mathbf{S}}{Dt} + \mathbf{W} \cdot \mathbf{W} + \mathbf{S} \cdot \mathbf{S} - \nu \nabla^2 \mathbf{S} = -\frac{1}{\rho} \nabla \nabla p. \quad (2.12)$$

As mentioned previously however, the unsteady irrotational straining (represented by $D\mathbf{S}/Dt$) and viscous effects ($\nu \nabla^2 \mathbf{S}$) contribute to the gradient of the pressure gradient field, but do not in fact indicate vortices and are therefore removed from consideration. Thus only the argument $\mathbf{W} \cdot \mathbf{W} + \mathbf{S} \cdot \mathbf{S}$ determines the existence of a local pressure minimum due to vortical motion. In accordance with the definition of the Hessian, a vortex core can now be defined as a connected region with two negative eigenvalues of the $\mathbf{W} \cdot \mathbf{W} + \mathbf{S} \cdot \mathbf{S}$ tensor. Now since the tensor is symmetric the eigenvalues, λ_1 , λ_2 and λ_3 will be real only if $\lambda_1 \geq \lambda_2 \geq \lambda_3$. A vortex can thus be educed if the second largest eigenvalue of $\mathbf{W} \cdot \mathbf{W} + \mathbf{S} \cdot \mathbf{S}$ is less than zero, $\lambda_2 < 0$.

2.2.2 Comparison

A comprehensive case by case comparison by Jeong and Hussain [70] clearly shows the superiority of the positive second invariant (\mathbb{Q}) and second largest eigenvalue (λ_2) methods compared to the vorticity and discriminant definitions. As mentioned before, the vorticity criterion will sometimes include irrotational straining near solid boundaries. It was also found that the vorticity magnitude produces spurious positives near streamwise vortices located in a shear flow and has a similar problem to the pressure definition: different

choices of vorticity level may result in distinctly different vortex patterns. The discriminant method does not suffer from false positives near walls or inaccuracies caused by shear flows. It does however, incorrectly indicate the presence of vortices in curved flows with a positive velocity gradient normal to the inside of the curvature. The discriminant criteria was also found to produce very noisy boundaries and small scale structures in the absence of net vorticity. None of the above problems were encountered for the λ_2 and \mathbb{Q} methods.

When comparing the second invariant and second eigenvalue definitions, the differences are less pronounced. Both methods seem to reliably describe the exteriors of vortex cores. The main difference was found to occur near centres of rotation, where the second invariant tends to exclude pockets of low rotational energy near the vortex axis from the core region (if straining influences exceed those of vorticity). It is doubtful whether this distinction is significant, since visualisations and other applications normally consider only vortex exteriors. Overall, provided Jeong and Hussain's analysis is correct, the $\lambda_2 < 0$ criteria seems to presents an unambiguous and accurate method for vortex eduction.

2.3 The Near-wall Turbulence Cycle

In turbulent flows coherent structures near the wall are generally held to be the cause of the drastic increase in drag and heat transfer in these regions. In addition, the transport of energy from these structures to the core flow is the source of the boundary layer's characteristic logarithmic profile [75]. Clearly a better understanding of the underlying mechanisms is important for improved treatment of the turbulent boundary layer. Given the tools for the reliable identification of these structures, the next step is to use these methods to investigate the dynamics of the near-wall region.

Solid boundaries interact with fluid flows by retarding motion tangential to the surface via viscous shear and by blocking the motion of fluid normal to the interface. Although walls are a defining influence with regard to mean flow properties, the effects are so varied that they are difficult to catalogue. With regard to turbulent properties however, solid boundaries have distinct local and non-local modes of influence. Here non-local modes

2. Turbulent Boundary Layers

are defined for the purposes of this investigation as bulk flow phenomena that affect the flow's turbulent characteristics, but are not in close physical proximity to the surface that produces them. Typical examples include flows with strong curvature, separation induced free shear layers and other bulk flow phenomena that encourage or attenuate turbulent structures. Non-local modes are typically not very Reynolds number dependent and as a result their effects are usually well reproduced by LES. The character and extent of these phenomena must still be taken into account however, since they can strongly influence the mesh spacing needed to resolve a particular portion of the flow. A subset of non-local effects in the form of large scale pressure gradients are discussed further in sec.2.4.2.

We define local modes of wall interaction as the retardation of the flow due to viscous shear and the limiting influence of the wall on turbulent scales of motion perpendicular to the surface. The near-wall shear functions as a source of turbulent energy for coherent structures in the buffer- and log-layers produced through various instability mechanisms. The dynamics of this turbulence production have been debated for many years (see Robinson [133] and Panton [118] for more comprehensive reviews). Although many prominent features such as low speed streaks, longitudinal coherent structures and a variety of vortical configurations have been catalogued in the near-wall region, their generation mechanisms and influence on each other have remained uncertain. Recently however, several researchers [54, 71, 88, 137] have formulated a more comprehensive theory on wall turbulence production supported by plethora of numerical experiments and physical observations at low Reynolds numbers. The theory in essence describes a self-regenerating cycle of lifted near-wall streaks, longitudinal vortices and internal shear layers and accounts for most of the turbulent phenomena observed in boundary layers to date. Although not the only theory extant today (see for example Zhou *et al.* [172] and Brooke and Hanratty [18]), the streak instability theory has been corroborated [71], at least for low to moderate Reynolds numbers. While other mechanisms, such as eddy roll up, surely contribute to near-wall turbulent formation (indeed some have been observed in experiment) they are not dominant and have been numerically shown to be unable to sustain the turbulence cycle in isolation [76].

There is also some evidence that the streak instability cycle does not remain the dom-

inant turbulence production mechanism at high Re [40, 59]. A displacement of coherent turbulence production from the near-wall region to the outer boundary layer occurs after $Re_\tau \approx 10000$, but the phenomenon is more characteristic of oceanic and planetary boundary layers than typical aerodynamic flows. For aerodynamic boundary layers the streak instability cycle, described in more detail in the next section, is therefore posited as the main source of coherent turbulent structures near the wall.

2.3.1 The Streak Instability Cycle

The two most prominent structural features of near-wall turbulence, are shown in fig.2.4 by a plane at $y^+ = 12$ coloured by velocity magnitude overlain with isosurfaces representing vortex cores via the $\lambda_2 < 0$ criterion. The base layer shows the streaks of low momentum fluid (blue) that have been lifted into the buffer layer, while the overlay shows the elongated streamwise vortices flanking the streaks. The former consist of long ($x^+ \approx 1000$) sinuous arrays of alternating streamwise velocity extremes with an average spanwise wavelength of $z^+ \approx 100$ [143]. Wall shear stress is higher than average beneath streaks of higher speed fluid and conversely lower underneath the lifted low velocity bands. The streamwise vortices are tilted slightly away from the wall and on average stay in the near-wall region for only ~ 200 wall units [71] before they drift towards the core flow. Each low speed streak has several vortices associated with it, having a typical streamwise spacing of $x^+ \approx 400$ [74]. Some of the streamwise eddies are connected to hairpin vortices in the outer part of the boundary layer [123], but most degenerate into less organised turbulence after leaving the buffer region [133].

It has become accepted [137] that the streaks are generated by the lifting of low speed fluid near the wall by the vertical velocity induced by the streamwise vortices, explaining their close proximity in fig.2.4. The formation mechanism of the streamwise vortices however, has until recently remained uncertain. Schoppa *et al.* [137] propose that the streaks have a significant and dynamic role in the formation of streamwise coherent structures through streak instability. Guided by channel flow solutions, linear stability analysis is used to show that typical near-wall streaks are unstable to sinusoidal perturbations (the commonly observed streak waviness in z). To isolate the instability of the vortex-less

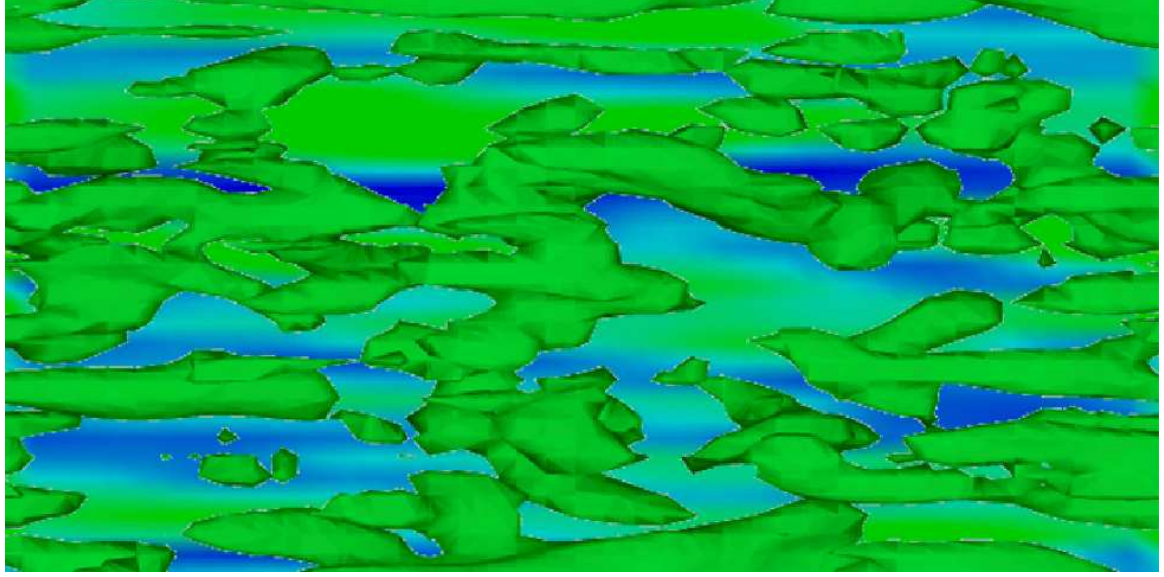


Figure 2.4: Velocity magnitude representing lifted low speed streaks (dark blue) at $y^+ = 12$ and isosurfaces of streamwise vortices, $\lambda_2 < 0$ for $y^+ < 100$.

streaks a base flow of the following form was generated,

$$U^+(x^+, y^+) = U_0^+(y^+) + (\Delta u_0^+/2) \cos(b^+ z^+) (y^+/30) \exp(-C_1 y^{+2} + 0.5), \quad (2.13)$$

$$V^+ = W^+ = 0, \quad (2.14)$$

where U^+ is the mean velocity profile. The streak's wall normal circulation, Δu_0^+ , spanwise wavenumber, b^+ and transverse decay, c_σ , are chosen to approximate a typical streak from previous minimal channel simulations (see fig.2.5).

The streak waviness, used to investigate the stability of the base flow in eq.2.13 has the form,

$$w(x^+, y^+) = c_\epsilon \sin(a^+ x^+) y^+ \exp(-c_\sigma y^{+2}), \quad (2.15)$$

$$u = v = 0, \quad (2.16)$$

where c_ϵ is the linear perturbation amplitude and a^+ is the x -wavenumber of the perturbation. These initial conditions are shown to evolve by linear instability into a natural instability eigenmode, the growth of which is characterised by an increase in total energy in Fourier modes ($\mathbb{E}_{10}(t)$) with a z -wavenumber of 0 (z mean) and an x -fundamental mode

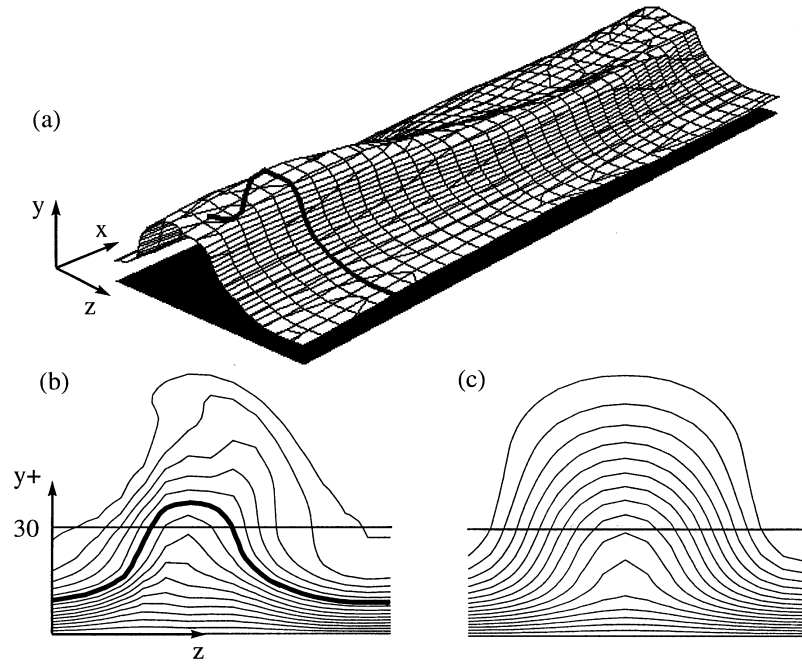


Figure 2.5: Lifted low speed streak at the quiescent phase of minimal channel regeneration, (a) $0.55U_c$ isosurface (b) Typical cross-stream distribution of \mathbf{u} (c) The analytical base flow (eq.2.13) used for stability analysis. (from Schoppa et al. [137].)

proportional to a . The way in which \mathbb{E}_{10} evolves with time for different Reynolds numbers is then utilised to posit the existence of autonomous inner-scaling dynamics, based on the similarity of streak instability growth at higher Re (for self-similar initial conditions). The physical consistency of this phenomenon is explained by first noting, that as Re increases, the wall vorticity, ω_w , increases according to the well known skin friction law, which in turn causes the dimensional streak spacing to decrease (so that the z^+ spacing of the streaks maintain the experimentally observed value in wall units of ~ 100). This reduced spacing increases the rate of streak annihilation caused by cross-diffusion, but the instability growth rate is also increased due to the enhanced wall vorticity. The balance between these factors (and therefore \mathbb{E}_{10}) seems to remain nearly constant at different Re . The analysis also shows that the streak has to be lifted some way into the buffer layer for instability to occur.

A more detailed representation of the streak instability process can be seen in fig.2.6.

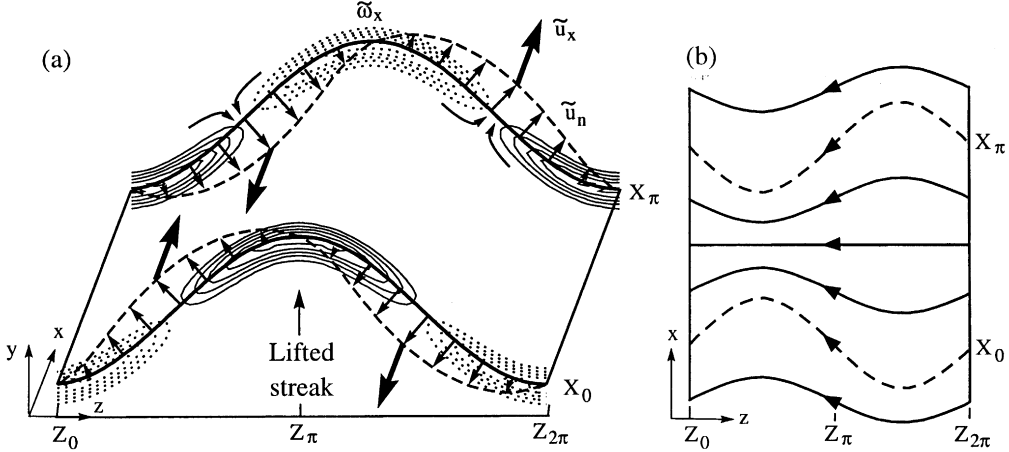


Figure 2.6: The streak instability mechanism in (a) perspective and (b) top view (from Schoppa et al. [137]).

In the diagram profiles of \tilde{u}_n , denoting the perturbation velocity normal to the base flow vortex lines, are overlayed with contours of $\tilde{\omega}_x$, the streamwise vorticity and the bold arrows denote the differential streamwise velocity (\tilde{u}_x) of the displaced vortex sheet. The thick lines in figs.2.6(a) and (b) indicate the base flow vortex lines, while the dashed counterparts depict perturbed vortex lines. The presence of streamwise vorticity, $\tilde{\omega}_x$, and the fact that a component of the perturbation velocity, \tilde{u}_x is normal to the base flow, shows that the sinuous instability introduced before is inherently 3D. The instability mechanism is dominated primarily by $\tilde{\omega}_x$ through the induction of \tilde{u}_n , which displaces the vortex sheet anti-symmetrically in both x and z (as shown in figs.2.6(a) and (b)). The displaced vortex sheet now experiences a differential streamwise velocity, \tilde{u}_x at any point on the sheet, eg. the vortex line at X_0 will move faster at $Z_{\pi/2}$ than at $Z_{3\pi/2}$. This in turn intensifies $\tilde{\omega}_x$ on top of the streak through vortex line tilting (fig.2.6(b)). The enhanced $\tilde{\omega}_x$ then further accentuates \tilde{u}_x , an so on, thereby completing the feedback loop responsible for the instability.

Having confirmed that streaks that are sufficiently lifted ($y^+ > 20$) from the wall are linearly unstable to perturbations in directions parallel to the surface, Schoppa *et al.* proceed to study their non-linear evolution using DNS. The DNS is initialised using eqs.2.13 and 2.15 to obtain a starting field free from extraneous perturbations. The first observa-

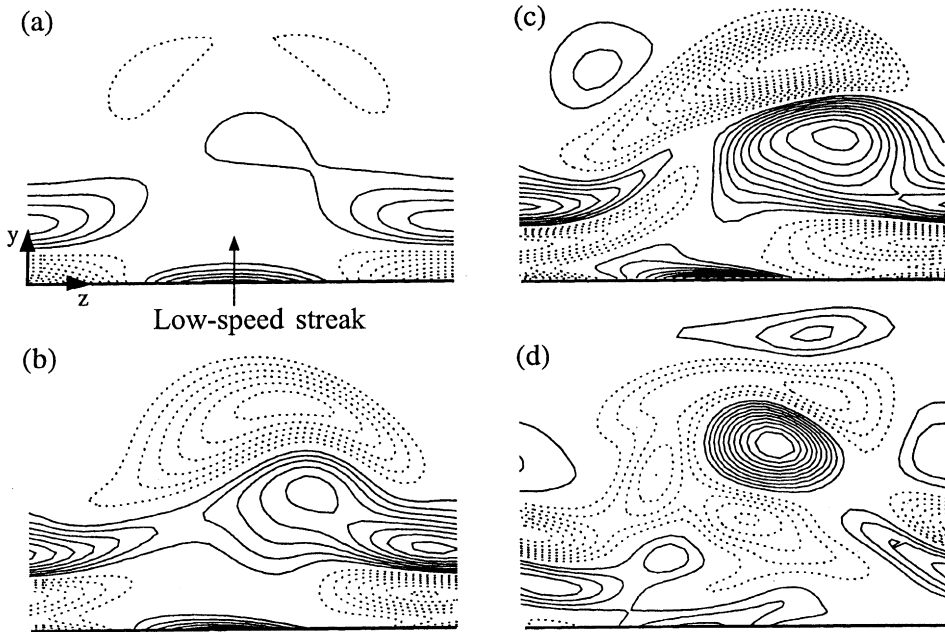


Figure 2.7: Streamwise vortex formation due to finite-amplitude streak instability, illustrated by cross-stream distributions of ω_x at (a) $t^+ = 1.7$, (b) $t^+ = 15$, (c) $t^+ = 103$ and (d) $t^+ = 928$. Planes in (b) and (c) are tracked with the instability phase speed of approximately $0.6U_c$ (from Schoppa et al. [137]).

tions (fig.2.7(a)-(c)) show the direct creation of streamwise vortices due to the growth of the sinuous amplitude of the underlying streak. The instability growth is initially characterised by increased circulation of the streamwise vortex sheets and then as the increasing perturbation amplitude becomes non-linear $+\omega_x$ begins to concentrate on the $+z$ side of the lifted streak (fig.2.7(b)) ($-\omega_x$ concentrates on the $-z$ flank at one half wavelength away in the x direction so that all events maintain periodic symmetry). With further increase of the instability's amplitude, intense stretching of ω_x sheets causes the formation of streamwise vortices through cross-sectional ω_x contraction and accompanying vorticity concentration (fig.2.7(c)). The streak instability then continues to sustain the streamwise vortex well after initial formation (see fig.2.7(d)), emphasising the phenomenon's importance to turbulence production. Although the stabilising influence of cross-streak diffusion will block vortex formation for very weak perturbations, the threshold is typically very low ($w'/U_c = 1\%$ at $y^+ = 30$), which is well within the level associated with

fully-developed wall turbulence. This method of vortex formation stands in contrast to previous theories, which postulated advective roll-up of the vortex sheet [74, 151] and/or parent-offspring regeneration [124].

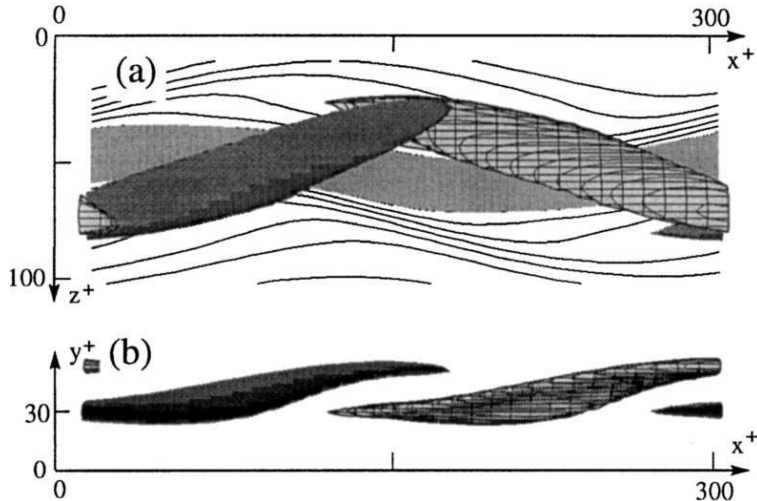


Figure 2.8: Streamwise vortices' (x, z) plane tilting, x -overlapping and location relative to a low speed streak, realized by 80% isosurfaces of $+ \omega_x$ (dark) and $- \omega_x$ (hatched) at $t^+ = 103$ (a) top view (b) side view (from Schoppa et al. [137]).

The three dimensional geometry of the instability generated vortices (with the overlapping of tilted opposite signed streamwise structures), fig.2.8, agrees very well with coherent structures extracted from a fully turbulent channel flow, fig.2.9. The coherent structures in fig.2.9 are an ensemble average of more than a 100 vortex realizations over a large number base flow/perturbation combinations, which removes the effects of streak irregularities and incoherent turbulence. The resulting image strongly suggests the presence of the postulated instability mechanism and its similarity to fig.2.8 is persuasive evidence that this vortex formation process is dominant in fully developed near-wall turbulence.

The streak instability mechanism also accounts for the other significant near-wall structures, namely internal shear layers and arch vortices. Internal shear layers occur at sharp streamwise $+u/-u$ interfaces, which are generated either by localised ejections [15] [133] or strong kinking of the low speed streaks [79]. The shear layers (figs.2.10(a) and (b)), indicated by wall detached layers of spanwise vorticity, ω_z , are generated through

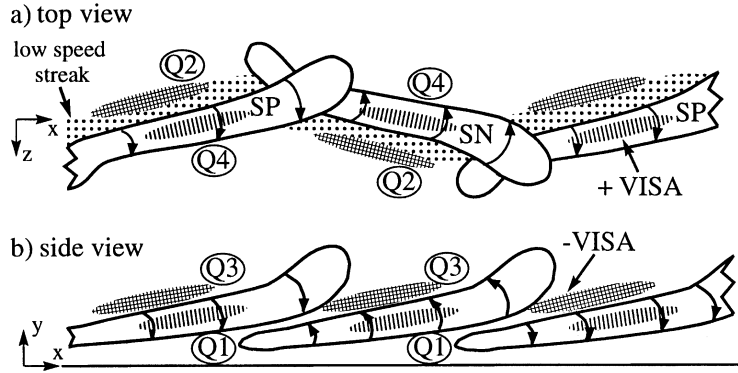


Figure 2.9: Near-wall induced coherent structures and associated events: \pm VISA (Variable Interval Spatial Averaging) of $\pm \partial u / \partial x$; quadrant Reynolds stresses Q_1 , Q_2 (ejection), Q_3 and Q_4 (sweep) and a kinked low speed streak (adapted from Jeong et al. [71]).

streak waviness on the opposite side of the streak to streamwise vortices in regions of negative $\partial u / \partial x$ (-VISA (Variable Interval Spatial Averaging) in fig.2.9). This region of -VISA is accompanied by stretching in a predominantly spanwise direction, compressing and intensifying the shear layer. Subsequently, the downstream lifted portion of the shear layer rolls up through 2D self induction into a locally spanwise vortex (figs.2.10(d) and (f)), which connects with the tilted downstream end of the adjacent streamwise CS to produce an arch vortex (figs.2.10(c) and (e)).

The streamwise and arch vortices now in turn serve to generate and amplify the low speed streaks by local lifting of the low-speed near-wall fluid in the wall-normal direction. Since the vortices advect faster than the local base flow, they leave behind a “tail” of lifted low speed fluid, which may spawn additional vortices. The tendency of positive streamwise vortices to form on the $+z$ side of the streak (and $-\omega_x$ on the $-z$ flank) also means that the lifting of low speed fluid by these vortices coincides with the existing streak position. The streak instability mechanism therefore serves to sustain the base streak against viscous cross diffusion, allowing additional instability and vortex formation, which in turn strengthens the streak, completing the cycle.

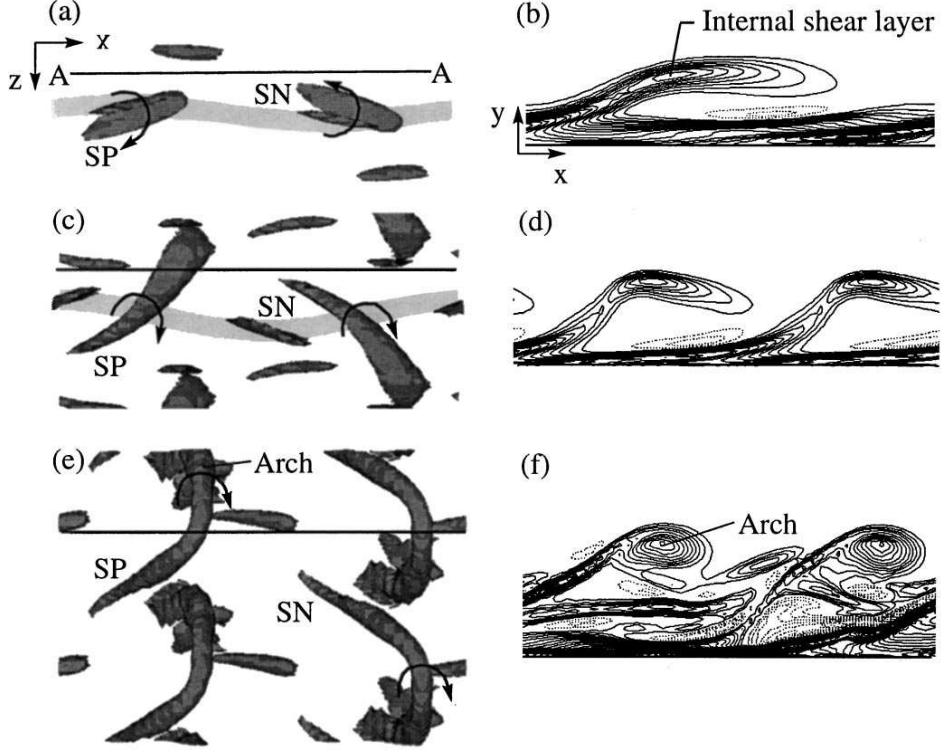


Figure 2.10: Internal shear layers and arch vortices formed by non-linear evolution of streak instability, from DNS data. (a,c,e) λ_2 isosurfaces of the evolution of vortices SP (streamwise positive) and SN (streamwise negative). (b,d,f) Contours of ω_z in the section A-A indicating formation of internal shear layer and arch vortex (from Schoppa et al. [137]).

2.3.2 Extent of the Near-wall Cycle

The streak instability cycle is bounded by the wall on one side and the outer flow on the other. In order to treat or model this region in LES it is necessary to know its extent and the characteristics of its interactions with these boundaries.

In the viscous sub-layer near the wall (see fig.2.11), shear is completely dominated by viscosity. In a typical **Zero Pressure Gradient** (ZPG) boundary layer this region extends to $y^+ \approx 8$. As one moves further into the flow, inertial effects begin to have an influence resulting in a zone of mixed contributions called the buffer layer ($8 \lesssim y^+ \lesssim 80$). Further out, inertia dominates and the region is known as the logarithmic layer. The observations of Schoppa and Hussain [137] seem to indicate that coherent structures produced by

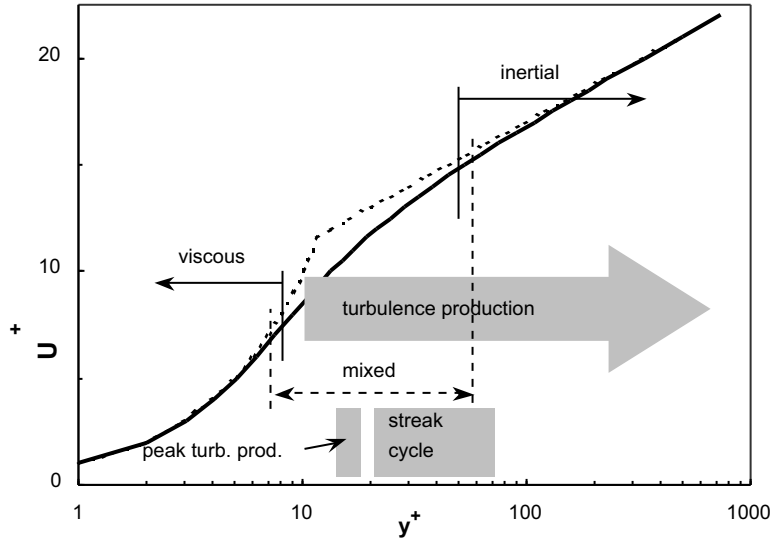


Figure 2.11: Boundary layer velocity profile.

the streak cycle form predominantly above $y^+ \approx 20$ (which is higher than the region of peak velocity fluctuation commonly witnessed near $y^+ \approx 10$). Since streamwise vortices form above and beside the upper flanks of a streak, it is possible to establish the lower boundary of the cycle more precisely by blocking some part of the instability process below a distance, δ^+ , from the wall. Jimenez and Pinelli [76] accomplish this in a DNS of a channel flow by using a damping function to selectively suppress spanwise variations of u (and therefore the near-wall streaks). From their results (fig.2.12) it is clear that suppressing the streaks below $\delta^+ \approx 25$ has hardly any effect on the wall shear, while extending the filter above $\delta^+ \approx 60$ causes the flow to laminarize suddenly and completely. For intermediate filter heights, the flow retains essentially turbulent characteristics, albeit somewhat different from those of a natural channel, suggesting that the regeneration cycle resides some distance away from the wall.

Figure 2.12(a) shows that the peak velocity fluctuations near the wall are reduced by about 30% of their natural values for the cases with $\delta^+ < 70$. This is not surprising, as this peak occurs at $y^+ \approx 10$ in natural flows and since the effect of the filter, which in all cases is well within the damped region, is to make the streamwise velocity uniform. What is significant, is that for the case $\delta^+ = 24$ the fluctuation intensities in the flow away from the wall ($y^+ > 60$) remain largely unchanged from the corresponding values

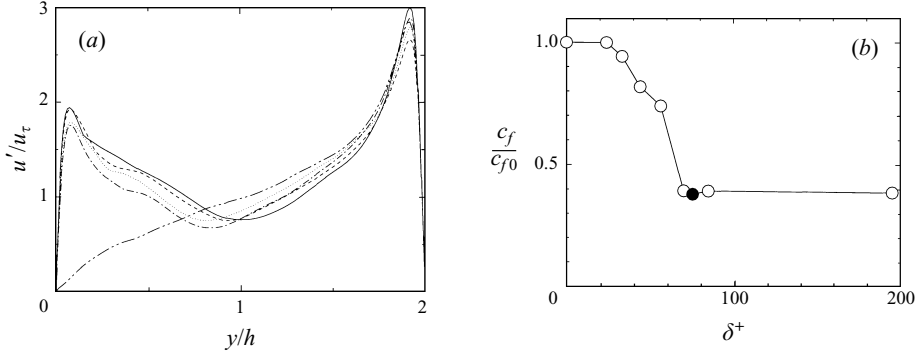


Figure 2.12: (a) Dependence of the streamwise velocity fluctuations on the filter height $\delta^+ = 24$ — ; 33 — — ; 44 · · · ; 56 - · - ; 70 - · - · . (b) Reduction in skin friction coefficient as a function of filter height (adapted from Jimenez and Pinelli [76]).

for the unfiltered wall. Coupled with the insensitivity of the wall shear to filters below $\delta^+ = 24$, it can be concluded that although the turbulent motions below this cutoff are strongly dependent on the instability cycle, the reverse is not true. In fact, the spatially averaged velocities in this region not only maintain the correct wall shear, but also serve as a sufficient lower boundary for the streak instability cycle.

Although the previous section sets the minimum and maximum y^+ of the lower boundaries necessary for a sustainable turbulence cycle, it does not clarify the relationship between the instability region and the interior flow. To investigate the extent of the near-wall cycle's dependence on the core's turbulent structures, a conceptually similar experiment may be conducted by diffusively damping all perturbations in the interior of the channel. Figure 2.13 depicts the results for a channel flow DNS with all fluctuation damped above $y^+ \approx 60$, which is the lowest limit for which turbulence survives.

The mean velocity profile shown in fig.2.13(a) has a roughly turbulent profile near the wall, even though there are no Reynolds stresses in the filtered part. The wall shear is about 50% lower than the control case, but this is partially due to the shift of the mean momentum flux toward the filtered wall. Indeed, fig.2.13(b) shows that the near-wall velocity (appropriately scaled) agrees reasonably well with the regular channel and that an incipient logarithmic region has developed despite the severe truncation of turbulent scales. Figures 2.13(c) and (d) depict similar robustness for the velocity and vorticity

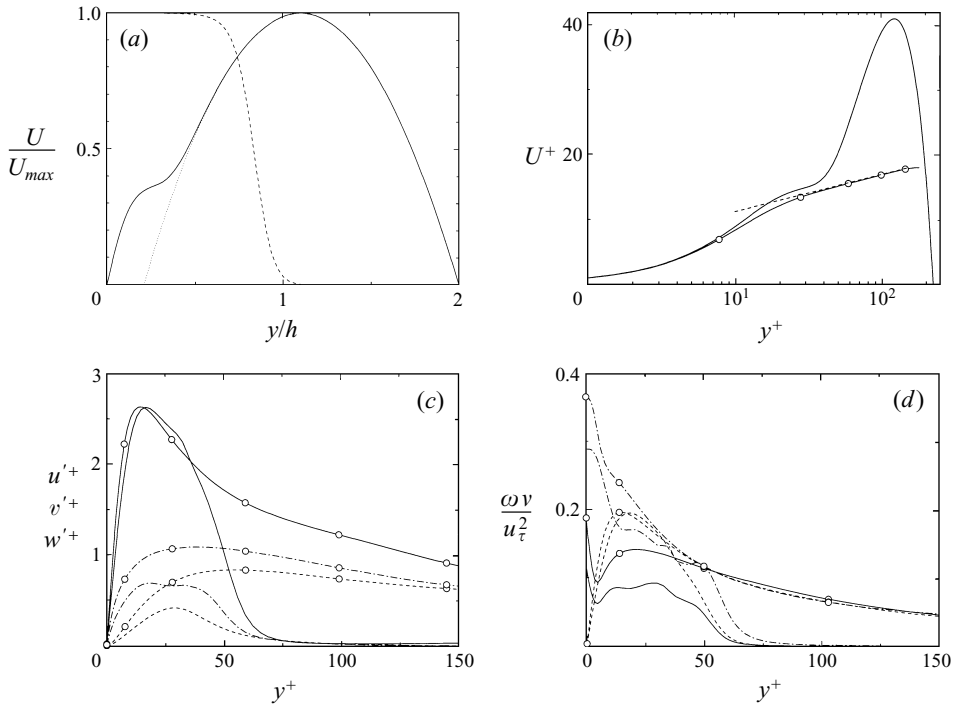


Figure 2.13: Explicitly filtered channel, $Re_\tau = 200$. In all cases curves with circles correspond to full channel by Kim et al. [82]. (a) — Mean streamwise velocity; – – filter; ··· laminar parabola. (b) — Mean streamwise velocity in wall units; – – $2.5 \log(y^+) + 5.5$. (c) Turbulent velocity fluctuations: — u' ; – – v' ; – · – w' . (d) Turbulent vorticity fluctuations: — ω_x' ; – – ω_y' ; – · – ω_z' (from Jimenez and Pinelli [76]).

fluctuations, especially their streamwise and wall normal components respectively. The conclusion is that the near-wall flow is essentially normal and self-sustaining, despite the absence of fluctuations in the outer flow above $y^+ \approx 60$ and therefore can function autonomously with regards to perturbations from the core. These statements are reinforced by further numerical experiments, in which Jimenez and Pinelli use very narrow spanwise and streamwise channel dimensions to suppress large scales of motion in the interior, while maintaining sufficient dimensions to sustain the near-wall cycle. The results are essentially similar, with the added observation that trends in fluctuation properties versus Reynolds number are accurately reproduced in the minimal channels.

The overall picture that emerges is one of near-wall turbulence sustained by the streak instability cycle in a region between $y^+ \approx 20$ and $y^+ \approx 60$. This cycle can survive without

structural input from the core flow, while maintaining for the most part the correct turbulent characteristics and is rather insensitive to damping of perturbations beneath its lower extent. This does not mean that near-wall statistics are completely independent of Reynolds number, since as mentioned above, some reliance is observed in all flows. Interaction with the core is therefore implied to some extent, which can either point to a contribution from one of the other regeneration mechanisms proposed in literature or to an interaction mechanism heretofore unconsidered. The streak cycle, however has been shown to be relatively autonomous and independent of these mechanisms.

2.4 Core Flow Interaction

Although, the near-wall cycle has been found to be insensitive to turbulent conditions in the core flow, the inverse is certainly not true. In addition, near-wall structures are known to be sensitive to certain gross flow properties, such as pressure gradient and wall transpiration. The effects and exact nature of these interactions are less well understood than the dynamics of the streak cycle, but still warrant consideration in the context of a near-wall treatment for LES.

2.4.1 Inverse Energy Cascade

There is a close analogy between the spatial structure of turbulent boundary layers and the spectral organisation of turbulence. If the Reynolds number is large enough, both the dynamics of turbulent boundary layers and the large scale spectral turbulent processes become independent of the smallest scale motions related to molecular viscosity. In the near-wall boundary layer, viscosity acts as a momentum sink to the core flow, in a similar fashion to the dissipative effect of the small scale end of the turbulent kinetic energy spectrum. The mean flow momentum and therefore mean kinetic energy is transferred to the surface layer by Reynolds stresses and there converted into turbulent kinetic energy and heat (through viscous dissipation). Most of the turbulent energy generated near the wall, is lost to dissipation because of large velocity gradients in this region. A significant portion is however transported to the outer flow through turbulent diffusion before it

dissipates. Since turbulence production in the core is generally small, this makes the surface layer the main source of turbulent energy for the entire flow.

To obtain a clearer picture of the balance of the turbulent energy budget (and thence its transfer mechanism), consider the equation for turbulent energy, $K = \langle \text{tr}(\mathbf{u}'^2) \rangle / 2$ [156, 159], expressed in the following form

$$\frac{\partial K}{\partial t} + \mathbf{U} \cdot \nabla K - \nabla \cdot (\nu \nabla K) + \nabla \cdot \psi = -\langle \mathbf{u}' \mathbf{u}' \rangle : \nabla \mathbf{U} - \epsilon, \quad (2.17)$$

where $\epsilon = \nu \langle (\nabla \mathbf{u}' + \nabla \mathbf{u}'^T) \nabla \mathbf{u}' \rangle$ is the viscous dissipation, while the first term on the right hand side represents local turbulent energy production through the working of the mean flow on the turbulent Reynolds stresses. The ψ term on the left hand side is a spatial energy flux caused by turbulent pressure gradients and turbulent convection and is defined as,

$$\psi = \langle \mathbf{u}' (p' + \text{tr}(\mathbf{u}'^2) / 2) \rangle. \quad (2.18)$$

If the flow is parallel and in equilibrium (*e.g.* channel flow) the time averaged streamwise derivatives and cross-stream velocities tend to zero. Assuming the contribution of viscous diffusion is small compared to the turbulent contribution, eq.2.17 reduces to,

$$\frac{\partial \psi_2}{\partial y} = -\langle \mathbf{u}' \mathbf{u}' \rangle : \nabla \mathbf{U} - \nu \langle (\nabla \mathbf{u}' + \nabla \mathbf{u}'^T) : \nabla \mathbf{u}' \rangle, \quad (2.19)$$

so that the only significant mean flux, is the wall-normal component, ψ_2 . Figure 2.14 shows this flux and the turbulent energy production budget for three DNS channel flows at different Reynolds numbers produced by Mansour *et al.* [99]. For the cases shown it is clear that net turbulent production occurs only in the outer viscous and buffer regions, while dissipation exceeds production everywhere else. This interpretation is reinforced by the energy flux, which is positive through most of the domain (except very near the wall), signifying a movement of energy away from the surface. Of particular note is the tendency for the flux at higher Reynolds numbers to become constant at intermediate wall normal distances corresponding to the position of the logarithmic layer. This equilibrium requires a local balance of turbulence production and dissipation, which must exist despite the dominance of production and dissipation terms in this region [156]. In addition, instantaneous statistics [76] show that the flux is a residual component of large scale

movement of energy perpendicular to the wall which is an order of magnitude larger than the mean. The exact balance in this region despite substantial instantaneous fluxes, points toward self-similarity of the energy flux in this region. This is not surprising considering similarity principles can be used to derive the shape of the logarithmic velocity profile, which has been more than adequately verified by experiment. Now similarity and dimensional arguments require that $\psi_2/\tau_{12}^{3/2}$ must be constant and since the mean Reynolds stress $\tau_{12} = -\langle u'_1 u'_2 \rangle$ is constant near the wall for equilibrium flows, the energy flux must also be so.

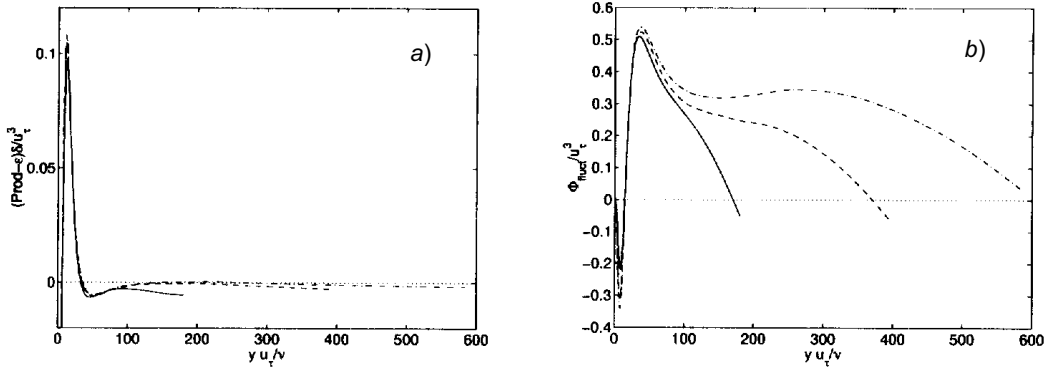


Figure 2.14: a) Local excess energy production, $-\langle \mathbf{u}' \mathbf{u}' \rangle : \nabla \mathbf{U} - \epsilon$, b) Turbulent energy flux, ψ_2 .
DNS channels ——— : $Re_\tau = 180$ [82]; - - - : $Re_\tau = 395$ [134]; - · - : $Re_\tau = 640$. [99].

In the central part of channels dissipation exceeds production by a significant margin and hardly any turbulence is produced there. Thus, most of the turbulent energy is provided by the flux from the walls. Since most of the turbulent energy is contained in the largest scale eddies and the eddy size is limited by the distance from the wall, the near-wall energy containing eddies will be small while those centred in the core will be large. The transfer of energy from the small to large scales is an example of an inverse energy cascade as opposed to the classical Kolmogorov cascade. Since the constant shear stress in the logarithmic layer implies a constant momentum flux, the transfer is as much of momentum as of energy. This mechanism, elucidated by Jimenez [75], describes a cascade organised by wall distance and eddy size, which transfers energy to smaller scales locally and to larger eddies away from the wall. The smallest scales of turbulence are

generally known to be isotropic and produce little mean Reynolds stress, therefore the momentum cascade must by default be carried by the larger eddies. The momentum transfer thus occurs in a finite range of the longest length scales at any (non-zero) distance from the wall. (Very near the wall smaller eddies become anisotropic and do contribute to momentum transfer, so that the length scale range that affects momentum transfer may become infinite with Reynolds number.)

Since the nature of the fluxes that are being transferred are different from that in the Kolmogorov cascade, the spectral slope of the cascade should be different to. If the small wave number (large length scale) limit, $ky_w \ll 1$, where the eddies are much larger than the near-wall distance is approached, the energy flux should become independent of the near-wall distance, y_w and the spectrum can only depend on the momentum flux $u_\tau^2 \sim \tau_w$ and the wavenumber k [75]. Dimensional considerations now require that the energy spectrum have the following shape,

$$\frac{\mathbb{E}(k)}{u_\tau^2} \sim k^{-1}. \quad (2.20)$$

The wavenumber range in which the relation 2.20 is valid can be estimated from time scale considerations [123] and lies in the interval $k\delta_b > O(1)$, $ky_w < O(1)$, where δ_b is the boundary layer thickness. Eddies larger than the boundary layer thickness are clearly impossible since they wouldn't fit, while ones much smaller than the near-wall distance are unable to interact with the surface and should therefore break down into smaller eddies according to the usual Kolmogorov cascade. Indeed, experiments [135] show that the k^{-1} range transitions to the Kolmogorov regime ($k^{-5/3}$) near $ky_w = 1$ in boundary layers and that the k^{-1} range grows longer as the wall is approached, supporting the conclusion that the near-wall momentum cascade is carried by eddies larger than the distance to the wall. Figure 2.15 depicts this organisation, including the implication that momentum transferring eddies are in some way “attached” to the wall. Since the spatial cascade is restricted to eddies larger than y_w , it is improbable that structures which are diffused into the core flow from the wall transfer a significant amount of energy to larger eddies there, because of the scale disparity. This view is essentially identical to the ‘attached eddy’ hypothesis first proposed by Townsend [159].

The basis of Townsend’s attached eddy model is derived from assumptions of structural

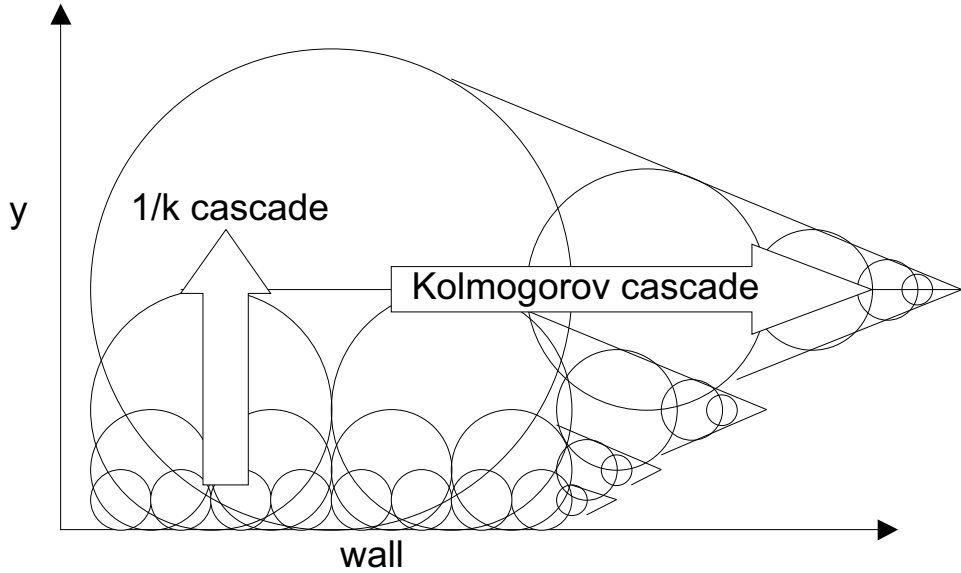


Figure 2.15: The two energy cascades in the near-wall inertial layer.

similarity and experimental correlation function data for inhomogeneous shear flows. In these flows the average large eddy motion is predicted to consist of pairs of inviscid parallel roller vortices. The eddies extract energy from the mean flow through vortex stretching, their axes are aligned with the principle direction of strain and their plane of circulation is slightly (negatively) inclined to the bulk flow direction. In flows constrained by a wall, eddies cannot have scales that are larger than the distance from the wall to the vortex centre. The presence of a solid boundary will therefore restrict the above double rollers in both the wall normal and longitudinal directions, resulting in (among other possibilities) a ‘double-cone’ eddy (fig.2.16), which locally preserves the characteristics of the double roller eddy, while satisfying the wall constraint. In the double-cone eddy, circulation takes place around the surfaces of two adjacent cones diverging from a common vertex near the wall and since the eddy is in ‘contact’ with the wall over its whole length, it is an attached eddy. Thus an eddy with its centre at a distance L from the wall may be of size no larger than $2L$, and its velocity field must be such that its motion is parallel to the wall at distances small compared to L . In addition the eddies are assumed to convect downstream, relative to the wall, at a ‘slip velocity’ precipitated by the viscous sub-layer,

and taken to be equal to the wall shear velocity in Townsend's analysis. The effect of this configuration is that the contribution of the eddy to Reynolds shear stress is zero closest to the wall, reaches a maximum value near the eddy centre and decreases again at larger distances. The wall parallel contribution of the eddy is however finite near the surface, so that a superposition of eddies necessary to produce a realistic stress distribution, result in an 'inactive' swirling flow near the surface, whose magnitude depends on the thickness of the boundary layer. Although these inactive motions do not directly contribute to the shear stress, there are indications [77] that they serve to modulate large streamwise coherent structures near the wall, thereby indirectly influencing the near-wall properties.

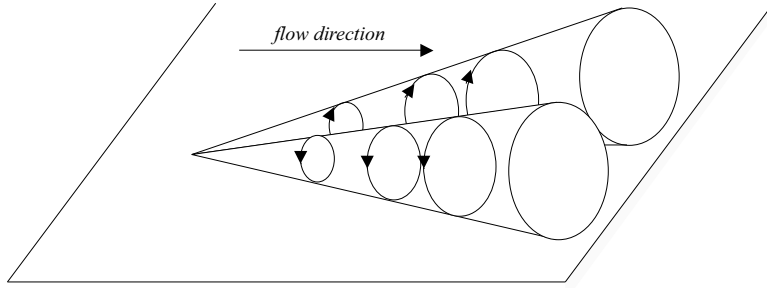


Figure 2.16: The double cone eddy (reproduced from Townsend [159]).

The idealised double-cone structure is clearly not in perfect agreement with visualisations of DNS flows, but does bear some resemblance to pairs of staggered lifted streamwise vortices produced by the streak instability mechanism (see for example Blackburn *et al.* [14]). Also, integration of the superposition of the whole range of attached eddy sizes and origins produces wall stress statistics that are qualitatively in agreement with experimental observations [159]. Thus, the attached eddy hypothesis viewed in the frame of the inverse energy cascade provides at least a tentative understanding of the transfer mechanisms in the inertial layer.

Individual eddy shapes are difficult to isolate (even with the methods outlined in sec.2.2) in the inertial region of a boundary layer. The interference created by overlapping vortices of different scales and character tends to obscure the large, low vorticity structures that would characterise the downstream end of a double roller type attached

eddy. Directly confirming the detail of the attached eddy hypothesis is therefore somewhat impractical using currently available vortex eduction methods. An extension of Townsend's concept, conforming more closely to experimental observations, has been proposed by Perry and Chong [122] and was later refined by Perry and Marusic [125]. The extended model consists of partially attached eddies in hairpin configurations that occur predominantly in the logarithmic layer and undulating spanwise vortices that dominate the turbulent statistics in the wake region. This "wall-wake" model, as it is termed, has been shown to reasonably recreate first order statistics [100] and in boundary layers, the magnitude and trends of Reynolds shear-stress spectra [114]. How these 'wake' eddies are formed is uncertain, but it seems likely that they are remnants of attached eddies that have separated from the wall and extract energy from the mean flow in a manner similar to double rollers. This mechanism becomes more apparent in strong adverse pressure gradient flows, where the maximum turbulence production shifts from near the wall toward the wake.

A conservative view (for modelling purposes) of the wall-inertial layer interaction thus entails a strong coupling of coherent features, which implies that the log-region cannot be divorced from the streak instability cycle unless detailed structural information is provided at the interface.

2.4.2 Effects of Pressure Gradient

Pressure gradients are known to have a significant influence on boundary layers in terms of both averaged statistics and instantaneous features and occur in the majority of flows of practical interest. With regards to a near-wall treatment for LES, this effect can have two possible influences: firstly, it may change the validity of assumptions used for matching LES to the wall treatment and secondly, it will almost certainly alter the form of the wall treatment itself. The time mean influence of pressure gradient has been extensively studied (see amongst others [16, 33, 103, 157, 158] and more recently [110, 111, 148, 167]). Most of these investigations have however focused on 'quasi-equilibrium' boundary layers, where a sustained pressure gradient is applied in an attempt to deduce simple parameter scaling laws similar to the zero pressure gradient case. Even though applicability of these

results to flows with large and rapidly varying pressure gradients is therefore uncertain, several pragmatic models have proven at least partially effective in predicting some of these cases [25, 33, 78, 158].

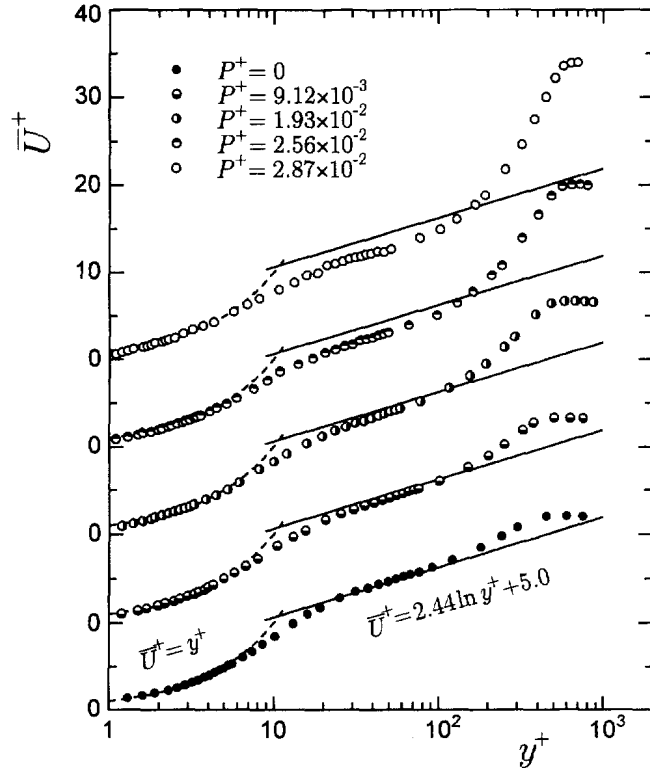


Figure 2.17: Experimental mean velocity profiles in boundary layers with mild adverse pressure gradient. Pressure gradient parameter $P^+ = \nu \frac{dp}{dx} \frac{1}{u_\tau^3}$ (reproduced from Nagano et al. [111]).

Pressure effects are broadly classified into **Favorable Pressure Gradients** ($\frac{dp}{dx} < 0$) (FPG) and **Adverse Pressure Gradients** ($\frac{dp}{dx} > 0$) (APG), where x is the streamwise direction. Both types have a relatively small influence on the near-wall region, provided they are small and no separation occurs [103, 148]. Favourable pressure gradients generally coincide with an increase of wall shear stress and a movement of fluid toward the wall and can lead to re-laminarization of the boundary layer if the FPG is large. Excepting re-laminarization, the qualitative effect of a FPG on the equilibrium shape of the law of the wall is mostly limited to an increase in gradients in the inertial and viscous layers, making it comparatively easy to account for. An adverse pressure gradient on the other hand,

can dominate the wall shear stress as principal parameter governing the boundary layer statistics and lead to flow separation when large and sustained.

Opposite to FPGs, adverse pressure gradients (a typical representation of which can be seen in fig.2.17) for the most part correspond to movement of stream lines away from the surface and a decrease in wall shear stress. Mean turbulent statistics are similarly effected, with absolute peak normal stresses parallel to the wall decreasing with a sustained APG. An interesting supplementary effect is that the value of these peak stresses actually increases in terms of wall units, so that the wall-limiting gradients of the turbulent intensities become larger with adverse pressure gradient (see fig.2.18 and Spalart and Watmuff [148]). This means that the viscous wall unit cannot in general be used to describe the unique features of even relatively mild APG flows.

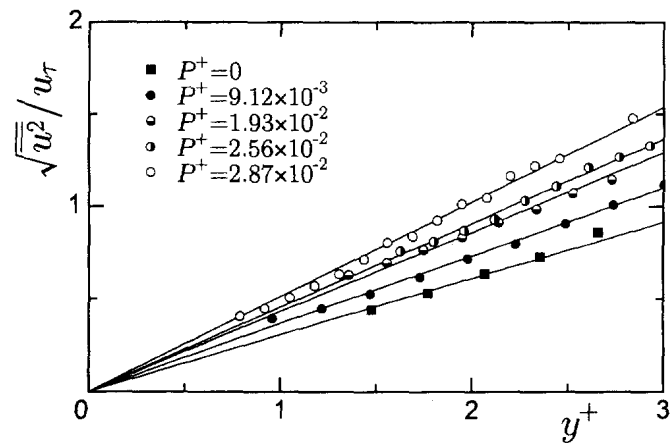


Figure 2.18: Wall limiting behaviour of u_{rms}/u_τ in an APG. Pressure gradient parameter $P^+ = \nu \frac{dP}{dx} \frac{1}{u_\tau^3}$ (reproduced from Nagano et al. [111]).

In flows undergoing APG driven separation deviations from equilibrium conditions are even more pronounced (see fig.2.19). As separation is approached the wall shear stress tends to zero, so that in the limiting case the velocity distribution becomes independent of the viscous wall scaling and instead depends solely on some pressure parameter (see Townsend [158]). After reattachment the flow is equally disturbed, with an inertial layer developing only some distance downstream. The persistence of the dip below the log-law suggest the presence of abnormally large length scales, which means that some of the large

energetic eddies formed in the shear layer above the separation bubble survive a long time before breaking up [27]. (It should also be noted that the Reynolds number of this flow is quite small ($Re_\theta \approx 300$ at the inlet) and the logarithmic region therefore nearly non-existent.) There are no wall models currently available that consistently reproduce these types of flow, so some loss of accuracy is to be expected if separation and reattachment regions are not sufficiently resolved in LES.

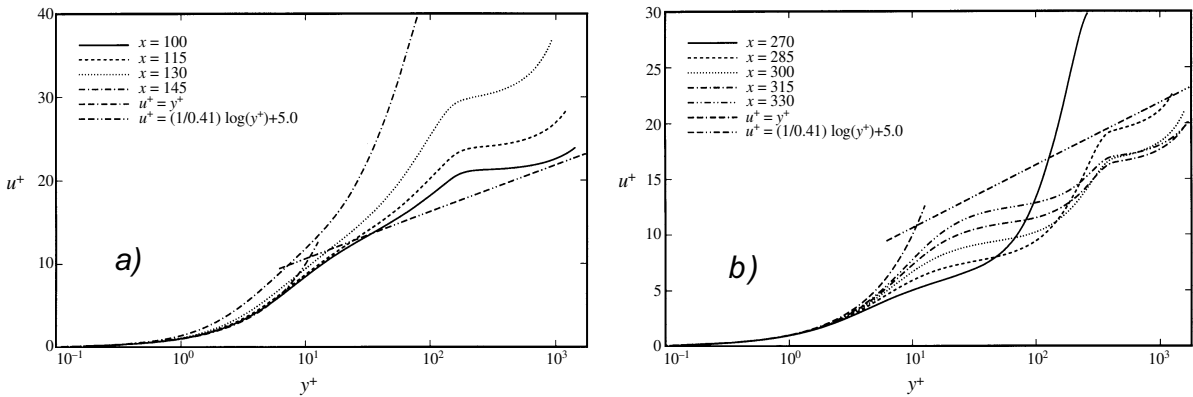


Figure 2.19: Mean streamwise velocities a) before and b) after separation. DNS of APG induced separation of a flat plate boundary layer (reproduced from Na and Moin [108]).

The effects of pressure gradients on eddy dynamics have not been nearly as widely studied as on the mean flow statistics. If a matching between a wall model and LES is to be made, the properties of the flow structures at the interface must be known, at least in a approximate sense. For example, if a wall model matches LES at the interface of the inertial and wake regions and a given pressure gradient causes this interface to be displaced in some way, the model would need to adjust in a consistent manner to maintain its accuracy. Thus the effect of pressure gradient on spatial and dynamic characteristics of the streak instability cycle and the other generation and transfer mechanisms in the boundary layer becomes important. Unfortunately, very little data of the type necessary for such an analysis is available. Much of the data that is available is scaled with viscous wall units, which are known to lose their uniqueness as scaling parameter in flows with appreciable pressure gradients, making the results difficult to interpret. If equilibrium is assumed, at least a qualitative idea of the position of the different layers for mild

APGs can be obtained from fig.2.17. The y^+ value of the intercept between the measured logarithmic region and the viscous layer can be seen to decrease with increased P^+ from ~ 12 to ~ 8 . However, since the wall friction velocity has decreased by more than a factor of 2 between $P^+ = 0$ and $P^+ = 2.87 \times 10^{-2}$, the actual wall normal distance of the interface is seen to increase in an APG. Using similar reasoning, the wake interface is found to stay at a fixed wall normal distance or change very slowly. The wake itself grows quite rapidly, which corresponds to a relative increase in turbulence production in the wake compared the near-wall region.

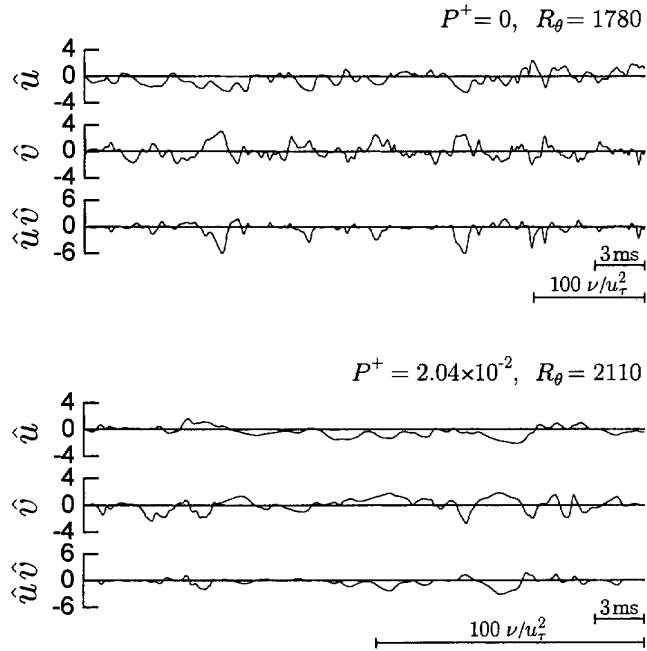


Figure 2.20: Signal trace of \hat{u} , \hat{v} and $\hat{u}\hat{v}$ for a mild APG boundary layer, $y^+ = 18$ (reproduced from Nagano *et al.* [111]).

For the eddy structure in mild APG flows the expected behaviour is that turbulent time and length scales will increase as near-wall fluid decelerates and the boundary layer grows thicker. This is borne out by the experimental results of Nagano *et al.* [111]. Figure 2.20 shows the normalised instantaneous signal trace of fluctuating velocity components in the buffer layer ($y^+ = 18$). Nagano *et al.* note that not only are the time scales extremely elongated compared to zero pressure gradient flow, but the shape of the turbulent statistics

traces have become different, appearing more gentle and less active. This should largely correspond to flow deceleration, but unfortunately interpretation of the effect on eddy size is complicated by the exclusion of local convection velocities from the time scale. The predicted increase in turbulent length scale is partially confirmed by Na and Moin's [109] DNS of a similar boundary layer.

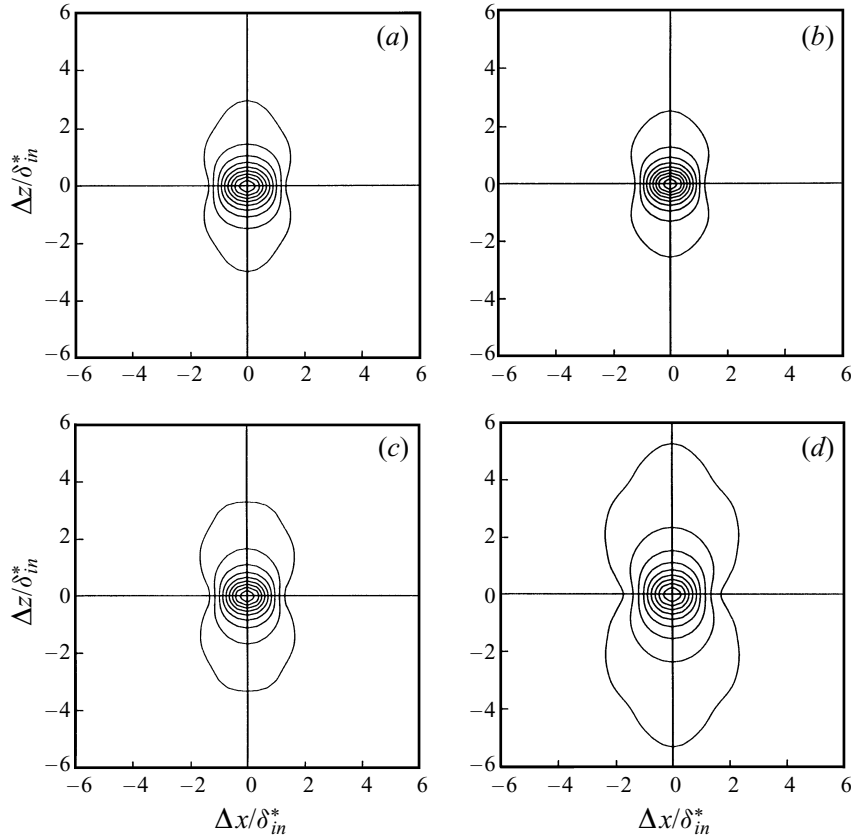


Figure 2.21: Contour plot of two-point correlation of wall-pressure fluctuations as a function of streamwise and spanwise separation. (a) $x = 0.5$ ZPG; (b) $x = 0.6$ FPG; (c) $x = 0.7$ APG; (d) $x = 0.85$ APG. Contour levels from 0.1 to 0.9, increment 0.1 [109].

Two point correlation of wall pressure as a function of streamwise and spanwise separation are depicted in fig.2.21 for a flow experiencing a ZPG(a), FPG(b), weak APG(c) and medium APG(d) consecutively. At all streamwise locations contours at small separations are roughly circular, but at larger separations the correlation becomes elongated in the spanwise direction. At $x = 0.6$ the flow has experienced a sustained FPG and

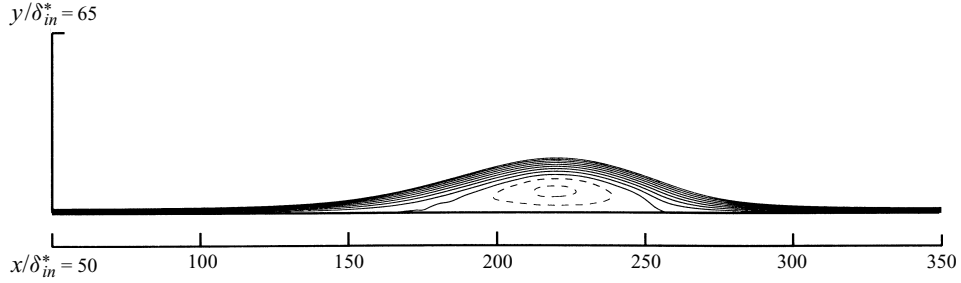


Figure 2.22: Mean streamlines of APG driven separation of a flat plate boundary layer [108]

the largest contour (corresponding to 0.1 which is indicative of large structures [109]) has decreased significantly in spanwise extent. The effect is small however, so that any modelling adjustments will typically be in the specification of the wall shear relation. The correlation lengths then increase rapidly as an APG is applied. Thus the ‘pressure’ integral length scale in the boundary layer decreases in a FPG and increases in a APG. Regarding the predominance of the spanwise correlations, it is known (see sec.2.3) that the principle eddies in the near-wall and inertial regions are elongated in the streamwise direction. The spanwise contribution thus probably originates in the wake region where the dominant eddy structure is thought to correspond to spanwise undulating vortices [125]. The non-local influence of pressure extrema allow these core structures to influence the near-wall correlations. The contribution of the near-wall structures to the streamwise correlation are impossible to separate from the wake component, but a gradual increase in scales is observable.

A clearer picture of the change in near-wall structures with pressure gradient can be obtained from Na and Moin’s [108] DNS of a separating turbulent boundary layer depicted in fig.2.22. Figure 2.23 shows contours of the two point correlation of the streamwise velocity fluctuations near the wall for several streamwise positions. Upstream of detachment ($x/\delta_{in}^* = 80, 120$) the influence of the streamwise elongated streaky structures on the correlations can be seen clearly. The streamwise elongation disappears slowly and contours become wider and more circular as the flow approaches the incipient detachment ($x/\delta_{in}^* = 160$). The initial $\sim 33\%$ decrease in streamwise correlation between positions (a) and (b) is almost entirely due to an equal decrease in the local eddy convection ve-

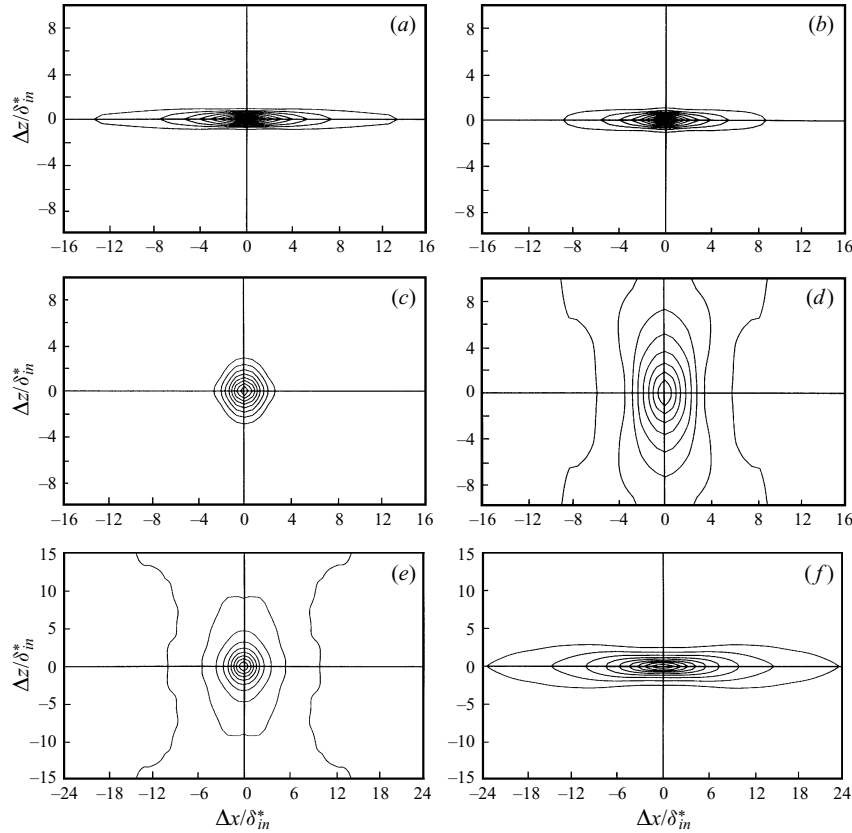


Figure 2.23: Contours of two point correlation of streamwise velocity fluctuations as a function of streamwise and spanwise separation at $y/\delta_{in}^* = 0.0042$. (a) $x/\delta_{in}^* = 80$; (b) $x/\delta_{in}^* = 120$; (c) $x/\delta_{in}^* = 160$; (d) $x/\delta_{in}^* = 220$; (e) $x/\delta_{in}^* = 270$; (f) $x/\delta_{in}^* = 320$. Contour levels from 0.1 to 0.9, increment 0.1 (Reproduced from Na and Moin [109]).

locity [109] caused by the overall flow deceleration. Unless separation occurs, the size of coherent near-wall structures in an APG thus seems to change very slowly in both the streamwise and spanwise directions. All length scales are however inclined to grow if the flow tends towards equilibrium.

After $x/\delta_{in}^* = \sim 120$ there is an abrupt change in near-wall eddy structure as can be seen from the skin friction lines (surface limiting streamlines) in fig.2.24. As the adverse pressure gradient becomes large, critical points appear in the friction lines before main separation. These correspond to small localised and short lived regions of flow reversal, which have much shorter streamwise length scales than the normal near-wall structures

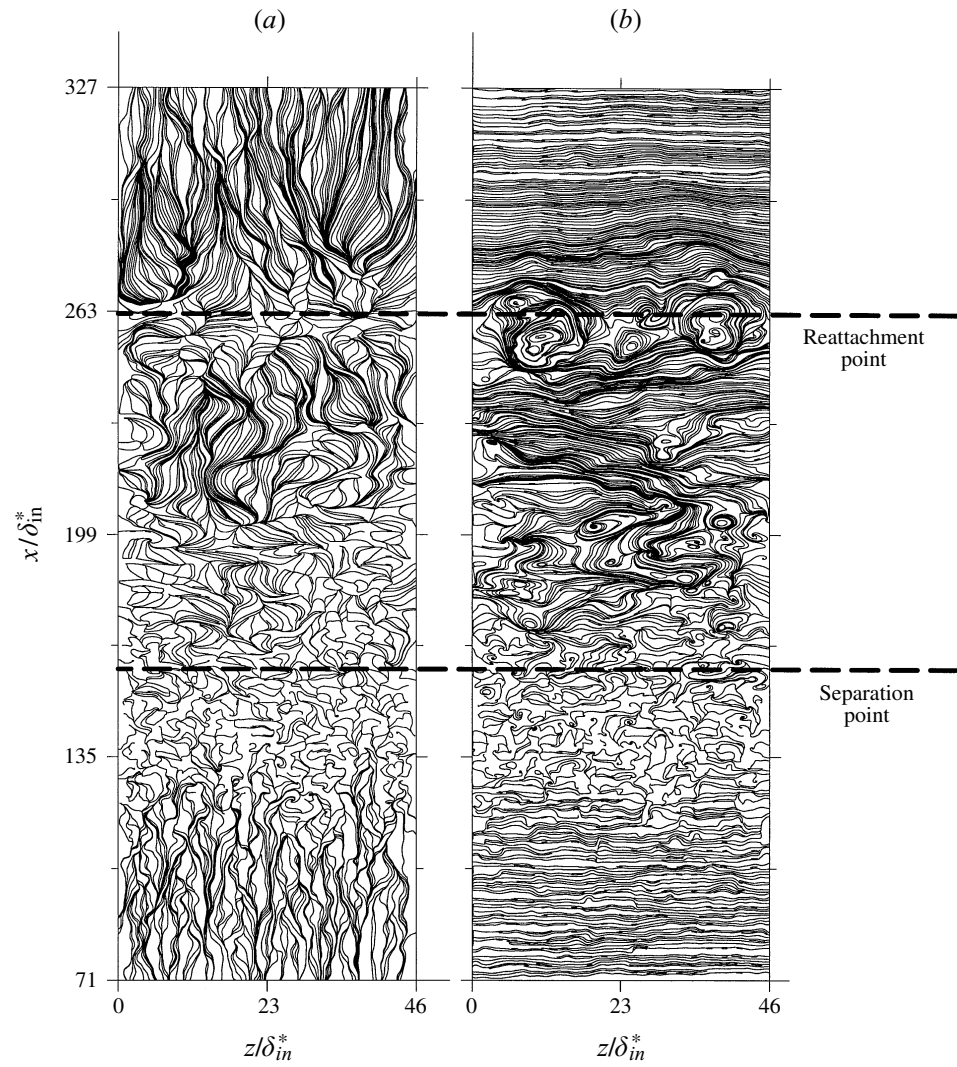


Figure 2.24: (a) Skin friction lines and (b) surface vorticity lines for APG driven separation of a flat plate boundary layer. (Reproduced from Chong et al. [30])

(which they tend to disrupt [30]). Under the separation bubble the spacing of critical points is much larger than in the mean attached flow and large nodes of separation and reattachment are apparent near the mean lines of separation and reattachment respectively. After reattachment streamwise elongated structures reform, but with much wider spanwise spacing than upstream of separation, probably owing to the reduced wall shear in this region (see also fig.2.23(f)). Above the separation bubble itself, the flow exhibits characteristics very reminiscent of a free shear layer [108], with dominant eddies consisting of spanwise orientated ‘rollers’ similar to those found in the attached wake. The influence of these structures can be seen in fig.2.23(e), as an elongation of the contours in the spanwise direction, produced as the reattaching flow convects the spanwise undulating vortices close to the surface.

With regards to LES, the decrease in streamwise length scales before, during and after separation, will necessitate increased computational resolution in these areas to compensate. Also, any approach using equilibrium boundary layer assumptions will suffer a loss of accuracy under APG and separated conditions, unless these effects are properly accounted for. The rapid growth of spanwise structures in the wake and shear layer (as depicted by the pressure and velocity correlations) bode well for LES, since there are indications that the accuracy of separating flows are dominated by the efficacy of their attendant free shear layers. Overall, since shear layers and wakes will presumably be well resolved, the main difficulty in simulating flows with strong pressure gradients will remain ensuring the accuracy of the wall treatment response.

2.5 Modelling Requirements

The most accurate way of treating the wall is to resolve all pertinent scales of motion in its vicinity (DNS). In most flow cases however, this is prohibitively expensive in terms of computational time. As an alternative, a model can be used to supply approximate statistics to the outer flow at some position either on or away from the wall. One of the most important parameters produced in this way is the momentum flux between the bulk flow and the boundary. This can either be in the form of the wall shear stress as for

2. Turbulent Boundary Layers

a two-layer or wall function model (see sec.3.3), or as an off-the-wall velocity boundary condition (e.g. a zonal model [112]). It has however been amply demonstrated by several researchers [6, 102] that specifying only the mean wall-normal momentum flux is not, in general, a sufficient wall boundary condition for LES. This is not surprising, given the structural properties of the boundary layer discussed in previous sections.

An attempt can now be made to translate some of the boundary layer's qualities into tentative wall treatment requirements. Figure 2.25 depicts the large scale structures found in the boundary layer that are thought to play a significant role in the production and transport of turbulent energy and momentum. The eddies depicted are not to scale and the diagram is purely intended to show the idealised morphology and relative distribution of coherent structures in a equilibrium boundary layer.

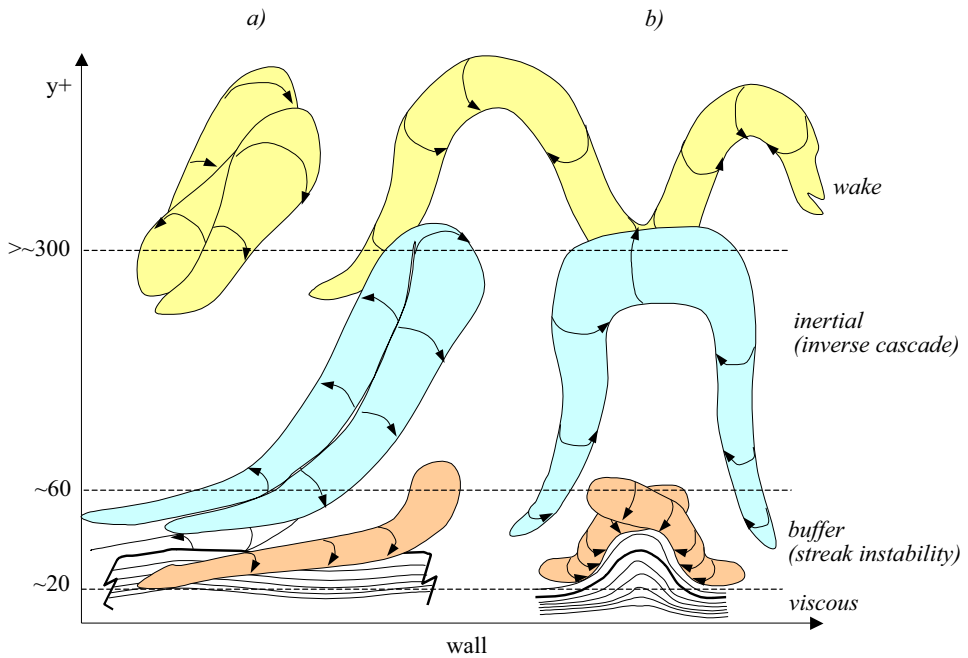


Figure 2.25: Schematic representation of coherent structures in a boundary layer: (a) side view and (b) front view with respect to flow direction. Pink represents the streak instability vortices, blue attached hairpin eddies and yellow spanwise 'rollers' in the wake.

In the 'viscous' region near the wall there are hardly any shear stress-producing coherent structures, with wall normal fluid motion induced by structures and incoherent

motion above accounting for most of the turbulent shear. Normal Reynolds stresses (the diagonal components of the turbulent stress tensor) are at a maximum, commonly attributed to large scale sweeping motion produced by wall attached eddies much larger than the local distance to the wall [159]. The most prominent features are the bottom parts of the streamwise elongated streaks described in sec.2.3.

Between $y^+ \approx 20$ and 60 lies the nominally autonomous streak instability cycle, where the lifted tops of the streaks interact with the mean shear to produce the unmistakable streamwise elongated vortices [137]. Most of the vortices produced in this way convect away from the wall and thereafter degenerate into less coherent turbulence [133]. Some of them stay in this region however, while their upper ends extend into the inertial layer [123], becoming the wall attached hairpin eddies predicted by Perry and Marusic's [125] wall-wake model. The process through which this happens has not yet been determined. In the mean, these attached vortices are the chief turbulent energy and momentum transfer mechanism in the inertial layer (if the Re number is high enough for one to exist) and are the cause of the characteristic logarithmic velocity profile. Although it has not been confirmed, it is likely that the undulating spanwise vortices found in the wake region are the product of the largest hairpin eddies that eventually detach from the wall and merge with each other. The fact that both sets of structures have sizes of the order of the boundary layer thickness and overlap in spatial distribution, supports this hypothesis. The wake eddies are also predicted by Perry and Marusic's model. In a normal ZPG boundary layer they have little influence on the overall flow, but in an APG they can coincide with the region of maximum turbulence production and behave similar to the structures found in a free shear layer [30].

The interdependence of the different structures in the boundary layer is very apparent. Clearly, a wall treatment that replaces or significantly alters the near-wall eddy dynamics, will have to account for this effect or risk severely corrupting the structures (and statistical properties) of the entire boundary layer. These effects were investigated by Cabot *et al.* [23] using Germano's dynamic model [46]. Their findings indicate a severe distortion of first order statistics in the first few off-the-wall grid points coupled with an over prediction in wall-shear and streamwise normal stresses, partially due to the dynamic model's under-

2. Turbulent Boundary Layers

prediction of SGS viscosity. Artificially correcting the near-wall SGS viscosity leads to somewhat better results, but the coarseness of their mesh produces near-wall velocities that are still unphysical and have excessively large fluctuations. Baggett [8] suggests that such under-resolved meshes cause the formation of large pseudo-streaks on the scale of the grid, which is usually much larger than the natural streak spacing of $y^+ \approx 100$. These unnaturally large structures are in turn linked to the corresponding increase in fluctuation values. Indeed, Cabot *et al.* speculate that the disruption of these structures may be the cause of improved results observed through the implementation of stochastic backscatter [102] and sub-optimal control methods [113]. Even these enhanced results display a lack of proper behaviour in the wake region, so that the cumulative effect of poor resolution and wall models is essentially a lower Reynolds number flow [23]. There are, however, two possible exceptions to this scenario.

Firstly, if the boundary layer eddies are small compared to the largest momentum carrying vortices (*i.e.* the boundary layer is thin compared to characteristic length scale of eddies produced through other processes, like shedding, shear layers *etc.*) and the flow is not overly sensitive to the exact representation of the boundary layer (as in transition or incipient separation), then the boundary layer structures can be excised from the LES computation with only a small loss of accuracy. In essence, it is assumed that if energy carrying scales are significantly larger than the scales in the boundary layer, there will be little interaction between the two, so that the dynamics of the dominant structures will be largely decoupled from those native to the boundary layer. Also, since most of the energy is contained in the larger structures, inevitable errors in the modelling of the near-wall eddies have a correspondingly smaller influence on the overall flow statistics (provided gross characteristics are modeled correctly). This approach, first proposed by Spalart *et al.* [149] is known as detached eddy simulation, since the wall-attached eddies are modeled, while ‘detached’ eddies are resolved. Matching a wall treatment to the outer flow is by definition only possible where an outer layer exists, so this type of approach is not likely to be feasible in well-developed bounded flows, such as pipes and ducts, where the influence of the wall is felt throughout the domain.

The second possible location for a static (no artificial structural support for wall-

attached eddies) wall treatment interface is hinted at in sec.2.3.2. Recall that the streak instability cycle is relatively insensitive to damping of perturbations below $y^+ \approx 20$ and can survive, albeit with some disturbances, if the damping height is kept below $y^+ \approx 60$. Visualisations also show that there are very few coherent structures present below this height and those that are (like the low speed streaks) have characteristic dimensions far in excess of the local distance to the wall. This suggests that matching a wall treatment to the interior flow at or below this critical height might be less likely to disturb the near-wall vortex dynamics, provided the local mesh can adequately resolve the streak instability cycle. Section 2.4.2 shows that the qualities of coherent structures at this matching height and the resolution they require, are relatively insensitive to pressure gradients and flow separation. An inner layer model can therefore be expected to be more generally valid than one matched outside the boundary layer. The drawback of this approach is of course, that the fine resolution required to capture the near-wall dynamics represents a much smaller saving in computational resources. Typically, wall-parallel dimensions cannot be much larger than in a fully resolved simulation ($\Delta x^+ \approx 30$, $\Delta z^+ \approx 20$), while the first wall-normal grid point must be around $y^+ \approx 10$ or less.

There thus appears to be four possible approaches in treating the near-wall region in LES:

1. Fully resolved,
2. Inner layer matching,
3. Arbitrary matching with structural support and
4. Outer layer matching.

Each method has its own advantages and drawback, but none of them currently offers a universal solution for all flow types and Reynolds numbers. It does however, present a framework within which to evaluate wall treatment candidates, which is the focus of the next chapter.

2. Turbulent Boundary Layers

Chapter 3

LES Principles and Modelling

Having investigated the vagaries of turbulent motion in fluids, we now turn to issues of modelling. Specifically we will examine the modelling inherent in the concept of Large Eddy Simulation with particular emphasis on the methods necessary to make this approach computationally tractable in the short and medium term. To this end, the chapter opens with a brief overview of the characteristics and current state of large eddy simulation. The later sections (and bulk of this chapter) will focus on currently available wall treatments and improvements necessary to successfully approximate the turbulent boundary layer.

3.1 Governing Equations

The basic equations for LES were first formulated by Smagorinsky [142] in the early 1960's. Since computational resources were severely limited an alternative to resolving all the scales of motion had to be conceived. Based on the theory of Kolmogorov [83], that the smallest scales of motion were uniform and the assumption that these small scales serve mainly to drain energy from the larger scales through the cascade process, it was felt that they [the small scales] could be successfully approximated. The large scales of motion, which contain most of the energy, do most of the transporting and are affected the strongest by the boundary conditions should therefore be calculated directly, while the small scales are represented by a model. This is the basis of LES.

3. LES Principles and Modelling

To separate the large scales of motion from the small some kind of averaging must be done. In LES this averaging operator is not the ensemble average as in RANS, but a filter which is a locally derived weighted average of flow properties over a volume of fluid. One of the properties of the filtering process is the filter width, Δ , which is a characteristic length-scale and has the approximate effect that scales larger than Δ (resolved or super-**Grid Scales** (GS)) are retained in the filtered flow field, while the contribution of scales smaller than Δ (**Sub-Grid Scale** (SGS)) must be modeled.

Formally, any flow variable, f , in LES is composed of a large scale and a small scale contribution:

$$\bar{f} = f - f'. \quad (3.1)$$

Throughout, the prime denotes the small scales and the overbar the larger scales (also referred to as grid or resolved scales). To extract the large scale components a filtering operation is applied, which is defined as:

$$\bar{f}(x) = \oint G(x, x'; \Delta) f(x') dx', \quad (3.2)$$

where Δ , in addition to being the filter width, is also proportional to the wavelength of the smallest scale retained by the filtering operation. $G(x, x'; \Delta)$, the filter kernel, is a localised function or function with compact support (*i.e.* the function is large only when x and x' are not far apart), that satisfies the condition:

$$\oint G(x, x'; \Delta) dx' = 1. \quad (3.3)$$

A graphical representation of the filtering process is shown in fig.3.1 with arbitrary filter kernel and a randomly fluctuating one-dimensional variable, f .

The most common filter kernels that have been applied to LES include:

- The Gaussian filter, which has the advantage of being smooth and differentiable

$$G(x, \Delta) = \sqrt{\frac{6}{\pi \Delta^2}} \exp\left(-\frac{6x^2}{\Delta^2}\right). \quad (3.4)$$

- The top-hat filter, which is simply an average over a rectangular region. It is the common choice for finite volume methods, primarily because the average is over a

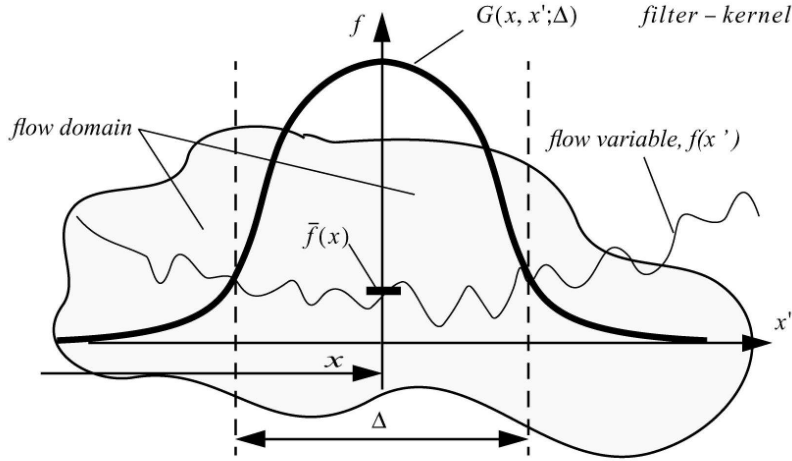


Figure 3.1: One-dimensional representation of an arbitrary filter function.

grid volume of the finite volume mesh where the flow variables are a piecewise linear function of x . This implies that if the filter width Δ , is chosen to be equal to the grid-spacing, the averaged and the local value of \bar{f} will be equal.

$$G(x, \Delta) = \begin{cases} \frac{1}{\Delta} & : \text{if } (|x'| \leq \frac{\Delta}{2}) \\ 0 & : \text{otherwise.} \end{cases} \quad (3.5)$$

- The sharp Fourier cutoff filter, which is best defined in Fourier space and eliminates all the wave numbers above a chosen frequency. This filter is normally used in conjunction with spectral methods since it is difficult to apply to inhomogeneous flows and doesn't smooth the resolved scale field as the previously mentioned filters tend to do.

$$\hat{G}(k, \Delta) = \begin{cases} 1 & : \text{if } (k \leq \frac{\pi}{\Delta}) \\ 0 & : \text{otherwise,} \end{cases} \quad (3.6)$$

where (\hat{G}) in this section denotes the Fourier coefficient of the filter function and k the wave number. The shape of these three filters and their Fourier transforms are shown in fig.3.2.

To illustrate the difference between the various filters they are applied to a test function and the spectra of the filtered variables are shown in fig.3.3. The top-hat and Gaussian

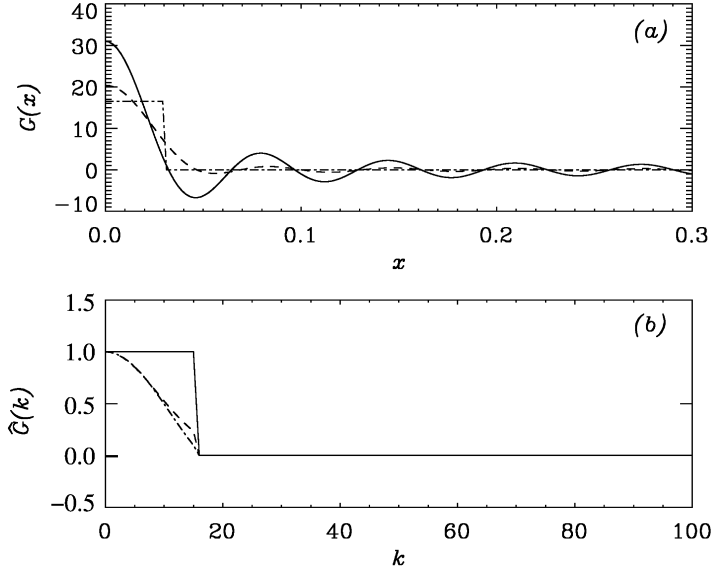


Figure 3.2: Filter functions. — sharp Fourier cutoff; - - - truncated Gaussian; - · - top-hat.
(a) Real space; (b) Fourier space (from Piomelli [128]).

filters give similar results as they both smooth the large and small scale fluctuations, while the Fourier cutoff filter only affects the scales below the cutoff wave number. This smoothing behaviour causes a relative increase in the required resolution for these filter types if they are to capture the same high frequency eddies as their spectral counterparts (*i.e.* spectral methods are more accurate).

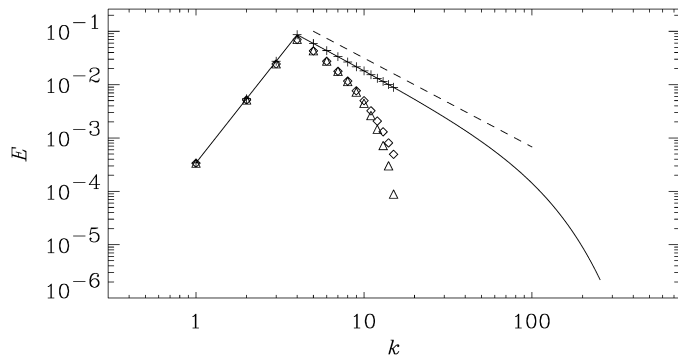


Figure 3.3: Filtering of a test function in Fourier space. --- unfiltered; + sharp Fourier cutoff; \diamond Gaussian; \triangle top-hat; - - - $k^{-5/3}$ (from Piomelli [128]).

If this filtering process is applied to the Navier-Stokes equations, one obtains the filtered equations of motion. Provided that the filter commutes with differentiation (*i.e.* Δ is constant), these appear at first glance to be very similar to the RANS equations. For incompressible flow they are:

$$\nabla \cdot \bar{\mathbf{u}} = 0 \quad (3.7)$$

$$\frac{\partial \bar{\mathbf{u}}}{\partial t} + \nabla \cdot (\bar{\mathbf{u}} \bar{\mathbf{u}}) = -\frac{1}{\rho} \nabla \bar{p} + \nabla \cdot \nu (\nabla \bar{\mathbf{u}} + \nabla \bar{\mathbf{u}}^T) \quad (3.8)$$

Although the definition of the velocity appearing above differs from that in the RANS equation, the issues of closure are conceptually very similar. Since $\bar{\mathbf{u}}\bar{\mathbf{u}} \neq \bar{\mathbf{u}}\bar{\mathbf{u}}$ a modelling approximation must be introduced to account for the difference between the two sides of the inequality:

$$\boldsymbol{\tau} = \bar{\mathbf{u}}\bar{\mathbf{u}} - \bar{\mathbf{u}}\bar{\mathbf{u}}. \quad (3.9)$$

In LES the term $\boldsymbol{\tau}$ is known as the sub-grid scale stress and has the property that $|\boldsymbol{\tau}| \rightarrow 0$ as $\Delta \rightarrow 0$, so that in the limit of small mesh spacing a DNS solution is returned. It is functionally similar to the Reynolds stress in RANS modelling, but predictably the physics of the problem is somewhat different in LES. The SGS stresses represent a much smaller part of the turbulent energy spectrum than the RANS turbulent energy, so that the accuracy of the stress model may be less crucial than in RANS computation. It must be noted however, that if the turbulent dissipation in the small scales is not accurately represented by the SGS model it can lead to a buildup of energy in the resolved scales and computational instability.

By applying the decomposition described at the beginning of this section to the velocity field, *i.e.* $\mathbf{u} = \bar{\mathbf{u}} + \mathbf{u}'$, the SGS stress can be decomposed into three separate terms:

$$\boldsymbol{\tau} = \overline{(\bar{\mathbf{u}} + \mathbf{u}')(\bar{\mathbf{u}} + \mathbf{u}')} - \bar{\mathbf{u}}\bar{\mathbf{u}} = (\bar{\mathbf{u}}\bar{\mathbf{u}} - \bar{\mathbf{u}}\bar{\mathbf{u}}) + (\bar{\mathbf{u}}\mathbf{u}' + \mathbf{u}'\bar{\mathbf{u}}) + \mathbf{u}'\mathbf{u}'. \quad (3.10)$$

Each of these terms has some physical significance:

- The first term, which can be computed from the resolved velocity field, represents the interaction of resolved eddies to produce sub-grid turbulence. It is generally known as the Leonard term.

3. LES Principles and Modelling

- The second bracketed term relates to the energy transfer between the resolved and unresolved scales. Energy can be transferred in either direction, but generally moves from the larger to the smaller eddies. This term physically represents the interaction between unresolved and resolved eddies and is known as the cross term.
- The last term represents the effect of small eddy interaction and is generally known as the SGS Reynolds stress.

While the SGS stress as a whole is Galilean invariant (independent of inertial frame) the cross and Leonard stresses are not. Also, the correlations that are used to model these stresses are approximations and therefore contain errors that defeat any attempt at precision. For these reasons the decomposition of SGS stresses (eq.3.10) has largely been abandoned in favour of modelling the SGS term as a whole.

3.2 Sub-grid Scale Modelling

The sub-grid scale models introduced in this section have many parallels with their RANS counterparts, with the caveat that a much smaller portion of the turbulence spectrum is modeled. A smaller modeled contribution translates into a smaller error potential, so that even comparatively simple SGS models can produce satisfactory results. Since this investigation is restricted to finite volume calculations, only models which can readily be utilised in this framework are included. Specifically, spectral and other methods which are employed predominantly in wavespace are not included, since they do not readily translate to complex domains. Also, “modeless” methods which attempt to mimic sub-grid scale turbulence by using a dissipative numerical scheme are deemed indefensible.

3.2.1 Algebraic Models

In LES the dissipative scales are generally not resolved. The main role of the SGS model is therefore to extract energy from the resolved scales, mimicking the drain associated with the energy cascade. This can be accomplished with an eddy-viscosity model (similar to the RANS approach), which is based on the hypothesis that the non-uniform component

of the SGS stress tensor is locally aligned with the resolved non-uniform part of the rate of strain tensor. The normal stresses are taken as isotropic and can therefore be expressed in terms of the SGS kinetic energy,

$$\boldsymbol{\tau} - \frac{1}{3} \text{tr}(\boldsymbol{\tau}) \mathbf{I} = \boldsymbol{\tau} - \frac{2}{3} K \mathbf{I} = -\nu_{SGS} (\nabla \bar{\mathbf{u}} + \nabla \bar{\mathbf{u}}^T) = -2\nu_{SGS} \bar{\mathbf{S}}, \quad (3.11)$$

where for incompressible flow, $\bar{\mathbf{S}}$ is the large-scale strain rate tensor,

$$\bar{\mathbf{S}} = \frac{1}{2} (\nabla \bar{\mathbf{u}} + \nabla \bar{\mathbf{u}}^T). \quad (3.12)$$

The isotropic part of the stress tensor, $\frac{1}{3} \text{tr}(\boldsymbol{\tau})$, is either modeled or expressed in the filtered pressure.

The first proposed relation for the sub-grid scale eddy-viscosity, the ‘Smagorinsky model’ [142], was derived from the simplifying assumption that the small scales are in equilibrium and dissipate entirely and instantaneously all the energy received from the resolved scales. Although there are other similar methods to derive the eddy-viscosity (see [94] & [89]), they all produce algebraic Smagorinsky models of the following type:

$$\nu_{SGS} = (C_S \Delta)^2 |\bar{\mathbf{S}}| \quad (3.13)$$

$$K = (C_I \Delta)^2 |\bar{\mathbf{S}}|^2 \quad (3.14)$$

$$|\bar{\mathbf{S}}| = (\bar{\mathbf{S}} : \bar{\mathbf{S}})^{1/2} \quad (3.15)$$

The value of the parameter C_S , the Smagorinsky ‘constant’, has been determined from isotropic turbulence decay [95] and ranges between 0.18 and 0.23 for such flows. The model suffers from one major deficiency: its excessive dissipation in laminar or high shear regions (caused by high $\bar{\mathbf{S}}$) so that the C_S parameter must be decreased in these situations. This has been accomplished with some success for near-wall flows by using the van Driest damping function, which reduces the sub-grid eddy-viscosity as a function of wall-normal distance. This is however somewhat undesirable, as the SGS model should preferably depend exclusively on the local flow properties. Also, the correlation between the Smagorinsky model and the actual turbulent stress behaviour is quite low, since the assumption that deviatoric SGS stresses and resolved strain rates align does not normally hold true [128]. Despite these and other drawbacks the Smagorinsky model has been

3. LES Principles and Modelling

relatively successful, probably because it dissipates energy at approximately the right overall rate.

3.2.2 Differential Sub-grid Models

The assumption of equilibrium means that the Smagorinsky model will become correspondingly less accurate the farther from this condition the flow strays. Unfortunately, non-equilibrium conditions commonly occur in free shear layers, separating and reattaching flows, boundary layers and wall dominated domains like pipes and channels and are thus too common to dismiss out of hand. The problem can be addressed by adding a history effect, such as transport equations for one or more of the sub-grid turbulence characteristics, to the model. The simplest such approach is a one-equation model.

Most one-equation models are also based on the eddy-viscosity concept, but in addition solve a transport equation for a sub-grid scale quantity on which the eddy viscosity depends. One such quantity is the sub-grid scale kinetic energy, defined as

$$K = \frac{1}{2} \sum_i (\tau_{ii}), \quad (3.16)$$

which provides a SGS velocity scale. Other possibilities include transported SGS viscosity or vorticity, such as the Spalart-Allmaras model described in sec.3.3.3.

The transport equation for SGS turbulent energy can be derived by first subtracting the filtered equations of motion from their exact non-filtered counterparts to give a relation for the fluctuating component of velocity \mathbf{u}' . Multiplying the result by the sub-grid velocity vector and contracting based on the assumption of SGS isotropy produces the one-equation turbulent energy model, one variant of which is given by Yoshizawa [171],

$$\frac{\partial K}{\partial t} + \nabla \cdot (K \bar{\mathbf{u}}) = \nabla \cdot [(\nu + \nu_{SGS}) \nabla K] - \epsilon - \boldsymbol{\tau} \cdot \bar{\mathbf{S}}, \quad (3.17)$$

where the SGS eddy-viscosity, ν_{SGS} , and the dissipation, ϵ , can be found from,

$$\nu_{SGS} = C_k K^{1/2} \Delta \quad (3.18)$$

$$\epsilon = C_\epsilon K^{3/2} / \Delta \quad (3.19)$$

The main deficiency of the one-equation models is that they don't address the discrepancy between the principal axes of the SGS stress and the rate of strain tensor [45]. This

is the same problem that the Smagorinsky model has and one that is common to most eddy-viscosity approaches. In fact, under ideal equilibrium circumstances one-equation models should perform no better than the Smagorinsky model. They do however, have the advantage of providing a more accurate time scale through the independent definition of the velocity scale and have shown advantages when used to model transitional flows or flows with large scale unsteadiness. In particular, a study of the performance of different SGS models in channel flows by Fureby *et al.* [44] has shown the one-equation model to be quite effective and superior to algebraic relations under these circumstances.

As mentioned previously, one major weakness of eddy-viscosity based models is the assumption of isotropy in the unresolved scales. While this condition holds true for a large subset of flows and filters, its validity is far from universal. If the mesh spacing is too large, the unresolved motion may be anisotropic: near a solid boundary even the smallest scales do not conform to the isotropy assumption and anisotropic grids will resolve even isotropic eddies differently depending on their orientation. Further refinement of the mesh inevitably reduces the problem, but a more satisfactory solution may be arrived at if the assumptions of isotropy are abandoned.

By neglecting isotropy assumptions and following a rationale similar to that employed by the one-equation turbulent energy model a transport equation for the complete SGS stress tensor, $\boldsymbol{\tau}$ can be derived. The first successful implementation of such a model was described by Deardorff [39] in an atmospheric boundary layer application. A more recent version derived by Fureby *et al.* [45] is reproduced here:

$$\frac{\partial \boldsymbol{\tau}}{\partial t} + \nabla \cdot (\boldsymbol{\tau} \bar{\mathbf{u}}) = -(\nabla \bar{\mathbf{u}} \cdot \boldsymbol{\tau}^T + \boldsymbol{\tau} \cdot \nabla \bar{\mathbf{u}}^T) + \underbrace{\nabla \cdot [(\nu + \nu_{SGS}) \nabla \boldsymbol{\tau}]}_{\mathbf{M}} + \underbrace{\frac{2}{5} k \bar{\mathbf{S}} - c_M K^{1/2} \Delta^{-1} \boldsymbol{\tau}}_{\Pi} - \underbrace{\frac{2}{3} \epsilon \mathbf{I}}_{\mathbf{E}}, \quad (3.20)$$

3. LES Principles and Modelling

where

$$k = \frac{1}{2} \text{tr}(\boldsymbol{\tau}), \quad (3.21)$$

$$\nu_{SGS} = c_k \Delta K^{1/2}, \quad (3.22)$$

$$\epsilon = c_\epsilon K^{1/2} / \Delta \quad (3.23)$$

$$c_k = 0.07, \quad c_M = 4.15, \quad c_\epsilon = 1.05.$$

$$(3.24)$$

The underbraced terms in eq.3.20 represent modeled quantities: \mathbf{M} is an approximation for the triple correlation tensor, $\mathbf{\Pi}$ models the pressure velocity-gradient and the dissipation tensor is approximated by the \mathbf{E} term, which is assumed to be isotropic. Fureby *et al.* have shown that the differential stress model produces backscatter similar to the linear combination model if the mesh is fine enough, but with the potential interscale transfer limited by the transported SGS energy. When the spatial resolution was decreased, the modeled energy transfer was one way, behaving more like an eddy viscosity model. The result is an adaptable SGS treatment that seemingly changes its response to best suit local conditions.

Sine the stress transported by eq.3.20 is symmetric (*i.e.* $\tau_{xy} = \tau_{yx}$) it requires the solution of only 6 tensor components. This is still considerably more expensive computationally than algebraic or one equation models. However, the large expense of the resolved pressure-momentum calculation means that the model will still only accounts for a comparatively small portion of the overall cost, somewhat ameliorating this drawback. The differential sub-grid stress models have been shown to perform very well, with advantageous properties over a range of flow conditions [45]. Whether the increased costs can be justified by the (sometimes marginal) performance improvements remains uncertain.

3.2.3 Scale Similarity and Linear Combination (mixed) Models

While eddy-viscosity models are able to represent the global dissipative effect of the sub-grid scales, their prediction of the correlation between the large rate of strain and the sub-grid stresses is generally poor. They also lack a mechanism for energy transfer from

the small scales to the large (backscatter) and thus fail to reproduce all aspects of the energy exchange on a local level.

The idea behind the scale-similarity model (Bardina *et al.* [11]) is that the smallest resolved eddies of size $O(\Delta)$ interact with the SGS eddies in a very similar way to which slightly larger resolved eddies (for example of size $O(2\Delta)$) interact with those of size $O(\Delta)$. Another way to think of the hypothesis is as a sort of extrapolation procedure from the smallest resolved to SGS scales, an approach which will generally work if there is a regular pattern in the data over the range extrapolated. The largest sub-grid scales can be obtained by filtering the SGS velocity $\mathbf{u}' = \mathbf{u} - \bar{\mathbf{u}}$ to give $\bar{\mathbf{u}'} = \bar{\mathbf{u}} - \bar{\bar{\mathbf{u}}}$. Now following Bardina's assumption and eq.3.9, the SGS stresses can be written as,

$$\boldsymbol{\tau} = \bar{\mathbf{u}}\bar{\mathbf{u}} - \bar{\mathbf{u}}\bar{\mathbf{u}} \approx \bar{\bar{\mathbf{u}}}\bar{\bar{\mathbf{u}}} - \bar{\bar{\mathbf{u}}}\bar{\bar{\mathbf{u}}} \quad (3.25)$$

which allows the calculation of the SGS stress directly from the resolved field. In practice, this method is only compatible with a system of explicit filtering (see sec.3.1) where the value of the filtered variable is not constant over the filtering region. An alternative and more general approach by Lui *et al.* [98] uses a second filter $\tilde{\Delta}$ (see sec.3.2.4) larger than the first to predict the SGS stress:

$$\boldsymbol{\tau} \approx \widetilde{\bar{\mathbf{u}}}\widetilde{\bar{\mathbf{u}}} - \widetilde{\bar{\mathbf{u}}}\widetilde{\bar{\mathbf{u}}} \quad (3.26)$$

In either case, the correlation between the scale similarity model and the exact SGS stress is relatively high. This indicates that the scale similarity model predicts important turbulent stress structures at the right locations. It is also found to transfer energy from the smallest to the larger resolved scales. Unfortunately, it hardly dissipates any energy and thus cannot serve as an independent SGS model. This problem can be alleviated by combining it with the eddy-viscosity model to produce the linear combination or mixed model,

$$\boldsymbol{\tau} = \bar{\mathbf{u}}\bar{\mathbf{u}} - \bar{\mathbf{u}}\bar{\mathbf{u}} - 2\nu_{SGS}\bar{\mathbf{S}} + \frac{1}{3}\text{tr}(\boldsymbol{\tau}), \quad (3.27)$$

which lacks the stability problems and has been shown to produce improved results [11] compared to the Smagorinsky model. It must be noted that the coefficients used to calculate the SGS eddy-viscosity above are different from those used in the Smagorinsky model.

3.2.4 Dynamic Models

If one takes the methods described in the similarity model a step further, the concept of a dynamic model results. First proposed by Germano *et al.* [46], it might be better described as a procedure, as the method can be applied to any of the previously described models. In dynamic procedures the coefficients of the SGS model are determined as part of the calculation, based on the energy content of the smallest resolved scales, rather than *a priori* input as in the Smagorinsky model. This is accomplished by assuming, analogous to the scale similarity model, that the behaviour of these scales is very similar to the sub-grid scales. By calculating the SGS model coefficients for these small scales and applying it to the LES, a kind of self-contained sub-grid scale model is produced.

To formally describe the procedure, first recall from eq.3.9 that the sub-grid scale stress that must be modeled in LES is:

$$\boldsymbol{\tau} = \overline{\mathbf{u}\mathbf{u}} - \overline{\mathbf{u}}\overline{\mathbf{u}}.$$

We now define a second or ‘test filter’, with a width $\tilde{\Delta}$ that is larger than or equal to the original filter-width, Δ (typically $\tilde{\Delta} = 2\Delta$; the tilde ($\tilde{\cdot}$) will henceforth denote the test filter). If this test filter is applied to the once-filtered Navier-Stokes equations (eq.3.8), the sub-grid stress that must be modeled in the test-filter level LES is given by,

$$\mathbf{T} = \widetilde{\overline{\mathbf{u}\mathbf{u}}} - \widetilde{\overline{\mathbf{u}}}\widetilde{\overline{\mathbf{u}}}. \quad (3.28)$$

Note at this stage that the large scale or resolved part of the SGS stress at the test filter level, otherwise known as the Leonard stress, can be explicitly computed from the LES field from the following relation,

$$\mathbf{L} = \widetilde{\overline{\mathbf{u}\mathbf{u}}} - \widetilde{\overline{\mathbf{u}}}\widetilde{\overline{\mathbf{u}}}. \quad (3.29)$$

It follows directly from the definitions above that:

$$\mathbf{L} = \mathbf{T} - \boldsymbol{\tilde{\tau}}. \quad (3.30)$$

Equation 3.30 has become known as the Germano identity, and forms the basis of the dynamic model. The use of the identity to calculate the model coefficients is illustrated in the following derivation by Piomelli [128].

First, define a generalised eddy-viscosity model to relate both sub-grid and sub-test grid stresses to their respective resolved fields, $\boldsymbol{\alpha}$ and $\boldsymbol{\beta}$.

$$\boldsymbol{\tau} = -2C_v\boldsymbol{\alpha}, \quad \mathbf{T} = -2C_v\boldsymbol{\beta} \quad (3.31)$$

Since the SGS stresses are replaced by the above modelling assumptions, substituting eq.3.30 into 3.31 produces only an approximation of the identity. In addition, the system of equations is over-determined with five independent equations available to calculate a single coefficient. In an attempt to remedy the problem, Lilly [96] proposed that the error produced by the approximation be minimised in accordance with the least-squares method. The error can be found from,

$$\mathbf{e} = \mathbf{L} - \mathbf{T} - \tilde{\boldsymbol{\tau}} = \mathbf{L} + 2C_v\mathbf{M} \quad (3.32)$$

where $\mathbf{M} = \boldsymbol{\beta} - \tilde{\boldsymbol{\alpha}}$ and C_v is assumed to be smooth on the scale so that it can be extracted from the filtering operation. The least-squares minimisation is then applied as follows:

$$\frac{\partial \langle \mathbf{e} : \mathbf{e} \rangle}{\partial C_v} = 2 \left\langle \mathbf{e} : \frac{\partial \mathbf{e}}{\partial C_v} \right\rangle = 0, \quad (3.33)$$

with $\langle \cdot \rangle$ denoting an appropriate ensemble average. Substituting eq.3.32 and its derivative into eq.3.33 produces,

$$\langle (\mathbf{L} + 2C_v\mathbf{M}) : \mathbf{M} \rangle = 0, \quad (3.34)$$

which simplifies to give the required coefficient,

$$C_v = -\frac{1}{2} \frac{\langle \mathbf{L} : \mathbf{M} \rangle}{\langle \mathbf{M} : \mathbf{M} \rangle}. \quad (3.35)$$

This procedure can now be applied to mixed models and models with two or more coefficients as well. Piomelli gives the minimised correlation for one-coefficient mixed models of the form

$$\boldsymbol{\tau} = \mathbf{A} - 2C_v\boldsymbol{\alpha}, \quad \mathbf{T} = \mathbf{B} - 2C_v\boldsymbol{\beta}, \quad (3.36)$$

as

$$C_v = -\frac{1}{2} \frac{\langle \mathbf{L} : \mathbf{M} \rangle - \langle \mathbf{N} : \mathbf{M} \rangle}{\langle \mathbf{M} : \mathbf{M} \rangle}, \quad (3.37)$$

where $\mathbf{N} = \mathbf{B} - \tilde{\mathbf{A}}$. Similarly, for a two-coefficient model

$$\boldsymbol{\tau} = C_L \mathbf{A} - 2C_v\boldsymbol{\alpha}, \quad \mathbf{T} = C_L \mathbf{B} - 2C_v\boldsymbol{\beta} \quad (3.38)$$

3. LES Principles and Modelling

which in addition requires that $\frac{\partial \langle \mathbf{e} : \mathbf{e} \rangle}{\partial C_L} = 0$, yields

$$C_L = -\frac{\langle \mathbf{M} : \mathbf{N} \rangle \langle \mathbf{L} : \mathbf{M} \rangle - \langle \mathbf{M} : \mathbf{M} \rangle \langle \mathbf{L} : \mathbf{N} \rangle}{\langle \mathbf{M} : \mathbf{N} \rangle \langle \mathbf{M} : \mathbf{N} \rangle - \langle \mathbf{M} : \mathbf{M} \rangle \langle \mathbf{N} : \mathbf{N} \rangle} \quad (3.39)$$

$$C_v = -\frac{1}{2} \frac{\langle \mathbf{M} : \mathbf{N} \rangle \langle \mathbf{L} : \mathbf{N} \rangle - \langle \mathbf{M} : \mathbf{M} \rangle \langle \mathbf{L} : \mathbf{N} \rangle}{\langle \mathbf{M} : \mathbf{N} \rangle \langle \mathbf{M} : \mathbf{N} \rangle - \langle \mathbf{M} : \mathbf{M} \rangle \langle \mathbf{N} : \mathbf{N} \rangle} \quad (3.40)$$

The ensemble average has the purpose of removing very sharp fluctuations of the coefficients, which would otherwise destabilise numerical calculations and make the model inconsistent, since the coefficients cannot be removed from the filtering operation.

This averaged least-squares version of the procedure has removed many of the problems associated with earlier dynamic models, such as spuriously large and negative eddy-viscosities. Several other approaches have also been tried with varying success, of which the most notable will be mentioned briefly. One of these, used by Germano, was to average the coefficients C_L and C_v over all homogeneous directions. This is possible only for flows with some degree of homogeneity. Piomelli [127] suggested the use of a combination of local spatial and temporal averaging, which is successful as long as the spatial region is large enough to smooth out the coefficients and does not contain too much inhomogeneity.

Although the above model coefficients are assumed constant, computed values can vary substantially with time and space, which invalidates the original assumption that removes them from the filtering operation. Recognising that a part of the stability problem comes from removing the model coefficient from the filter, Ghosal *et al.* [48] used an integral formulation of the identity (eq.3.29), that rigorously removes the mathematical inconsistency. The expense of this added confidence is the solution of an integral equation at each time-step. An improvement on this method may be obtained by subjecting the integral equation to the constraint that the total viscosity (molecular and SGS) must never be less than zero. The solution of this integral through the use of least-squares method leads to a constrained optimisation problem and is known as the dynamic localisation model. This method is reported to produce very good results at the cost of some increase in calculation time [48].

The introduction of dynamic models has caused significant progress in the sub-grid scale modelling of transitional flows and has resolved many of the problems encountered with traditional "static" models. In free shear and channel flows the dynamic model

automatically adjusts, by lowering the coefficient in areas of high shear and near the walls, a function that is normally performed by the van Driest damping function. Another advantage is that the eddy viscosity automatically goes to zero in laminar regions of the flow.

The major drawback of this approach is that additional averaging, either in homogeneous directions, along streamlines or in local regions of the flow, is necessary to avoid excessive fluctuations in the model coefficients. The local average, which is most commonly used in more complex cases, also ideally requires that the flow tend toward local homogeneity or that the averaging volume is large enough to smooth the model coefficients. Also, unless the scheme is somehow artificially bounded, the dynamic procedure occasionally produces negative dissipation. This is interpreted by some as transport of energy from the unresolved to the resolved scales. However, if left unchecked this energy transfer can violate the conservation of energy law and lead to unphysical results.

Other Models

Although the models treated in this section constitute the most commonly used, only a portion of the available SGS model implementation have been presented. In fact, it is possible to convert nearly any model used for RANS calculation into an equivalent LES version. Rarely however, has the increased cost of additional differential equations been justified by substantially improved accuracy. Another area of SGS models that was not treated is spectral models, which deal in the distribution of turbulent energy over the range of length scales. These methods are applicable only to homogeneous turbulence and are therefore not generally used in flows of engineering interest.

Also, recall that all the models in this section treat the sub-grid scale stress as an added dissipation. However, if one looks at the original filtered equation (3.8), it is plain that the terms being approximated are in fact convective. Furthermore, negative eddy-viscosity (in dynamic models) has been interpreted to account for energy transfer from small to larger scales even though negative dissipation is clearly unphysical. No model reviewed to date has attempted to account for this in a consistent fashion.

3.2.5 SGS Model Choice

A one-equation type model will be used throughout this project. This choice is motivated by several factors, chief among which is a comparative SGS model study done by Fureby *et al.* [44]. In an investigation of fully developed channel flows the one-equation model is outperformed only by the full SGS stress model (which is computationally more expensive). Secondly, one-equation models provide a distinct benefit when compared to “zero” equation models (e.g. Smagorinsky), since they account for non-equilibrium effects and provide an independent SGS velocity scale at a small increase in cost. This translates into increased accuracy, particularly in more complex flow arrangements.

It was decided not to include the dynamic procedure, based partially on the considerations expounded in the previous section. The dynamic model is also known to become quite inaccurate in cases with badly resolved walls regions [23] (which will occur during this study), since the assumptions of scale similarity no longer hold near the boundary. Similarly, the dynamic model is not expected to perform well in cases where there is a large separation of scales or forcing at the smallest grid scales, (e.g. badly resolved shear layers), since it also assumes equilibrium of the sub-grid energy cascade. In addition, the uncertainties inherent in the choice of averaging method for the SGS coefficients have not been satisfactorily resolved for arbitrary flows without homogeneous averaging directions.

3.3 Wall Treatments

There are currently many different LES wall treatments and permutations in use and under investigation. Although this section will attempt to give a comprehensive review of the topic, some of the less well known models may be omitted. As mentioned previously, most wall models attempt to predict the wall shear stress. This characteristic is not however, universal: several treatments exist that can only be termed as “auxiliary-models”, in that they attempt to reproduce secondary properties of the near-wall flow and are therefore unusable on their own. These include, but are not limited to, modelling of the sub-grid scale viscosity (or equivalent properties) and structural characteristics of the near-wall flow. Some representative approaches will be covered at the end of the section

after the momentum transfer models.

3.3.1 Equilibrium Stress Models

The core assumption of this class of wall model is that the stresses in the boundary layer are in some kind of average or instantaneous equilibrium. This has the additional implication, that some form of the logarithmic law of the wall should be applicable in the near-wall region. In general, these models thus use an approximate correlation to specify the wall shear stresses as a function of the local velocity at the first off-the-wall grid point (fig.3.4). This removes the no-slip boundary condition and its associated costs from the LES calculation.

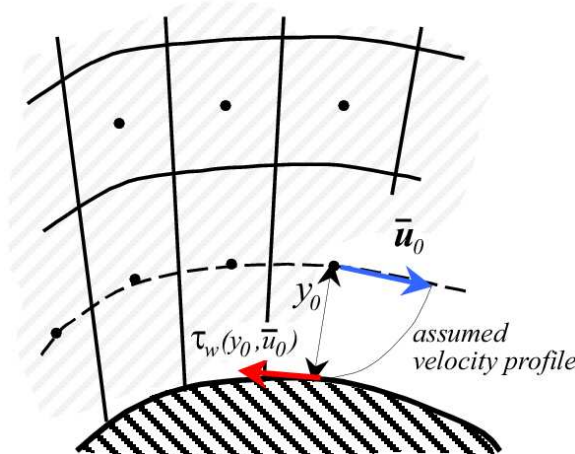


Figure 3.4: Wall function implementation.

Deardorff Model

Although not a equilibrium stress model in the strictest sense, Deardorff's [38] model constitutes what is probably the first LES wall treatment. It is applicable to wall bounded flow at infinite Reynolds number and uses second wall normal derivatives to constrain the wall parallel velocities, such that the log law is satisfied in the mean. Formally, Deardorff's

boundary conditions are described by:

$$\frac{\partial^2 \bar{u}}{\partial y^2} = -\frac{1}{\kappa y_0^2} + \frac{\partial^2 \bar{u}}{\partial z^2}, \quad (3.41)$$

$$\bar{v}_w = 0, \quad (3.42)$$

$$\frac{\partial^2 \bar{w}}{\partial y^2} = \frac{\partial^2 \bar{w}}{\partial x^2}. \quad (3.43)$$

Besides enforcing a logarithmic profile eqs.3.41 and 3.43 also have the implication that the second derivative of the deviatoric part of velocity, $u' = \bar{u} - U$, in all directions are equal. In other words, Deardorff assumes that the turbulence in the near-wall layer is isotropic. Although Deardorff's model has had some success simulating channel flows at infinite Reynolds number, it is limited. It does not account for the effects of viscosity, and is therefore exclusively applicable to infinite Reynolds number flows. Coupled to the impermeability condition this means that the near-wall shear stresses are entirely due to sub-grid scales.

Schuman-Grotzbach (SG) Model

The first true equilibrium stress model, was proposed by Schumann [136] for use in channels and annuli at finite Reynolds numbers. The basic premise behind the Schumann's model is that deviations from the streamwise mean wall shear stress are linearly correlated with deviations of the streamwise velocity from its mean value. The earliest form of the model requires that the mean wall shear be known *a priori* (from the driving pressure gradient for example) making the method less than effective as a predictive tool.

These conditions can be expressed algebraically as:

$$\tau_{xy,w} = \frac{\bar{u}(x, y_0, z)}{\langle \bar{u}(x, y_0, z) \rangle} \langle \tau_w \rangle, \quad (3.44)$$

$$\bar{v}_w = 0, \quad (3.45)$$

$$\tau_{zy,w} = \nu_t \frac{\bar{w}(x, y_0, z)}{y_0}, \quad (3.46)$$

where the subscripts $\langle_{xy} \rangle$ and $\langle_{zy} \rangle$ denote the streamwise and spanwise directions respectively and $\langle \tau_w \rangle$ is the specified mean wall shear. The mean wall shear is also used to calculate the mean near-wall velocity $\langle \bar{u}_0 \rangle = \langle \bar{u}(x, y_0, z) \rangle$ in eq.3.44 from the logarithmic

law of the wall,

$$\langle \bar{u} \rangle (x, y_0, z) = \frac{u_\tau}{\kappa} \log \left(\frac{y_0 u_\tau}{\nu} E \right) \quad (3.47)$$

where $u_\tau = \sqrt{\langle \tau_w \rangle / \rho}$. Thus requiring that the streamwise velocity satisfy the logarithmic profile on the mean and be in phase with the instantaneous wall shear. The spanwise shear is specified by assuming the turbulent properties derived from the SGS model are constant throughout the near-wall cell

Grotzbach [52] adapted Schumann's original model by calculating the mean velocity, $\langle \bar{u}_0 \rangle$, as time and spatial average for $y = y_0$, thereby removing the requirement that the pressure gradient be known *a priori*. The mean wall shear, $\langle \tau_w \rangle$ can then be found from the logarithmic law,

$$\frac{\langle \bar{u}_0 \rangle}{u_\tau} = \frac{1}{\kappa} \log \left(\frac{y_0 u_\tau}{\nu} E \right) \quad (3.48)$$

This modification still imposes the logarithmic law in the mean, which implies that the first off-the-wall point in the SG model must be in the logarithmic layer (typically $y^+ \gtrsim 30$). The model can therefore be expected to significantly distort the eddy dynamics in the boundary layer if used on its own, with the effects becoming more pronounced as the near-wall cell heights increases. Comparisons by Cabot *et al.* [23] have shown anomalous behaviour when using equilibrium stress models in both the 'wake' beyond the logarithmic region and the first few near-wall points. The velocity in the wake is consistently underpredicted indicating abnormal eddy structures in this region, while wall stress and near-wall velocities are over predicted in relation to the bulk flow [113]. This implies incorrect modelling of the wall attached eddies that normally dominate transfer mechanisms in the inertial layer. Despite these drawbacks, it has seen wide use owing to its simplicity and ease of implementation. Some examples are plane channel flow [52, 126, 136] and flow through an annulus [136], both of which show fair comparison with experimental data.

Shifted Model

Numerical experiments by Rajagopalan and Antonia [130] have shown that Schumann's assumption regarding the correlation between the velocity in the logarithmic layer and the wall shear stress, is generally valid. Their results also show however, that the correlation improves markedly if a streamwise displacement is introduced between the velocity and

3. LES Principles and Modelling

the wall. This displacement is attributed to the existence of inclined streamwise structures near the surface. A further increase of correlation is also observed in the DNS data if small scale perturbations are removed by means of filtering, an operation implicit in the LES approach. Piomelli *et al.* [126] incorporate these results in their modification of the SG model, by introducing a streamwise displacement Δ_s into the correlation between instantaneous velocity and wall shear. In addition, a modification of spanwise shear stress to resemble the streamwise implementation of eq.3.44 was also found to improve results, producing the following set of boundary conditions:

$$\tau_{xy,w} = \frac{\bar{u}(x + \Delta_s, y_0, z)}{\langle \bar{u}_0 \rangle} \langle \tau_w \rangle, \quad (3.49)$$

$$\bar{v}_w = 0, \quad (3.50)$$

$$\tau_{zy,w} = \frac{\bar{w}(x + \Delta_s, y_0, z)}{\langle \bar{u}_0 \rangle} \langle \tau_w \rangle. \quad (3.51)$$

The optimum value of Δ_s was found, from experiment and DNS [130], to be approximately $\Delta_s = (1 - |y_0|) \cot(8^\circ)$ for $30 < y_0^+ < 50 - 60$ and $\Delta_s = (1 - |y_0|) \cot(13^\circ)$ for $y_0^+ > 60$. The shifted model has been tested in plane channel flow at moderate Re [10, 126] and found to produce very good agreement for both mean velocity and stress profiles compared to experimental and DNS data. Application to square duct and rotating channel flows [10] produced somewhat worse results, which is primarily ascribed to the inapplicability of the logarithmic law in certain regions of these flows. In terms of its effect on the near-wall eddy dynamics, problems similar to the SG model are to be expected. The relatively large near-wall cells ($\Delta y^+ > 60$) will be unable to support the turbulence producing streak instability cycle, and no attempt is made to artificially account for its effects.

Ejection Model

Another refinement of the SG model, the ejection model, attempts to incorporate the effects of rapid fluid motion, towards or away from the wall, on the wall shear stress. Observations by Piomelli *et al.* [126] reveal, that during sweep-ejection events, the impingement of high speed fluid on the wall produces stretching of the vortices parallel to the wall and consequently an increase in near-wall turbulence intensity. Ejections cause the opposite effect, namely a decrease in wall shear stress. The modified boundary conditions

that incorporate these observations can be represented as follows:

$$\tau_{xy,w} = \langle \tau_w \rangle - Cu_\tau \bar{v}(x + \Delta_s, y_0, z), \quad (3.52)$$

$$\bar{v}_w = 0, \quad (3.53)$$

$$\tau_{zy,w} = \frac{\bar{w}(x + \Delta_s, y_0, z)}{\langle \bar{u}_0 \rangle} \langle \tau_w \rangle, \quad (3.54)$$

where C is a dimensionless constant of order one, u_τ is the friction velocity and $\langle \tau_w \rangle$ is calculated from the logarithmic law. All other values are calculated as stipulated in previously described models. Testing of this model has mostly been limited to plane channel flows [126]. Results are similar to those produced by the shifted model and the same drawbacks regarding eddy dynamics apply.

Instantaneous Model

All of the wall treatments based on the SG model require a space and time averaged value for \bar{u} at $y = y_0$ and therefore make the implicit assumption that the average streamwise velocity approaches a finite non-zero value as the averaging intervals are increased. This is not always the case, especially in flows with recirculation and/or large scale unsteadiness. In regions of separation and reattachment for example, the mean wall parallel velocity may tend toward zero, invalidating the model assumptions. Also, in order to reproduce the logarithmic law on average, the SG based models assume a linear relationship between deviations from the mean velocity and deviations in the wall shear, a hypothesis that has not been substantiated.

The instantaneous model, first proposed by Mason and Callen [101], overcomes these problems by requiring that the velocity at the first grid point satisfy the law of the wall locally and instantaneously. This has the obvious drawback that the velocity-stress relationship is not guaranteed to satisfy the logarithmic profile on average. For a smooth wall the instantaneous boundary conditions are:

$$\frac{\bar{u}_\parallel}{u_\tau} = \frac{1}{\kappa} \ln \left[\frac{y_0 u_\tau}{\nu} E \right], \quad (3.55)$$

$$\bar{v}_w = 0, \quad (3.56)$$

where u_\parallel is the velocity parallel to the surface and the instantaneous wall stress must be evaluated from the shear velocity. Because of its instantaneous nature, the model displays

3. LES Principles and Modelling

two conflicting tendencies: 1) as the distance from the wall increases, the correlation between fluctuations of u_{\parallel} and τ_w degrades, so that some of the original assumptions become invalid far above the boundary, 2) increasing the size of the wall adjacent cell (and thus the SGS length scale) will cause the value of the instantaneous large scale velocity to tend toward the mean velocity forcing the wall shear to follow suit. Mason and Thomson [102] suggest that the former concern is of more importance, since large values of y_0 suppress resolved near-wall turbulence to an unacceptable extent. They recommend the following inequality as a necessary condition for the application of eqs.3.55 and 3.56 on a fine mesh:

$$y_0 \frac{\partial p}{\partial x} \ll \varsigma_{\tau}, \quad (3.57)$$

where ς_{τ} is the standard deviation of the wall shear stress, and the pressure gradient is along the mean flow direction.

The instantaneous model was used by Mason and Callen [101] in the simulation of an atmospheric boundary layer, but produced rather inconclusive results, ascribed to an under resolved near-wall region. Mason and Thomson [102] conducted similar calculations, but included a stochastic backscatter model (discussed in a later section) with greatly improved results. Also, channel flow simulation at various Reynolds numbers by Cabot *et al.* [20, 23] show no significant differences between the instantaneous model and those based on the SG model, making the instantaneous implementation preferable for flows that include recirculation and/or large instabilities.

Alternative Wall Functions

Most of the documented stress equilibrium models rely on the standard logarithmic law of the wall. There are several inherent limitations associated with this approach, notably a lack of pressure gradient sensitivity, a required minimum value of $y_0^+ \approx 30$ and an inability to account for moderate to strong non-equilibrium effects. At least some of these shortcomings can be rectified by using more advanced wall functions. One of the most widely known “universal” velocity profiles, is Spalding’s law [146], which is essentially a

fit of the laminar, buffer and logarithmic regions of an equilibrium boundary layer.

$$y^+ = u^+ + \frac{1}{E} \left[e^{\kappa u^+} - 1 - \kappa u^+ - \frac{1}{2} (\kappa u^+)^2 - \frac{1}{6} (\kappa u^+)^3 \right], \quad (3.58)$$

where $\kappa = 0.42$ and $E = 9.1$ are constants and $y^+ = y_0 u_\tau / \nu$ and $u^+ = \bar{u}_0 / u_\tau$ respectively. By substituting the known values of y_0 and \bar{u}_0 next to the wall, eq.3.58 can be transformed into a non-linear equation for u_τ , which can be easily solved using an iterative procedure (like the Newton-Raphson method) to provide the wall shear. The major advantage of using such a unified wall function, is that the first off-the-wall grid point can be placed in the buffer or viscous regions ($y_0^+ < 30$) without the loss of accuracy associated with the logarithmic profiles limited validity. This allows for local refinement near the wall without the need to switch from one wall function implementation to another. Thus, provided the rest of the boundary layer and wall parallel directions are also adequately resolved, the simulation should recover a DNS boundary layer solution as the near-wall cell size tends toward zero.

The above wall functions are strictly valid only in zero pressure gradient equilibrium flows. Recently however, several wall functions have been developed that in some way account for the effects of sustained pressure gradients on the near-wall velocity profile. Shih *et al.* [138] derived such a function, that has similar characteristics to Spalding's law (i.e. valid up to the wall). It is loosely based on Tennekes and Lumley's [156] asymptotic solution for boundary layers in adverse pressure gradients with zero wall stress and has the following form:

$$(Y_p^+)^2 = U_2^+ + e^{-(2\beta/\alpha)} \left[e^{(U_2^+/\alpha)} - 1 - \frac{U_2^+}{\alpha} \right], \quad (3.59)$$

$$Y_\tau^+ = U_1^+ + \frac{1}{E} \left[e^{\kappa U_1^+} - 1 - \kappa U_1^+ - \frac{1}{2} (\kappa U_1^+)^2 - \frac{1}{6} (\kappa U_1^+)^3 \right], \quad (3.60)$$

3. LES Principles and Modelling

where

$$Y_\tau^+ = \frac{y_0 u_\tau}{\nu}, \quad (3.61)$$

$$Y_p^+ = \frac{y_0 u_p}{\nu}, \quad (3.62)$$

$$U_1^+ = \frac{|\tau_w|}{\tau_w} \frac{U_1}{u_\tau}, \quad (3.63)$$

$$U_2^+ = 2 \frac{|dp_w/dx|}{dp_w/dx} \frac{U_2}{u_p}, \quad (3.64)$$

$$u_p = \left(\nu \frac{dp_w}{dx} \right)^{1/3}, \quad (3.65)$$

$$\bar{u}_0 = U_1 + U_2. \quad (3.66)$$

Here dp_w/dx is the streamwise pressure gradient at the wall and $\alpha \approx 5$ and $\beta \approx 8$ according to experimental data of Stratford [154]. To find the wall shear stress, it is first necessary to solve for U_2 using eqs. 3.65, 3.64, 3.62 and 3.59. U_2 and eq.3.66 can then be used to find U_1 , which in conjunction with eqs.3.60, 3.61 and 3.63 provides the shear velocity, u_τ , using the same method as employed for Spalding's function. To date, this generalised law of the wall has only seen limited testing in RANS simulations of a backward facing step and a dump-combustor, but has delivered relatively good results. Its applicability and possible implementation in LES, where instantaneous pressure gradients can dominate mean values, remains to be ascertained. It must be noted that this approach is still only valid in quasi-equilibrium flows, *i.e.* where the streamwise length scale and boundary layer thickness are large compared to the viscous length scale and where streamline tangential gradients change slowly.

Summary

Overall, stress equilibrium models should be more accurate if they are matched to the core LES flow in or below the buffer layer, thereby retaining the streak instability cycle as integral part of the near-wall eddy dynamics. This has the added effect of greatly reducing the real influence of the wall function compared to the generic no-slip boundary condition. Matching at greater heights will not only excise this region from the calculation, but the coarse near-wall resolution implicit in such a scheme will also invalidate the isotropy assumption associated with most SGS models. Depending on the treatment of near-wall

SGS viscosity, the model will tend to severely disrupt eddy and mean flow characteristics and will do so in rather unpredictable ways.

In addition, if the matching height is chosen is an appreciable fraction of the boundary layer thickness ($y_0^+ = O(\delta_b)$) near-wall turbulence production will be completely removed from the LES calculation [101]. This more or less conforms to the concept of outer layer matching discussed in sec.2.5, but if one considers that shedding and other large scale vortex formation mechanisms are unlikely to be associated with equilibrium boundary layers, this approach loses some of its appeal. It does however have merit as a boundary condition for “far walls”, *i.e.* surfaces that have equilibrium boundary layers but have little significant influence, except to retard the rest of the flow.

3.3.2 Two-layer Models

The essence of the two-layer approach lies in decoupling the grid encompassing the bulk flow from a much finer near-wall grid used to resolve the boundary layer (also known as the sub-layer). The two grids generally overlap with some kind of explicit coupling in the matching region. Simplified transport equations and models are then applied on the sub-layer mesh, reducing the cost of the solution. Standard LES equations are solved on a grid with coarse near-wall cells, using the model-supplied wall shear stress as boundary conditions. The stresses are calculated by integrating the simplified boundary layer equations on the grid embedded between the wall and some point in the LES domain (usually the first off-the-wall grid point).

In terms of their modes of interaction with the LES part of the calculation, two-layer models are generally identical to their stress-equilibrium counterparts: the model uses velocities and pressure gradients from the LES solution and returns the wall shear stresses.

Thin Boundary Layer Equations (TBLE)

The most commonly used simplified equations in two-layer equations are known as the “thin boundary layer equations”, which describe an essentially two-dimensional RANS or unsteady RANS flow near the wall. Their derivation from the full Navier-Stokes equations,

does not require the equilibrium stress assumption as in the previous models. It does however, assume that in the very thin wall region parallel (x and z) length scales are much greater than wall-normal (y) scales and that y derivatives are much greater than x , z derivatives. Accordingly, viscous terms dependent on wall parallel gradients are neglected and wall-normal pressure gradients are assumed to be small,

$$\frac{\partial f(\mathbf{u})}{\partial y} \gg \frac{\partial f(\mathbf{u})}{\partial(x,z)}, \quad (3.67)$$

$$\frac{\partial \bar{p}}{\partial y} \rightarrow 0. \quad (3.68)$$

After including the Boussinesq approximation for the Reynolds stress terms, the resulting set of equations, in which " ~ " denotes space and/or time averaging, are

$$\frac{\partial \tilde{u}_i}{\partial t} + \nabla \cdot (\tilde{u}_i \tilde{\mathbf{u}}) = -\frac{\partial \tilde{p}}{\partial x_i} + \frac{\partial}{\partial y} \left[(\nu + \nu_t) \frac{\partial \tilde{u}_i}{\partial y} \right], \quad i = 1, 3 \quad (3.69)$$

$$\tilde{v} = - \int_0^y \left(\frac{\partial \tilde{u}}{\partial x} + \frac{\partial \tilde{w}}{\partial z} \right) dy. \quad (3.70)$$

These equations are now solved on a fine wall-normal sub-layer mesh (see fig.3.5). The matching between the sub-layer and the LES mesh usually occurs at the cell centre of the wall adjacent cell of the coarse mesh, but other matching points such as the top of the first off-the-wall cell are possible. The horizontal pressure gradient term in eq.3.69 is derived from the LES flow at the matching point by using time or space averaging to obtain a mean value compatible with the TBLEs. This means that there is no need to find a pressure solution in the sub-layer, which has the added implication that the wall normal velocity can be found from the continuity equation (3.70). The wall-parallel velocities are also matched to their space and/or time filtered equivalent in the interior flow at the interface. The wall normal velocities are not matched though, as they are completely specified by eq.3.70.

Eddy-viscosity in the Sub-layer

Although some variations to this approach have been proposed, (see the "off-the-wall" boundary condition [22]) they have not seen much use to date so that the major differences between existing two-layer models resides in their treatment of eddy-viscosity in the sub-

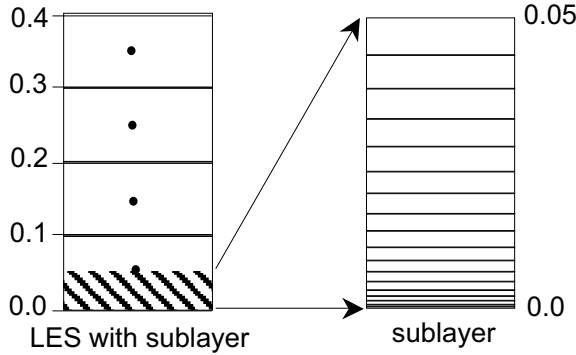


Figure 3.5: Typical two-layer model implementation (cross-hatched region) embedded in the lower half of the wall cell.

layer. The simplest of these is probably the mixing length model [10],

$$\nu_t = (\kappa y_w)^2 D(y_w) |S| \quad (3.71)$$

where κ is the von Karman constant, y_w is the distance to the wall, $|S|$ is the magnitude of the local rate of strain and D is an *ad-hoc* damping function used to ensure the correct limiting behaviour for ν_t in the viscous layer. In the literature there are various forms of this “van Driest” damping function, all of which can be expressed as follows:

$$D(y_w) = \left[1 - e^{-\left(\frac{y_w u_\tau / \nu}{A^+}\right)^n} \right]^m, \quad (3.72)$$

where A^+ is an adjustable constant, normally in the range of $15 - 30$, u_τ is the friction velocity and the parameters m and n have been used in the following combinations: $n = 1, m = 2$ [20, 57] and $n = 3 - 4, m = 1$ [10]. LES results using the TBLEs with the mixing length model and “van Driest” damping function in rotating pipe and square duct flows [10], have shown marked improvement over the standard equilibrium SG model and its derivatives in regions where the wall function assumptions do not hold.

Slightly more complex, is the adaptation of the Johnson-King [78] model for the thin boundary layer equations [20, 21],

$$\nu_t = \kappa y_w u_s D^2, \quad D = 1 - e^{-\frac{y_w u_d / \nu}{A^+}} \quad (3.73)$$

In the simplified **Johnson-King** (JK) model, both velocity scales u_s and u_d are taken equal to the shear velocity $u_\tau = \sqrt{\tau_w}$. The simplified model has been used in the LES

3. LES Principles and Modelling

simulation of a backward facing step [21]. Results in the recovery region were found to be a lot better than those under the recirculation bubble, but were in all cases somewhat improved from equilibrium stress results. Calculations of a cylinder in a cross flow by Wang *et al.* [164] produced similar results, with wall shear being over predicted in the recirculating region behind the cylinder.

The full JK model for the sub-layer uses velocity scales that are weighted averages u_τ and u_m , where u_m is the square root of the maximum Reynolds stress ($-\bar{uv}$), occurring at a distance y_m above the wall:

$$u_s = (1 - \gamma)u_\tau + \gamma u_m, \quad \gamma = \tanh \frac{y_w}{l}, \quad l = \frac{u_\tau y_m}{u_\tau + u_m}, \quad (3.74)$$

$$u_d = \max(u_m, u_\tau). \quad (3.75)$$

In LES, finding the maximum Reynolds stress above the wall is complicated by the fact that its position and magnitude fluctuates wildly in space and time. A running time average must be used in conjunction with a search routine to find the maximum stress at a given horizontal location, greatly increasing the complexity and cost of this method. The full JK model predicts excessively large wall stresses in both the recirculating and recovery regions of a backward facing step [21]. This and previous models' over prediction of near-wall turbulent viscosity is thought to be due to the significant contribution of the advective terms in eq.3.69 to the sub-layer Reynolds stress.

A modification of the simplified JK model, the dynamic sub-layer model, was recently proposed by Cabot and Moin [24] to take this factor into account. Turbulent viscosity in the sub-layer is calculated according to eq.3.73, but the value of κ is allowed to vary so that the mixing-length eddy viscosity approximately matches the SGS viscosity at the edge of the sub layer, $\langle \nu_t \rangle = \langle \nu_{SGS} \rangle$. The averaging denoted by the angular brackets has to be performed over a large surface and/or some time period to provide reasonably smooth data [163]. In addition, the poor behaviour of ν_{SGS} in the near-wall cells means that the sub-layer matching point must be moved to the second layer of interior nodes from the wall. This makes it very difficult to implement, especially on a complex mesh. The dynamic sub-layer model has shown improvements in wall shear predictions over the conventional versions in LES of both backward facing step flows [24] and flow over an

asymmetric trailing edge [163].

Summary

In terms of near-wall resolution and eddy dynamics, two-layer models suffer from the same problems associated with their stress equilibrium counterparts: the coarser the near-wall mesh, the larger the disruption of the interconnected eddy structures in the boundary layer. They do however have the advantage of providing considerably improved wall stress predictions in areas of the flow that do not conform to the equilibrium assumptions. Although they only increase the cost of a LES calculation by 20% to 30% compared to wall functions, two-layer models have an obvious drawback. Unlike wall functions, which are easily applied to any near-wall cell, they require a secondary mesh which extends continuously along all boundaries to be treated in this fashion and matches accurately to the bulk mesh. Constructing such a sub-layer grid when the surface is smooth and the near-wall bulk mesh is well behaved is not very challenging. However, if the surface becomes complex or the mesh size and quality changes rapidly, this can become a much more difficult prospect. The use of a layered (prismatic) near-wall mesh can alleviate much of the issues associated with changing bulk meshes, but surfaces with high curvature or sudden changes in orientation can invalidate the original assumptions of small streamwise velocity and wall-normal pressure gradients. This will tend to lessen the accuracy of the two-layer approach in regions where such conditions are prevalent. In addition, the increase in complexity due to the need for a sub-layer mesh, solving the thin boundary layer equations and coupling the system to the bulk flow, can be considerable when compared to single continuum approaches.

3.3.3 Detached Eddy Simulation (DES)

The description DES was originally coined by Spalart *et al.* [149] and refers to an approach where unsteady RANS turbulence modelling and mesh spacing is used in the boundary layer, while LES is employed in the core and separated regions of the flow. In the near-wall regions, the RANS turbulence model, which has been calibrated in thin shear layer flows, has complete control over the solution. In the LES region, the turbulence model

3. LES Principles and Modelling

changes to an SGS formulation. The turbulence modelling in the LES regions thus has a comparatively small influence compared to that in the RANS region, since the larger energy carrying eddies are resolved, allowing for smaller margin of error and providing more realistic core conditions for the RANS portions of the flow. In terms of its boundary layer extent, DES is presented as a wall treatment of the outer layer matching type (see sec.2.5). Thus the streak instability cycle, the inertial layer and most of the wake region are subsumed by the RANS portion of the model (see fig.3.6). In fact the DES solution should in theory reduce to the equivalent RANS result, unless the flow contains some feature that introduces large scale unsteadiness into the outer flow. A prime example of this occurs during main flow separation. Under these conditions DES can be considered a good approximation as long as the length scales of the energy containing structures produced by the separation are much larger than those that would populate a resolved upstream boundary layer. Since most solutions will contain no resolved eddies in the boundary layer upstream of separation, DES becomes more plausible if rapid new instabilities of larger scale overwhelm the modeled turbulence inherited from the boundary layer in the post-separation shear layer. DES in this form is therefore inherently unsuited to cases where the flow is dominated and/or strongly affected by wall-attached eddies (examples are fully developed channels [8, 116] and similar flows with fully developed inlet conditions, such as backward facing steps and diffusers). DES produces savings over conventional LES by removing the wall parallel resolution requirements of attached eddies, through the use of the near-wall RANS model. Although wall-normal resolutions typically require spacings in wall units of order one to resolve the rapidly varying velocity gradient, the total number of grid points is still found to scale only with the logarithm of Re_τ (rather than a power) [116].

Placing the RANS/LES interface at intermediate heights (in the boundary layer) was found to produce more or less the same difficulties encountered with the previous two approaches [8]. In addition to the smearing effects of the coarse wall parallel resolution, the high modeled turbulence serves to damp resolved structures in the near-wall region. The result is a flow in which the eddy dynamics correspond to those at a much lower Re , including an artificial ‘buffer’ layer between the LES and RANS portions and increased

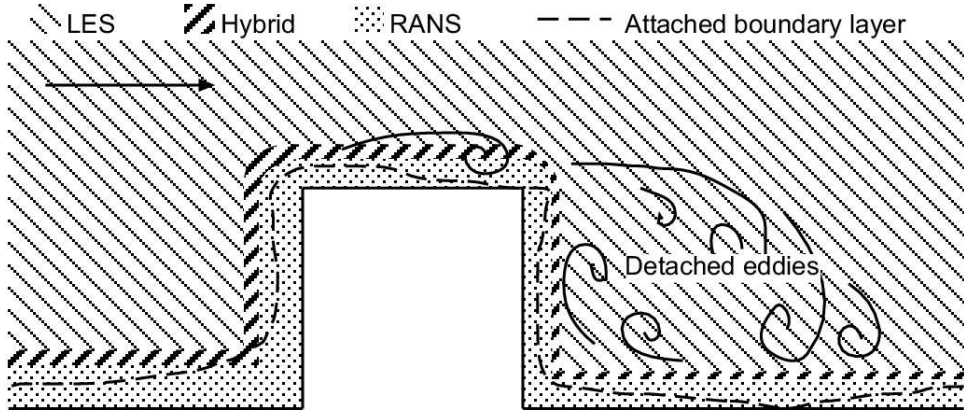


Figure 3.6: Typical distribution of DES turbulence zones for flow over a bluff body.

spanwise streak spacings and eddy sizes. In the limit of mesh refinement however, the solution should in general tend to that of a fully resolved LES, making DES a possible candidate for inner layer matching.

Spalart-Allmaras Model

For their DES formulation, Spalart *et al.* [149] use the Spalart-Allmaras (S-A) one-equation eddy viscosity model [147] as their base RANS turbulence model, included here for completeness. The eddy viscosity ν_t is given by,

$$\nu_t = \tilde{\nu} f_{v1}, \quad (3.76)$$

$$f_{v1} = \frac{\chi^3}{\chi^3 + c_{v1}^3}, \quad (3.77)$$

$$\chi \equiv \frac{\tilde{\nu}}{\nu}, \quad (3.78)$$

and ν is the molecular viscosity, while $\tilde{\nu}$ is the working variable that obeys the transport equation

$$\frac{D\tilde{\nu}}{Dt} = c_{b1} \tilde{S} \tilde{\nu} + \frac{1}{c_\sigma} [\nabla \cdot ((\nu + \tilde{\nu}) \nabla \tilde{\nu}) + c_{b2} (\nabla \tilde{\nu})^2] - c_{w1} f_w \left[\frac{\tilde{\nu}}{y_w} \right]^2, \quad (3.79)$$

$$\tilde{S} \equiv \omega + \frac{\tilde{\nu}}{\kappa^2 y_w^2} f_{v2}, \quad (3.80)$$

$$f_{v2} = 1 - \frac{\chi}{1 + \chi f_{v1}}. \quad (3.81)$$

3. LES Principles and Modelling

Here ω is the vorticity magnitude and the function f_w is given by

$$f_w = g \left[\frac{1 + c_{w3}^6}{g^6 + c_{w3}^6} \right]^{1/6}, \quad (3.82)$$

$$g = r + c_{w2} (r^6 - r), \quad (3.83)$$

$$r = \frac{\tilde{\nu}}{\tilde{S} \kappa^2 y_w^2}. \quad (3.84)$$

The wall boundary condition is $\tilde{\nu} = 0$ and the constants are $c_{b1} = 0.1355$, $c_\sigma = 2/3$, $c_{b2} = 0.622$, $\kappa = 0.41$, $c_{w1} = c_{b1}/\kappa^2 + (1 + c_{b2})/c_\sigma$, $c_{w2} = 0.3$, $c_{w3} = 2$ and $c_{v1} = 7.1$.

The transport equation 3.79 contains a destruction term, which is proportional to $(\tilde{\nu}/y_w)^2$, where y_w is the distance to the closest wall. If this term is balanced with the production term, it adjusts the viscosity to scale with the local deformation analogue, \tilde{S} and y_w : $\tilde{\nu} \propto \tilde{S} y_w^2$. This form is very similar to that found in the Smagorinsky model where the sub-grid scale viscosity scales with the local rate of strain, $|S|$ and the grid spacing, Δ : $\nu_{SGS} \propto \Delta^2 |S|$. Thus the S-A model with y_w replaced by a length related to Δ can be a SGS model.

To accomplish the transition from near-wall RANS based simulation to LES treatment of the interior flow in one formulation, the near-wall distance y_w is replaced by \tilde{d} defined as,

$$\tilde{d} = \min(y_w, C_{DES} \Delta) \quad (3.85)$$

which acts as the S-A RANS model for $y_w \ll \Delta$ and a SGS model for $\Delta \ll y_w$. In DES the grid size Δ is defined as the largest cell edge length, $\Delta \equiv \max(\Delta x, \Delta y, \Delta z)$. As a result, even though the grid is anisotropic and $\Delta y \ll \tilde{d}$ in the boundary layer, it is usually the case that $y_w \ll \Delta = \Delta_{\parallel}$, giving RANS behaviour. Tests in isotropic turbulence have provided confidence in the S-A model in its SGS capacity, and allowed C_{DES} to be calibrated at 0.65 [140].

The S-A DES model is relatively new, but despite this has been tested in a range of comparatively difficult flows, including aerofoils at high angles of attack [140], channel flows [116] and cylinders in cross streams at high Re [160]. In channel flows, the model performs little better than conventional near-wall treatments (as expected), but relatively

good accuracy (compared to unsteady RANS) is achieved for cases including large unsteady separation. Several of these calculations were conducted at Reynolds numbers far in excess of what can be calculated using well resolved LES ($Re = 10^4 - 10^6$). Although the S-A model is one of the best known DES models, it is not the first approach to utilise the zonal RANS/LES combination. In fact, most of the stress equilibrium and two-layer models require some form of augmented turbulent viscosity to compensate for the lack of resolution in the near-wall region. What makes S-A DES attractive, is the capability of the model to treat an entire boundary layer including the outer “wake” region [160]. This contrasts with the conventional mixing-length and van Driest damping approaches which are only accurate in a self similar boundary layers and then only up to the outer edge of the logarithmic region.

Other DES Models

As mentioned above, the Spalart-Allmaras model is not the only, nor the first DES approach. Although not termed DES at the time, one of the first such models can be attributed to Schumann [136], whose model splits the SGS stress into isotropic and anisotropic components. The anisotropic component is then treated via mixing length approach that is equivalent to a RANS turbulence model near the wall and a SGS model in the interior flow. The decomposition of the unresolved Reynolds stresses can be expressed as,

$$\boldsymbol{\tau} - \frac{1}{3}\text{tr}(\boldsymbol{\tau})\mathbf{I} = \underbrace{\nu_{SGS}(\bar{\mathbf{S}} - \langle \bar{\mathbf{S}} \rangle)}_{locally\ isotropic} - \underbrace{\nu^*\langle \bar{\mathbf{S}} \rangle}_{inhomogeneous} \quad (3.86)$$

where $\bar{\mathbf{S}}$ is the local rate of strain tensor and the angular brackets denote time and/or spatial averaging. The coefficients ν_{SGS} and ν^* are eddy viscosities accounting for the locally isotropic and inhomogeneous parts of the unresolved turbulent stresses respectively. The inhomogeneity is introduced to account for the mean shear associated with the wall, which should reduce to zero in a fully isotropic turbulence, thus recovering the classical formulation. The ‘isotropic’ eddy viscosity ν_{SGS} can be obtained using any of the models described in section 3.2, while the ‘inhomogeneous’ part can be found from a Prandtl

3. LES Principles and Modelling

mixing length model which is known to be valid in an equilibrium boundary layer.

$$\nu^* = \tilde{d}^2 |\bar{\mathbf{S}}|, \quad (3.87)$$

$$\tilde{d} = \min(\kappa y_w, c_s \Delta) \quad (3.88)$$

where eq.3.87 with $\tilde{d} = \kappa y_w$ is the RANS mixing length model and $\tilde{d} = c_s \Delta$ returns a form of the Smagorinsky SGS model with $c_s \approx 0.1$. If the characteristic cell length, Δ , in the near-wall region is larger than the energy-containing eddies, fluctuations in that region will not be resolved, with the effect that the resolved rate of strain will tend toward the average value. Since the large eddies in the near-wall region are known to be anisotropic this value will be non-zero, with the result that the inhomogeneous term on the r.h.s. of eq.3.86 will be much larger than the isotropic one. This in turn implies that the inhomogeneous eddy viscosity will dominate in an under-resolved near-wall region and for cell dimensions that are larger in the wall parallel than normal directions (*i.e.* $y_w \ll \Delta$), that it will be equivalent to a RANS viscosity. Far from the wall the resolved strain rate will be more isotropic, allowing the influence of the SGS model to dominate. Also $\Delta \ll y_w$ giving LES behaviour. This approach can be extended into the buffer and viscous sub-layers by adding a van Driest type damping term to the mixing length equation (3.87).

The major drawback of this approach is the averaging inherent in the $\langle \bar{\mathbf{S}} \rangle$ term in eq. 3.86. As with the averaged velocity required for the SG stress equilibrium model (eqs.3.44,3.45 and 3.46), obtaining these quantities is not normally feasible in flows with separation and/or large scale unsteadiness. Although it will cause a reduction in accuracy, the problem may be somewhat alleviated by simplifying the model through the assumption that $\bar{\mathbf{S}} \approx \langle \bar{\mathbf{S}} \rangle$ for $y_w \ll \Delta$ and $\bar{\mathbf{S}} \gg \langle \bar{\mathbf{S}} \rangle$ for $\Delta \ll y_w$. Implicit in this scheme, is that anisotropies near the wall are not resolved, while all inhomogeneous scales away from the wall are. The resultant modelling of the SGS shear stress is identical to that proposed in eq.3.11, but the SGS viscosity is calculated using the length scales from eq.3.88, thus providing RANS eddy viscosities near under-resolved walls and SGS eddy viscosity in the core. For the approximation $\bar{\mathbf{S}} \approx \langle \bar{\mathbf{S}} \rangle$ to be realistic, the same type of near-wall mesh required for the S-A model must be used, so that a considerable amount of spatial

averaging is implicit in the mesh spacing.

There are many other possible permutations using this general scheme, for example an advanced RANS turbulence model can be used to calculate the mean turbulent eddy viscosity field, which can then be explicitly blended with the SGS viscosity as a function of wall distance [8]. Another option would be to calculate the value of the turbulent length scale using an independent transport equation (*e.g.* ϵ -equation) and then using the minimum of this length scale and Δ to determine the unresolved turbulent velocity scale and thus the eddy viscosity. A formulation of this form would allow for high Reynolds number or even two layer DES models, which would be more versatile than the standard (low Re) S-A DES model, and thus warrants some investigation.

Summary

Although not necessarily intrinsic to the method as a whole, the use of the relative near-wall distance/cell size (y_w/Δ) as the switch between RANS and LES treatment in S-A type DES models, makes the mesh construction process very important. The requirement that RANS viscosity be imposed up to the edge of the boundary layer (with thickness δ_b) means that the wall parallel mesh spacing must be of the order δ_b/C_{DES} . Too small wall parallel mesh spacing will place the matching point inside the boundary layer, resulting in the low Reynolds number effects described earlier for an intermediate matching without structural support. Making the wall-parallel cell sizes much larger than δ_b/C_{DES} , will not only cause a reduction in accuracy because of the poor resolution, but will also unnaturally damp large scale fluctuations produced at sites of massive separation. This implies at least a modicum of foreknowledge about the flow configuration, but not anything in excess of that required for a sufficient low Re RANS mesh [150]. A more appealing prospect would be to use some form of dynamic mesh adjustment to ensure the mesh has the correct properties. There are however several unresolved issues, such as how to determine the boundary layer thickness, that hamper the implementation of such an adaptive approach.

The zonal approach employed in DES allows for the treatment of much higher Re number flows than would otherwise be the case. The validity of modelling the entire boundary layer depends entirely on the importance of the eddies therein and whether their

3. LES Principles and Modelling

exclusion will adversely effect the overall solution. It is thus of limited use in flows which are dominated by boundary layer effects, such as channel flows, pipe flows and derivative configurations. In aerodynamic and similar bluff body flows, where the thickness of the boundary layer is small compared to overall length scales and separation induced vortices, the model is predicted to deliver LES quality results at vastly reduced costs. The approach as a whole is however, comparatively young and has to date undergone only a limited amount of testing and model calibration.

3.3.4 Structural Support Models

When any of the preceding models are matched to the LES region at an intermediate height ($10 \lesssim y^+ \lesssim \delta_b^+$), the resolved eddies in the LES section of the boundary will be distorted. Most near-wall treatments adequately account for the effect of the unresolved eddies on the turbulent shear within their region of influence. They do not however in general, account for the effect that the lack of these eddies has on resolved structures further from the wall that are normally strongly coupled to them. The errors introduced in this manner corrupt the wall normal momentum transfer rate in an unpredictable way and cannot be accounted for through the addition of a supplemental eddy viscosity [8]. ‘Structural support’ models remedy this problem by attempting to reproduce the effects of the unresolved near-wall scales on the resolved ones in at least a statistical sense.

Stochastic Backscatter Model

Probably the first structural support model, the stochastic backscatter procedure developed by Mason and Thomas [102] aims to account for the above mentioned effect by applying a scaled random acceleration to the resolved velocity field. First, they use dimensional arguments to show that the ensemble averaged value of the energy backscatter from SGS to resolved scales can be approximately found from,

$$\frac{\partial K}{\partial t} = C_B \left(\frac{l}{\Delta} \right)^5 \epsilon = \nu_{SGS} |\bar{\mathbf{S}}|^2 \frac{C_B (l/\Delta)^5}{1 + C_B (l/\Delta)^5}, \quad (3.89)$$

where K is the turbulent energy content of the resolved field, Δ is the filter length scale and C_B is a constant provisionally calibrated to 1.4 from energy spectrum considerations.

l is the SGS mixing length, related to Δ as follows,

$$\frac{1}{l^2} = \frac{1}{\Delta^2} + \frac{1}{(\kappa y_w)^2}, \quad (3.90)$$

for a smooth wall. Now a random vector potential field with mean zero is created for the entire flow. Since only the divergence free part of the acceleration is of interest (the irrotational part is absorbed into the pressure definition), it is obtained from the curl of the potential field. Using the known probability distribution of the random field and the ensemble averaged value of the energy backscatter rate from eq.3.89, the scaling factor for the acceleration field is now adjusted so that the following relation is satisfied,

$$\frac{\partial K}{\partial t} = |\mathbf{a}|^2 t_{et} = |\boldsymbol{\varsigma}|^2 \Delta t, \quad (3.91)$$

where $\boldsymbol{\varsigma}$ is the standard deviation of the acceleration vector, \mathbf{a} and $\frac{\partial K}{\partial t}$ is set from eq.3.89. A further assumption is made, namely that the exact frequency of the energy input is not critical, leading to the replacement of the eddy turnover time t_{et} in 3.91 with the time step, Δt . Thus, although the mean rate of energy backscatter is approximately fixed, neither the correct time nor space scales are enforced. The scaled random accelerations now become a source term in the momentum equations.

The introduction of backscatter increases the cost of the simulation somewhat, mostly due the CPU time required to calculate the random fields at each time step. Calculations of a high Re planetary boundary layer, using instantaneous wall functions and the Smagorinsky model, show that the addition of backscatter markedly improves the results [102]. Unfortunately, the model has not extensive testing to date and many of the assumptions leading to eq.3.89 have little theoretical basis, making evaluation difficult.

Linear Stochastic Estimation (LSE)

Using sub-optimal control theory, Nicoud *et al.* [114] derive the instantaneous fluctuating components of the wall shear stresses that best reproduce the desired mean velocity profile (a logarithmic profile) in the core LES flow. The evolution of these stresses can then be linearly correlated to the instantaneous velocity field in a way that minimises the least squares error of the conditionally averaged fluctuating wall shear. The size of these stress

3. LES Principles and Modelling

fluctuations are therefore not necessarily physically correct, but rather have values that best reproduce the mean velocity field and thus the momentum cascade in the interior flow. The exact form of the LSE wall model for the fluctuating stress components is given by

$$\begin{aligned} \tau_w^{12\prime}|_{m,n} &= \sum_{k=-n_z}^{n_z} \sum_{j=1}^{n_y} \sum_{i=-n_x}^{n_x} L_{ijk}^{11} [u_{m-i,j,n-k} - \langle u(y_0) \rangle] \\ &+ \sum_{k=-n_z}^{n_z} \sum_{j=1}^{n_y} \sum_{i=-n_x}^{n_x} L_{ijk}^{13} w_{m-i,j,n-k}, \end{aligned} \quad (3.92)$$

$$\begin{aligned} \tau_w^{32\prime}|_{m,n} &= \sum_{k=-n_z}^{n_z} \sum_{j=1}^{n_y} \sum_{i=-n_x}^{n_x} L_{ijk}^{31} [u_{m-i,j,n-k} - \langle u(y_0) \rangle] \\ &+ \sum_{k=-n_z}^{n_z} \sum_{j=1}^{n_y} \sum_{i=-n_x}^{n_x} L_{ijk}^{33} w_{m-i,j,n-k}, \end{aligned} \quad (3.93)$$

where the parameters n_x, n_y, n_z determine the number of velocity points used in the convolution sums to estimate the wall stress at each wall location (denoted by subscript pair m, n). L_{ijk} is the correlation tensor field derived from optimal control methods and the averaging denoted by $\langle \cdot \rangle$ is performed in a plane adjacent to the wall. The more neighbouring points included in the computation, the better the *a-priori* comparison using correlation coefficients. Very limited improvement was however found when increasing the number of neighbours correlated to the wall shear fluctuations above two in each direction.

Although separate calibrations were not compared, LSE coefficients derived for a channel flow at $Re_\tau = 4000$ were found to produce good results (compared to the SG model) at Reynolds number far below and in excess of the calibration case. The entire approach is however, configured to reproduce the logarithmic profile, so lacks generality. It also requires the calculation of the same mean velocity and stress values used in the SG model, which as stated previously, creates problems in flows which include unsteady separation. Generalisation of the correlation coefficients to algebraic relations that include significant effects from Reynolds number, pressure gradient, non-linearities, grid size and other transported quantities presents the possibility of a truly universal wall treatment for LES. The method is still in early stages of development however and will require much additional work to reach this level of maturity.

Self-similarity Model

The self-similarity model [112] attempts to add structural support to a existing wall model by assuming that the time-evolution of the flow on two planes parallel to the wall is self-similar. The method consists of building two-point statistics for the flow at an artificial boundary away from the wall by using information from the core flow, at a plane further from the wall ($y_1 > y_0$). The one-point statistics, such as velocity and turbulence intensity, must still be derived using one of the previously presented wall stress models.

The underlying idea is to use a scaling law to reconstruct the deviations from the mean velocity at some distance from the wall from the velocity field in the core flow. It is implemented as follows:

$$\frac{\partial \bar{\mathbf{u}}'_0}{\partial t} = \gamma \frac{\mathbf{U}''_0}{\mathbf{U}''_1} \frac{\partial \bar{\mathbf{u}}'_1}{\partial t}, \quad (3.94)$$

where $\bar{\mathbf{u}}'$ is the resolved deviation from the mean velocity and \mathbf{U}'' consists of the roots of the mean turbulent normal stresses (found from $\sqrt{\langle \mathbf{u}^2 - \langle \mathbf{u} \rangle^2 \rangle}$), which must also be determined via modelling or *a priori* calculations for the plane $y = y_0$. In the most successful approach, dynamically determined scaling coefficients, $\gamma = \gamma_i$, are imposed on the time scale of the velocity fluctuations. This dynamic estimation is done by using two additional planes inside the computed flow domain: plane y'_0 just above y_0 and plane y'_1 just above y_1 . The scaling parameters measured for the pair y'_0, y'_1 are then used to connect the y_0, y_1 planes.

The self similarity model was applied to channel flow at $Re_\tau = 1000$. Some of the results were very promising, but finally inconclusive, leaving ample opportunity for further investigation. The fact that the model is essentially bootstrapping information about flow structures at the boundary raises some difficult questions about the origin and dynamics of these structures.

Structural support models, although necessary for accurate intermediate matching, are still very much in their infancy and require much additional testing and development to make them computationally robust and more generally applicable. As such, the merits of their implementation in current form are somewhat questionable.

3.3.5 Local Mesh Refinement

None of the wall treatments presented in the previous section as yet has the capability to accurately reproduce the near-wall region under all conditions. It is therefore advisable to numerically resolve all the energetic scales in flows where the accurate characterisation of this layer is of importance. This is especially true under non-equilibrium and other conditions for which the modelling assumptions are not valid.

Normally, near-wall structures scale as a function of the viscous wall units only, requiring constant values for Δx_i^+ . The total number of grid points in each direction in a domain with dimensions L_i , reference length, l and free stream velocity, U_∞ , can thus be approximated from [132],

$$\begin{aligned} N_i &= \frac{L_i}{\Delta x_i} = \frac{\nu}{\Delta x_i u_\tau} \frac{L_i}{l} \frac{l U_\infty}{\nu} \sqrt{\frac{\tau_w}{\rho U_\infty^2}} \\ &= \frac{1}{\Delta x_i^+} \frac{L_i}{l} Re \sqrt{\frac{C_f}{2}}. \end{aligned} \quad (3.95)$$

If it is assumed that L_i/l is of size $O(1)$ and $C_f \sim Re^{-2\alpha}$ with values of α in the range $0.1 - 0.125$, then the total number of grid points, N , in the domain scales as,

$$N_i \sim Re Re^{-\alpha}, \quad (3.96)$$

$$N = N_1 N_2 N_3 \sim Re^{2.6}. \quad (3.97)$$

The significant structures in the outer part of the boundary layer (wake) cannot be larger than boundary layer thickness δ_b however, so that the required mesh spacing is proportional to $\Delta x_i/\delta_b$. The number of grid points required to resolve the outer layer in each direction is

$$N_i = \frac{L_i}{\Delta x_i} \sim \frac{L_i}{\delta_b}. \quad (3.98)$$

Assuming that the outer layer is some fixed fraction of δ_b and that the boundary layer thickness scales like $Re^{0.2}$ (flat plate), then the total number of grid points scales like

$$N = N_1 N_2 N_3 \sim Re^{0.2} Re^{0.2} Re^0 \sim Re^{0.4} \quad (3.99)$$

The resolution requirements for the near-wall region thus quickly exceed those of the outer flow as the Reynolds number increases.

How these resolution requirements impact the calculation depends a great deal on the type of mesh that is being used. Traditionally two broad categories of grids are employed in finite volume CFD, structured and unstructured meshes. Structured meshes generally form a regular grid, with neighbouring elements implicitly known to any given cell due to its location in the mesh. Structured meshes are simpler to implement, allow easy control of the order of accuracy and conservation properties, and due to the implicit nature of their neighbour addressing are computationally considerably less costly than the unstructured alternative. All these advantages come at the cost of flexibility. Structured meshes are restricted to hexahedral elements, so that any local increase in resolution must be propagated throughout the mesh, which can lead to a large number of mesh elements in regions where they are not essential. Taken in the context of the boundary layer, geometric constraints result in streamwise and spanwise spacings that must be more or less constant to satisfy the inner layer requirements (while the wall-normal spacing can be varied), leading to over-resolution in the core.

This problem can be alleviated by using unstructured grids. Unstructured grids, while not as computationally efficient on a cell-by-cell basis as their structured counterparts, allow the use of arbitrary shaped mesh elements. These arbitrary elements allow for the transition between regions of mesh density, which in turn allows for local flow dependent grid adaptation to improve computational accuracy without the penalty of global refinement. The negative side of this flexibility is the loss of the implicit neighbour addressing and regular grid of the structured mesh. Instead of implicit neighbour addressing, the elements of unstructured meshes must store this information in an explicit form. It is this “indirect” addressing that contributes most to the reduced computational efficiency of unstructured meshes on modern computers.

Local grid refinement can also be used for 1) complex separated flows, where a fine grid is required to resolve separating shear layers and the turbulent wake and 2) to reduce the grid density (and thus overall cost) in non-critical portions of the calculation domain (*e.g.* far walls, inviscid regions). In addition, unstructured grids allow for the treatment of arbitrarily complex geometries with greater flexibility and less mesh distortion than multi-block methods. As a result unstructured meshes have become more and more popular in

3. LES Principles and Modelling

recent times.

Despite its advantages, LES in conjunction with local grid refinement has in the past mostly been used in a few canonical flows [84], [120] and only more recently been employed in more complex geometries [85, 160]. The reasons for this are many fold: firstly, even with a near-perfect adapted mesh, that only resolves the minimum turbulent structures, the required number of cells and time step considerations for an aerodynamic flow (aircraft, automobiles) would still require computational resources orders of magnitude in excess of currently available systems. Secondly, mesh refinement invariably introduces numerical inaccuracies, in the form of discretisation and commutation errors into the calculation (commutation errors are explained in sec.4.5.1). These require more complicated and expensive discretisation and interpolation schemes to achieve the necessary orders of accuracy and have consequently seen only limited implementation and testing [85]. There are however indications [34] that at least some of these errors are treatable and/or localised to the refinement boundaries, so that the prospect of achieving improved (relative to block structured grids) accuracy with simple numerical schemes and localised refinement on unstructured meshes becomes plausible. Some type of mesh refinement will necessarily be part of this study and a more detailed look at the its implementation will be presented in Chapter 4.

3.3.6 Choice of Wall Treatment

The pros and cons of the various wall treatments have been outlined in the preceding sections. Although some are specifically and/or generally more accurate than others, the final choice of model must in the end be tempered by pragmatism. The envisioned application is the simulation of large Reynolds number external aerodynamic and aero-acoustic flows around automobiles and comparable bluff bodies. As such, full resolution of the boundary layer eddies, even with local refinement, would be prohibitively expensive. In addition, the flow is expected to exhibit large scale unsteadiness and separation, making any assumptions of spatial homogeneity unrealistic. This invalidates many of the models that rely on spatial averages to provide mean near-wall statistics. Unfortunately, the complex geometry and disparate flow regimes also make the applicability of the structural

support class of models uncertain, at least at their current stage of development.

The most promising avenue of approach appears to be the detached eddy technique, applied as either an inner or outer layer matching model and combined with local mesh refinement. In addition, wall functions will be used in combination with DES and outer layer matching to further reduce the calculation costs in applicable areas. The current project will attempt to validate this methodology for several distinct models and flow regimes. More specifically, the SGS kinetic energy model will be modified through the use of RANS eddy viscosity treatments and surface shear stress relations similar to the DES approach. The resulting versions are compared to modified S-A DES results and experimental data sets. More detailed methodologies are presented in the next chapter.

Chapter 4

Computational Methodology

The models and wall treatments presented in Chapter 3 are only a comparatively small part of what constitutes a functional LES solution method. The discretisation of the filtered Navier-Stokes equations, the pressure-velocity coupling, the numerical solution of the resultant matrices along with a plethora of ancillary functionality constitutes the bulk of the methodology. Fortunately, most of these methodologies have been extensively covered in various manuals, text books and other publications, so that only the portions that relate directly to LES need be reproduced here, and then only for completeness. The majority of this chapter will however focus on the distinctive requirements and issues produced by a LES implementation in a numerical solver, particularly on an unstructured finite volume mesh. We will also briefly explore the actual model implementation and examine the errors introduced by these, the numerical methods and other approximations. Finally, mesh refinement will be revisited, along with practical methods to make it more useful and a strategy introduced to limit the effect of the commutation error.

4.1 Governing Equations

Since the modeled contribution to turbulence in LES is typically relatively small, it is imperative that numerical and discretisation errors be kept to a minimum lest their effects dominate the solution. On the other hand, the methodology should be general enough to be applied to complex geometries such as those found in engineering flows. It should also

4. Computational Methodology

be flexible enough to cope with accurate local spatial discretisation, allowing non-uniform mesh distribution and associated cost savings. Finally, the discretisation of the governing equations should facilitate ready and efficient parallelisation, without which only very limited LES would be possible.

There are several numerical methods currently used for LES. These include the widely employed **F**inite **E**lement (FE), **F**inite **D**ifference (FD), **F**inite **V**olume (FV) and Spectral methods along with the more exotic approaches such as the Lattice-Boltzmann method. In research-orientated investigations higher order (4th order and above) discretisation will be referred to as such throughout) FD discretisation and spectral methods are commonly used because of their accuracy. They however require body fitted coordinates in the case of FD or homogeneous directions for Spectral methods to take full advantage of their capabilities, thus limiting their application to fairly simple canonical cases. FE methods do not require these considerations while retaining the potential for higher order accuracy. Unfortunately, their formulation does not guarantee local conservation of dependent variables (*e.g.* mass), which is arguably more important in fluid dynamics than the formal accuracy of the method. While some of the shortcomings of the other methods can be addressed, the FV method, which is the most widely used in commercial CFD today, was found to offer the best compromise of flexibility and accuracy for the problem at hand. The integral formulation means that conservation laws are satisfied exactly and recent advances allow for arbitrarily complex FV grids.

There are probably more variations within the family of finite volume methods than there are different numerical approaches. Investigating each variation is beyond the scope of this work, so only the current implementation is described. The spatial discretisation features unstructured boundary fitted meshes with a collocated cell-centred variable arrangement. Non-dissipative second order discretisation in space and time is employed in conjunction with fully implicit time stepping for a good compromise between speed and accuracy. The system of partial differential equations is treated in a segregated way, each one being solved separately with explicit coupling between the results. The non-linear differential equations are linearized before discretisation and higher order terms are lagged in time.

The combination of the unstructured grid formulation and the ability to mesh arbitrarily complex geometries allows the method to meet the requirements for generality and flexibility. When coupled with second order discretisation schemes a versatile, robust and accurate system results. The current implementation is derived from the FOAM library [69] of computational classes and although not novel in concept, includes several variations that make it well suited to LES.

Since the methods described here will mainly be applied to external aerodynamics at low Mach numbers only methodologies for incompressible, Newtonian flows with constant thermo-physical properties are considered. From sec.3.1 the governing equations for the Large Eddy Simulation of such a fluid, which have been convoluted with a filter of uniform width, Δ , are given by:

$$\nabla \cdot \bar{\mathbf{u}} = 0, \quad (4.1)$$

$$\frac{\partial \bar{\mathbf{u}}}{\partial t} + \nabla \cdot (\bar{\mathbf{u}} \bar{\mathbf{u}}) = -\frac{1}{\rho} \nabla \bar{p} + \nabla \cdot \nu (\nabla \bar{\mathbf{u}} + \nabla \bar{\mathbf{u}}^T) + \nabla \cdot \boldsymbol{\tau}, \quad (4.2)$$

Here $\bar{\mathbf{u}}$ is the filtered velocity, ρ is the fluid density, \bar{p} the filtered pressure, ν the kinematic viscosity and $\boldsymbol{\tau}$ the sub-grid scale stress tensor which has to be modeled to close the system. These differential equations represent the conservation of mass and momentum respectively and apply to an infinitesimal region of space. In the finite volume approach, they are integrated over a control volume and in time to produce the integral form of the governing equations.

$$\int_V \nabla \cdot \bar{\mathbf{u}} dV = \int_{\partial V} d\mathbf{A} \cdot \bar{\mathbf{u}} = 0, \quad (4.3)$$

$$\begin{aligned} \int_t^{t+\Delta t} \left[\frac{d}{dt} \int_V \bar{\mathbf{u}} dV + \int_V \nabla \cdot (\bar{\mathbf{u}} \bar{\mathbf{u}}) dV - \int_V \nabla \cdot \nu_{eff} (\nabla \bar{\mathbf{u}} + \nabla \bar{\mathbf{u}}^T) dV \right] dt \\ = - \int_t^{t+\Delta t} \left[\frac{1}{\rho} \int_V \nabla \bar{p} dV \right] dt, \end{aligned} \quad (4.4)$$

Here ν_{eff} is the sum of the kinematic and modeled sub-grid scale turbulent viscosity. Equations 4.3 and 4.4 must now be transformed via discretisation into a corresponding system of algebraic relations. The solution of these produces a set of values corresponding to the solution of the original equations at some predetermined points in space and time, provided certain criteria and boundary conditions are met. The specification of these time

and space divisions, discretisation practices and boundary conditions constitute the bulk of this chapter.

4.2 Discretisation Practices

Discretisation denotes the approximation of a continuous function by discrete sub-entities. The FV method solves the problem of fluid flow, its governing and other constitutive relations by discretising both the solution domain and the governing equations.

4.2.1 Domain Discretisation

Domain discretisation can be subdivided into spatial discretisation and temporal discretisation. Spatial discretisation defines the solution domain as a collection of well defined sub-volumes that fill and bound a region of space. Each of these control volumes (CV) encapsulates a computational point \mathbf{P} at its centroid. The typical CV, an example of which is displayed in fig.4.1, is bounded by a set of convex faces of arbitrary shape resulting in polyhedral cells and an arbitrary unstructured mesh. In fig.4.1 \mathbf{d} is the vector connecting adjacent cell centres \mathbf{P} and \mathbf{N} , and \mathbf{A} is the face normal area vector for the common face between the cells. While all main dependent variables $\bar{\mathbf{u}}$, \bar{p} , etc. are defined at the cell centroid \mathbf{P} resulting in a collocated arrangement, some derived properties may be defined at the cell face, f .

For a transient problem such as LES, temporal discretisation involves dividing the time domain into a finite number of time intervals or steps. These can be uniform or dependent on solution parameters, but since the time domain is a parabolic coordinate [121] (i.e. a solution is obtained by marching forward from an initial condition) only their size, Δt needs to be specified.

4.2.2 Spatial Discretisation

Instead of following the entire discretisation procedure for each partial differential equation (PDE), we shall instead examine the discretisation for a generic transport equation on

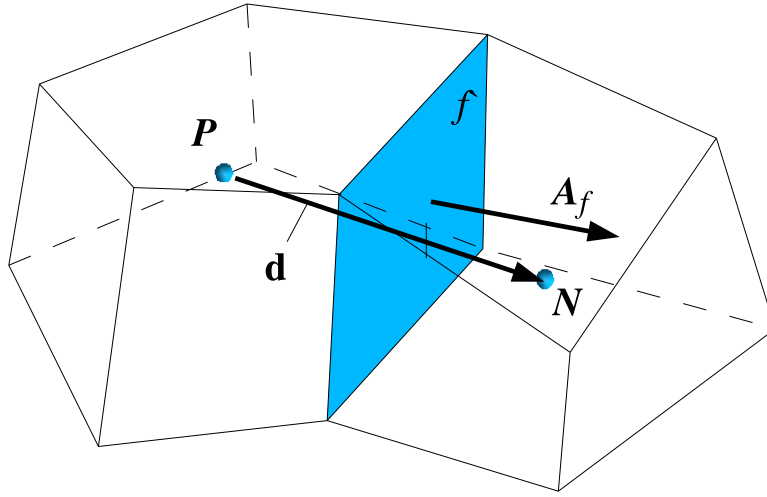


Figure 4.1: Control volume for finite volume discretisation.

a term by term basis. This derivation is generally applicable with exceptions treated separately in a later section. Spatial and temporal integration are also examined separately, with temporal integration treated in sec.4.2.3.

$$\underbrace{\frac{d}{dt} \int_V \phi dV}_{\text{Temporal derivative}} + \underbrace{\int_V \nabla \cdot (\bar{\mathbf{u}}\phi) dV}_{\text{Convection}} - \underbrace{\int_V \nabla \cdot (\Gamma_\phi \nabla \phi) dV}_{\text{Diffusion}} = \underbrace{\int_V S_\phi(\phi) dV}_{\text{Sources}}. \quad (4.5)$$

Here ϕ is the transported quantity, *i.e.* velocity, mass or sub-grid scale turbulent energy, and Γ is the diffusivity coefficient. This is a second-order equation since the diffusion term includes a second derivative. To represent this term with acceptable accuracy, the order of the discretisation must be equal to or higher than the equation to be discretised. To conform to this level, temporal discretisation must also be second order. As a consequence of this requirement, all dependent variables are assumed to vary linearly around the point \mathbf{P} and time t , so that:

$$\phi(x) = \phi_P + (\mathbf{x} - \mathbf{x}_P) \cdot (\nabla \phi)_P, \quad (4.6)$$

$$\phi(t + \Delta t) = \phi^t + \Delta t \left(\frac{\partial \phi}{\partial t} \right)_t. \quad (4.7)$$

Each of the terms in eq.4.5 will now be treated separately, starting with the spatial functions. Gauss' theorem will be used throughout to reduce many of the volume integrals to their surface equivalents e.g.

$$\int_V \nabla \cdot \phi dV = \int_{\partial V} d\mathbf{A} \cdot \phi, \quad (4.8)$$

4. Computational Methodology

where ∂V is the surface bounding the volume V and $d\mathbf{A}$ is an infinitesimal surface element with outward pointing normal on the surface ∂V . A series of volume and surface integrals now need to be evaluated over the control volume to second order. Taking into account the variation of ϕ and x around \mathbf{P} (eqs.4.6) it follows that,

$$\int_{V_P} \phi(x) dV = \phi_P V_P, \quad (4.9)$$

where V_P is the cell volume. Recalling that all the cell faces are convex and using similar assumptions as above, integration of the divergence operator over the cell surface produces:

$$\int_{V_P} \nabla \cdot \phi dV = \int_{\partial V_P} d\mathbf{A} \cdot \phi = \sum_f \left(\int_f d\mathbf{A} \cdot \phi \right) = \sum_f \mathbf{A} \cdot \phi_f, \quad (4.10)$$

where the subscript f denotes face centred indexing and \mathbf{A} is the outward pointing surface area vector. The face values, ϕ_f of the variables have to be calculated by some form of interpolation, to be described later.

Convection Term

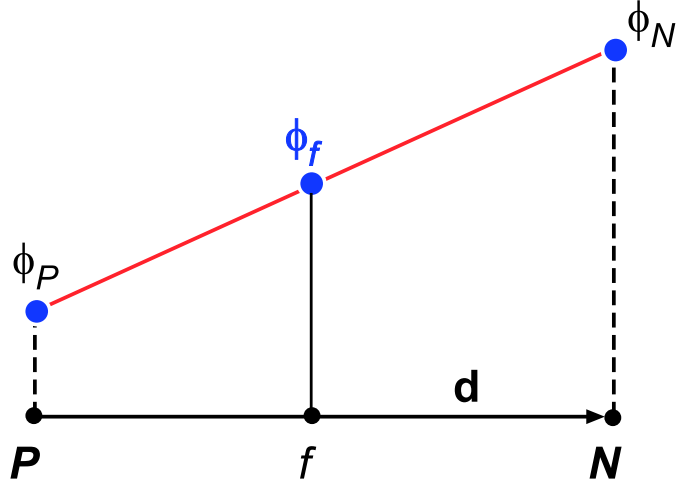


Figure 4.2: Face interpolation.

The discretisation of the convection term can be obtained using eq.4.10 to produce,

$$\int_{V_P} \nabla \cdot (\bar{\mathbf{u}}\phi) dV = \sum_f \mathbf{A} \cdot (\bar{\mathbf{u}}\phi)_f = \sum_f (\mathbf{A} \cdot \bar{\mathbf{u}}_f) \phi_f = \sum_f F \phi_f, \quad (4.11)$$

where F is the volume flux through the face,

$$F = \mathbf{A} \cdot \bar{\mathbf{u}}_f. \quad (4.12)$$

The flux, F depends on the face value, $\bar{\mathbf{u}}_f$, of the filtered velocity. This can be calculated in a similar fashion to ϕ_f described below, with the caveat that the velocity field from which the fluxes are derived must be such that FV continuity equation is obeyed, *i.e.*

$$\int_V \nabla \cdot \bar{\mathbf{u}} dV = \int_{\partial V} d\mathbf{A} \cdot \bar{\mathbf{u}} = \sum_f \left(\int_f d\mathbf{A} \cdot \bar{\mathbf{u}} \right) = \sum F = 0. \quad (4.13)$$

Since linear variation of the dependent variable is assumed, the face centred value can be found from a simple interpolation between the cell values at \mathbf{P} and \mathbf{N} (where \mathbf{N} indicates the neighbouring cell, fig.4.2):

$$\phi_f = f_x \phi_P + (1 - f_x) \phi_N, \quad (4.14)$$

Here the interpolation factor, f_x , is defined as the ratio of the distances fN and PN (fig.4.2), *i.e.*

$$f_x = \frac{fN}{PN}. \quad (4.15)$$

The practice is commonly known as **Central Differencing** (CD) and has been shown to be second order accurate even on unstructured meshes [42]. The CD scheme has some drawbacks however, chief among which is its tendency to produce unphysical oscillations in the solution when the convection term strongly dominates the rest of the system. This is typically a product of unboundedness and can create particular problems in a coupled system like the Navier-Stokes equation. Boundedness in this context refers to the solution at a particular computational point being bounded by the solution values at surrounding points which influence it. For increasing convection dominance the solution will become increasingly non-physical and may diverge. This problem can be alleviated without impacting the formal order of the scheme by applying a higher order filter in the form of a forth order dissipation term [64]. As has been mentioned previously however, higher than second order schemes are cumbersome to implement on a unstructured mesh. In addition, the forth order derivative may become very large due to discontinuous phenomena and itself become a source of instability.

4. Computational Methodology

An alternative discretisation that improves stability and boundedness, is **Upwind Differencing (UD)**. In the scheme's first order variant the face value of ϕ is determined according to the direction of the flux:

$$\phi_f = \begin{cases} \phi_f = \phi_P & : F \geq 0 \\ \phi_f = \phi_N & : F < 0 \end{cases} \quad (4.16)$$

Unfortunately, even second order variations of UD like linear upwind [166] tend to introduce numerical diffusion into the system. This is particularly problematic with LES since the contribution of the modeled turbulent diffusivity is typically very small, so that even modest false diffusion can produce large inaccuracies.

Although higher values may be tolerated ($\gtrsim 1000$ is the limit in the author's experience), the central differencing scheme may become unstable for cell Reynolds numbers exceeding 2.

$$Re_c \approx \frac{\Delta \bar{\mathbf{u}}}{\Gamma_\phi} > 2 \quad (4.17)$$

The cure for these local oscillations is thus in principle very simple: mesh refinement. In regions of the domain where accurate representation of the flow is crucial to the result, this may be the only reasonable course of action. In non-essential portions of the solution domain unboundedness may be treated by adding some upwinding and thus numerical diffusion to damp the oscillations. Throughout this investigation, central differencing with mesh refinement will be the default approach unless otherwise noted.

Diffusion Term

Using a similar approach as above, the diffusion term in eq.4.5 can be discretised as follows:

$$\int_{V_P} \nabla \cdot (\Gamma_\phi \nabla \phi) dV = \sum_f \mathbf{A} \cdot (\Gamma_\phi \nabla \phi)_f = \sum_f (\Gamma_\phi)_f \mathbf{A} \cdot (\nabla \phi)_f, \quad (4.18)$$

where $(\Gamma_\phi)_f$ can be found from eq.4.14. If the mesh is orthogonal, i.e. the vectors \mathbf{d} and \mathbf{A} in fig.4.1 are parallel, the face gradient of ϕ term can be expressed as follows:

$$\mathbf{A} \cdot (\nabla \phi)_f = |\mathbf{A}| \frac{\phi_N - \phi_P}{|\mathbf{d}|}. \quad (4.19)$$

This employs a compact computational molecule and is more accurate than simply interpolating the cell centred gradients,

$$\left(\widetilde{\nabla}\phi\right)_f = (f_x (\nabla\phi)_P + (1 - f_x) (\nabla\phi)_N). \quad (4.20)$$

where

$$(\nabla\phi)_P = \frac{1}{V} \sum_f \phi_f. \quad (4.21)$$

and the tilde signifies the interpolated gradient quantity. Although both methods are second order accurate, eq.4.20 uses a larger computational molecule and has a larger truncation error than the first method [66].

If the mesh is not orthogonal, as is often the case, eq.4.19 is no longer second order accurate and needs to be supplemented as follows:

$$\mathbf{A} \cdot (\nabla\phi)_f = \underbrace{|\mathbf{A}_d| \frac{\phi_N - \phi_P}{|\mathbf{d}|}}_{orthogonal} + \underbrace{\mathbf{A}_\Delta \cdot \left(\widetilde{\nabla}\phi\right)_f}_{non-orthogonal}, \quad (4.22)$$

where the vector \mathbf{A}_d represents the component parallel to \mathbf{d} and \mathbf{A}_Δ is the remainder that must satisfy the equality (see fig.4.3):

$$\mathbf{A} = \mathbf{A}_d + \mathbf{A}_\Delta. \quad (4.23)$$

The first method is used to calculate the orthogonal component of the face gradient, while the interpolated gradient contributes the non-orthogonal component, thus maintaining overall second order accuracy. Since the non-orthogonal term has a larger computational molecule, it is treated explicitly using values either from the previous iteration or old timestep to keep the number of entries in the system matrix low.

There is some scope for variability of the component vectors \mathbf{A}_d and \mathbf{A}_Δ within the constraints of eq.4.23. Several such configurations are explored by Jasak [66] with the conclusion that the approach known as “over-relaxed” is the most robust, convergent and computationally efficient. In the “over-relaxed” approach the orthogonal vector component is calculated from,

$$A_d = \frac{\mathbf{d}}{\mathbf{d} \cdot \mathbf{A}} |\mathbf{A}|^2 \quad (4.24)$$

This approach increases the importance of the term in ϕ_P and ϕ_N with increased non-orthogonality, as shown by the face area decomposition in fig.4.3.

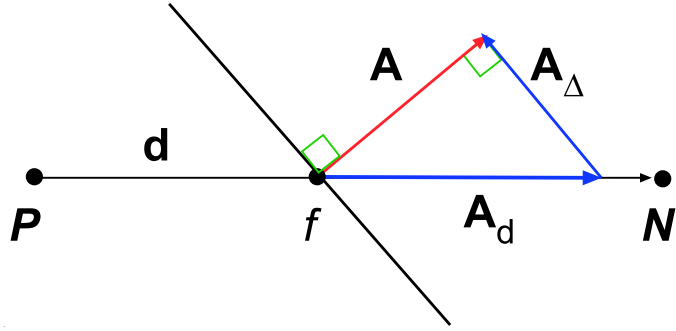


Figure 4.3: Decomposition of the face area vector due to non-orthogonality using the “over-relaxed” approach.

While the diffusion term is bounded on orthogonal meshes, addition of the non-orthogonal correction can produce negative coefficients leading to unboundedness and instability, particularly if the mesh non-orthogonality is high. Under such conditions, the non-orthogonal contribution has to be limited, which reduces the formal accuracy of the diffusion term. In LES, where the results are particularly sensitive to the order accuracy of the equations system, care must thus be taken to keep mesh non-orthogonality within reasonable bounds.

Source Terms

All terms of a transport equation that cannot be written as convection, diffusion or temporal contributions are here loosely classified as source terms. Source terms typically consist of a general function of ϕ and other variables, that need to be linearized to be incorporated in the solution matrix:

$$S_\phi(\phi) = S_c + S_p \phi. \quad (4.25)$$

where S_c and S_p can also depend on ϕ . Following the mid-point rule from eq.4.9 the volume integral is calculated from,

$$\int_{V_P} S_\phi(\phi) dV = S_c V_P + S_p V_P \phi_P. \quad (4.26)$$

4.2.3 Time Integration

Next we consider the temporal derivative and integration of the generalised transport equation (4.5) in time. Using the same rationale employed to produce eqs.4.3 and 4.4 the integral relation for the generic transport equation can be written as,

$$\begin{aligned} \int_t^{t+\Delta t} \left[\frac{\partial}{\partial t} \int_V \phi dV + \int_V \nabla \cdot (\bar{\mathbf{u}}\phi) dV - \int_V \nabla \cdot (\Gamma_\phi \nabla \phi) dV \right] dt \\ = \int_t^{t+\Delta t} \left[\int_V S_\phi(\phi) dV \right] dt. \end{aligned} \quad (4.27)$$

Using eqs.4.10, 4.18 and 4.26, eq.4.27 can be rewritten as,

$$\begin{aligned} \int_t^{t+\Delta t} \left[\left(\frac{\partial \phi}{\partial t} \right)_P V_P + \sum_f F\phi_f - \sum_f (\Gamma_\phi)_f \mathbf{S} \cdot (\nabla \phi)_f \right] dt \\ = \int_t^{t+\Delta t} [S_e V_P + S_p V_P \phi_P] dt. \end{aligned} \quad (4.28)$$

It should be noted that temporal discretisation of the transient term in eq.4.28 need not be the same as the temporal discretisation of the spatial terms (convection, diffusion and sources). Each term can be treated differently to yield different accuracies. As long as the individual terms are second order accurate, the overall accuracy will also be second order.

Time Centered Crank-Nicholson

Keeping in mind the assumed variation of ϕ with t (eq.4.7), the temporal derivative and time integral can be calculated directly as follows:

$$\left(\frac{\partial \phi}{\partial t} \right)_P = \frac{\phi_P^n - \phi_P^{n-1}}{\Delta t}, \quad (4.29)$$

$$\int_t^{t+\Delta t} \phi(t) dt = \frac{1}{2} (\phi^{n-1} + \phi^n) \Delta t, \quad (4.30)$$

where $\phi^n = \phi(t + \Delta t)$ and $\phi^{n-1} = \phi(t)$ represent the value of the dependent variable at the new and previous times respectively. Eq.4.29 provides the temporal derivative at a

centered time between times $n - 1$ and n . Combining eqs.4.28, 4.29 and 4.30 produces,

$$\begin{aligned} \frac{\phi_P^n - \phi_P^{n-1}}{\Delta t} V_P &+ \frac{1}{2} \left[\sum_f F\phi_f - \sum_f (\Gamma_\phi)_f \mathbf{A} \cdot (\nabla\phi)_f \right]^n \\ &+ \frac{1}{2} \left[\sum_f F\phi_f - \sum_f (\Gamma_\phi)_f \mathbf{A} \cdot (\nabla\phi)_f \right]^{n-1} \\ &= +\frac{1}{2} [S_c V_P + S_p V_P \phi_P]^n + \frac{1}{2} [S_c V_P + S_p V_P \phi_P]^{n-1}. \end{aligned} \quad (4.31)$$

The Crank-Nicholson temporal discretisation scheme is second order accurate in time and requires the face and cell-centred values of ϕ and $\nabla\phi$ along with the convective and diffusive fluxes for both the current and new time levels. Since the flux and non-orthogonal component of the diffusion term have to be evaluated using properties at the new time, the Crank-Nicholson scheme requires inner-iterations during each time step. Coupled with the memory overhead due to the large number of stored variables, this means the scheme is expensive compared to the Backward Differencing scheme described below.

Second Order Backward Differencing

Since the variation of ϕ in time is assumed to be linear, eq.4.29 provides a second order accurate representation of the time derivative at $t + \frac{1}{2}\Delta t$ only. Assuming the same value for the derivative at time t or $t + \Delta t$ reduces the accuracy to first order. However, as intimated before, if the temporal derivative is discretised to second order, the whole discretisation of the transport equation will be second order without the need to centre the spatial terms in time. The scheme so produced is called Backward Differencing (BD) and uses three time levels,

$$\phi^{n-2} = \phi^{t-\Delta t} \quad (4.32)$$

$$\phi^{n-1} = \phi^t \quad (4.33)$$

$$\phi^n = \phi^{t+\Delta t} \quad (4.34)$$

to calculate the temporal derivative. Now time level $n - 2$ expressed as a Taylor expansion around n is written as:

$$\phi^{n-2} = \phi^n - 2 \left(\frac{\partial \phi}{\partial t} \right)^n \Delta t + 2 \left(\frac{\partial^2 \phi}{\partial t^2} \right)^n \Delta t^2 + O(\Delta t^3) \quad (4.35)$$

Recall also that the Taylor expansion for time $n-1$ around n with a third order truncation error is given by,

$$\phi^{n-1} = \phi^n - \left(\frac{\partial \phi}{\partial t} \right)^n \Delta t + \frac{1}{2} \left(\frac{\partial^2 \phi}{\partial t^2} \right)^n \Delta t^2 + O(\Delta t^3) \quad (4.36)$$

Combining this with eq.4.35 produces a second order approximation of the temporal derivative at the new time, n :

$$\left(\frac{\partial \phi}{\partial t} \right)^n = \frac{\frac{3}{2}\phi^n - 2\phi^{n-1} + \frac{1}{2}\phi^{n-2}}{\Delta t} \quad (4.37)$$

By neglecting the temporal variation in the face fluxes and derivatives, eq.4.37 produces a fully implicit second order accurate discretisation of the general transport equation,

$$\begin{aligned} \frac{\frac{3}{2}\phi^n - 2\phi^{n-1} + \frac{1}{2}\phi^{n-2}}{\Delta t} V_P &+ \sum_f F\phi_f^n - \sum_f (\Gamma_\phi)_f \mathbf{S} \cdot (\nabla \phi)_f^n \\ &= S_c V_P + S_p V_P \phi_P^n \end{aligned} \quad (4.38)$$

Analysis has shown [66] that the Backward Differencing method, although cheaper and considerably easier to implement than the Crank-Nicholson method, results in a truncation error four times larger than the latter. This is due to the assumed lack of temporal variation in face fluxes and derivatives. This error manifests itself as an added diffusion similar to that produced by upwind differencing of the convection term. As mentioned previously, this added diffusion is undesirable in LES where the sub-grid diffusion may be very small and could be easily overwhelmed by the error. In practice however the cell-face Courant number, defined with reference to fig.4.1 as

$$CFL = \frac{\bar{\mathbf{u}}_f \cdot \mathbf{n}}{|\mathbf{d}|} = \frac{F |\mathbf{A}|}{|\mathbf{A}| |\mathbf{d}|}, \quad (4.39)$$

has to be restricted to a value below 1 to promote stability of the CD scheme. As a result the timestep will tend to be very small, which keeps the size of the temporal diffusion error to a minimum. Given its ease of implementation and comparatively low cost, the Backward Differencing scheme is thus the preferred method.

4.2.4 Navier-Stokes Discretisation

Although the general transport equation is a useful introduction to discretisation practices, there are some aspects specific to the Navier-Stokes (NS) system that require special

attention. Recall the incompressible form of the LES NS equations expressed by eqs.4.1 and 4.2. The convection term, $\nabla \cdot (\bar{\mathbf{u}} \bar{\mathbf{u}})$, introduces non-linearity into the system that cannot be treated in the generalised fashion, while the pressure-velocity coupling introduces a second unknown variable into the system. A closer look at the modeled turbulent diffusion term ($\boldsymbol{\tau}$) is also warranted, since the diffusion coefficient is a dependent variable and therefore non-constant.

Turbulent Diffusion

Although other approaches exist, the effect of SGS turbulence on the resolved scales (*i.e.* the Navier-Stokes system) is typically and throughout this thesis modeled as an added viscosity (see sec.3.2) similar to that employed in RANS type modelling. It is thus convenient to bundle the diffusion contributions associated with molecular viscosity and SGS turbulence into a single stress term:

$$\begin{aligned} \mathbf{B} &= \nu (\nabla \bar{\mathbf{u}} + \nabla \bar{\mathbf{u}}^T) + \boldsymbol{\tau} \\ &= (\nu + \nu_{SGS}) (\nabla \bar{\mathbf{u}} + \nabla \bar{\mathbf{u}}^T) \\ &= \nu_{eff} (\nabla \bar{\mathbf{u}} + \nabla \bar{\mathbf{u}}^T) \end{aligned} \quad (4.40)$$

where ν_{eff} represents the effective viscosity. The gradient and transpose gradient terms are normally discretised separately. The stress tensor is split into two parts, one treated as a diffusion and the other as a source term, for reasons of computational efficiency. If the transposed velocity gradient was also treated as a diffusion flux, it would link all three velocity components into a single equation system, *i.e.* the value of each velocity component would become dependent on the current value of both the other components. While such a linked system of equations can be solved, it requires significantly more computer resources (especially memory) and the implementation of a specialised solver not available in the current code base. The transpose term for time $t + \Delta t$ is therefore calculated using the velocity from time t . Using the discretisation techniques of eq.4.18

for the diffusion term and the mid-point rule for the transpose term produces,

$$\begin{aligned} \int_{V_P} \nabla \cdot \mathbf{B} dV &= \int_{V_P} \nabla \cdot [\nu_{eff} (\nabla \bar{\mathbf{u}} + \nabla \bar{\mathbf{u}}^T)] dV \\ &= \sum_f (\nu_{eff})_f \mathbf{A} \cdot (\nabla \bar{\mathbf{u}})_f + \nabla \cdot [\nu_{eff} (\nabla \bar{\mathbf{u}}^{n-1})^T] V_P, \end{aligned} \quad (4.41)$$

where the face velocity gradients, $(\nabla \bar{\mathbf{u}})_f$, are approximated using eq.4.19 and the cell centred gradient term, $(\nabla \bar{\mathbf{u}}^n)$, calculated from eq.4.10. Once the substitutions have been made the terms can be regrouped according to the properties of the coefficients as follows:

$$\int_{V_P} \nabla \cdot \mathbf{B} dV = a_{dP} \bar{\mathbf{u}}_P + \sum_N a_{dN} \bar{\mathbf{u}}_N + a_{dC} \quad (4.42)$$

where

$$a_{dP} = \sum_f \frac{|\mathbf{A}|}{|\mathbf{d}|} \quad (4.43)$$

$$a_{dN} = \frac{|\mathbf{A}|}{|\mathbf{d}|} \quad (4.44)$$

$$a_{dC} = \sum_f \mathbf{A}_\Delta \cdot (\nabla \bar{\mathbf{u}}^{n-1})_f + \nabla \cdot [\nu_{eff} (\nabla \bar{\mathbf{u}}^{n-1})^T] V_P \quad (4.45)$$

Note that a_{dC} depends only on the velocity at the previous time.

Convection Term

The non-linear $\nabla \cdot (\bar{\mathbf{u}} \bar{\mathbf{u}})$ transport of momentum term results in quadratic functions in velocity and must therefore be linearized. Taking the generalised convection discretisation (4.11) and replacing ϕ with $\bar{\mathbf{u}}$ produces the momentum convection term. Linearization is achieved by substituting the value of the velocity from the previous iteration for one of the terms as follows:

$$\begin{aligned} \int_{V_P} \nabla \cdot (\bar{\mathbf{u}} \bar{\mathbf{u}}) dV &= \int_{\partial V} d\mathbf{A} \cdot (\bar{\mathbf{u}} \bar{\mathbf{u}}) = \sum_f \mathbf{A} \cdot \bar{\mathbf{u}}_f \cdot \bar{\mathbf{u}}_f \\ &\approx \sum_f (\mathbf{A} \cdot \bar{\mathbf{u}}_f^{n-1}) \cdot \bar{\mathbf{u}}_f^n = \sum_f F^{n-1} \cdot \bar{\mathbf{u}}_f^n \end{aligned} \quad (4.46)$$

The flux used to solve the velocity at the new time is thus lagged via the current time velocity field. Approximating the face based quantities in eq.4.46 with the CD (or any

other) scheme produces the cell based momentum convection term,

$$\sum_f F^{n-1} \cdot \bar{\mathbf{u}}_f = a_{cP} \bar{\mathbf{u}}_P + \sum_N a_{cN} \bar{\mathbf{u}}_N \quad (4.47)$$

where the coefficients a_{cP} and a_{cN} are explicit functions of $\bar{\mathbf{u}}^{n-1}$.

Pressure Equation

In this study the PISO (Pressure Implicit with Splitting of Operators) procedure proposed by Issa [62] is used to couple the pressure to the velocity via flux conservation. The pressure equation is derived as a semi-discretised form of the momentum equation (eq.4.28) using the discretisation techniques described in previous sections.

$$a_P \bar{\mathbf{u}}_P = \mathbf{H} - \nabla \bar{p}. \quad (4.48)$$

Here the pressure gradient term remains undiscretised and both sides have been divided through with the cell volume to allow face interpolation of the coefficients. Now a_P consists of the sum of the coefficients of $\bar{\mathbf{u}}_P$,

$$a_P = a_{cP} + a_{dP} + a_{tP} \quad (4.49)$$

where a_{tP} is the coefficient of $\bar{\mathbf{u}}_P$ from the temporal scheme (eq.4.31 or 4.38). The \mathbf{H} vector is a combination of all the neighbour matrix coefficients multiplied with their velocities and all the non-linear source terms sans the pressure gradient, but including the current time contributions.

$$\mathbf{H} = \sum_N (a_{cN} + a_{dN}) \bar{\mathbf{u}}_N + a_{tC} + a_{dC}. \quad (4.50)$$

where a_{tC} is the portion of the temporal derivative not dependent on $\bar{\mathbf{u}}^n$, which depends on the time discretisation scheme. Dividing both sides of eq.4.48 by a_P produces an expression for $\bar{\mathbf{u}}$,

$$\bar{\mathbf{u}}_P = \frac{\mathbf{H}}{a_P} - \frac{\nabla \bar{p}}{a_P}. \quad (4.51)$$

Interpolating eq.4.51 to express the face velocity gives,

$$\bar{\mathbf{u}}_f = \left(\frac{\mathbf{H}}{a_P} \right)_f - \left(\frac{\nabla \bar{p}}{a_P} \right)_f. \quad (4.52)$$

Using the techniques introduced in eq.4.10 the discretised form of the continuity equation (4.1) can be written as:

$$\nabla \cdot \bar{\mathbf{u}} = \sum_f \mathbf{A} \cdot \bar{\mathbf{u}}_f = 0. \quad (4.53)$$

Substituting $\bar{\mathbf{u}}_f$ from eq.4.52 into the above relation produces the pressure equation:

$$\nabla \cdot \left(\frac{1}{a_P} \nabla \bar{p} \right) = \nabla \cdot \left(\frac{\mathbf{H}}{a_P} \right) = \sum_f \mathbf{A} \cdot \left(\frac{\mathbf{H}}{a_P} \right)_f. \quad (4.54)$$

The Laplacian on the l.h.s. of eq.4.54 and the pressure gradient on the r.h.s. of eq.4.48 can be discretised in a manner similar to the diffusion term in sec.4.2.2, resulting in the final form of the Navier-Stokes system:

$$a_P \bar{\mathbf{u}}_P = \mathbf{H} - \sum_f \mathbf{A} \cdot \bar{p}_f \quad (4.55)$$

$$\sum_f \mathbf{A} \cdot \left(\frac{1}{a_P} \right)_f (\nabla \bar{p})_f = \sum_f \mathbf{A} \cdot \left(\frac{\mathbf{H}}{a_P} \right)_f. \quad (4.56)$$

The procedure used to solve the unknown variables \bar{p} and $\bar{\mathbf{u}}$ is depicted as a flowchart in fig.4.4. The individual steps of the solution procedure are described below:

1. The procedure starts with the initial conditions for the unknown flow variables ($\bar{\mathbf{u}}$, \bar{p}), turbulent quantities (K or $\tilde{\nu}$) and face fluxes, F . The initial properties of the LES fields are typically derived from unsteady RANS calculations.
2. The first step of the solution cycle is updating the turbulent properties using the initial or previous time-step values of $\bar{\mathbf{u}}$, F and \bar{p} . The discretised equations of this step are described in sec.4.3.
3. The momentum predictor step solves a tentative velocity using the old-time values of \bar{p} and F and eq.4.55. Solution of the matrix is achieved by employing an iterative Conjugate Gradient method (CG). Convergence time is accelerated by preconditioning this matrix using the procedures detailed by Van der Vorst [162](Bi-CGSTAB) applicable to asymmetric matrices. The resultant tentative velocity field does not in general satisfy the continuity equation.

4. Computational Methodology

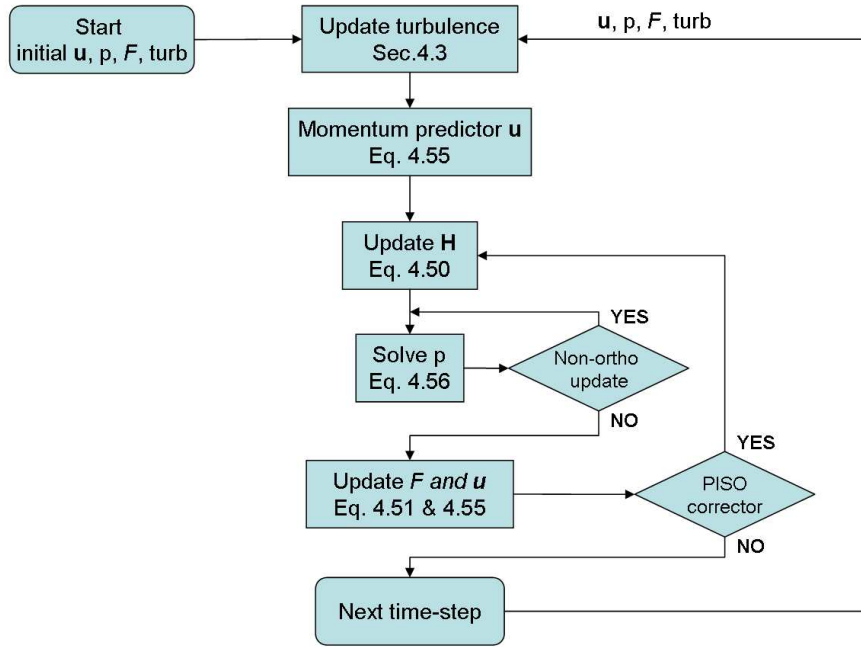


Figure 4.4: PISO solution procedure

4. The tentative velocity serves to update the off-diagonal matrix components, \mathbf{H} (eq.4.50).
5. This is in turn used in the solution of the pressure equation (eq.4.56). The system matrix for the pressure equation is solved using the Incomplete Choleski preconditioned Conjugate Gradient (ICCG) method [63].
6. Due to the explicit nature of the non-orthogonal component of the face interpolation of \bar{p} , the pressure equation has to be solved iteratively. Typically, a single or at most two corrector steps are sufficient to converge the non-orthogonal component.
7. The solution of the pressure is followed by the projection of the velocities and fluxes into a divergence free form (eqs.4.55 and 4.52 respectively).
8. Steps 4-7 are now repeated iteratively until the dependent variables stop changing. Since the timesteps associated with LES are generally small, this rarely requires more than 2-3 iterations.

9. Finally, the calculation moves to the next time step, where the current values are used as initial guesses for the next cycle of the solution.

4.3 Modelling Implementation

The two SGS models chosen for this investigation, one-equation turbulent energy and the Spalart-Allmaras, can for the most part be discretised according to the general practices already outlined. Small deviations do exist however and since these models form the focus of this investigation, their implementation will be described to a reproducible level of detail. For simplicity sake, the volume and time integrals are not depicted.

4.3.1 One-equation Turbulent Energy Model

The one-equation turbulent energy model detailed in sec.3.2.2 obtains the turbulent SGS viscosity (ν_{SGS}) from a transport equation for the sub-grid scale turbulent energy, which is assumed to be isotropic. The transport equation is given by eq.3.17:

$$\underbrace{\frac{\partial K}{\partial t}}_{time} + \underbrace{\nabla \cdot (K \bar{\mathbf{u}})}_{convection} - \underbrace{\nabla \cdot [(\nu + \nu_{SGS}) \nabla K]}_{diffusion} = \underbrace{-\epsilon - \boldsymbol{\tau} : \bar{\mathbf{S}}}_{sources}$$

In eq.3.17 the temporal, diffusive and source term contributions to the transport equation can be discretised in an identical fashion to that introduced in the preceding sections. The only noteworthy change is the differencing scheme employed to calculate the face centred value of K . The CD scheme is known to be unbounded, which can lead to negative K values and failure of the iterative sequence. The bounded upwind differencing scheme on the other hand is overly diffusive under most flow conditions. The alternative is to employ some type of blended scheme that combines certain aspects of both methods to produce a compromise scheme that is bounded but potentially sacrifices some of the accuracy of central differencing. For this purpose, the GAMMA switching/blending scheme first introduced by Jasak [67] is employed.

The GAMMA scheme uses CD in the bulk of the solution, but when the interpolation tends to unboundedness, some UD is introduced to stabilise the equations. Detection of possible unboundedness is done by means of a gradient comparison: with reference to

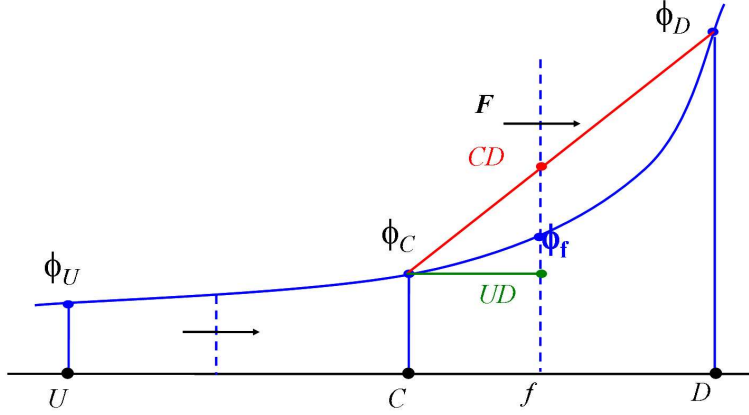


Figure 4.5: Shape of variable profile for $0 < \tilde{\phi}_C < \beta_m$.

fig.4.5, which represents the local profile of the dependent variable around the point C with U and D being points upwind and downwind relative to C respectively. Boundedness of the solution is guaranteed if ϕ_C is bounded by the values in its neighbouring cells, i.e. $\phi_U > \phi_C > \phi_D$ or $\phi_U < \phi_C < \phi_D$. To evaluate this condition as compactly as possible a “normalised variable” $\tilde{\phi}_C$ is defined such that,

$$\begin{aligned}\tilde{\phi}_C &= \frac{\phi_C - \phi_U}{\phi_D - \phi_U} \\ &= 1 - \frac{(\nabla\phi)_f \cdot \mathbf{d}}{2(\nabla\phi)_C \cdot \mathbf{d}}\end{aligned}\quad (4.57)$$

where $\tilde{\phi}_C < 0$ or $\tilde{\phi}_C > 1$ indicates unboundedness. If this were simply used to switch between UD and CD when unboundedness was detected, the likelihood exists that the switching itself would contribute to instability in the solution, preventing convergence. To counteract this tendency, a damping factor β_m is introduced that acts to dampen the discontinuity when switching schemes, as follows:

$$\phi_f = \begin{cases} \phi_C & : \tilde{\phi}_C < 0 : \text{UD} \\ \left(1 - \frac{\tilde{\phi}_C}{\beta_m} (1 - f_x)\right) \phi_C + -\frac{\tilde{\phi}_C}{\beta_m} (1 - f_x) \phi_D & : 0 < \tilde{\phi}_C < \beta_m : \text{Blended} \\ f_x \phi_C + (1 - f_x) \phi_D & : \beta_m < \tilde{\phi}_C < 1 : \text{CD} \\ \phi_C & : \tilde{\phi}_C > 1 : \text{UD} \end{cases} \quad (4.58)$$

The scheme, although not second order accurate everywhere, performs well in most circumstances producing stable, smooth solutions with reasonable levels of accuracy.

All other terms on the r.h.s. of eq.3.17 are treated as sources. The first term ϵ represents turbulent dissipation at the smallest scales and thus acts as a sink for turbulent energy and is linearized as follows,

$$\epsilon = C_\epsilon K^{3/2} \Delta = \left(C_\epsilon \sqrt{K^{n-1}} \Delta \right) K^n. \quad (4.59)$$

Here K^{n-1} is lagged in time. The second source term in eq.3.17 represents the decay of turbulence from the resolved scales to the sub-grid scales via the energy cascade. It is also dependent on the SGS energy, but because the term is always positive, it is lagged in time to improve the stability of the solver.

$$\begin{aligned} \boldsymbol{\tau} \cdot \bar{\mathbf{S}} &= [\nu_{SGS} (\nabla \bar{\mathbf{u}} + \nabla \bar{\mathbf{u}}^T)] : \bar{\mathbf{S}} \\ &= \nu_{SGS} |\bar{\mathbf{S}}|^2 = C_k \sqrt{K^{n-1}} \Delta |\bar{\mathbf{S}}|^2. \end{aligned} \quad (4.60)$$

When Yoshizawa's one equation SGS turbulent energy model is used for well resolved LES, *i.e.* resolution of all the energetic scales of motion, it requires very little special handling to accommodate a wall. The base model however requires some modification to incorporate the DES approach, but at the same time, it is desirable that the treatment reduces to the well-resolved formulation on a fine mesh. The DES treatment specifies that the near-wall region is treated in an unsteady Reynolds average fashion. Any turbulence modelling that is effective for RANS simulations can thus potentially be used for DES in the near-wall region.

Chen and Patel [28] demonstrated the effectiveness of a two-layer approach for RANS by replacing the standard $k - \epsilon$ turbulence modelling near the wall with Wolfshtein's one-equation model [169]. Since the standard high-Re $k - \epsilon$ model and the one equation model are fairly similar except for the obvious lack of dissipation equation in the latter (even the coefficients are similar), Wolfshtein's model also appears to be a good candidate for a DES near-wall treatment. The model also employs a transport equation for turbulent kinetic energy, but all length scales and thus the dissipation rate are determined by proximity to the wall and the shear velocity,

$$\epsilon = K^{3/2}/l_\epsilon, \quad (4.61)$$

$$\nu_t = C_\mu \sqrt{K} l_\mu, \quad (4.62)$$

4. Computational Methodology

where the length scale l_μ and l_ϵ contain the necessary damping effects in the near-wall region in terms of viscous wall units,

$$l_\mu = C_l y_w \left[1 - e^{-y^+/A_\mu} \right], \quad (4.63)$$

$$l_\epsilon = C_l y_w \left[1 - e^{-y^+/A_\epsilon} \right], \quad (4.64)$$

Here $C_l = \kappa C_\mu^{-3/4}$, ensuring smooth transition between the near-wall and outer regions. In addition, $A_\epsilon = 2C_l$ is assigned to recover proper asymptotic behaviour for ϵ in the sub-layer, while the third parameter, A_μ , is experimentally determined to be in the range $20 - 30$. Both l_μ and l_ϵ tend toward $C_l y_w$ as the distance from the wall increases, so that the disparate influences of A_μ and A_ϵ quickly fade towards the interior. The net effect is that only the K -equation needs be solved in the near-wall region.

It is relatively straightforward to add the Wolshtain approach to the SGS turbulent energy model to give a basic DES model. Using a switch similar to the Spalart-Allmaras approach new turbulent length scales l_k and l_ϵ can be defined:

$$l_k = \min \left(\kappa y_w \left[1 - e^{-y^+/A_k} \right] / C_S, V^{1/3} \right), \quad (4.65)$$

$$l_\epsilon = \min \left(\kappa y_w \left[1 - e^{-y^+/A_\epsilon} \right] / C_S, V^{1/3} \right), \quad (4.66)$$

where C_S can be derived by assuming equilibrium conditions in the sub-grid scales and has a value of $C_S \approx 0.1 \sim 0.15$ for the standard range of values for C_k and C_ϵ . Numerical experiments using fully developed channel flows show that $A_k \approx 26$ is an optimum value for A_k , while A_ϵ retains its previous definition. By replacing Δ in the equations for ν_{SGS} and ϵ , the following relations are produced,

$$\epsilon = C_\epsilon K^{3/2} / l_\epsilon, \quad (4.67)$$

$$\nu_{SGS} = C_k \sqrt{K} l_k, \quad (4.68)$$

which will give RANS-like behaviour near the wall (but only if cells are too coarse to resolve significant eddies in this region) and LES in the interior flow. A conceptually similar near-wall length scale approach is used by Mason and Thomas [102], but without the near-wall damping effect. It is thus only applicable to relatively coarse near-wall meshes, but still lends a measure of validity to the current proposal. At first glance, this

implementation appears equivalent to the Smagorinsky - van Driest damping combination widely used in LES, where the SGS length scale is modified in the near-wall region as follows:

$$l_{SGS} = C_S \Delta \left[1 - e^{-y^+/A^+} \right] \quad (4.69)$$

The difference is of course, that eq.4.67 couches the length scale in terms of absolute near-wall distance, while eq.4.69 relies on the cells in this region being of the correct size to represent the turbulent length scale, thus making it applicable only on relatively fine meshes. Both these models are implemented for comparison during the initial investigation.

4.3.2 Spalart-Allmaras

The Spalart-Allmaras (S-A) model first introduced in sec.3.3.3 is formulated as a transport equation for a transformed turbulent viscosity, $\tilde{\nu}$ (eq.3.76). Revisiting the S-A transport equation (eq.3.79) we see the familiar temporal, convective and diffusive components on the l.h.s. ,

$$\begin{aligned} \frac{\partial \tilde{\nu}}{\partial t} + \nabla \cdot (\tilde{\nu} \bar{\mathbf{u}}) - \frac{1}{\sigma} \nabla \cdot [(\nu + \tilde{\nu}) \nabla \tilde{\nu}] \\ = \underbrace{c_{b1} \tilde{S} \tilde{\nu}}_{production} + \underbrace{\frac{1}{\sigma} c_{b2} (\nabla \tilde{\nu})^2}_{transport} - \underbrace{c_{w1} f_w \left[\frac{\tilde{\nu}}{d} \right]^2}_{dissipation} \end{aligned}$$

which are treated in the standard way. On the right hand side are the $\tilde{\nu}$ dissipation and production terms and also a non-linear diffusion-type term. To improve the stability of the solution, the production term is calculated as an explicit function of $\tilde{\nu}^{n-1}$,

$$\tilde{\nu}_{production} = c_{b1} \left[|\nabla \times \bar{\mathbf{u}}| + \frac{\tilde{\nu}^{n-1}}{\kappa^2 d^2} f_{v2} \right] \tilde{\nu}^{n-1} \quad (4.70)$$

$$(4.71)$$

where f_{v2} is a function of $\tilde{\nu}^{n-1}$ which can be found from eq.3.81. The square of the gradient is linearized as follows:

$$\tilde{\nu}_{transport} = \frac{c_{b2}}{c_\sigma} \nabla \tilde{\nu}^{n-1} \cdot \sum_f \mathbf{A} \cdot \tilde{\nu}_f \quad (4.72)$$

4. Computational Methodology

with the face based value calculated using linear interpolation. The viscosity destruction term is also linearized into a semi-implicit term as follows,

$$\tilde{\nu}_{dissipation} = - \left[c_{w1} f_w \frac{\tilde{\nu}^{n-1}}{\tilde{d}^2} \right] \cdot \tilde{\nu} \quad (4.73)$$

where f_w is also a function of $\tilde{\nu}^{n-1}$ that can be found from eq.3.82.

The implementations of the S-A DES model used in this study is a modification of the original proposed by Spalart *et al.* [149]. The main difference is in the definition of the SGS length scale Δ . The Spalart-Allmaras DES model derives its turbulent length scale from eq.3.85

$$\tilde{d} = \min(y_w, C_{DES}\Delta) \quad \text{with } \Delta = \max(\Delta x, \Delta y, \Delta z)$$

Although the evaluation of Δ according to this definition is trivial on a structured hexagonal mesh aligned with the coordinate system, inconsistencies soon begin to appear if an unstructured mesh with polygonal elements is used. In an attempt to circumvent this difficulty, two new definitions for Δ are proposed:

- The maximum edge length, uses the maximum edge length along the cells faces as a length scale. This definition generally returns values in accordance with the original formulation's intent, but will become inaccurate for polygonal cells with high face counts.
- The cube-root of the cell volume, $V^{1/3}$, is the definition used most widely in LES, but will return values equivalent to the original definition only in the case of axis-aligned, equal-sided hexagonal cells. For anisotropic cells (*i.e.* cells which are not perfect cubes), the values of Δ will be somewhat smaller than those given by the initial definition (see fig.4.6).

Both definitions for Δ are incorporated in the model and the differences in results they produce are briefly explored in the results section.

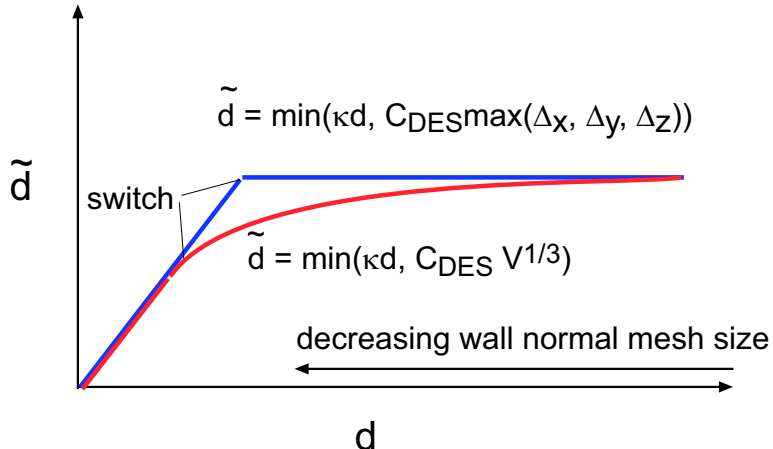


Figure 4.6: Variation of \tilde{d} with wall distance, d , and cell size.

4.4 Boundary Conditions

The prescription of a problem is divided into physical boundary conditions such as walls, inlets and outlets; and the initial conditions which constitute the known field values prior to the first timestep of the calculation. The problems treated as part of this investigation are dominated by boundary properties, while initial conditions, which unless noted otherwise are derived from RANS solutions, have a transient effect.

4.4.1 Basic Boundary Conditions

This first section examines the discretisation and implementation of the more common boundary conditions: fixed value, fixed gradient and periodic. We follow this with a description of the more specialised boundaries used during this investigation: turbulent inlets and walls. Figure 4.7 shows the nomenclature associated with a arbitrary control volume with a boundary face, b . The nomenclature is similar to that introduced for non-orthogonal treatment in sec.4.2.2, except that the cell centre to cell centre vector \mathbf{d} is redefined as the cell centre to boundary face centre vector.

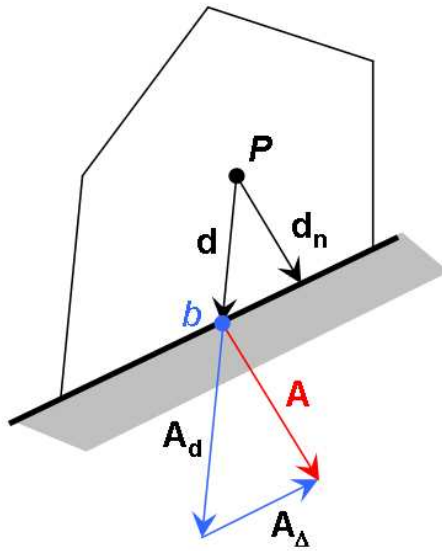


Figure 4.7: A control volume adjacent to a boundary.

Fixed Value

The fixed value boundary condition prescribes the value of the generic variable ϕ at the face b to be ϕ_b . In the convection term (eq.4.11) discretisation given by

$$\int_{V_P} \nabla \cdot (\bar{\mathbf{u}}\phi) dV = = \sum_f F\phi_f,$$

the boundary face contribution to the r.h.s. sum is simply

$$(F\phi_f)_{f=b} = F_b\phi_b, \quad (4.74)$$

where F_b is the specified flux across the boundary face.

In the diffusion term discretised according to eq.4.18

$$\int_{V_P} \nabla \cdot (\Gamma_\phi \nabla \phi) dV = \sum_f (\Gamma_\phi)_f \mathbf{A} \cdot (\nabla \phi)_f .$$

the face normal gradient of ϕ at b needs to be calculated. To accomplish this we use an explicit corrector similar to eq.4.22:

$$\mathbf{A} \cdot (\nabla \phi)_b = |\mathbf{A}_d| \frac{\phi_b - \phi_P}{|\mathbf{d}|} + \mathbf{A}_\Delta \cdot (\nabla \phi)_P . \quad (4.75)$$

The main difference is that the adjacent cell centre instead of interpolated face gradient is used to calculate the explicit component. The area vector decomposition ($\mathbf{A} = \mathbf{A}_d + \mathbf{A}_\Delta$) is identical to that described in sec.4.2.2.

Unless otherwise noted, the fixed value boundary is used under the following conditions:

- walls - Constant uniform velocity: $\bar{\mathbf{u}} = (0, 0, 0)$,
- inlets - Non-uniform, constant velocity: $\bar{\mathbf{u}} = \mathbf{U}(x, y, z)$,
- outlets - Constant, uniform pressure: $\bar{p} = p_{out}$.
- symmetry - Constant, uniform boundary-normal component of velocity, $\bar{\mathbf{u}}_n = (0, 0, 0)$

Here “constant” and “uniform” refer to the distribution of the boundary values in time and space respectively. The boundary conditions for turbulent properties are described in sec.4.4.2.

Fixed Gradient

This boundary condition prescribes the normal gradient, g_b on the boundary face,

$$\frac{\partial \phi}{\partial n_b} = \mathbf{n}_b \cdot (\nabla \phi)_b = g_b, \quad (4.76)$$

where

$$\mathbf{n}_b = \frac{\mathbf{A}}{|\mathbf{A}|}. \quad (4.77)$$

When applied to the convection term, ϕ_b must be calculated from the cell centred value together with the variation resulting from the prescribed gradient, thus

$$\begin{aligned} \phi_b &= \phi_P + \mathbf{d}_n \cdot (\nabla \phi)_b \\ &= \phi_P + |\mathbf{d}_n| g_b. \end{aligned} \quad (4.78)$$

with

$$\mathbf{d}_n = \mathbf{n} (\mathbf{d} \cdot \mathbf{n}). \quad (4.79)$$

4. Computational Methodology

Since the face gradient is prescribed, the diffusion term for the fixed gradient boundary face simply becomes,

$$(\Gamma_\phi)_b |\mathbf{A}| g_b. \quad (4.80)$$

The fixed gradient conditions is used for the following boundaries,

- walls, inlets, symmetry - Constant, uniform pressure gradient, $\frac{\partial p}{\partial n_b} = 0$,
- outlets - Constant, uniform velocity gradient, $\frac{\partial \bar{\mathbf{u}}}{\partial n_b} = (0, 0, 0)$,
- symmetry - Constant, uniform gradient of boundary parallel component of velocity, $\frac{\partial \bar{u}_\parallel}{\partial n_b} = (0, 0, 0)$.

Periodic

Periodic boundaries are used to approximate infinite homogenous directions in the channel flow and asymmetric plane diffuser cases. This is accomplished by linking the coupled boundaries directly in the system matrix. This means that, from the perspective of the solver, a coupled cell pair although separated by space are adjacent in the computational system. As such, no special descritisation practices are required to account for this boundary type.

4.4.2 Turbulent Wall Properties

Modelling of the near-wall regions has already been discussed (sec.3.3) and the implementations used during this investigation were detailed in sec.4.3, so all that remains is to describe the boundary conditions. In this section turbulent wall boundary conditions are addressed, starting with the wall function, which is identical to both approaches.

Wall Function

The wall function selected for this investigation is the “universal” profile, eq.3.58,

$$y^+ = u^+ + \frac{1}{E} \left[e^{\kappa u^+} - 1 - \kappa u^+ - \frac{1}{2} (\kappa u^+)^2 - \frac{1}{6} (\kappa u^+)^3 \right],$$

Which is assumed to apply to the parallel component of velocity between the wall and the first off-the-wall grid point. With reference to fig.4.7 the wall normal vector \mathbf{d}_n and the wall parallel velocity found from

$$\bar{\mathbf{u}}_{\parallel} = \bar{\mathbf{u}}_P - \mathbf{n} (\bar{\mathbf{u}}_P \cdot \mathbf{n}), \quad (4.81)$$

are substituted into the relations for y^+ and u^+

$$y^+ = \frac{|\mathbf{d}_n| u_{\tau}}{\nu} = \frac{y_w u_{\tau}}{\nu}, \quad (4.82)$$

$$u^+ = \frac{|\bar{\mathbf{u}}_{\parallel}|}{u_{\tau}} = \frac{u_{\parallel}}{u_{\tau}}, \quad (4.83)$$

leaving only one unknown, the shear velocity u_{τ} . Since eq.3.58 is non-linear in u_{τ} , the solution must be obtained iteratively. For this we use the well known Newton-Raphson method,

$$u_{\tau} = u_{\tau}^{n-1} - \frac{f}{f'}, \quad (4.84)$$

where u_{τ}^{n-1} is the shear velocity from the previous iteration and f and f' can be found from:

$$f = u^+ - y^+ + \frac{1}{E} \left[e^{\kappa u^+} - 1 - \kappa u^+ - \frac{1}{2} (\kappa u^+)^2 - \frac{1}{6} (\kappa u^+)^3 \right] \quad (4.85)$$

$$f' = \frac{\partial f}{\partial u_{\tau}} = -\frac{u^+}{u_{\tau}} - \frac{y^+}{u_{\tau}} + \frac{1}{E} \left[-\frac{\kappa u^+}{u_{\tau}} e^{\kappa u^+} + \frac{\kappa u^+}{u_{\tau}} + \frac{1}{u_{\tau}} (\kappa u^+)^2 + \frac{1}{2u_{\tau}} (\kappa u^+)^3 \right] \quad (4.86)$$

$$\dots \quad (4.87)$$

The Newton-Raphson method converges rapidly to a tight tolerance when applied as described above. By using initial values from the previous timestep 1 or 2 iterations are normally sufficient, thus imposing a comparatively small computational overhead. The predicted wall shear can now be derived from the friction velocity,

$$\frac{\tau_w}{\rho} = u_{\tau}^2 \frac{|\bar{\mathbf{u}}_{\parallel}|}{|\bar{\mathbf{u}}_{\parallel}|}. \quad (4.88)$$

Unfortunately, the wall function describes the near-wall flow only in a statistical sense, instantaneous values can and do deviate significantly from the averaged profile [128]. In an unsteady LES calculation, this can lead to inaccurate results. Thus for y_0^+ in the buffer or logarithmic layer where turbulence plays a significant role, the wall function can only be used reliably under special conditions.

4. Computational Methodology

Recall the filtering process employed in sec.3.1. The value of the dependent variable at a grid point represents a spatial average of that variable within (and possibly around) the cell. It is thus possible to choose the extent of the near-wall cell such that the implicit average of the solution approaches the ensemble average inherent in the wall function, i.e. $\tau_w \rightarrow \langle \tau_w \rangle$. Typically this is achieved by choosing very large wall parallel dimensions for the cell. It has been shown [149] that a surface parallel extent between 200 – 400 wall units is required to approach such an averaged state. Obviously, cells with such large dimensions are completely incompatible with a pure LES approach as they would be incapable of resolving any significant turbulent structures in the boundary layer. As a result wall functions of this type are generally only effective in combination with a DES approach as described in sec.3.3.3.

The wall function's continuous nature however means that we can combine poorly resolved DES boundary layers with well resolved ($y_0^+ < 9$) boundary regions in the same domain without changing the modelling approach, simply by manipulating the mesh spacing. It must be conceded that such an approach can include transitional zones where well and poorly resolving meshes meet to produce hybrid regions of questionable accuracy. This deficiency is acknowledged and an attempt is made to minimise such situations throughout the study.

One-equation SGS Energy Model

Inlet, outlet and periodic boundaries for the K -equation, are handled in an identical fashion to those used for the momentum equation. The distribution of turbulent energy generally exhibits a local maximum close to the wall [156], which necessitates a different implementation depending on the near-wall grid point's distance from the surface in terms of wall units, *i.e.* y^+ . Based on equilibrium conditions, the boundary conditions are assumed to be:

$$K = 0 \quad \text{for } y_0^+ \leq 20, \tag{4.89}$$

$$\frac{\partial K}{\partial y_w} = 0 \quad \text{for } y_0^+ > 20, \tag{4.90}$$

where $\partial K / \partial y_w$ is the wall normal derivative. The boundary condition defined above are far from exact, especially near the region of peak K , but were found to be generally good approximations for $y_0^+ \ll 20$ or $y_0^+ \gg 20$. It must be emphasized that employing such large wall-normal spacing in the wall adjacent control volume can lead to a decrease in accuracy due to the poor resolution of turbulent structures and modelling inaccuracies.

Spalart-Allmaras (S-A) Model

Boundary conditions for the Spalart-Allmaras viscosity, $\tilde{\nu}$, are set to zero at all wall boundaries irrespective of the wall normal cell size. For the S-A model the switch to the zero gradient boundary condition is not required since the maximum in the transported S-A viscosity occurs at $y^+ > 100$, unlike the turbulent energy K , for which the maximum occurs at a much smaller wall normal distance. This is more clearly illustrated by employing the Spalart-Allmaras model in “pure” RANS mode. Figure 4.8 compares the distributions of transported quantities for the S-A and SGS turbulent energy model ($\tilde{\nu}$ and K respectively) in a fully developed channel flow where the wall parallel grid spacing is much larger than the wall normal distance. The mesh is far too coarse in wall-parallel directions to resolve any turbulent motion and the length scale is everywhere proportional to the wall distance. As a result, both models operate in “RANS” mode throughout the domain and all turbulent contributions are provided by the respective models. The differences in the formulation of the transported properties means that the wall-normal distance of the maxima varies considerably. Since the resolution of such maxima is generally critical to accurate near-wall treatment, this suggests that the S-A model will be somewhat more robust in dealing with badly resolved near-wall regions.

All other S-A boundary conditions are the same as those employed by the eddy viscosity model.

4.4.3 Turbulent Inlets

Specification of inlet boundary conditions in LES is a well known issue. The importance of inlet flow specification can vary significantly from problem to problem. Under some conditions the flow in the interior can be linked only weakly to the turbulent characteristics

4. Computational Methodology

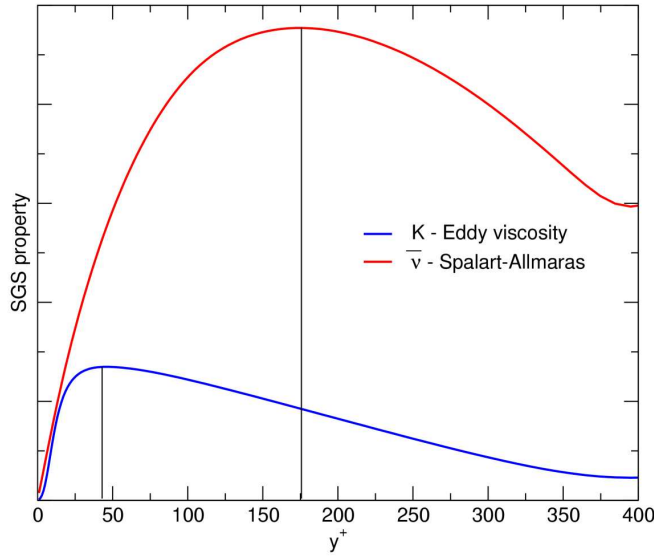


Figure 4.8: Variation of transported turbulent quantities in RANS of a channel flow.

of the inlet. This typically occurs where turbulent features generated in the interior through shear layers and shedding phenomena are much stronger and of larger scale than those present at the upstream boundary. Conversely, if there is little or no scale separation between the internally generated and externally specified scales, then the accuracy of the latter's stipulation becomes critical. In the worst-case scenario the character of the flow in the solution domain can be so strongly coupled to the inlet boundary that the specification of the latter largely determines the properties of the former. During this investigation the asymmetric plane diffuser case is expected to be strongly coupled to the resolved inlet turbulence specification. In the wing mirror cases on the other hand, turbulence generated in the domain is much more prominent than that convected through the inlet. These dependencies are discussed in more detail in secs. 5.2.3 and 6.1.1.

A LES turbulent inlet is expected to carry a stochastically varying velocity distribution with spatial scales varying between the mesh spacing and the integral size. In addition, these fluctuations should obey the constraints of the governing Navier-Stokes equations; *i.e.* the flow field should be divergence-free. Physically, it is also desirable that the fluid structures introduced at the inlet should actually look like turbulence and reproduce the correct turbulent and other mean statistics of the flow.

For cases where the resolved inlet turbulence is important several approaches have been pursued with varying success:

- **Random noise.** The simplest method is to superimpose random fluctuations on the mean inlet profile. This cannot reproduce the physical structure of turbulence and in the author’s experience the fluctuations are rapidly damped out because of the lack of structure. Some work has been done to scale and otherwise manipulate the random distribution to produce a more realistic flow [91, 144], and has met with some success but requires more work for general application.
- **Turbulence synthesis.** This class of inlets is related to the above, but employs artificial methods to reconstruct turbulent structures with approximately the right scales and spacing. A typical approach is to employ a stochastic time-dependent variation of the coefficients of the Fourier decomposition of the mean flow [155]. Such approaches produce spatial coherent structures with the correct times-scales and can be tuned to produce good approximations of the first moment characteristics. At present, prediction of the correct vortex topology of boundary layer (and other) turbulence is not yet possible, resulting in inaccurate dynamics and second moment statistics.
- **Pre-computation,** where the turbulence at inlet is self-similar, the upstream flow can be approximated as a domain of infinite length by employing periodic streamwise boundaries (see fig.4.9a). This solution of this upstream region is then produced before the main calculation starts. There are two distinct methods for introducing the pre-calculated data into the main simulation. The simplest, but most resource intensive, involves simply building up a time series library of the flow at the pre-computation outlet of sufficient duration to provide inlet conditions for the entirety of the main simulation. This method is expensive both in terms of computational time and storage space. Provided the pre-computation domain is sufficiently large, this approach should provide inlet flow with very little periodicity or other numerical artefacts. The second approach involves re-using a similar but much smaller data set over and over again. Here, periodicity induced by the small data set is counteracted

4. Computational Methodology

by employing random phase-amplitude jittering [32], coordinate transformations and other numerical permutation techniques to change the character of the inlet data. All the pre-computation methods have been shown to work reasonably well under most conditions. They are however awkward to implement and use, and are very sensitive to the position of the inlet.

- **Mapped inlet** Developed as part of this project, this method employs a simple scaled mapping of the velocity field from some plane in the interior of the domain to specify the inlet velocity and turbulence properties (see fig.4.9b). Scaling is used to enforce a specified bulk flow rate, but may also be employed under some self-similar conditions to approximate a growing boundary layer. Since the mapped portion is part of the main computational domain, this method is considerably simpler to use than a pre-computed library; it does not require a separate case; has minimal storage overhead; and the increase in overall cost, dependent on the inlet domain extent, is usually modest. Being part of the same domain as the solution also has a drawback: if disturbances in the flow propagate upstream into the vicinity of the mapping plane, they will be mapped onto the inlet. Such mapped disturbances can then create a feedback effect by exacerbating the original disturbance which is again mapped to the inlet, etc. In this way the resulting flow in the inlet section can diverge significantly from the equilibrium conditions that are normally required. This issue can be addressed by positioning the inlet section and especially the mapping plane sufficiently far upstream from any large scale unsteadiness in the main domain to avoid contamination.

For the purposes of this investigation, the accuracy provided by the pre-computed and mapped inlets made them most suitable for the asymmetric plane diffuser described in sec.1.3.2, which requires a fully developed plane channel flow as inlet condition. The weak pressure-driven separation found in the diffuser, is very sensitive to upstream flow properties, including transported turbulent quantities (K and $\tilde{\nu}$) and resolved eddy structures. Extending the inlet section of the domain to allow for the natural development of equilibrium turbulent statistics would be prohibitively expensive, making the methods

described above the only viable alternative.

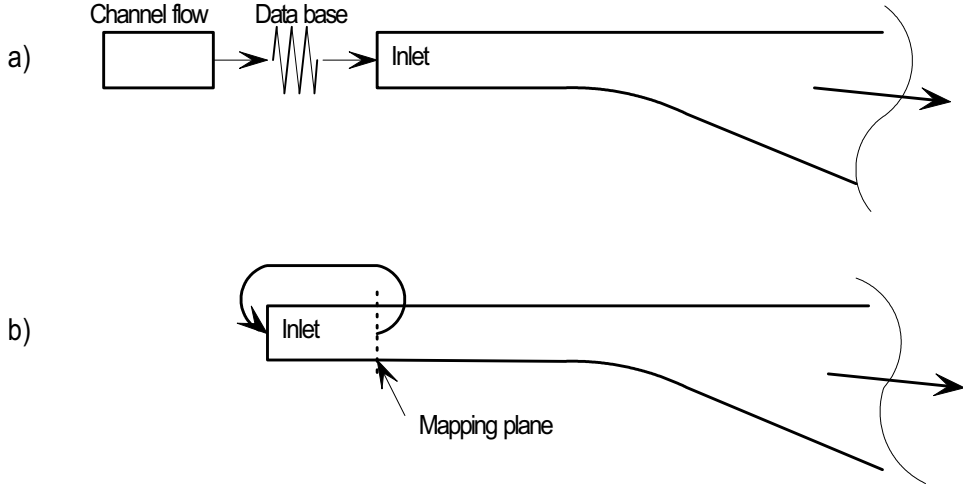


Figure 4.9: Inlet boundaries for the plane diffuser a) pre-computed and b) mapped.

Figure 4.9 (a) and (b) depict the implementation of the pre-computed and mapped inlets respectively. The pre-computed method used here is of the “large library” type, with enough realizations of the inlet to complete an entire flow-through time of the main domain. This duration was found to be more than sufficient to prevent distorted statistics due to the recycling of the recorded inlet data. In addition, the channel flow calculations were conducted with the same mesh spacing and time step used at the inlet of the main domain, removing the need for temporal or spatial interpolation. The second method employed in this investigation, fig.4.9b, uses field values from inside the flow domain to achieve the same effect. For the implementation of the mapped inlet the channel section is extended an additional four inlet heights upstream to minimise the effects of contamination by the downstream flow and to provide the streamwise dimensions to maintain a minimal periodic channel flow. A sampling plane is then inserted at the position of the old inlet. Field values at the location of the plane are mapped onto the upstream boundary at each timestep to provide the inlet conditions. A comparison of the results produced by the two methods is performed in sec.5.2.3.

Of course, not all LES calculations are as sensitive to the turbulent properties at the inlet as the diffuser. The main case used in this investigation, the wall mounted side mirror, shows very little dependence on turbulent structures at the inlet boundary. In

fact, experimental measurements have shown that the typical eddy in this region is no larger than the grid spacing [56], so that the turbulence can be satisfactorily modeled as a sub-grid stress and only the mean resolved velocity distribution need be specified.

4.5 Errors and Mesh Refinement

In LES both modelling and discretisation errors (as opposed to just the discretisation errors in RANS) are dependent on the grid quality and spacing. Some of the generic discretisation errors have been touched upon briefly in previous sections (see sec.4.2.2). In the following sections we will look at these and other sources of error, how they affect LES and how this effect can be reduced through careful mesh generation and other measures.

4.5.1 Errors in LES

For the purposes of this discussion the sources of error present in an LES calculation have been divided into three categories. The first, **discretisation errors**, represents the errors inherent in the discretisation process. Most of these types of error are present in all finite volume CFD calculations, but some combine in unusual ways in LES, necessitating a more detailed description and investigation. For incompressible single-phase Newtonian LES calculations at moderate Reynolds numbers, **modelling errors** refer to inaccuracies in sub-grid scale turbulence prediction, wall treatments and boundary conditions. In combination these errors contribute significantly to the problem of near-wall treatment in LES and partially determine the meshing requirements of such calculations. At first glance, the filtering operation described in sec.3.1 appears straightforward and superficially similar to the equivalent RANS convolution. Large scales are resolved while small scales are modeled. The filtering operation can however introduce many more complications when the mesh size changes rapidly and/or the flow is poorly resolved. **Filtering errors** investigates some of these issues.

These categories mentioned above are somewhat artificial and by no means exhaustive. There can be considerable overlap between the various mechanisms, but this framework nonetheless provides a convenient way for studying and comparing their relative influences.

Discretisation Errors

Discretisation errors in the current context result mainly from two sources: the first is the validity of the assumption that dependent variables vary linearly across control volumes; in other words, the truncation error associated with the second order approximation of temporal and spatial variations. The second group of discretisation errors is a direct result of poor mesh quality. Chief among these are non-orthogonality and skewness errors.

In Reynolds-averaged calculations, where the ensemble averaged flow field is simulated and structures in the flow are of the order of the integral length scale, increasing the resolution of the computational grid will monotonically improve the approximation of the “true” solution. In LES this is not necessarily the case. The commonly employed implicit filtering technique, where the smallest scales of motion are omitted purely by the computational grid’s inability to properly resolve them, does not guarantee that the smallest resolved scales will be well resolved. On the contrary, it is generally accepted that they will be poorly resolved [49] with this technique. Thus, gradients associated with near-grid scales will be inaccurately computed and increasing grid resolution will only expose smaller scales to this inaccuracy while the cutoff is in the inertial range. Although the error for near-grid scales has been shown to remain more or less constant for different mesh densities [49], the improved resolution of larger scales does reduce the overall numerical error. Unfortunately, another important aspect of LES exhibits identical grid-dependent behaviour: the SGS turbulence model. It has been suggested [50] that the effect of the error in the discretisation of the smallest resolved scales is of the order of (and may exceed) the influence of the modeled sub-grid stresses. Since all turbulent LES calculations rely heavily on the SGS model as a sink for turbulent energy, inaccuracies at this level could adversely affect the solution. A possible solution is to employ an explicit convolution filter larger than the nominal grid spacing as displayed in fig.4.10 [53]. Decoupling the LES filter from the grid spacing means the smallest unfiltered eddies can be well resolved greatly improving the accuracy of these scales. Unfortunately such a scheme has several requirements that makes it less than ideal for implementation in a general unstructured CFD code. Firstly, increasing the filter size beyond that of the local grid spacing requires explicit filtering, *i.e.* some weighted averaging of neighbouring cell

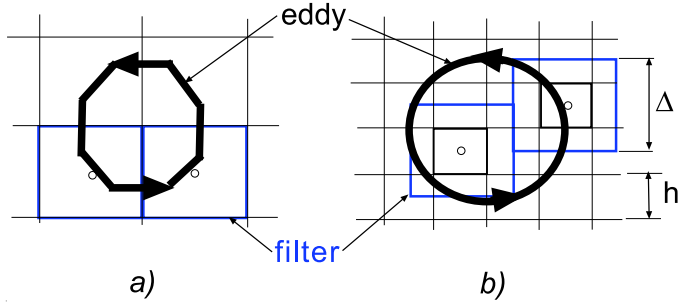


Figure 4.10: The effect of top-hat filter size on smallest eddies a) Implicit filter b) Explicit filter $\Delta = 2h$.

values, that can be costly and cumbersome. Secondly, increasing the filter size relative to the cell size, means that either a) the grid spacing must be reduced to maintain a constant smallest resolved scale which increases cost, or b) the size of the smallest resolved scale will increase (decreasing accuracy). Whether an optimum increase in filter vs. mesh scale exists that will produce improved accuracy over an equal-cost implicit filter calculation is uncertain, further muddying the resolution of this issue. Fortunately, experience has shown that the effect of discretisation error in the smallest scales does not in general result in dissipation or dispersion errors that overwhelm the modeled contributions [119]. Still, this is an inconsistency in the LES approach that should be noted, especially as methodologies are refined and greater accuracy and reliability is sought.

The influence of mesh non-orthogonality on the solution procedure was described in sec.4.2.2. It was also noted that an excessive non-orthogonal contribution can lead to unboundedness that will cause the solution procedure to fail. Thus while the formal accuracy of the non-orthogonal component is second order, in practice the magnitude of the term must sometimes be limited to prevent unbounded behaviour. In this investigation limiting of the component (if necessary) is performed such that the magnitude of the non-orthogonal contribution does not exceed a specified fraction of the principal orthogonal contribution (see eq.4.22).

$$\mathbf{A} \cdot (\nabla \phi)_f = D_d + \min(1, C_{lim}) D_\Delta \quad (4.91)$$

$$C_{lim} = \alpha_{lim} |D_d| / [(1 - \alpha_{lim}) |D_\Delta|] \quad (4.92)$$

where D_d and D_Δ are the orthogonal and non-orthogonal contributions respectively:

$$D_d = |\mathbf{A}_d| \frac{\phi_N - \phi_P}{|\mathbf{d}|} \quad (4.93)$$

$$D_\Delta = \mathbf{A}_\Delta \cdot (\nabla \phi)_f \quad (4.94)$$

The limiter is controlled by the coefficient α_{lim} , which can have a value between 0 and 1. A value of 0 switches the non-orthogonal contribution off; when set to 1 the full non-orthogonal components is applied, while a value of 0.5 results in a limiter such that the non-orthogonal contribution does not exceed the orthogonal part. Depending on the amount of limiting employed this action of course reduces the strict accuracy of the solution to between first and second order. The limiter was however found to improve the stability of the solution on meshes with high non-orthgonality and is thus a necessary compromise. Throughout this investigation an attempt is made to minimize non-orthgonality in the computational grid. A limiter of $\alpha_{lim} = 0.5$ is non-the-less employed for those instances where high non-orthogonality does occur. Since the general quality of the meshes are very good however, the impact of the associated reduced accuracy will be localised and of limited impact.

Skewness error is another numerical diffusion-type error that reduces accuracy, decreases solution stability and can distort turbulence dynamics in its vicinity. Fig.4.11 can be used to explain the origin and nature of the problem.

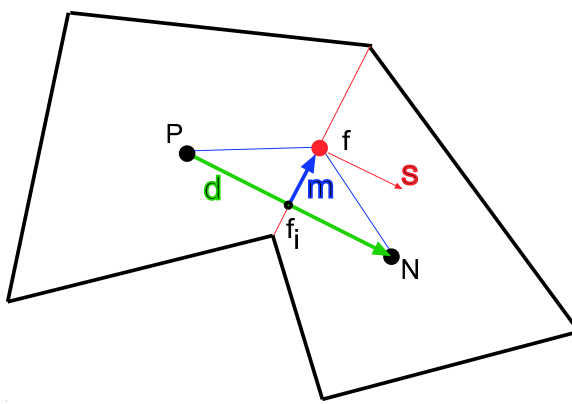


Figure 4.11: Face skewness error.

Simply put, the skewness error arises when the vector, \mathbf{d} connecting two adjacent cell centres does not pass through the centre of their communal face. Under such conditions,

4. Computational Methodology

face values based on linear interpolations no longer accurately represent the value at the face centre, which effectively reduces the accuracy to first order. For the convection term, this results in a diffusion-like truncation error [66]:

$$E_{skew} = \sum_f \mathbf{A} \cdot (\bar{\mathbf{u}} \delta\phi)_f, \quad (4.95)$$

where

$$\delta\phi_f = \phi_f - \phi_{fi} = \mathbf{m} \cdot (\nabla\phi)_f, \quad (4.96)$$

$$\mathbf{m} = \mathbf{x}_f - \mathbf{x}_{fi}, \quad (4.97)$$

allowing E_{skew} to be transformed into,

$$\begin{aligned} E_{skew} &= \sum_f \mathbf{A} \cdot [\bar{\mathbf{u}}_f \mathbf{m} \cdot (\nabla\phi)_f] \\ &= \nabla \cdot (\bar{\mathbf{u}}_f \mathbf{m} \cdot \nabla\phi). \end{aligned} \quad (4.98)$$

As in the case of mesh non-orthogonality, the skewness error predicted by eq.4.98 can be removed using the face interpolate of the cell centred gradient $(\nabla\phi)_P$. This however, increases the size of the computational molecule and can potentially cause unboundedness. As the skew correction contribution grows, this occurrence becomes more likely, making highly skewed meshes very undesirable.

The non-orthogonality and skewness errors emphasise the importance of mesh quality in LES, especially since the non-dissipative convection schemes that have to be employed to maintain resolved turbulence in themselves do not guarantee boundedness. In addition to the formal definitions, experience has repeatedly and unequivocally shown that meshes with a large amounts of skewness and non-orthogonality are certain to produce unstable simulations and unphysical numerical artefacts due to the unboundedness of the correction terms or the lack thereof.

Modelling Errors

As stated previously modelling errors include inaccuracies in the sub-grid scale model. These inaccuracies, as pertains to the various sub-grid implementations, were discussed

in Chapter 3 with reference to the properties of turbulent flows put forward in Chapter 2. It remains only to emphasise their effect on flows of practical interest.

Most successful sub-grid models constitute a form of feedback that will increase sub-grid dissipation in response to elevated resolved turbulent motion. Provided this feedback causes dissipation of turbulence at approximately the right overall level and all other factors being equal, the LES prediction tends to fairly be accurate. Since the contribution of the LES model decreases with increased grid density, the errors produced by the model can be decreased to arbitrarily small values simply by refining the mesh. Under adverse conditions the mesh required to minimise the error can become unrealistically fine, making the calculation prohibitively expensive. Some of the chief phenomena contributing to the breakdown of the basic modelling strategies are strong sub-grid scale anisotropy, backscatter, non-equilibrium and specific properties of near-wall flows. Each of these issues has been addressed earlier to some extent, but a modelling strategy that brings all these approaches together in a cost-effective way still proves elusive. While such an approach will not be pursued in this project, some of the difficulties inherent therein can be outlined, as they have bearing on problems encountered during the course of this investigation.

- **Sub-grid anisotropy:** At the base of the majority of the current generation of finite volume SGS models lies the assumption of sub-grid scale isotropy, *i.e.* that the turbulent motions smaller than a filter cutoff in the inertial range are spatially symmetric. While this is the case for the ideal situation of homogeneous decaying turbulence, the same does not generally hold true for complex flows like shear layers and more acutely, boundary layers. The affects of approximating the SGS tensor as a combination of the resolved rate of strain and a scalar turbulent viscosity can have serious negative effects on the resolved scale motion. In a boundary layer, for instance, SGS motion principally acts to increase mixing in the wall normal direction. Applying the isotropic assumption to this situation causes increased damping of larger scale spanwise motions necessary to maintain the near-wall cycle. As shown in sec.2.3.2 such damping can have a deleterious effect on the entire boundary layer's dynamics. The most promising solution to this problem is to employ a second mo-

4. Computational Methodology

ment closure SGS model, such as that of Deardorff (sec.3.2.2), to directly calculate the SGS forces. Such models are somewhat more expensive and have seen little testing in complicated and taxing engineering environments. Although validations done to date have shown clear advantages in using the stress closure approach [44], these have been too small to warrant wholesale adoption of the method. Future developments of LES methodology will almost certainly revisit this approach, as it addresses some fundamental issues and provides capabilities not present in more basic models.

- **Backscatter:** The common label for the transfer of turbulent energy from the SGS to the resolved scale (see also sec.3.3.4), ‘backscatter’ is a known physical phenomenon and its inclusion in some form generally improves LES predictions. This inverse transfer is thought to be small however, and some studies have shown only marginal improvements when the phenomenon is explicitly modeled [139]. This small perceived influence and uncertainties relating to the backscatter timescale have kept backscatter model implementation from consideration in this investigation.
- **Non-equilibrium:** Although non-equilibrium effects have a limited impact on all GS-SGS turbulent energy transfers the effect is greatest at locations of turbulent transition and large-scale turbulence generation. Here the resolved scale pre-turbulent motion might have finite values while SGS turbulence is small or non-existent (if the resolved flow is laminar and unsteady). In effect, the turbulent cascade has not yet had enough time to fill the inertial and dissipative ranges with energy from the resolved motions. Algebraic models like the Smagorinsky model cannot distinguish between equilibrium and non-equilibrium turbulence and as a result will apply excessive damping to transitional structures. In practice, this can prevent transition from laminar to turbulent flow [128]. An improvement of the zero-equation concept, SGS transport equations (like those employed during this investigation) do consider non-equilibrium effects through the modelling of a continuous SGS quantity (*e.g.* K , $\tilde{\nu}$) . Although this class of models performs well under non-equilibrium large-scale turbulence production conditions, the source terms can-

not normally distinguish between stresses derived from turbulent fluctuations and those derived from steady velocity gradients. The result is that even laminar flows will evoke a SGS response that will render predictions of laminar portions of the flow inaccurate and unphysically damp pre-turbulent oscillations, possibly delaying transition. Dynamic models (sec.3.2.4) perform much better in transitional flows because the SGS coefficients are determined by the resolved fluctuations. Conversely, they will have trouble with some large scale turbulent production events where the resolved scales are filled with energy but the sub-grid scales have not yet had enough time to reach equilibrium. Although this effect will be short-lived due to the small timescales associated with the SGS eddies, a better solution is probably a dynamic SGS transport equation which incorporates the best aspects of both approaches [105].

- **Near-wall treatment:** LES wall treatments and their characteristics have been extensively discussed in previous chapters (see sec.3.3 and 4.3). Most SGS models perform reasonably well in the near-wall region, provided mesh resolution is adequate [44]. For the high Reynolds number flows simulated during this investigation such resolutions would be prohibitively expensive. The response of SGS models given under-resolved boundary layers thus becomes important. Critically, the larger near-wall scales rarely bear much resemblance to the smallest energetic eddies (sec.2.5). This poses a particular problem for dynamic models, which derive SGS properties from the resolved scale. The small scales also have a large degree of anisotropy, further complicating the issue. Finally, the mean velocity gradients deviate so far from linearity that a wall function-type approach is necessitated for coarse near-wall meshes. It is generally accepted that none of the currently available near-wall treatment/SGS model combinations can accurately model the diversity of practical boundary layer flows on under-resolved meshes [6, 24, 112, 116, 128]. It is therefore important that the limitations of the model be understood and strategies to minimise the impact on the overall solution are formulated.

Viewing the one-equation SGS turbulent energy and Spalart-Allmaras DES models

4. Computational Methodology

in the context of the above modelling deficiencies provides additional motivation for the practices employed in this investigation. Although neither of the implemented models include explicit consideration for anisotropy, the RANS type near-wall approach inherent in DES neatly excises the problematic near-wall region from the LES portion of the calculation. Where a RANS type near-wall treatment is not tractable, the mesh needs be refined to provide a well-resolved boundary layer. The problem of SGS anisotropy, while still present, is thus partially alleviated since the near-wall region is either treated in a Reynolds averaged fashion (in which case resolved scales are less pronounced) or well resolved. Backscatter is disregarded in the current implementation owing to its uncertain (typically small) influence and physical characteristics. Both models employed include transport equations for SGS quantities (K , $\tilde{\nu}$), so non-equilibrium effects are handled appropriately provided they are not transitional in nature. Laminar flows cannot be treated accurately with the current versions of these models and should be avoided if possible. The DES approach and the inclusion of wall functions address some of the problems associated with under-resolved boundary layers: in RANS mode the models are tuned to produce the correct wall shear for fine wall-normal grid spacing. When the wall-normal spacing becomes large, wall functions are employed to produce at least an approximate boundary condition. Whenever the RANS portion of the DES approach is invoked, boundary layer vortices will be damped and the near-wall calculation will necessarily become less accurate. As such the DES approach is best employed where the near-wall region is not the dominant source of turbulence production.

Filtering Errors

There are two sources of error termed filtering errors, because of their relation to the filtering process used to derive the LES equations. The first is connected to the way in which the filter truncates the smallest scales and is known as the “aliasing error”. The second is the product of grid/filter inhomogeneity and is termed the “commutation error”.

To understand the source of the aliasing error consider again fig.3.2. The implicit top-hat filter used for the current finite volume approach exactly matches the control volume of the cell. The filter is thus expressed as a spatial average over the volume of the cell.

While the boundaries of this averaging volume are sharply defined in physical space, the same is not true for wave-space. With reference to fig.3.2b, it can be seen that the top-hat filter differentially affects many frequencies above and below the cutoff wavenumber. Thus, high frequency scales smaller than the filter size can and will exist in an LES using a filter that is not sharp in Fourier-space. In addition, some frequencies larger than the grid scale will also be poorly resolved because of discretisation errors. Coupled with the non-linear term in the momentum equation and the discrete nature of the grid, under-resolved eddies pose a particular problem: they can appear in wavespace as fluctuations of lower frequency than should be allowed by their length scales. Effectively this will manifest itself as a displacement of energy to wavenumbers larger than the nominal cut-off wavenumber. Under conditions where a considerable portion of turbulent energy is contained in the smallest resolved scales, this irregularity can prove particularly disruptive through an increase in turbulent dissipation. Aliasing errors most strongly affect dynamic-type models which rely heavily on the smallest scales to determine SGS properties [47]. The error can be countered by employing specially designed explicit filters [153] similar to those proposed in sec.4.5.1 to aggressively damp out wavelengths below the cutoff. SGS transport models suffer less inaccuracy from aliasing errors than dynamic models and since filtering is quite costly and complicated on unstructured meshes it will not be pursued at this stage.

Unless the filter size is constant, the filtering operation defined in eq.3.2 does not necessarily commute with differentiation, *i.e.* $\overline{\frac{\partial \phi}{\partial x}} \neq \frac{\partial \bar{\phi}}{\partial x}$. Specifically, when the local mesh size changes due to geometric and physical considerations and the implicit top-hat filter is used with its size tied strictly to the local cell dimensions, then the non-commutation of the filter should introduce extra terms into the LES equations. Neglecting these terms produces a truncation error that is generally known as a “commutation error”.

We can illustrate the origin of the commutation error by examining a filtering operation applied to a simple one-dimensional curve. Figure 4.12 displays such a curve, in this case a parabolic profile defined by:

$$\phi = 1 - x^2, \quad (4.99)$$

$$\frac{\partial \phi}{\partial x} = -2x. \quad (4.100)$$

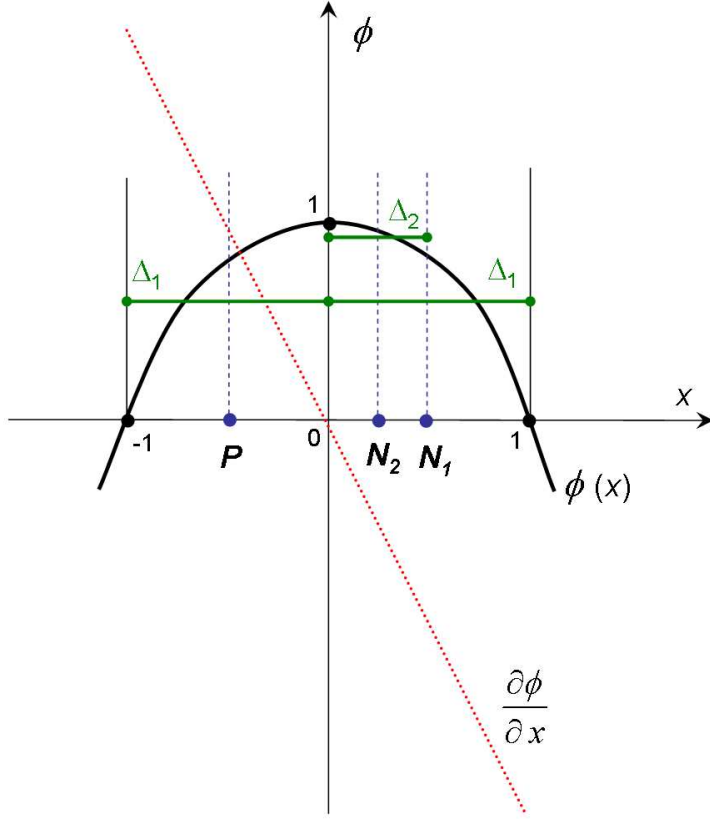


Figure 4.12: Filtering of a parabolic function.

First filter the function ϕ around points P and N_1 using a symmetric top-hat filter, Δ_1 , of magnitude 1:

$$\bar{\phi}_P = \frac{1}{|\Delta_1|} \int_{-1}^0 \phi dx = \frac{2}{3}, \quad (4.101)$$

$$\bar{\phi}_{N_1} = \frac{1}{|\Delta_1|} \int_0^1 \phi dx = \frac{2}{3}. \quad (4.102)$$

Now consider the filtered gradient of ϕ and the gradient of $\bar{\phi}$ at $x = 0$, the location where the filter kernels for the two points meet:

$$\left(\frac{\partial \phi}{\partial x} \right)_0 = \frac{1}{|\Delta_1|} \int_{-0.5}^{0.5} -2x dx = 0, \quad (4.103)$$

$$\left(\frac{\partial \bar{\phi}}{\partial x} \right)_0 = \frac{\bar{\phi}_{N_1} - \bar{\phi}_P}{x_{N_1} - x_P} = 0. \quad (4.104)$$

For the constant filter size, the derivatives are equal and the filtering operation can be seen to commute with differentiation. If however, the filter size is not constant, a different

picture emerges. With reference to fig.4.12, replace point N_1 with N_2 and employ a smaller filter Δ_2 with a magnitude of 0.5 around N_2 .

$$\bar{\phi}_{N_2} = \frac{1}{|\Delta_2|} \int_0^{0.5} \phi dx = \frac{11}{12}, \quad (4.105)$$

$$\left(\frac{\partial \bar{\phi}}{\partial x} \right)_0 = \frac{\bar{\phi}_{N_2} - \bar{\phi}_P}{x_{N_2} - x_P} = \frac{1}{6}. \quad (4.106)$$

The fact that the gradient in eq.4.106 is no longer equal to that calculated from eq.4.103 means that the non-constant filter does not commute with differentiation. (Note that for this case, a symmetric filter will always produce $\left(\frac{\partial \bar{\phi}}{\partial x} \right) = 0$ irrespective of its size.) The error introduced due to non-constant filter width is thus:

$$\left[\frac{\partial \phi}{\partial x} \right]_{err} = \overline{\frac{\partial \phi}{\partial x}} - \frac{\partial \bar{\phi}}{\partial x} \quad (4.107)$$

On a regular mesh on which the cell size changes slowly and smoothly in space, the commutation error will thus tend to zero. However, at domain boundaries and in areas of abrupt grid refinement its influence can rival the modeled SGS force [161]. Both instances are depicted in fig.4.13. In well resolved boundary layers the no-slip momentum boundary condition specifies the wall velocity as exactly zero. For this specification to be a valid filtered quantity, the filter volume at the wall must also be zero; otherwise an average over the adjacent fluid volume will produce a non-zero velocity at the boundary. The filter size should thus change from some finite value to zero between the first off-the-wall cell and the wall. Although the exact effects have not been quantified, this has been shown to produce significant errors [12] that may rival the SGS Reynolds stress in magnitude. Fortunately, the primary calculations performed during this investigation employ DES modelling which uses a Reynolds Averaged formulation in the near-wall region. Since the RANS methodology does not use spatial filtering for averaging it avoids this particular issue.

The commutation error associated with mesh refinement boundaries cannot be so easily avoided since the phenomenon can occur anywhere in the domain. Yet local mesh refinement is a crucial cost-saving strategy for LES. Since explicit filters have been ruled out for the current investigation, recent work in deriving commutative filters for complex geometries [161] is of limited utility. Lacking more detailed knowledge of the effect of the

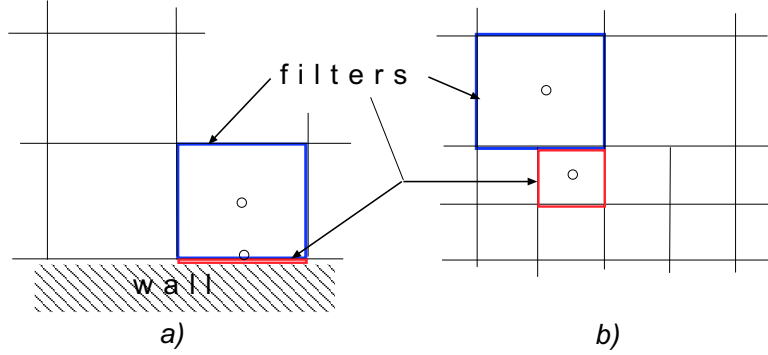


Figure 4.13: Change in filter size at a) the wall b) sudden mesh refinement.

commutation errors, the only viable option is to adopt a meshing strategy that places refinement boundaries away from flow regions of critical importance. In so doing, we assume that the primary influence of the error will be local to the vicinity of the mesh refinement, with limited transport of its influence away from such zones. It is very difficult to prove such an assertion, but it is not unreasonable, given that this influence is thought to be of the order of the SGS stress (which is small and local).

Sudden refinement and the change in the filter size has an additional effect on the SGS model and the LES solution. When the fluid moves from a coarse mesh region to a finer mesh region, or vice versa, an unphysical non-equilibrium state will exist for finite levels of resolved and unresolved turbulence. Eddies advected from a coarse to a finer mesh will be better resolved on the finer grid, but since the SGS turbulent length scale is directly related to the cell and thus the filter size, there will be a sudden decrease in the SGS viscosity. In other words, the SGS and resolved scale turbulent content will change comparatively slowly while the SGS length-scale will change near instantaneously. Moving from a fine to a coarse mesh will produce its own difficulties: scales too fine to resolve on the coarse mesh, instead of being translated to SGS energy, will express themselves as strong aliasing errors when transported onto the coarse grid. The sudden increase in filter scale will again impact the transported SGS quantity negatively, by producing too much SGS turbulent viscosity in the larger cells. These effects can be seen clearly in fig.4.14 and will introduce additional inaccuracies in the calculation.

Although the LES filter width cannot be altered without explicit filtering or changing

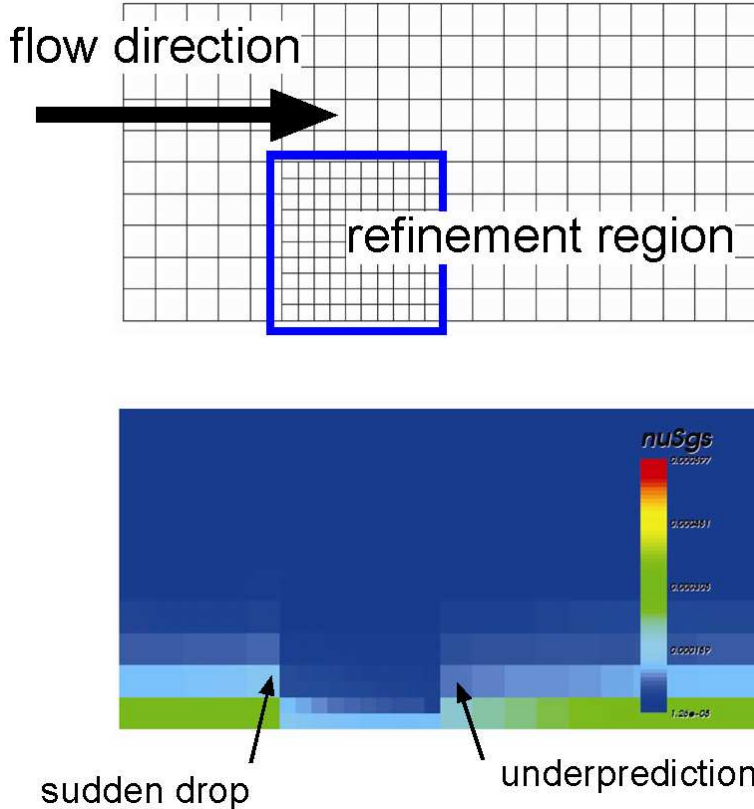


Figure 4.14: Effect of local refinement on transported SGS properties.

the grid size, the SGS turbulent length scale Δ , can. In this investigation, smoothing the distribution of the SGS turbulent length scale near grid refinement boundaries is used to alleviate some of the problems associated with these features. Instead of allowing the SGS length scale to follow the filter scale exactly, Δ is smoothed using a biased wave scheme. This scheme smoothes the distribution by increasing the SGS length scale of cells that neighbour larger control volumes, so that the value of Δ can never be smaller than the cell derived one. This produces the length-scale to mesh distribution depicted in fig.4.15.

The gradient of the smoothed distribution is fixed by an adjustable coefficient, $C_{\Delta S}$.

$$\Delta_P = \max(\Delta_P, \Delta_N/C_{\Delta S}) \quad (4.108)$$

Ideally, for sudden refinement, the smoothed length scale should have a gradient that allows the grid-scale turbulence to populate smaller resolved scales with turbulent energy at the same rate at which the SGS turbulent energy decreases. For a sudden increase

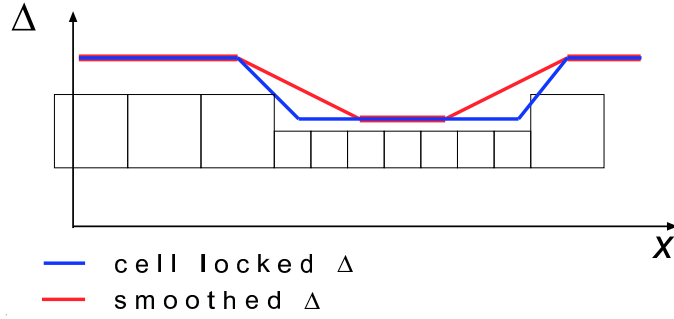


Figure 4.15: Distribution of a smoothed SGS turbulent length scale on a one-dimensional mesh.

in grid spacing, the SGS turbulent viscosity should evolve such that there is minimal discontinuity between the values in the smaller and larger cells. This elevated turbulent viscosity before sudden coarsening of the mesh, has the additional benefit of limiting aliasing and other dispersion errors through its increased viscous dissipation (which affects the smallest scales more strongly). In practice, the value of $C_{\Delta S} \approx 1.15$ is chosen so that equilibrium is reached over 4-5 cells from the refinement boundary [84]. The effect of Δ smoothing on the transported SGS viscosity in fig.4.16 is marked compared to the control case (fig.4.14).



Figure 4.16: Transported SGS viscosity in the presence of local refinement with turbulent length-scale smoothing.

As demonstrated, errors in CFD and specifically LES are pervasive. Fortunately, calculation techniques and models exist in LES that can reduce errors to insignificant

magnitudes. The main concern now becomes one of cost: what level of accuracy is affordable and what cost-benefit characteristics will different approaches have. There is seldom a “wrong” or “right” computational/modelling strategy in LES, only more or less cost-effective ones. In the methodologies outlined in this section, significant errors in some areas were sometimes accepted in favour of low cost and simplicity (*eg.* omission of explicit filter). Whether this approach is optimal is hard to determine without a project of much larger scope. Certainly, the results displayed in later sections of the thesis speak volumes about the general robustness of the LES approach.

4.5.2 Refinement Indicators

In sec.3.3.5 motivations for embedded mesh refinement were put forward, based on the disparity of turbulent scales and required accuracy in different parts of the problem domain. The difficult question is of course where to increase or decrease the cell density. Currently, the vast majority of mesh generation is done via trial and error, or based on past experience and a few general guidelines. Some solution-adaptive methods do exist, but a lack of generality and robustness has prevented widespread uptake. While an automatic mesh generation technique for LES is a very desirable goal and will surely be the object of future development, it is not within the scope of this project. Instead, some physical characteristics and indicators will be examined with an eye on providing guidelines for determining cell sizes in different parts of the domain.

Wall Treatment Requirements

The properties of boundary layers and the near-wall turbulence cycle were discussed in Chapter 2. Along with accuracy requirements and modelling restriction (Chapter 3) these place certain limits on the type of grid spacing that can be used to simulate a near-wall region in LES and DES.

For highly accurate well-resolved LES of boundary layers the need exists to capture nearly all scales of motion down to the wall. Experience has shown [44] that this requires very fine ($y_w^+ \approx 1 - 2$) wall-normal resolution to properly capture sweep-ejection events and strong non-linearities close to the boundary. We have also seen that the structures

4. Computational Methodology

that are critical to the dynamics of the near-wall turbulent cycle have larger but still comparatively small dimensions in the spanwise and streamwise directions ($z^+ \approx 20, x^+ \approx 30$ respectively). In addition, boundary layer theory indicates that the integral length-scale away from the wall (but still in the logarithmic region) scales as κy_w , giving another tool for determining mesh requirements inside boundary layers.

When the DES approach is being used adjacent to the wall, the low Reynolds number RANS turbulence models combined with rapidly changing gradients also require the wall normal spacing to be of the order of a single wall unit ($y_w^+ \approx 0.5 - 2$). Wall-tangential dimensions have to be a lot larger to ensure that the implicitly averaged mean cell value tends toward the URANS ensemble average, since small scale near-wall turbulence is modeled and should therefore not be resolved. Suggested dimension are of the order of 200-400 wall units in both the streamwise and spanwise directions [150], ensuring averaging over several of the low-speed streamwise streaks produced by the near-wall cycle.

Where the DES approach is being used and the prediction of wall shear is not critical to the solution, the wall normal spacing requirement can be relaxed and wall stress calculations replaced by a wall-function approximation. The continuous wall function employed during this investigation is fairly accurate in the viscous, buffer or logarithmic regions of the boundary layer ($y_0^+ \lesssim 300$). Beyond this point the accuracy of the wall function decreases as the influence of the wake region becomes more important. It should be noted that many of the wall function assumptions break down in high pressure gradient or non-equilibrium flows, implying that this method can only be used with any degree of confidence along a flat plate-type boundary layer.

Walls are of course not the only source of turbulence; free shear layers constitute an equally important site for turbulence production and interactions. Shear layers have the advantage over boundary layers that the turbulent eddies are not constrained by the wall so that a higher degree of scale similarity exists between the largest and smallest scales, thus improving modelling accuracy. The integral length scale is only dependent on the width of the shear layer, requiring considerably less resolution than energetic boundary layer eddies to capture. Unfortunately, shear layers are not fixed in space as boundary

layers tend to be. Additionally, their exact position can easily depend on the properties of the shear-layer itself, making *a priori* location of mesh refinement to improve shear-layer resolution more difficult. Fortunately, there are several flow properties that can be used to adjust the mesh for the presence of shear-layers via an iterative approach.

Error Estimation

Using traditional *a posteriori* error estimation techniques (Taylor series expansions, moment and residual estimates, *etc.*) with implicitly (and even explicitly) filtered LES flow fields is problematic. Firstly, LES solution fields are not smooth, finer scales are simply added as the resolution increases. Thus, there can be no concept of convergence of discretisation error as the mesh size decreases as the smallest scales will always be equally resolved (or under-resolved). Secondly, LES is intrinsically transient, making adaptive meshing very expensive even if the discretisation error could be sensibly evaluated on an instantaneous basis.

An alternative approach is to consider the long time mean of the LES solution to be equivalent to the ensemble average. This assumption will be valid for any statistically steady flow, including all the cases considered in this investigation. Error estimation applied to such fields will only detect “discretisation” errors of the time mean properties, so that modifications based on these estimates are applicable to all solution times. Through judicious averaging, mean errors in the transport of mean quantities such as velocity and SGS properties can be detected.

In the present study the residual error estimate [68] was adopted for use with the time mean LES field, both for its simplicity and good accuracy. The residual in this case is a function that measures how well the local solution satisfies the original governing equations. To explain how it is derived, consider the discrete one-dimensional representation of ϕ in fig.4.17. There are two ways to calculate the value of the function at the face between locations P and N .

The first, ϕ_f , is obtained through linear interpolation between points P and N (eqs.4.14

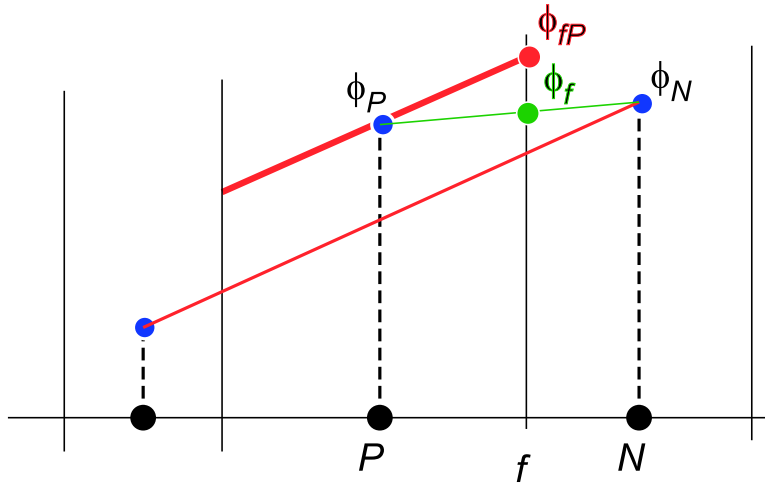


Figure 4.17: Discrepancy between the interpolated and extrapolated face values.

and 4.15),

$$\phi_f = f_x \phi_P + (1 - f_x) \phi_N \quad (4.109)$$

This is the method used to calculate face properties for finite volume discretisation.

For volume integrals, second order discretisation assumes a linear variation of the dependent variable, ϕ over the control volume P . This fixed gradient can be used in conjunction with the cell-centred value of ϕ_P to find the face value ϕ_{fP} (from eq.4.6),

$$\phi_{fP} = \phi_P - (\mathbf{x}_f - \mathbf{x}_P) \cdot \nabla \phi_P \quad (4.110)$$

$$(4.111)$$

While the interpolated face value along with the cell-centred volume integral satisfies the integral form of the governing equations, it is clear from fig.4.17 that the two approaches do not necessarily produce the same face values for ϕ .

If the interpolated face values and gradients in the generic steady-state transport equation (eq.4.5) are replaced by the face values calculated from the cell-centred value and gradient of ϕ , the magnitude of the inequality will be an indicator of the error due to the assumed piecewise linear distribution [66]. This inequality is known as the residual

error and for a single control volume it can be expressed as,

$$\begin{aligned} res_P(\phi) &= \int_{V_P} [\nabla \cdot (\mathbf{U}\phi) - \nabla \cdot (\Gamma_\phi \nabla \phi) - S_e - S_p \phi_P] dV \\ &= \sum_f \mathbf{S} \cdot \left[\mathbf{U}_f \phi_{fP} - (\Gamma_\phi)_f (\nabla \phi)_P \right] - S_e V_P - S_p \phi_P V_P \end{aligned} \quad (4.112)$$

Replacing \mathbf{U} , Γ_ϕ and ϕ with their time-averaged counterparts allows application of the method to the mean LES fields. As a consequence of the temporal averaging all indicated errors will pertain only to mean properties and gradients and errors in the temporal discretisation will be neglected. Errors in cyclical or intermittent phenomena are thus unlikely to be detected by this method when contrasted with more permanent flow features.

Turbulence Indicators

One of the main premises of SGS modelling is that the cutoff between the resolved and unresolved scales falls in the inertial range of turbulent length scales. The scales smaller than the cutoff are assumed to be somewhat universal in character and amenable to approximation. Whether this assertion is true or not depends partially on the local flow characteristics, but largely on whether the grid is fine enough to resolve the eddies above the inertial range. *A priori* knowledge of what this length scale is at any given location in space outside of a boundary layer is a matter of guess work and experience. However, given an approximate LES solution it should be feasible, at least in theory, to make an estimate of the largest length scales in the inertial range.

The most straightforward way to achieve this is to extract a turbulent energy spectrum from the time history of the flow, by performing a Fourier transform of the resolved and SGS turbulent energy recorded over a long time period. When this spectrum is displayed on a logarithmic plot of turbulent energy versus wavenumber, the extent of the inertial range can be identified via inspection from its characteristic slope (eq.2.1),

$$\mathbb{E}(k) = C_k \epsilon^{2/3} k^{-5/3},$$

However, not all flow regimes produce this behaviour: boundary layer and transitional flows have completely different spectral characteristics and low Reynolds number flows may simply not contain enough scales for such a range to be distinguishable. These

4. Computational Methodology

problems aside, such a method would be far too resource intensive to offer a practical indicator of mesh quality.

As an alternative, assumptions of isotropy can be used to derive a relation for an idealised turbulent spectrum, from which an estimate for the length scale of the inertial range can then be obtained. Such an assumed spectrum is provided by Von Kármán's interpolation formula [175] which can be used in conjunction with some mean flow properties to derive the length scales associated with the inertial range. The Von Kármán formula describes the turbulent spectrum from the largest scale vortices to the inertial subrange where it reduces to the Kolmogorov spectrum,

$$\mathbf{E}(k, t) = \frac{55}{9} \frac{\Gamma\left(\frac{5}{6}, k\right)}{\sqrt{\pi} \Gamma\left(\frac{1}{3}, k\right)} \frac{u'^2}{k_e} \frac{\left(\frac{k}{k_e}\right)^4}{\left[1 + \left(\frac{k}{k_e}\right)^2\right]^{\frac{17}{6}}}, \quad (4.113)$$

Here k_e is the wavenumber characteristic of the energy containing eddies which is given by

$$k_e = \frac{0.51}{\alpha} \frac{\epsilon}{u'^3}, \quad (4.114)$$

with α Heisenberg's constant bracketed in the range $0.20 \rightarrow 0.62$ by experimental investigations, while the mean turbulent dissipation ϵ and turbulence intensity

$$u' = \sqrt{2(K_{resolved} + K_{sgs})} \quad (4.115)$$

can be derived from the LES solution (Chapter 3). Since the inertial subrange is known to have a slope proportional to $k^{-5/3}$ and the Kármán distribution has a predictable shape that includes the $k^{-5/3}$ slope, the wavenumber at which the equilibrium range begins can be detected by searching for this feature. Given the wavenumber a length can be derived using Taylor's frozen turbulence hypothesis so that the length scale of the largest eddies in the inertial subrange can be found from [73]:

$$\Delta_i = \frac{\sqrt{2}}{\pi k_i}, \quad (4.116)$$

where k_i is the wavenumber associated with the inertial subrange. As emphasised in sec.4.5.1, the mesh must be considerably (about 4-8 times) finer than a particular eddy

size to properly resolve that scale. Initial investigations using the assumed spectrum to derive the inertial length scale have shown some promise, but the surfeit of assumptions, variable constants and uncertainty surrounding the mesh spacing/length scale relationship means that the method in its current form lacks robust predictive capabilities.

A simpler approach is to assume similarity of the turbulent spectral distributions throughout the solution domain. Although this does not give the length scale of inertial range eddies in absolute terms, it does allow the ratio of resolved to unresolved turbulence to be used as a relative indicator of mesh quality. We define the resolution indicator, M such that

$$\langle M \rangle = \frac{\langle K_{sgs} \rangle}{\langle K_{resolved} + K_{sgs} \rangle} \quad (4.117)$$

where the angled brackets denote long time averaging. Thus M can vary between 0 and 1, with a value of $M = 0$ indicating DNS and $M = 1$ indicating steady state resolved flow with all turbulence being modeled. Refining the mesh will mean more energy in the resolved scales and thus a smaller value of M and conversely a coarser mesh should produce larger values. By fixing a target value for M , the mesh resolution can now be varied so that the fraction of unresolved to total turbulent energy is constant throughout the domain. Consistent use of such an approach, aside from spatially homogenising modelling accuracy, would result in much less subjectivity when comparing LES results from different meshes and make LES in general more complete by removing the unpredictable dependency of solutions on mesh spacing from the comparison.

Few methodologies in LES are without some drawbacks and the method described above is no exception. The spectral characteristics of laminar, transitional and near-wall flows are markedly different from the typical turbulent energy distribution. This makes the use of eq.4.117 uncertain and even untenable in the case of laminar regions. Even more importantly, the DES approach described in sec.3.3.3 depends explicitly on employing RANS type turbulence modelling near the wall. Such regions will always have very high percentages of modeled turbulence irrespective of mesh resolution. Additionally, masking RANS zones from the adaptive refinement procedure is difficult because the transition from RANS modeled turbulence levels to LES levels is not sharp but rather smeared over an indeterminate region. Despite these difficulties, the turbulent fraction indicator should

4. Computational Methodology

still provides a useful tool for assessing relative grid density requirements in a wide range of flows with practical interest.

It is evident that there is as yet no foolproof way of efficiently and automatically prescribing mesh density for all LES and DES calculations. Neither are the approaches described here all-inclusive: the Courant number, for instance, places a limit on the minimum cell size that may be used in conjunction with a specific timestep due to stability concerns. Experience remains an important factor in mesh construction even though the indicators described in this section provide some guidelines with which to perform this task. In the next chapter several of these practices are put to the test and the applicability of different modelling approaches evaluated.

Chapter 5

Basic Test Cases

In this chapter two relatively simple flows are used to test the implementation of the current LES approach: a plane channel flow and an asymmetric plane diffuser. The channel case demonstrates the basic accuracy and validity of the LES implementation, while the diffuser introduces more demanding flow regimes to the computation. The comparatively low Reynolds numbers allow good resolution of the boundary layer and the lack of gross flow obstacles ensures large scale shedding and the associated shear layers will not be present. Thus, in general, these cases cannot be used to validate outer layer matching approaches. Even the most demanding high Reynolds number calculations may however have regions of embedded refinement where a flow feature of particular importance is intermediately-well to well-resolved. Assessing accuracy under these conditions is thus of some importance, a task that the diffuser case with its incipient separation and weak shear layer is well suited to. Furthermore, starting with less costly calculations allows familiarisation with the myriad unique issues and peculiarities related to LES calculation without risking the considerable waste of time associated with failed high Re LES calculations.

5.1 Plane Channel Flow

LES of fully developed turbulent flow in a plane channel at $Re_\tau = 395$ ($Re_\tau = hu_\tau/\nu$, $u_\tau = \sqrt{\tau_w/\rho}$, h channel half height) is considered first. The influences of the different near-wall

5. Basic Test Cases

viscosity treatments from the previous section are compared and the basic implementation of the LES code tested. Next, a study of the effects of grid density on the LES results is performed and aspects of the wall function approach are evaluated.

5.1.1 Computational Setup and Reference Details

The case chosen for the initial testing of numerical and model implementations, the plane channel flow shown in fig.5.1, consists of two infinite parallel plates bordering an equilibrium turbulent flow. To approximate this configuration, a finite sub-domain of the channel is taken and periodic boundaries are applied in the streamwise and spanwise directions. These boundaries should be placed sufficiently far apart, that the largest eddy structures in the flow fit comfortably within the resulting domain. Given a channel with height $2h$, the general consensus seems to be that adequate overall dimensions of the computational domain should be about $2\pi h \times 2h \times \frac{3}{2}\pi h$ [10, 20, 126, 136] in the streamwise, wall normal and spanwise directions respectively. However, following encouraging results by Fureby *et al.* [44] using a minimal channel approach at the same Reynolds number, a somewhat smaller computational domain was chosen ($4h \times 2h \times 2h$) to minimise computational cost. As will be seen later, although the domain length is too short to incorporate the longest streamwise structures, it performs more than adequately when compared to DNS results.

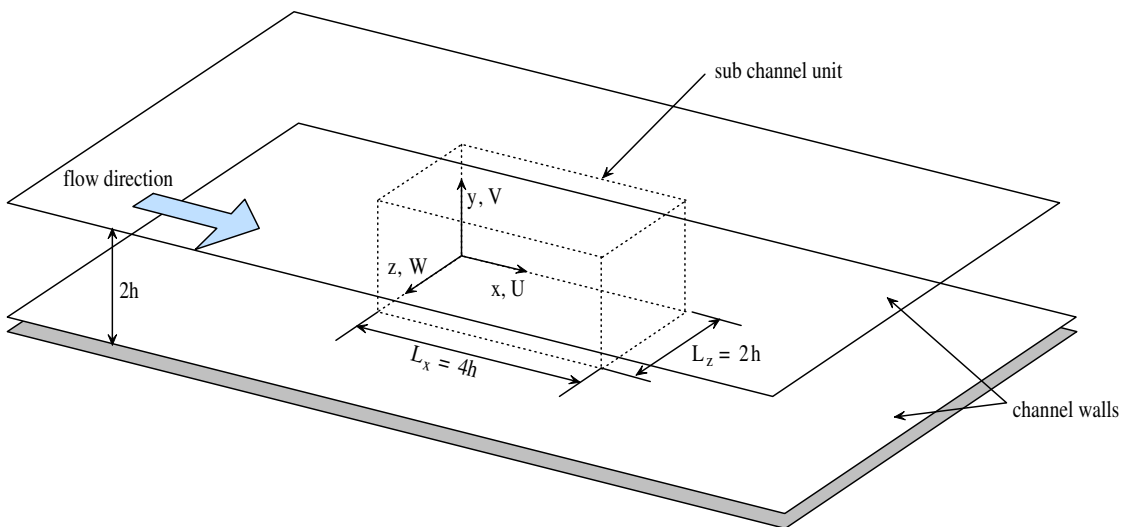


Figure 5.1: Schematic representation of the problem domain for the channel flow simulations.

The LES channel flows shown in this report are all compared to DNS simulations performed by Kim *et al.* [82] at a friction Reynolds number of $Re_\tau = 395$. The DNS simulation has the following properties: $U_b = 0.1335m/s$, $\nu = 2e - 5m^2/s$, $L_x = 4\pi h$ and $L_z = 2\pi h$ and the results can be considered an exact solution of the Navier-Stokes equations for purposes of the present comparison. To ensure consistency, the streamwise bulk velocity, U_b , through the channel is adjusted to be equal to the average DNS value by varying an imposed streamwise constant pressure gradient, $\partial P/\partial x$. The time averaged value of this quantity is equivalent to the mean wall shear stress and can be compared to the corresponding DNS value. Once a statistically steady state is reached, averaging is performed over a time interval of $50h/u_\tau$ (about 200 flow-through times), followed by a combined streamwise and spanwise averaging over the entire channel. Profiles were generally found to be symmetric to within 0.5%, which indicates that the time averaging is sufficient for a statistically representative sample.

5.1.2 Channel Flow Initialization

In the absence of free-shear layers and shedding phenomena, the near-wall cycle as detailed in sec.2.3, is the only source of fluid turbulence in a flow. This near-wall turbulence cycle is naturally initiated through a process of transition, that comes about as a result of the growth of small initial perturbations or imperfections on the wall boundary. The channels simulated during this investigation have no such initial perturbations, very little imperfections to introduce them and thus require some form of artificial perturbation to initiate the process.

Typically, a supercritical laminar channel flow (*i.e.* with Re in or above the transition range) on a regular block-structured mesh takes many flow-through times before perturbations produced by numerical noise and/or round off errors finally trigger the transition to the turbulent regime. This is very costly and should be avoided. Early tests showed that simply adding perturbations to the domain in the form of random noise was ineffective: the random velocity components have no structure and do not obey continuity and as a result are rapidly damped by the pressure equation. What is thus required is a method that can create initial structured vortical motions that preferably have the

5. Basic Test Cases

proper statistical characteristics. Some candidates include Fourier-based decomposition coupled with stochastic variation of statistical elements, wavelet approaches and structure functions [32, 155]. A much simpler solution can however be derived from sec.2.3.1. Recall that the near-wall turbulent cycle creates and is in turn regenerated by long sinuous streamwise streaks of lifted low-speed fluid right next to the wall. This implies that if these streaks can be recreated artificially, their interaction with the mean shear should cause linear instabilities. The instabilities in turn will produce vortices and shear layers, ultimately kick-starting the entire near-wall cycle. The flow is initialised using a laminar parabolic profile (logarithmic initial profiles were found to result in a subsequent large scale motion of fluid away from the wall, which decreases the effectiveness of the imposed perturbations). Near-wall parallel streaks of slow and faster moving fluid are produced by modifying this base parabolic flow, U_0^+ by means of eq.2.13,

$$U^+(x^+, y^+) = U_0^+(y^+) + (\Delta u_0^+/2) \cos(b^+ z^+) (y^+/30) \exp(-C_1 y^{+2} + 0.5), \\ V^+ = W^+ = 0.$$

These streaks of themselves will not cause instability and need to be perturbed slightly to give them the wavy character that in turn will produce streamwise vortices. This is achieved by a second relation, eq.2.15 that introduces a spanwise velocity component normal to the streaks.

$$w(x^+, y^+) = c_\epsilon \sin(a^+ x^+) y^+ \exp(-c_\sigma y^{+2}), \\ u = v = 0.$$

The constants, b^+ and a^+ in these two relations are chosen to produce a sparse streak spacing ($z^+ \approx 200$), equivalent to the buffer layer in wall normal extent ($y^+ = 30$) and with a maximum intensity of about 10% of the bulk fluid velocity. The wavenumber imposed through the spanwise perturbations produces approximately three such undulations within the extent of the domain. The result of this initialisation can be seen in fig.5.2, which depicts the contours of streamwise and spanwise velocity on a plane at $y^+ = 20$.

The solution of the plane channel will now rapidly become turbulent as the sinuous streaks induce vortex formation and further instability. This is depicted in fig.5.3 by

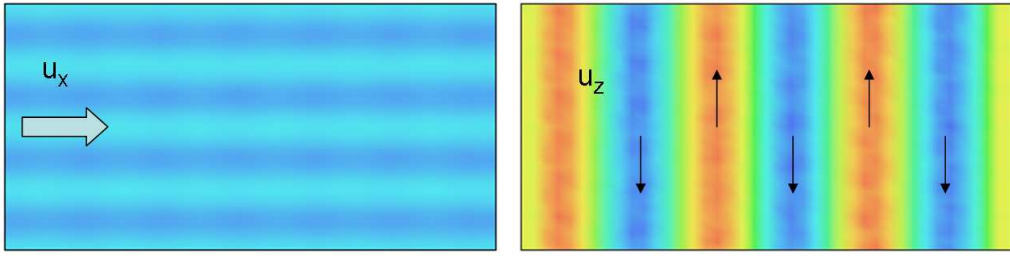


Figure 5.2: Initial velocity magnitude contours for a steady bulk channel flow with an imposed perturbation scheme, $y^+ = 20$. Streamwise velocity (left) and spanwise velocity (right)

several snapshots of the flow at representative times after the introduction of the perturbations. The realizations on the left hand side of the figure show velocity contours at $y^+ = 20$. In the right hand plots the most energetic vortical structures coinciding with this distribution are depicted by the isosurface of the vortex indicator function, \mathbb{Q} (eq.2.4). Time is normalised by the bulk timescale t^* which is equivalent to a flow-through time of the domain,

$$t^* = L_x/U_b, \quad (5.1)$$

where U_b is the mean bulk velocity and L_x is the size of the domain in the streamwise direction.

After a single flow-through time ($t/t^* = 1$) the influence of the spanwise perturbations on the streamwise streaks has produced strong oscillations in the base flow. The overlying vortices induced by this pattern link up to form a very regular, diamond grid-like distribution. The solution at this stage is still very regular and a predictable result of the initial conditions. After about two and a half flow through times the flow is rapidly starting to become chaotic. The initial streaks, while still discernible, are displaying a marked jaggedness: bifurcations in the low velocity fluid occur with seeming randomness and unpredictable sweep events produce localised pockets of high velocity fluid. This degeneration is mirrored in the overlying vortex structures which are clearly losing the cohesion seen at earlier times. At six flow-through times the flow is completely turbulent. Mixing and vortex formation is still considerably more vigorous than in an equilibrium channel because of the larger velocities at the centre of the domain. The parabolic velocity profile

5. Basic Test Cases

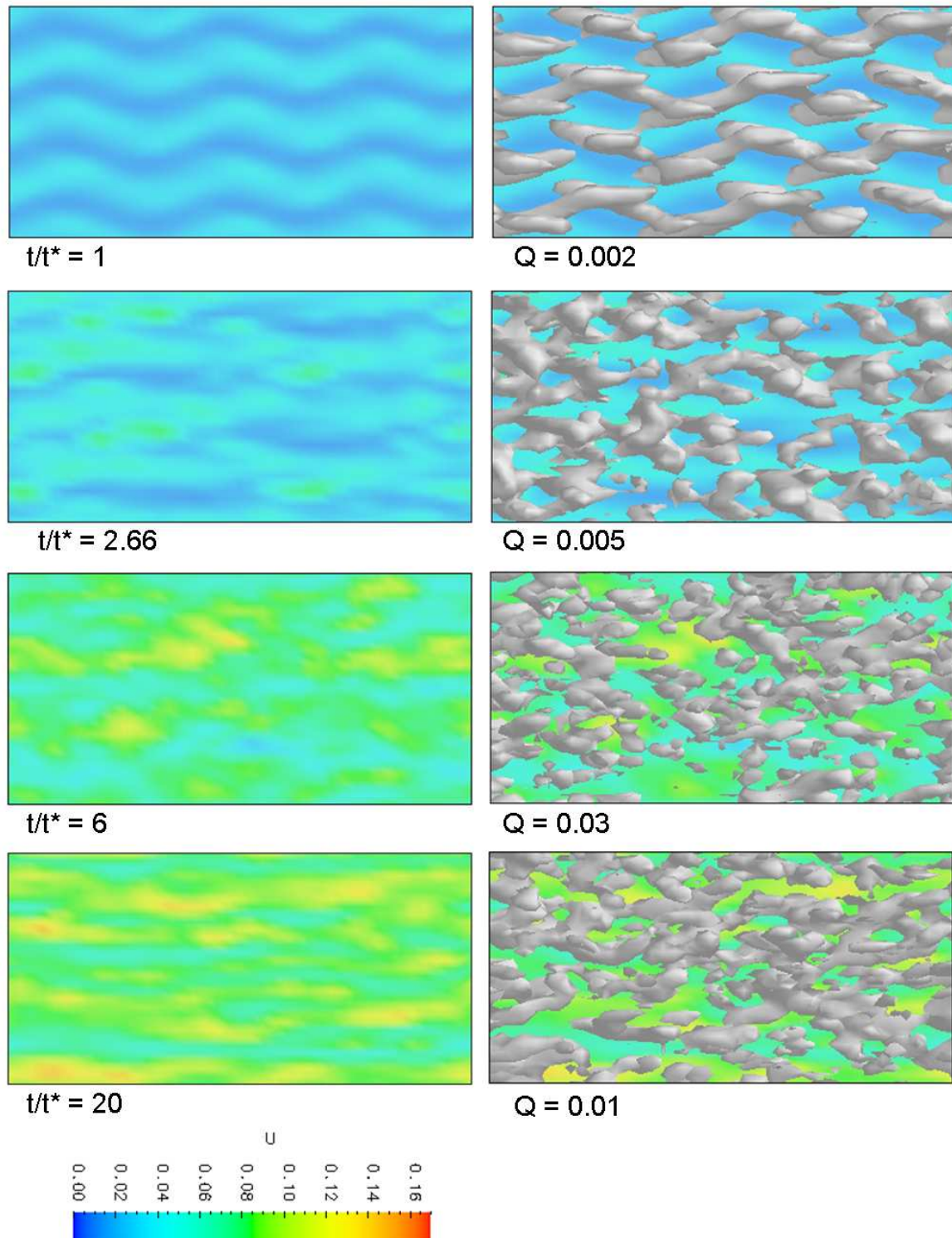


Figure 5.3: Transition to turbulence: Velocity magnitude and vortex cores in a plane channel at different times after imposed perturbations, $y^+ = 20$.

contains considerably more kinetic energy than a turbulent profile of equivalent volume flux and this surplus energy must be dissipated or redistributed before equilibrium can be reached. Streaks are clearly present, but they are far removed from the smooth undulating structures typical of fully developed boundary layers. The rough fragmented appearance of the near-wall velocity distribution is a direct result of the energetic large scale mixing that is predominant in the flow at this stage. The last picture in the series shows the boundary layer at near-equilibrium conditions. Redistribution of the mean velocity profile is more-or-less complete and all the features of a typical wall layer are present: long undulating streaks with a spacing of approximately one hundred wall units and the overlying streamwise vortices that are produced by the streaks and in turn regenerate them. The near-wall turbulence cycle is in progress.

Overall, the transition to turbulence occurs fairly rapidly: initial vortical structures induced by the specified flow grow in strength along with small quasi-random perturbations. The growth of the perturbations eventually causes the first vortices to break up asymmetrically. Once the regular vortex pairing is broken, non-linear effects allow turbulent mixing (and vortex formation) rates to grow successively faster. Turbulence production and therefore momentum transfer continue to increase until the parabolic profile has been eroded. Equilibrium, corresponding to the logarithmic velocity distribution, is subsequently established at less energetic levels.

5.1.3 Model Comparison

Computations were conducted using the SGS turbulent energy model with 1a) no wall treatment, 1b) Van Driest damping and 1c) the Wolfshtein wall treatment and 2) with the standard Spalart-Allmaras DES model. A mesh with the resolution to perform LES of the turbulent structures in the buffer layer was constructed, by grading it towards the walls. The approximate wall-parallel dimensions of these structures can be ascertained from turbulent dynamics described in sec.2.3, resulting in cells with dimensions, $\Delta x^+ = 35$, $\Delta z^+ = 20$ and $\Delta y^+ \in [2, 20]$ geometrically graded towards the wall. The mesh contains $45 \times 100 \times 40 = 180000$ cells.

Figure 5.4(top) shows profiles of the total shear stress, T_{xy} and the sub-grid scale

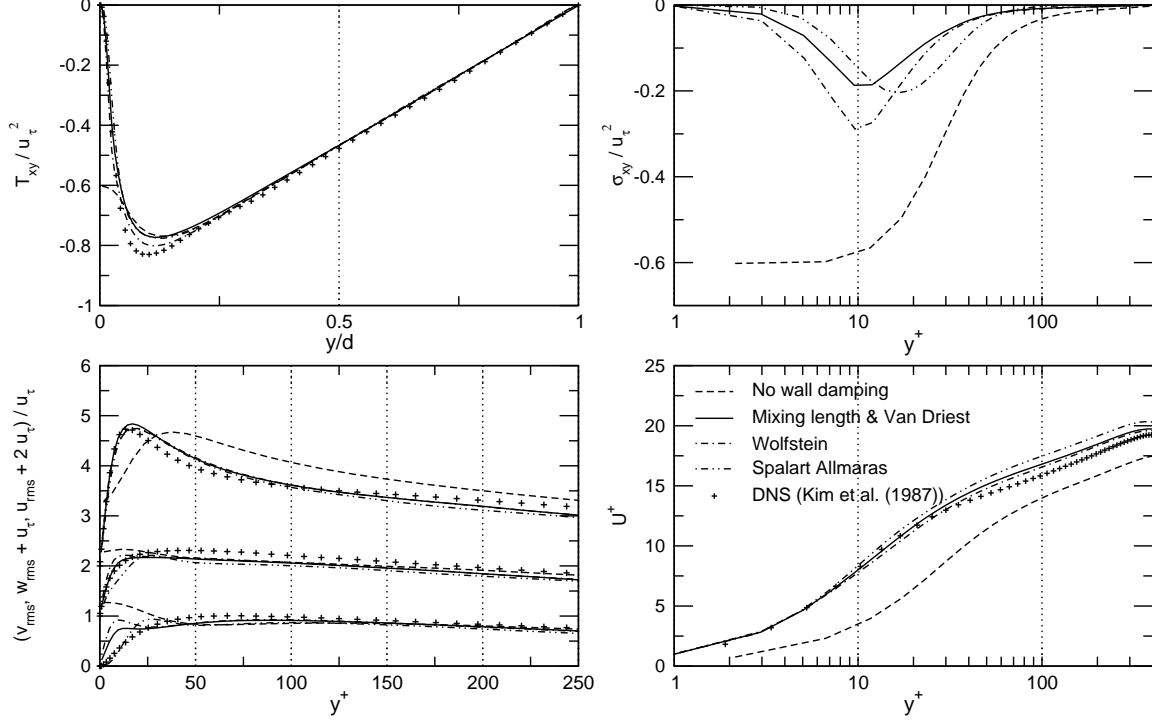


Figure 5.4: Total Reynolds shear stress (top left), T_{xy} , SGS shear stress, σ_{xy} (top right), square root of the second order velocity moments T_{xx} , T_{yy} and T_{zz} (bottom left), resolvable streamwise velocity U_b normalised by the shear velocity (bottom right); for the various near-wall turbulence treatments.

component of the shear stress, σ_{xy} . At $Re_\tau = 395$, the resolved fraction of the flow is dominant over the SGS contribution in the wake, so there is little difference between the wall treatment approaches in this region. In the near-wall viscous and buffer regions, the differences are slightly more pronounced: the treatments that incorporate wall distance effects show fair agreement with each other and the DNS data, in that the turbulent contribution tends to zero at the wall and the peak values occur at approximately the same wall-relative displacement. Wolfshtein's model gives fractionally better results than the S-A and Van Driest models, probably due to a better specification of the near-wall dissipation length scale. As expected, the lack of wall damping in the case without a wall model causes severe near-wall deviations in the simulation. This is primarily caused

by the SGS turbulent viscosity contribution, which does not tend to zero as the wall is approached, but remains more or less constant owing to the finite turbulent length scale derived from the mesh spacing. Turbulence intensities are investigated by examining the individual components of the total stress tensor $\mathbf{T} = \langle (\bar{\mathbf{u}} - \langle \bar{\mathbf{u}} \rangle) \times (\bar{\mathbf{u}} - \langle \bar{\mathbf{u}} \rangle) \rangle$, shown in fig.5.4 bottom left. Only minor differences between the wall-damped models are apparent for the streamwise component, u_{rms} , with Wolfshtein's model displaying fractionally better peak intensity agreement than the other two. Again, the undamped case shows significant deviation from the DNS, with elevated values of u_{rms} in the core of the flow. Levels are under-predicted near the wall because of the unphysical damping of the resolved motions by the high SGS viscosity. All the predictions for the spanwise turbulent energy component, w_{rms} , in the core are similar and slightly below the DNS values. Some differences become apparent near the wall. The elevated predictions in the undamped case (for both the spanwise and wall-normal components) is mostly due to the erroneous SGS behaviour. The other two SGS energy models perform significantly better, while the S-A model shows a slight under-prediction, which corresponds to a shift in the peak SGS energy contribution away from the wall. The shortcomings of assuming isotropy of the SGS turbulence near the wall is apparent in the wall normal stresses, v_{rms} , the deviation of which from the DNS data is primarily due to the SGS contribution. The effect is not as pronounced for the S-A model, but it also under predicts the SGS contribution for the other shear and normal stresses in this region. The comparison of mean streamwise velocity (fig.5.4 bottom right) most clearly shows the effect of neglecting the damping effects of the wall on the modeled turbulence length scale. The large near-wall SGS turbulent viscosities predicted by this approach produce a velocity profile, which while superficially resembling the classical boundary layer distribution, is in fact shifted a considerable distance away from the wall (in wall units). These findings are in agreement with results of Baggett [8] for RANS-based near-wall models: although the usual streaks and streamwise vortices in the buffer layer are damped by the excessive modeled viscosity, similar structures are spontaneously generated farther from the wall. This creates a kind of “super” buffer layer, with characteristics of much lower Re flow. The damped one-equation models predict the wall-shear much better, albeit with slightly elevated velocity distributions in

5. Basic Test Cases

the logarithmic region. The Wolfshtein model again shows the closest agreement with the DNS data.

Wall Model	C_f/C_{f0}
None	1.28
Van Driest	0.96
Wolfshtein	0.98
S-A DES	0.88

Table 5.1: Relative wall shear stresses for different near-wall turbulence treatments

A comparison of mean wall shear stress relative to the DNS value, C_{f0} , which was derived from the time-mean value of the driving pressure gradient, can be seen in table 5.1. The undamped simulation performs badly, as expected and the inappropriateness of the S-A DES model for attached eddy dominated flows is confirmed by its under prediction of the mean wall shear. Both wall-damped SGS energy calculations perform similarly. As a result, only Wolfshtein's approach, which was generally the more accurate of the two, is employed for the study of resolution effects in the next section.

5.1.4 Mesh Resolution

The effects of progressively coarser meshes on turbulent statistics and eddy structure in channel flows are investigated in this section. Again, the $Re_\tau = 395$ DNS results of Kim *et al.* [82] are used for comparison. The results on under resolved meshes in channel flows are useful in determining the limit of resolution requirements necessary to produce reasonable LES simulations of the boundary layer and in particular the streak instability cycle in the buffer layer. For this purpose, six different meshes are constructed for the domain described in sec.5.1.1. Their characteristics are summarised in table 5.2 with dimensions based on the DNS friction velocity.

Calculations are performed using the Wolfshtein near-wall SGS treatment and other parameters are identical to those described in secs.5.1.1 and 5.1.3.

A comparison of time mean LES results for the total Reynolds shear stress, T_{xy} and

Case no.	Δx^+	Δz^+	Δy^+	Cell count, N_c
1	35	20	$\in [2, 20]$	180 000
2	39.5	26.3	$\in [4, 40]$	60 000
3	52.7	40	15.8	30 000
4	79	52.7	26.3	9 000
5	105.3	79	39.5	3 000
6	158	158	79	500

Table 5.2: Channel flow mesh densities, varying wall normal spacings are graded toward the wall.

Resolution	y_0^+	C_f/C_{f0}
$45 \times 100 \times 40$	1	0.98
$40 \times 50 \times 30$	1.8	0.93
$30 \times 50 \times 20$	7.9	0.90
$20 \times 30 \times 15$	13.2	0.88
$15 \times 20 \times 10$	19.8	0.86
$10 \times 10 \times 5$	39.5	0.33

Table 5.3: Relative wall shear stresses for different mesh resolutions

5. Basic Test Cases

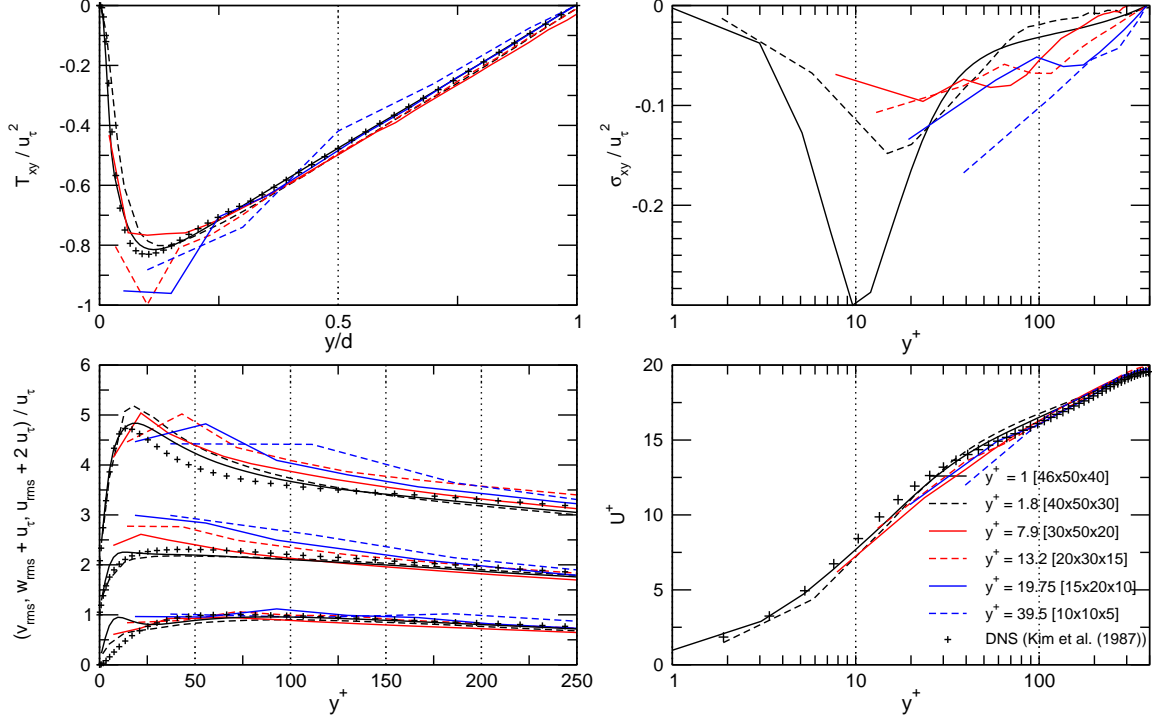


Figure 5.5: Total Reynolds shear stress, T_{xy} (top left); SGS shear stress, σ_{xy} (top right); square root of the second order velocity moments T_{xx} , T_{yy} and T_{zz} (bottom left); resolvable streamwise velocity U_b , normalised by the DNS shear velocity (bottom right) for the various channel flow mesh densities.

the sub-grid scale shear stress contribution, σ_{xy} are shown in the top two graphs of fig.5.5. The three finest meshes compare relatively well with the DNS data, with progressively coarser meshes producing correspondingly worse results. The coarsest meshes significantly over-predict both the near-wall shear and normal stresses (fig.5.5 bottom left). This effect is consistent with published results for under-resolved meshes, and is primarily due to excessive resolved scale motion. Similar to the undamped case in the previous section (where excessive turbulent viscosity damps the near-wall eddies), coarse near-wall meshes are incapable of carrying the fine near-wall turbulence producing features. Some of these structures are, however, spontaneously reproduced on a larger scale as a kind of pseudo turbulence, which corresponds to the increased grid spacing. The increase in scale

also necessitates a movement of eddy foci further from the surface, as indicated by the peak values of the streamwise turbulence intensity, u_{rms} (fig.5.5, bottom left). In terms of overall stress predictions, most of the cases do a fairly adequate job of representing these quantities in the core section of the flow. The notable exception is the coarsest mesh [$10 \times 10 \times 5$], which produces incorrect trends and severely displaced peaks in the shear and normal stress distributions respectively. Although this mesh is clearly far too coarse for adequate LES, it should also be noted that this is also the only case where the wall-adjacent cells fail to even partially resolve the near-wall turbulence cycle as defined in sec.2.3, (for which the limit was set at $\Delta y^+ \approx 60$ [76]). The turbulence dynamics thus produced probably differs significantly from the known system, contributing to the observed deviations. All the cases show relatively good agreement with the DNS data for the resolvable mean streamwise velocity, U_x in the core region of the channel, with increasing over predictions for coarser meshes (fig.5.5, bottom right). This is not really surprising, considering that all the simulations shared the same bulk velocity and were normalised by the same value of u_τ . The viscous and especially the buffer region exhibit consistent under prediction compared to the DNS. Again, this deviation tends to increase with a reduction in mesh resolution. This trend is tied to the rate of momentum transfer from the core to the wall, which decreases in concert with the mean wall shear shown in table 5.3. As can be seen, the agreement of the LES wall shear with DNS decreases more or less monotonically with resolution. The exception being the coarsest mesh case, which probably fails to capture essential turbulent features, and therefore completely misrepresents the wall shear. It should also be noted that all the results shown to date are either forms of inner layer (the two finest meshes) or intermediate matching (the rest) with no structural support. As such, the decrease in accuracy is to be expected, since Wolfshtein's model is not designed to act in this regime.

Figure 5.6 shows the effects of mesh resolution on the instantaneous near-wall structures. The left-hand column depicts the lifted low velocity streaks as contours of the velocity magnitude in the near-wall cells, while the right-hand column shows the overlying vortex structures near the surface. On the finest mesh, fig.5.6(a), the undulating streaky structures conform to known configurations, with a spanwise spacing of $\Delta z^+ \approx 100 \sim 110$

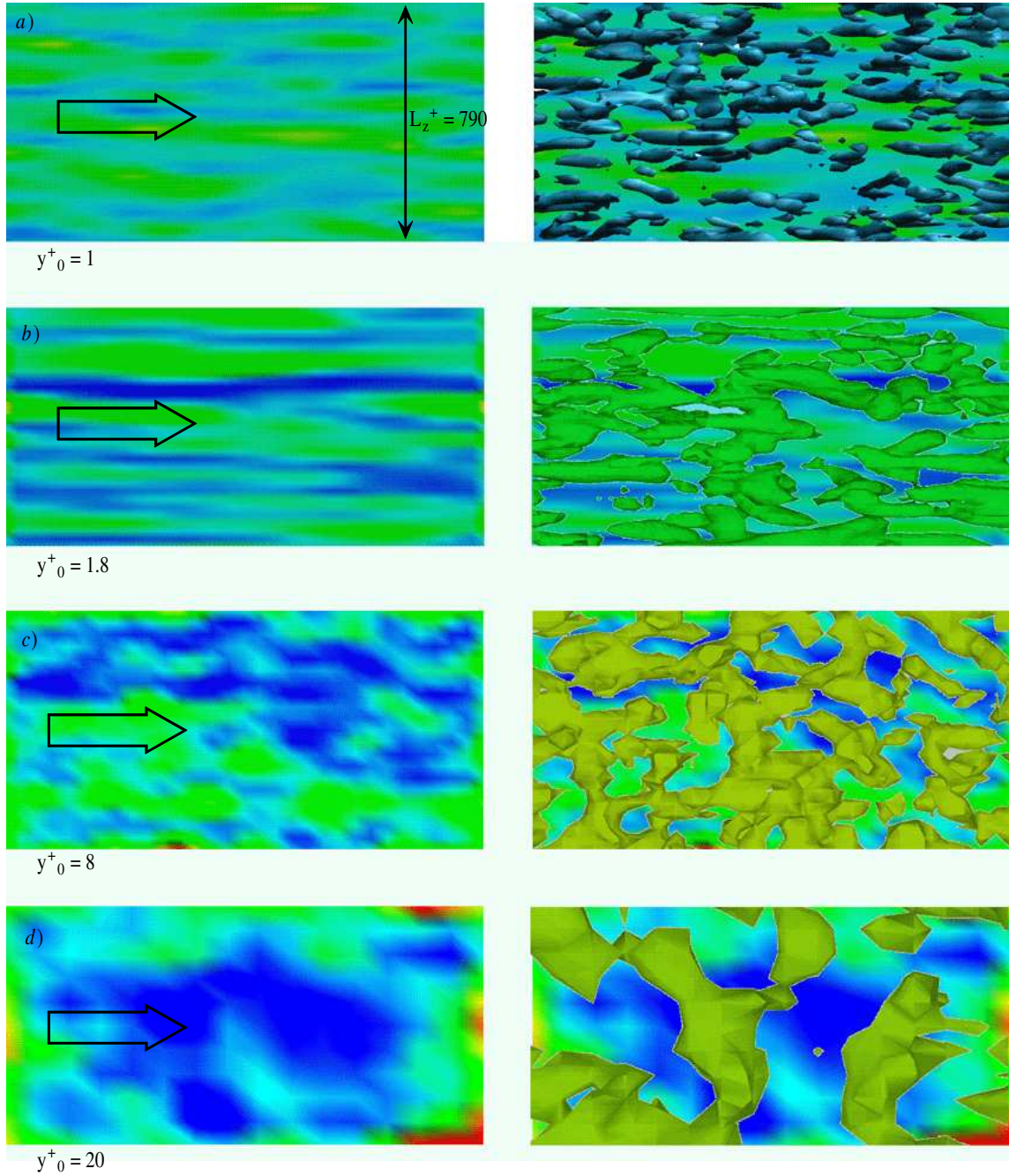


Figure 5.6: Low velocity near-wall streaks depicted by contours of the velocity magnitude, with blue indicating troughs (left) and attendant vortex structures visualised through the the second invariant of the velocity gradient tensor, $\mathbb{Q} > 0$ (right), for different mesh densities. From top to bottom: a) $46 \times 100 \times 40$, b) $40 \times 50 \times 30$, c) $30 \times 50 \times 20$, d) $15 \times 20 \times 10$.

and streamwise lengths of $\Delta x^+ \in [1000, 1600]$. It is also apparent, from the fact that some of the streaks traverse the entire domain, that the streamwise dimension of the calculation is somewhat too short to contain them. The effects of this on the overall solution is difficult to quantify, but can ultimately assumed to be small considering the accuracy of the simulation. The isosurfaces depicting vortex cores are constrained by the need to remove inertial layer and wake structures from the visualisation. As a result, they are somewhat condensed, showing only the “strongest” regions of the eddies. The remaining vortex portions nevertheless show good agreement with expected distributions and orientations: the streamwise vortices are seen to consistently form on the flanks of the lifted streaks, and some of them “curl” across the tops of the low velocity ribbons, as predicted by streak-instability cycle theory [137]. The second finest mesh (fig.5.6(b)) shows similar streak distributions to the first case. Undulations are somewhat less pronounced and the streaks tend to straddle the calculation domain more frequently. This can be ascribed to the 25% reduction in spanwise resolution, but the fact that the figure represents an instantaneous realization makes this somewhat uncertain. The near-wall vortex structures for this case also occur along the streak flanks, but are somewhat more widely spaced, with larger dimensions than for the finest mesh. Also apparent is a slight increase of the preponderance of spanwise-aligned structures, a feature which becomes more pronounced as the mesh coarsens. Although streak-like structures are still evident in the third velocity magnitude plot (fig.5.6(c)), they have become very erratic and seem to break into shorter sections with large cross-stream components. In addition, their spanwise spacing has significantly increased to $\Delta z^+ \approx 160$. The attendant vortices, show a marked increase in spanwise orientations, partly due to corresponding streak direction, but also due to increased cross-streak curvature of the eddies. The wall-adjacent cell for this mesh has normal dimensions of $\Delta y^+ = 16$, which implies that it only partially resolves the layer where the low-speed streaks would normally occur, leading to the observed deviations. The final plot has a resolution in the wall-adjacent cell of only $\Delta x^+ = 105; \Delta y^+ = 40; \Delta z^+ = 80$. This is far too coarse to resolve the streaks and the overlaying streamwise vortices, as is clear from the velocity magnitude contours in fig.5.6(d). The domain size is also too small to allow the realization of larger pseudo-streak structures. Although the overlying vortices

5. Basic Test Cases

still seem to form predominantly on the sides of low velocity regions, this correlation has become quite tenuous. The eddies have also lost their predominantly streamwise orientation, more closely resembling the spanwise wake structures than those normally found near the wall. Overall it appears that reproducing a reasonable near-wall turbulence cycle through the use of inner layer matching requires wall-adjacent cells with dimensions of at least $\Delta x^+ \lesssim 60 \sim 80$; $\Delta y^+ \lesssim 10$; $\Delta z^+ \lesssim 30$. Resolutions much coarser than this start to influence the eddy dynamics in unphysical ways, by forcing more of the turbulent energy into larger scale structures, so that the resolved motions resemble those from lower Reynolds number flows. In addition, these structures are not connected to the wall via the correct dynamics, contributing to the inaccuracy of wall shear stress prediction.

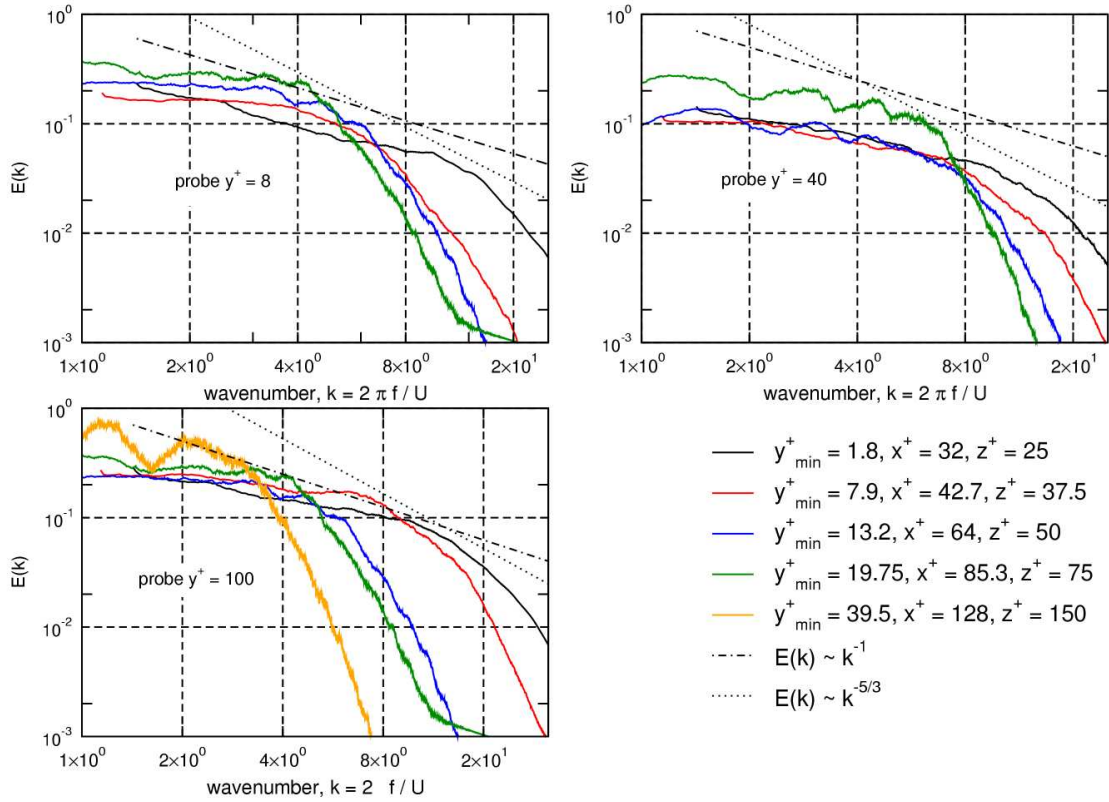


Figure 5.7: Spectrum of the total resolved turbulent energy at different wall normal displacements: $y^+ = 8$ in the viscous layer (top left); $y^+ = 40$ in the buffer layer (top right); $y^+ = 100$ in the logarithmic region (bottom right).

By looking at the energy spectrum of the resolved fluctuations (fig.5.7) a better idea of the effect of the different resolutions on the frequency range and scales of the energy containing eddies can be obtained. The plots are a one-dimensional spectral representation of the turbulent kinetic energy at different points in the flow, corresponding to y^+ values of 8 in the viscous sub-layer, 40 in the buffer layer and 100 in the logarithmic region. The different coloured lines represent the varying resolution, with black being the well resolved case. The dotted line is the $k^{-5/3}$ power curve, which corresponds to the gradient of the inertial range, while the dot-dashed line represents the k^{-1} curve associated with the inverse energy cascade. It is clear that more of the turbulent energy is expressed as larger lower frequency eddies as the wall and general mesh resolution coarsens. The right energy content seems to be approximately maintained for the better resolved cases, especially in the core flow. The coarsest meshes, on the other hand, tend to over-compensate for their lack of resolution with excessive energy contained in the large scales. This is consistent with the vortex visualisations of fig.5.6 and points toward insufficient turbulent dissipation and thus inaccurate SGS turbulent viscosity prediction for coarse resolutions. None of the profiles exhibit a well developed inertial range, mostly because the measuring points are not in regions where isotropic turbulence dominates. Some of the spectra in the viscous and buffer regions do however tend toward the predicted k^{-1} slope, with good agreement found for the three finer cases. This seems to indicate adequate resolution in this area. The fact that the coarser meshes don't reproduce this range very well is in line with the experienced drop in accuracy, which reflects directly on the rate of momentum and energy transfer carried by the resolved eddies of the inverse cascade. Other minor deviations can be ascribed to the fact that, in general, only the streamwise fluctuation component and the co-spectrum of the shear stress, $\mathbb{E}_{12}(k_1)$, display a strong k^{-1} spectrum [75].

An identical mesh density study conducted for the Spalart-Allmaras model produced quite different results (see table 5.4). The model is tuned for DES-type meshes which cannot resolve the smallest scales of motion near the wall and its complex terms produce unexpected behaviour on meshes that do not conform to the DES requirements. It is thus not surprising that the S-A model performs poorly on well resolved LES meshes compared

Resolution $N_{cx} \times N_{cy} \times N_{cz}$	y_0^+	C_f/C_{f0}
$45 \times 100 \times 40$	1	0.88
$40 \times 50 \times 30$	1.8	0.85
$30 \times 50 \times 20$	7.9	0.91
$20 \times 30 \times 15$	13.2	0.80
$15 \times 20 \times 10$	19.8	0.87
$10 \times 10 \times 5$	39.5	0.91

Table 5.4: Relative wall shear stresses for Spalart-Allmaras DES model on different mesh resolutions

to the one-equation eddy viscosity model. What is surprising is that the model produces better wall shear predictions at coarser resolutions. This may be purely fortuitous as the results do not show any identifiable trends. In fact, the coarsest two meshes in this series do not support any resolved scale turbulence at all, operating purely in RANS mode with all resolved structures damped by the high turbulent viscosity. It is encouraging however that no matter what the resolution the results do not deviate to far from the target value. Despite its unpredictability and lack of accuracy when used for well resolved LES the S-A model has a relatively low variance (compared to the K equation) over a range of mesh sizes, making it a viable choice when a robust wall model is required.

5.1.5 Summary

Simulations of the plane channel flow have provided validation for two different SGS models with different wall treatment approaches. The SGS turbulent energy model with either Van Driest damping or with an adaptation of Wolfshtein's mixing length near-wall treatment, both provide excellent agreement with DNS results. The bad performance of the case lacking a near-wall treatment, showed the necessity for some kind of modelling adaptation in this region if DNS-like resolution is to be avoided. As expected, the Spalart-Allmaras DES model, which is primarily configured for outside layer matching, does not

perform as well as the other models on the fine mesh.

The calculation of the same channel, but with successively coarser mesh resolutions, has provided insight into the effects of grid density on turbulent flow statistics and structural dynamics. The limit of the grid size necessary to support the correct near-wall turbulent cycle was approximately determined and the effects of and errors attributed to under-resolution were examined. Wolfshtein's approach was shown to produce fairly accurate average results even on very coarse meshes, as long as reasonable resolution is maintained in the viscous and buffer regions ($\Delta^+ \lesssim 40$). Finally, it was found that the use of the wall function at small wall-normal displacements has a much smaller influence on the overall results than the mesh density.

5.2 Asymmetric Plane Diffuser

Although a well resolved simulation of the asymmetric diffuser is certainly possible, it would still be comparatively costly. Given that the validity of the methodology has been established, this section will rather focus on the simulation of the test case using sub-optimal mesh resolutions. Conceptually the exercise is similar to the calculations performed with the varying mesh densities on the channel, but somewhat more challenging flow features, in the form of incipient separation and reattachment, will be under scrutiny.

The first simulations conducted were two-dimensional Reynolds Average calculations, which serve to highlight the advantages of LES over said methods and incidentally provides a comparison of several of these models under difficult conditions. This is followed by LES simulations of the diffuser which show the method's remarkable robustness over a wide range of mesh densities. These calculations primarily gauge LES' ability to predict separation and reattachment when compared to the experiment data of Buice and Eaton [19]. The effectiveness of the Spalart-Allmaras DES model in this geometry is also evaluated and some permutations of its base formulation investigated. Finally, local mesh refinement methodologies are tested.

5.2.1 Computational Setup and Reference Details

The flow in the asymmetric plane diffuser has several desirable features which make it a good test case for the validation of LES and wall treatments. In particular:

- The flow belongs to a class of ‘mild’ pressure-driven separation, from a smooth wall. In contrast with geometry-induced separation (*i.e.* from sharp edges), this configuration requires a much more exacting near-wall treatment. In addition, these kinds of flows are prevalent in automotive aerodynamics [5, 168] and are therefore of immediate interest.
- The inflow conditions are unambiguously defined. The experimental inlet duct has a length of more than 100 duct heights, thereby guaranteeing that the flow entering the expansion is a fully developed turbulent channel flow. For validating the computation of spatially evolving, fundamentally unsteady flow, it is crucial to know the upstream conditions with a high degree of accuracy.
- The wall shear based Reynolds number of the incoming channel flow is $Re_\tau \approx 500$. Although well resolved LES and even DNS of the full diffuser is feasible, it is still very expensive. On the other hand, the Reynolds number is high enough to make the flow only weakly dependent on this parameter [117], lending some generality to the envisaged results.
- The flow exhibits many regions of interesting physics, such as the detached shear layer driving the separation bubble, a flat plate boundary under the influence of a strong adverse pressure gradient and incipient separation and reattachment in the outlet duct.
- Two sets of experimental data produced by Obi *et al.* [117] and Buice and Eaton [19], along with a well resolved LES simulation from Kaltenbach *et al.* [81] are available for comparison.

Since the flow is dominated (at least near the inlet) by the fully developed channel boundary layers, the diffuser is not a good test case for DES as defined by Spalart *et al.*

[149], which has more merit as an outer layer matching method. It does however represent a good opportunity to test the limits of inner layer matching treatments and the effects of grid density and local refinement in weakly separating flows.

The diffuser geometry (shown in fig.5.8) with a Reynolds number, $Re_b = U_b h / \nu = 18000$ (h = inlet channel height), mimics the experimental configuration of Buice and Eaton [19]. The corresponding wall shear based Reynolds number is $Re_\tau = u_\tau h / (2\nu) \approx 500$. The underlying coordinate system was chosen to coincide with the intersection of the deflected wall and the lower inlet channel wall. The nominal inlet plane is located at $x/h = -5$, where the upstream influence of the diffuser on the channel flow is assumed to be negligible [81]. The parallel flow from the inlet duct enters the diffuser with a characteristic expansion ratio of $a = h_{inlet}/h_{outlet} = 4.7$ and an included angle of $\sim 10^\circ$. Both of the corners at the ends of the inclined plane are rounded with a radius of $4.3h$. The expanding section extends over 21 inlet heights, followed by the outlet section with a length of $\sim 30h$. Simulations were performed on various meshes, with a spanwise domain length of $2h$ to incorporate spanwise structures present in the separated region, a width found to produce acceptable LES results in an independent study [81]. The mesh is generally stretched toward the wall and streamwise in the diffuser section to maintain proportionality with the domain's vertical extent. The computational time step is limited by the need to resolve the turbulence in the inlet section, which has similar requirements to the channel flow. Since the total required integration time is proportional to the the local diffuser height and inversely proportional to the bulk velocity (inertial timescale, $t^e = 0.5h(x)/U_b(x)$), the large difference in aspect ratios between the inlet and outlet necessitates very lengthy integration times. In general, results are sampled over 10 flow-through times of the domain, which amount to approximately $3000 \times t_{inlet}^e$ seconds. This is also long enough to converge the low-frequency unsteadiness at the outlet of the diffuser which has a period of roughly $t_{inlet}^e = 100$. In addition to time averaging, spatial averaging is performed in the homogeneous direction to obtain the final flow statistics.

The diffuser case's boundary conditions generally conform to the specifications stipulated in sec.4.4. The spanwise direction is connected via periodic boundaries for all transported quantities. The downstream boundary is of the zero gradient/fixed pressure

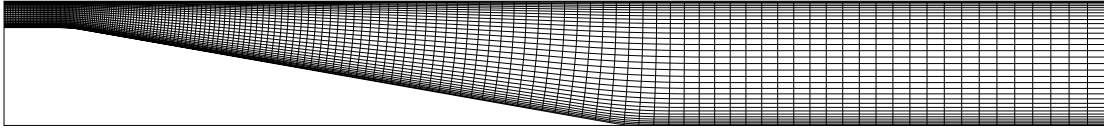


Figure 5.8: Computational domain for the asymmetric plane diffuser, showing a subset of the computational grid.

type with limiters imposed for the LES to prevent inflow induced by energetic exiting vortices. The top and bottom walls are standard no-slip with wall-functions being activated for larger near-wall cells ($y^+ > 10$). The fully developed turbulence at the inlet boundary requires detailed specification of the turbulent properties as described in sec.4.4.3. We briefly compare the results for a recorded and mapped type inlet at the beginning of sec.5.2.3 to choose between the two approaches. Other initial conditions in the bulk of the domain are supplied from a RANS solution of the flow.

5.2.2 RANS Diffuser Results

Before any LES calculations were attempted, various RANS models were tested on the diffuser test case. This had two purposes: firstly, LES is assumed to be more accurate than RANS in separated flows, but is known to be much more computationally demanding. The RANS results are therefore needed to prove LES' superiority and to justify the investment in additional computational resources. Secondly, evaluation of the different RANS results provide an independent comparison of the models for weakly separating and reattaching flow regimes.

Meshes for the RANS calculations are all two-dimensional, with only a single cell in the spanwise direction. For low Reynolds number models, the mesh is graded towards the walls, to provide wall-normal spacing of $\Delta y^+ \approx 1$ in the near-wall cells. The models with wall functions have a wall-normal mesh spacing such that the first of-the-wall grid point lies in the logarithmic layer ($y_0^+ \approx 30$). In both cases, streamwise mesh spacing is chosen to provide more or less square cells in the centre of the flow domain. Some mesh sensitivity studies were also conducted, with only the best results represented here.

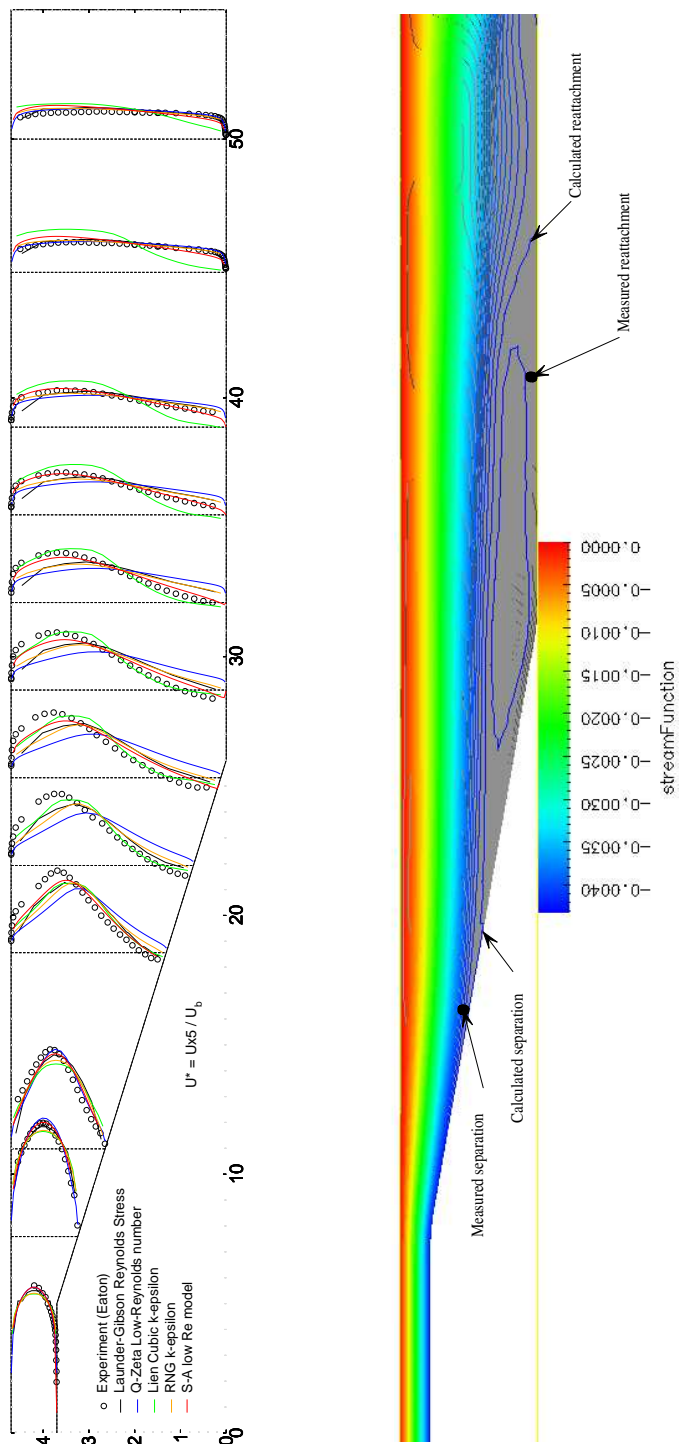


Figure 5.9: Velocity distribution for RANS diffuser: streamwise velocity, U_x (left) for various models and streamlines (right) for Lien-Cubic $K - \epsilon$ RANS model.

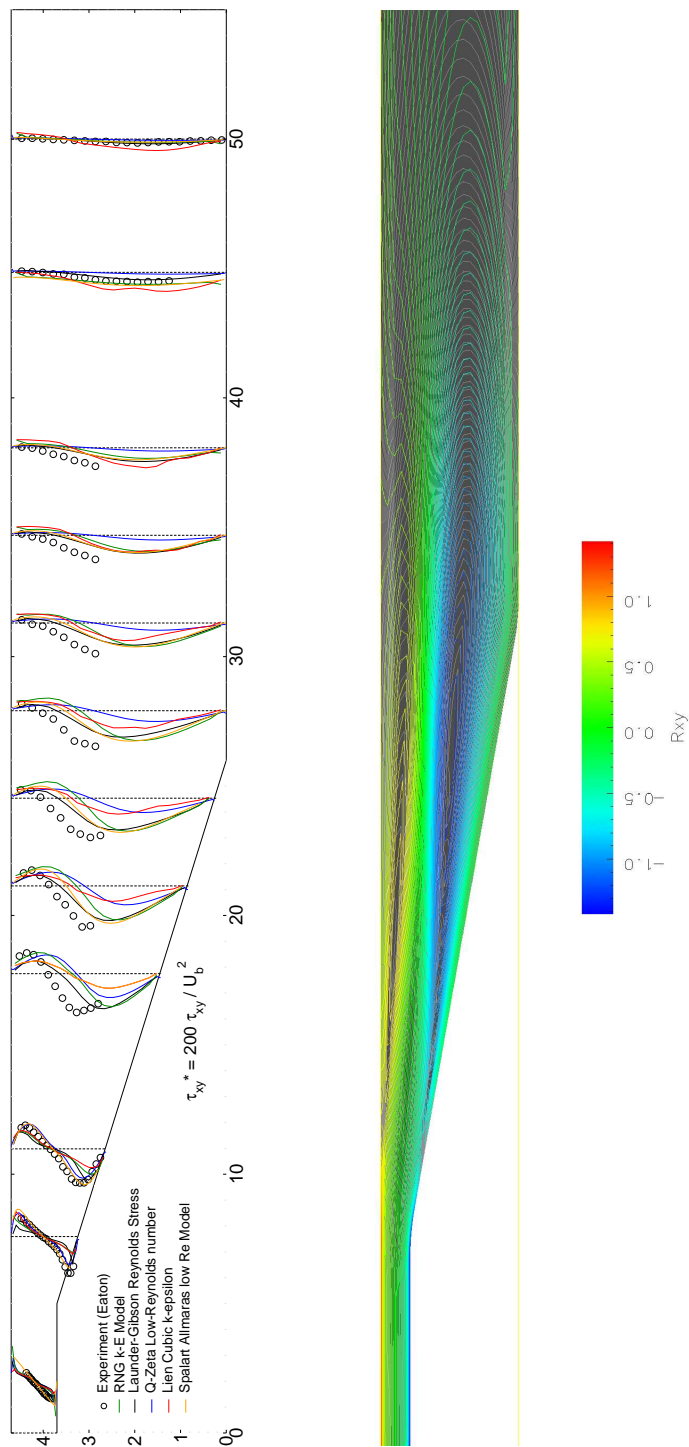


Figure 5.10: Shear stress distribution for RANS diffuser R_{xy} : wall normal profiles (left) for various models and contours (right) for RNG $K - \epsilon$ RANS model.

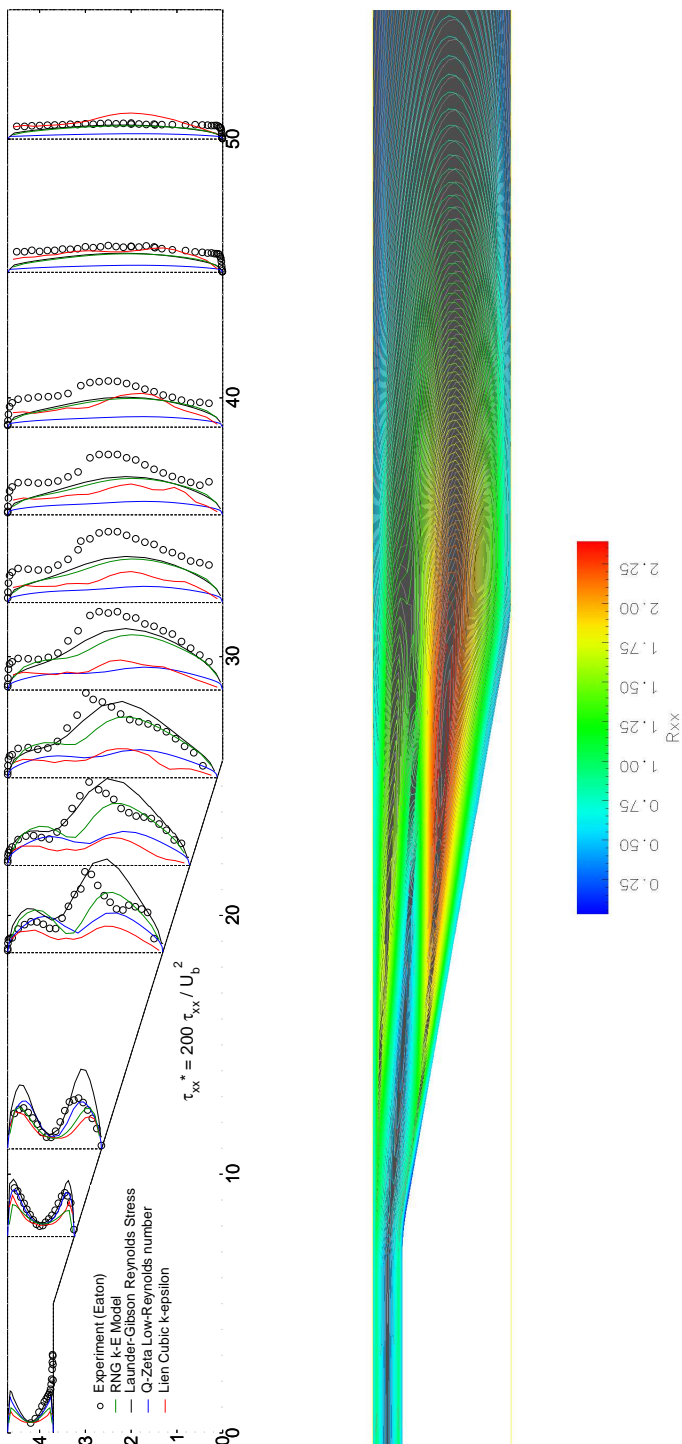


Figure 5.11: Normal stress distribution for RANS diffuser, R_{xx} : wall normal profiles (left) for various models and contours (right) for RNG $K - \epsilon$ RANS model.

5. Basic Test Cases

Boundary conditions are similar to those used for LES, but with inlet quantities fixed at values provided by converged channel flow solutions. Calculations were performed using a steady-state flow solver, with all normalised residuals allowed to converge below 10^{-6} . A representative set of turbulence models were used in the investigation: Standard $K - \epsilon$, RNG $K - \epsilon$ [170], Lien's Cubic model [3, 4], Gibson-Launder Reynolds stress model [2], Q-Zeta low Reynolds number model [1] and the Spalart-Allmaras low Reynolds number model [147]. For the results, only the better performing models are displayed in the various categories.

Figure 5.9 compares the RANS results for the streamwise velocity U_x , with the experimental results (Buice and Eaton [19]). All the models perform well in the inlet section, which is basically a fully developed channel flow, as can be expected. In the separated region most of the models under-predict the strength of the recirculating flow, with the Lien Cubic model comparing the best with experiment. The Q-Zeta model performs the worst, totally failing to predict separation. Along the upper wall the RANS models collectively under-predict the jetting effect, probably owing to unphysically high turbulent dissipation. Near reattachment and in the recovery region the Spalart-Allmaras model outperforms the rest, comparing quite well with Buice and Eaton's data. The Lien-Cubic model is very inaccurate in this region, predicting reattachment more than four inlet heights downstream from its actual location and over predicting the jet along the top wall, which should be fading at these streamwise locations. The streamlines on the r.h.s. in fig.5.9 clearly depict the extent of the separation bubble predicted by the Lien's Cubic model. This model gives the best forecast of the separation point, within two inlet heights of the measured location, while the other models place this point at various distances further downstream. In general, the RANS models misrepresent the velocity distribution in and above the separation bubble and fail to predict the maximum velocities correctly at most of the sections.

The Spalart-Allmaras model provides the best prediction of the turbulent shear stress in the diffuser throat, shown on the left in fig.5.10. In the rest of the diffuser, the Reynolds stress model provides the most accurate results, but both it and the other models under-predict the peak stress values and fail to capture the peak's location. Figure 5.10 depicts

the overall distribution of the shear stresses for the RNG $K - \epsilon$ model. The positive stress region above the inclined plane (orange) extends too far from the top wall and the shear layer (blue) that drives the recirculation bubble is to weak and to close to the bottom wall, a symptom of the under predicted separation.

The streamwise portion of the turbulence intensity is represented by a component of the normal Reynolds stresses, R_{xx} , in fig.5.11. At the inlet and in the narrowest section of the diffuser the Q-Zeta model provides the best comparison with experiment. In and above the separation zone, the Reynolds stress and RNG models give a better prediction, but still fail to calculate the magnitude and position of the peak stresses correctly. Downstream, in the recovery region, most of the models under predict the magnitude of the turbulence intensity, especially along the top wall and in the middle of the flow. This is a product of both excessive turbulent dissipation and the inaccuracies coupled to the separation bubble and its attendant shear layer.

Looking at fig.5.12, most of the RANS models provide a fair approximation of the dimensionless pressure distribution, $C_p = 2\Delta p/U_b^2$ along the diffuser, in general predicting values a little below the measured ones. However, only the Lien-Cubic and to a lesser extent the Reynolds stress model capture the inflection point in the experimental pressure distribution at $x/h \approx 25$, an indicator of the separation bubble. The deficiencies in the RANS velocity distributions, are mirrored in the wall shear stress distributions. As can be seen on the r.h.s. of fig.5.12, all the RANS solutions under predict the shear stress along the top wall by a factor of two or more. This too is coupled to small, or in the case of the Spalart-Allmaras and Lien-Cubic models, “thin” separation bubbles, which result in a smaller jetting effect along the top wall. The wall shear along the bottom wall is a good indicator of the extent of the separated region. Of the models tested, only the RNG $K - \epsilon$, Lien Cubic and Spalart-Allmaras models capture this feature. Although the extent of the bubble in the Lien-Cubic and Spalart-Allmaras results is more or less of the correct streamwise proportions, its wall normal dimensions are under predicted in both cases. This general deficiency is probably due to the inability of RANS models to describe the properties of the energetic eddies in the mixing layer.

The best overall results are arguably provided by the Spalart-Allmaras model, which is

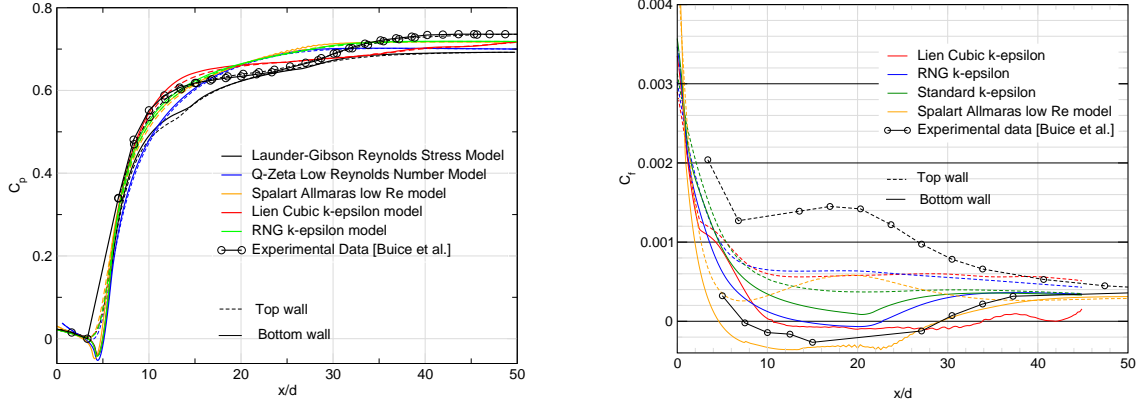


Figure 5.12: Diffuser wall statistics: Pressure coefficient (left), Wall shear stress coefficient (right)

promising considering its implementation as a LES sub-grid scale treatment. It provides a fair representation of the streamwise velocity, outperformed only by the Lien Cubic model and only in the first half of the diffuser. It must be noted, that the high Reynolds number models all suffer from their dependency on the logarithmic wall function, which is obviously inaccurate in the strong pressure gradient, non-equilibrium flows present in the diffuser. In the next section, the best results from the RANS simulations will be compared to the various LES calculations and experimental data.

5.2.3 LES of the Diffuser

In this section, the results from several LES calculations using various mesh resolutions and Wolfshtein's near-wall treatment coupled with the one-equation SGS turbulent energy model, are presented. The finest mesh is loosely based on the considerations put forward in sec.5.1.4 as part of the LES of channel flow investigation. Two successively coarser meshes are also constructed and compared to the finest mesh and experimental data. The purpose of these calculations is primarily to investigate the effects of sub-optimal mesh resolution on LES of weakly separating flows. Table 5.5 gives a summary of the grid information for the various resolutions. Note that even the finest mesh is quite coarse in the spanwise direction and the near-wall region. These types of resolutions will be typical

of more demanding "engineering" flows and though reduced accuracy may be expected, a successful wall treatment must still produce reasonable results.

Case	Inlet Resolution			Cell distribution		Cell count	
	Δx^+	Δy^+	Δz^+	N_x	N_y	N_z	
LD21	120	50	100	173	20	20	69200
LD20	80	33	67	283	30	30	254700
LD17	60	25	50	371	40	40	593600

Table 5.5: Grid spacings in wall units, and directional cell counts used in the simulations.

First however, a choice must be made regarding the specification of turbulent inlet conditions. To this end two calculations using the medium diffuser mesh and the different inlet prescriptions (recorded and mapped) are compared. For the mapped LES calculations both the velocity and transported turbulent properties are mapped across the inlet section which is extended 4 inlet heights upstream to accommodate a fully developed channel flow solution. Initial conditions for the mapped section are supplied from equilibrium channel flow solutions similar to those depicted in sec.5.1. The recorded inlet uses a equilibrium channel flow solution of a domain of similar extent to the mapped method's extension, with the timestep and grid spacing exactly matched to the main diffuser mesh. The outflow from the channel calculation is recorded for a period sufficient to perform the entire diffuser calculation, *i.e.* the inflow library is not replayed, manipulated or transformed in any way.

From the results in fig.5.13 it is immediately apparent from the lack of inflection point in the wall pressure distribution and shear stress along the bottom wall, that the case with the recorded inlet displays no recirculation bubble on the mean. In addition, sharp local minima in the wall shear are found around $x/h = 0$, that are not mirrored in the

5. Basic Test Cases

LES or experimental data. This corresponds to the beginning of the diffuser section and coincides with a very small, but intense recirculation zone. The cause is thought to be the “rigidity” or jetting effect of the independently prescribed inlet condition, the effect of which should decrease if the boundary is moved further upstream. (As an aside, a similar but less intense spike is observed in the well resolved LES results of Kaltenbach *et al.* [81], who also use a type of recorded inlet.) For this particular configuration of mesh density and inlet plane, the mapped inlet performs considerably better than its recorded counterpart. The possibility certainly exist that the utility and performance of the recorded inlet can be improved by moving it further upstream and/or by transforming the mean and turbulent inlet quantities in some way. However, given the results produced by the mapped inlet to date and its ease of use and flexibility compared to the recorded case, this additional development was deemed superfluous. As a result the internally mapped inlet is used for all subsequent LES diffuser calculation.

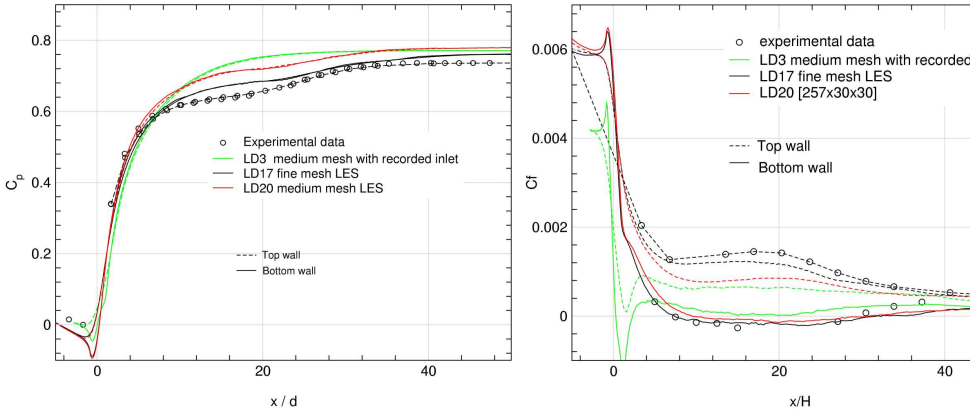


Figure 5.13: Effect of inlet boundary on LES diffuser wall statistics: Pressure coefficient (left), Wall shear stress coefficient (right)

An instantaneous realisation of a typical diffuser velocity distribution in the $x - y$ plane can be seen in fig.5.14. Although not as representative as a time mean plot, it does convey a more intuitive feel for the scales and structures present in the diffuser flow. Figure 5.14a shows the overall flow distribution calculated using the finest mesh. Very apparent is the development of the shear layer between the fast moving (green) flow along the top wall and the slower recirculating (blue) flow at the bottom of the expansion.

Large scale mixing is clearly visible as inclusions of slower moving fluid penetrating into the faster stream (and *vice versa*). Other important features are the regions of flow separation and reattachment. Reattachment in this snapshot appears to be a gradual diffuse process as the flow decelerates into the wider downstream section. Separation on the other hand, more clearly depicted in fig.5.14a, is a more vigorous feature. The sudden change in the lower boundary caused by the circular rounding necessitates a rapid change in flow direction that is accompanied by large pressure gradients. This pressure gradient can induce momentary flow reversals which in turn result in large oscillations in the jet issuing from the channel section. Also readily apparent is the lack of a clear separation line. In fact, the flow has repeated pockets of slow moving fluid that are in the process of leaving the inclined wall separated by faster moving fluid that is clearly still attached. This is a likely sign that the separation phenomenon is a marginal process, *i.e.* a slightly shallower diffuser would not have exhibited this feature. The fact that the LES calculation reproduces this is very encouraging.

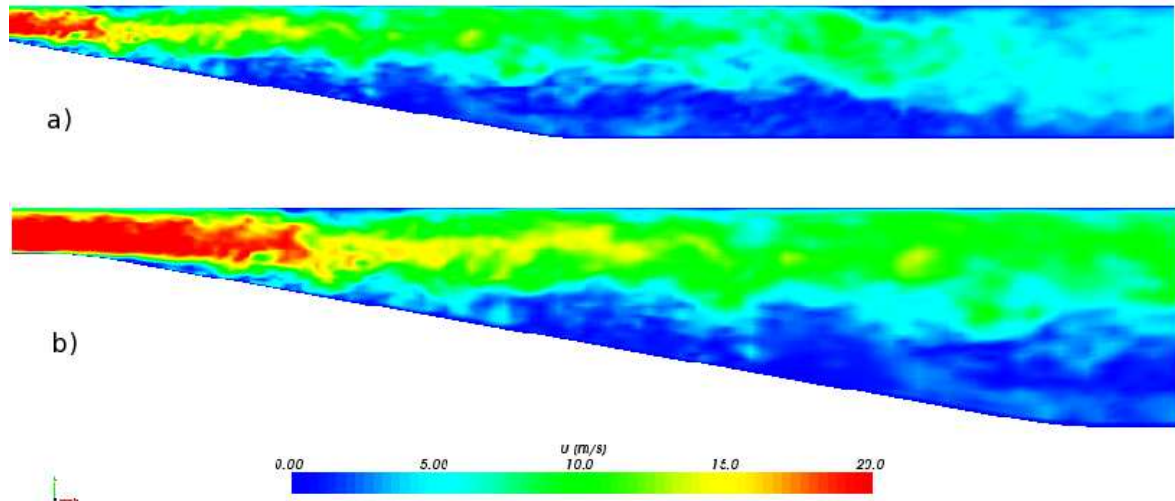


Figure 5.14: LES instantaneous velocity magnitude in the diffuser a) Entire domain b) Expansion section.

The second instantaneous plot fig.5.15 focuses on the typical shape and distribution of turbulent properties in the diffuser flow. Again, the solution employs the one-equation

5. Basic Test Cases

SGS energy model on the finest mesh. The top image (fig.5.15a) depicts a typical distribution of the sub-grid scale turbulent kinetic energy, K in the expanding section, while the lower image (fig.5.15b) shows resolved vortices via isosurfaces of the second invariant of the velocity gradient tensor. Elevated values of SGS energy are normally associated with large resolved scale stresses. High values of K along the bottom wall at the entrance to the expansion are a product of a very strong rapidly fluctuating shear layer in this region. The smaller maxima along the top wall is most likely a result of the same phenomena: the flow bending toward the lower wall forces the line of maximum shear away from the top wall and the reduced dissipation away from the boundary allows a rapid increase in turbulence. A local maximum of this quantity also stretches some way along the centre of the domain and coincides with the free-shear layer that drives the recirculation bubble along the bottom wall. The high values experienced along the downstream portion of the top wall are at least partially due to the reduced resolution in this region which places greater reliance on the SGS model. It is also interesting but unsurprising to note that the SGS and resolved scale turbulence overlap for the most part. The vortex cores are coloured by the local deviatoric pressure, which shows a low-high-low-high foci corresponding to the staggered velocity distribution observed along the inclined wall: also a product of the oscillating channel jet. Unfortunately the intensities of the vortices vary greatly between the channel and expanded sections, making it very difficult to visualise all significant vortices in this region without them completely obscuring each other. The vortices that are shown also coincide with regions of high shear. There is a definite increase in scale as eddies are advected away from the wall. This is partially due to the removal of the limiting influence of the boundary, but is also influenced by the adverse pressure gradient in this region. Reduction in the bulk velocity as the diffuser expands means the shear-layer rapidly decreases in intensity, with the result that vortices in the fully expanded region are of much lower intensity than those near the inlet section.

Focussing on the vortices along the bottom wall at the start of the expansion (fig.5.16) some interesting features are revealed. From top to bottom the images show *a*) spanwise view of vortex cores coloured by the velocity magnitude, *b*) the same viewed from above and *c*) neutral coloured vortex cores overlaying the mean shear stress magnitude on the

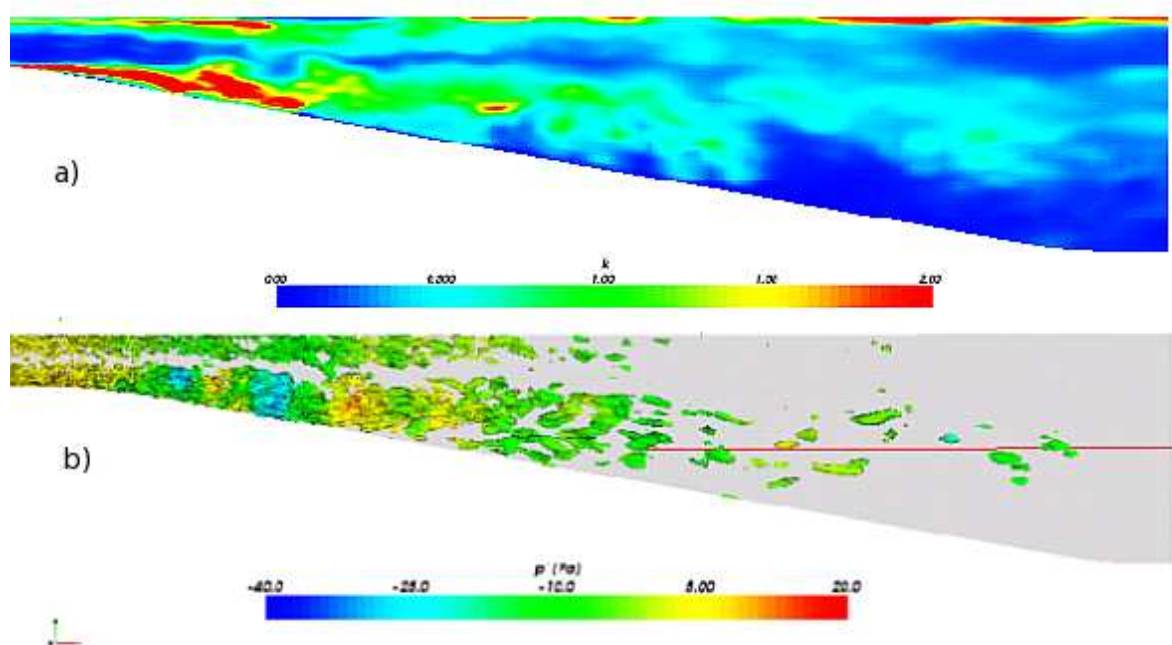


Figure 5.15: LES instantaneous turbulence properties in the diffuser a) SGS turbulence intensity b) Resolved vortical structures visualised via isosurfaces of $Q > 5e+5$, the second invariant of $\nabla \bar{\mathbf{u}}$ and coloured by the deviatoric pressure magnitude, $\bar{p}' = \bar{p} - \langle \bar{p} \rangle$.

5. Basic Test Cases

lower wall. In fig.5.16a the growth of eddies as they enter the expansion can be seen quite clearly. Initially small structures from the channel flow section enter the expansion and then begin to grow as they are strained in the spanwise direction. The boundary layer, which concentrates velocity gradients in a thin near-wall region in the channel rapidly grows thicker under the influence of the negative pressure gradient in the diffuser. Larger vortex structures can thus be subjected to a more intense differential force, which results in the rapid growth and predominance of streamwise elongated structures in the region under focus. The colouring of the vortex surfaces in fig.5.16b shows this process even more clearly: the upstream ends of the structures can be seen to be embedded in lower velocity fluid than the downstream portions, which are also further from the inclined wall than the former. Also very apparent is the spanwise inhomogeneity of the turbulent properties. The strength and position of the adverse pressure gradient is strongly influenced by the behaviour of the large recirculation region downstream of the expansion throat which can fluctuate considerably. This variability will in turn strongly influence the growth of the boundary layer and thus the locus of the maximum shear. Visualisations also confirm that the boundary layer is much more strongly attached in the upper region of fig.5.16b than in the lower portion, where more turbulence production is clearly occurring.

Although the instantaneous nature of the vortices introduce some uncertainty, fig.5.16c shows yet another unexpected feature of the emerging flow: the wall shear indicates a clear minimum right after the expanding section is entered followed by a local maximum before the stress falls off into the recirculating region. This behaviour is caused by insufficient rounding of the curved interface between the bottom channel wall and the inclined wall. A sharp reduction in wall shear is thus experienced initially as the flow attempts to separate over the rounding. Thereafter it increases to a maximum as the bulk flow adjusts to the change in flow direction, flattening the boundary layer. Subsequently, the strong adverse pressure gradient causes a growth of the inflection in the boundary layer profile which eventually causes the flow to detach into the recirculation zone. This behaviour is reflected (albeit tenuously) in the instantaneous overlayed vortical structures. As noted previously, the increase in shear layer thickness that accompanies incipient separation (quick decrease in wall shear) is a strong source of turbulence generation. This is borne

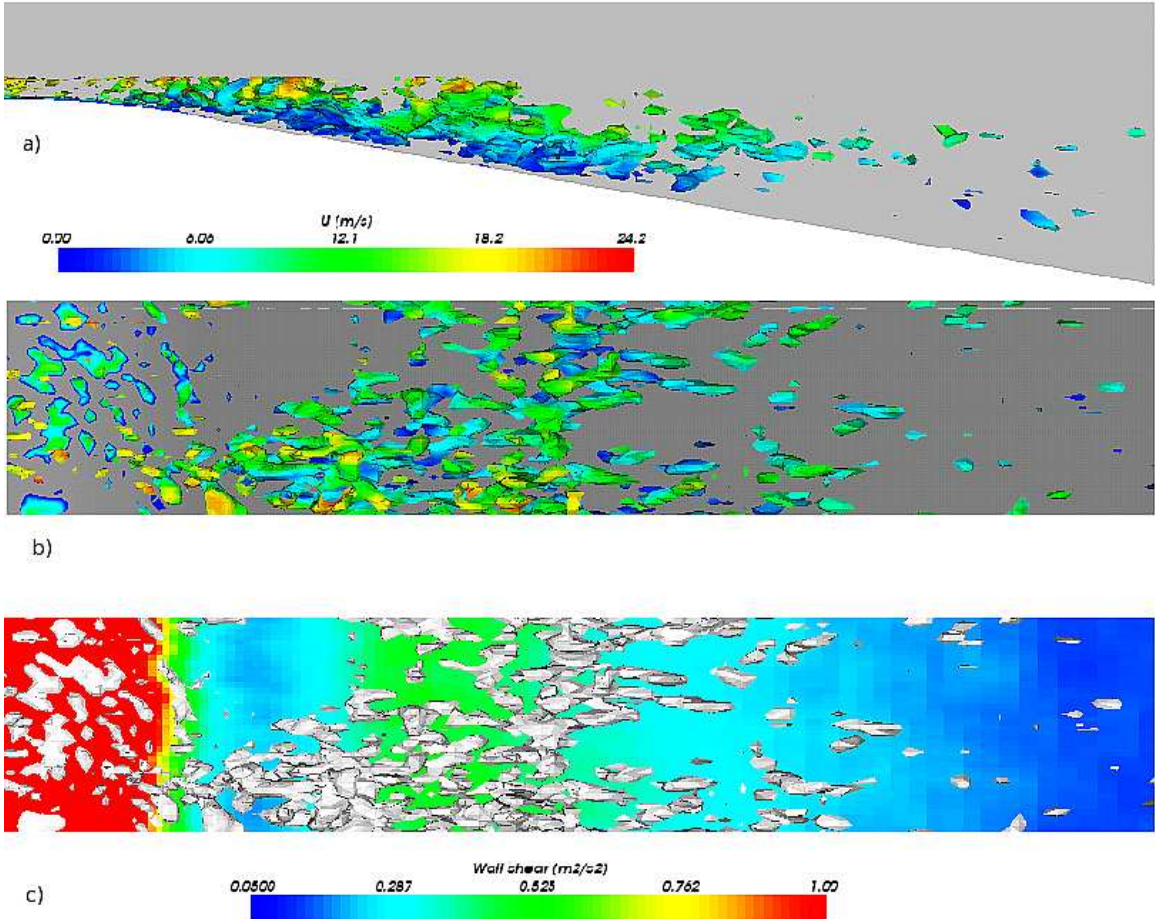


Figure 5.16: Vortex cores around the separation point depicted by $Q > 2 \times 10^6$ and coloured by the velocity magnitude a) Side view, b) top view c) top view showing contours of the mean wall shear along the inclined wall.

out by the overlaid vortices which show strong growth at the early inflection and at the transition to large scale separation.

The overall picture that emerges is of a flow dominated by the dynamics of the shear layer that drives the recirculation region. The sudden expansion at the start of the diffuser provides a strong instability mechanism that is associated with high turbulence production, which in turn feeds into the shear layer. The response from the shear layer to elevated turbulence will be to increase mixing, momentum transfer and thus the recirculation rate. Increased backflow will eventually evoke very low pressures in the recirculation zone and

5. Basic Test Cases

along the inclined wall which will act to collapse the bubble and produce delayed separation. The change in separation point and intensity will reduce turbulence production at the diffuser inlet which will cause a thinner shear layer, decreased mixing and raise the pressure in the recirculating zone. The elevated pressure along the inclined wall will now increase the chances of early separation completing the cycle.

The first comparison plot, fig.5.17, shows the LES streamwise velocity distributions, U_x , at different streamwise positions along with the experimental data and the Spalart-Allmaras RANS results. Immediately evident is the excellent agreement of the fine mesh case in the expansion section and especially along the top wall and in the recirculation region. None of the RANS models were able to predict these features correctly, which implies that the resolved scale turbulence, captured by the LES, is not adequately modeled by the RANS approach. The effect of mesh refinement on LES is also apparent: successively finer meshes producing correspondingly improved results. The expectation is thus for further improvement to result from additional refinement. The only clear deficiency of the fine mesh velocity results, appears along the bottom wall after reattachment. The LES reattachment point is predicted 2.5 inlet heights downstream of the experimentally determined position (fig.5.17 r.h.s.). In addition, boundary layer recovery after reattachment is significantly delayed, a feature coupled to a slight over-prediction of streamwise velocity in the centre of the outlet section. Preliminary investigation links this phenomena to under predicted cross-stream momentum transfer in the shear layer above the recirculation bubble, possibly caused by inadequate resolution of the main turbulent eddies in this region.

This hypothesis is partly confirmed by the wall-normal shear stress comparison plotted in fig.5.18a. Although the LES again outperforms the RANS results in the majority of the diffuser, it is clear that there are some significant errors. The magnitude of the peak stress is over predicted by more than 50% in the first part of the shear layer between $x/h = 0$ and $x/h = 20$, albeit at the correct positions. After $x/h \approx 28$, where the velocity starts to show significant inaccuracies, the shear stress is under-predicted and, despite limited experimental data, its peak location seems to have shifted to close to the bottom wall. It can only be assumed that this occurrence is coupled to the “weak” reattachment and

subsequent recovery observed in the velocity distribution. Also, the excessive LES shear stress near the bottom wall is attributed to the coarse mesh, a phenomena common to most under resolved LES calculations, but exacerbated in this case by the naturally high stresses in this region. Overall, the combined observations seem to indicate inadequate turbulent energy dissipation along in the inclined wall in the vicinity of $x/h \approx 10$ and excessive dissipation, possibly caused by the coarse mesh, near $x/h \approx 30$ in the transported shear layer. Again, comparison of different mesh resolutions show improved correlations with grid refinement, while the r.h.s. of fig.5.18 allows an overview of the overall shear stress distribution of the fine mesh LES results.

In fig.5.19 far left, the largest discrepancies in the LES results are exposed in the streamwise component of the normal stress. This is the only statistic where a RANS result compares better than the corresponding LES. Following the stress intensities from the inlet, it can be seen that the fine grid LES is quite accurate in the channel flow section. As soon as the flow enters the diffuser section, a large over prediction in the normal stresses becomes apparent, both along the top wall and at the positions corresponding to the free shear layer bounding the separation bubble. On the positive side, the positions of these peaks seem to be accurately portrayed (compared to the RANS values), at least until the flow reaches the outlet section. After the flow exits the diffuser, the shear layer peak can be seen to gradually shift toward the wall, in contrast with the more or less constant wall-normal displacement of the experimental peak. Eventually, this shift causes a severe under prediction of the streamwise normal stresses in the centre of the outlet channel. The peak near the top wall also behaves abnormally, increasing in strength with streamwise displacement, rather than merging smoothly with the profile in the bulk flow. Near the outlet, the LES profile more closely resembles a developed channel flow, preceding this development in the experimental profile by tens of inlet heights. The exact cause of this anomalous behaviour is not certain, but investigation of the resolved versus unresolved contributions, reveal that it is not due to the SGS model contribution, which is an order of magnitude smaller than the resolved scales. Comparing the streamwise component to the wall-normal normal stress component profiles in fig.5.19 middle right, shows that there is limited spatial correlation between the two. The peaks in both the streamwise

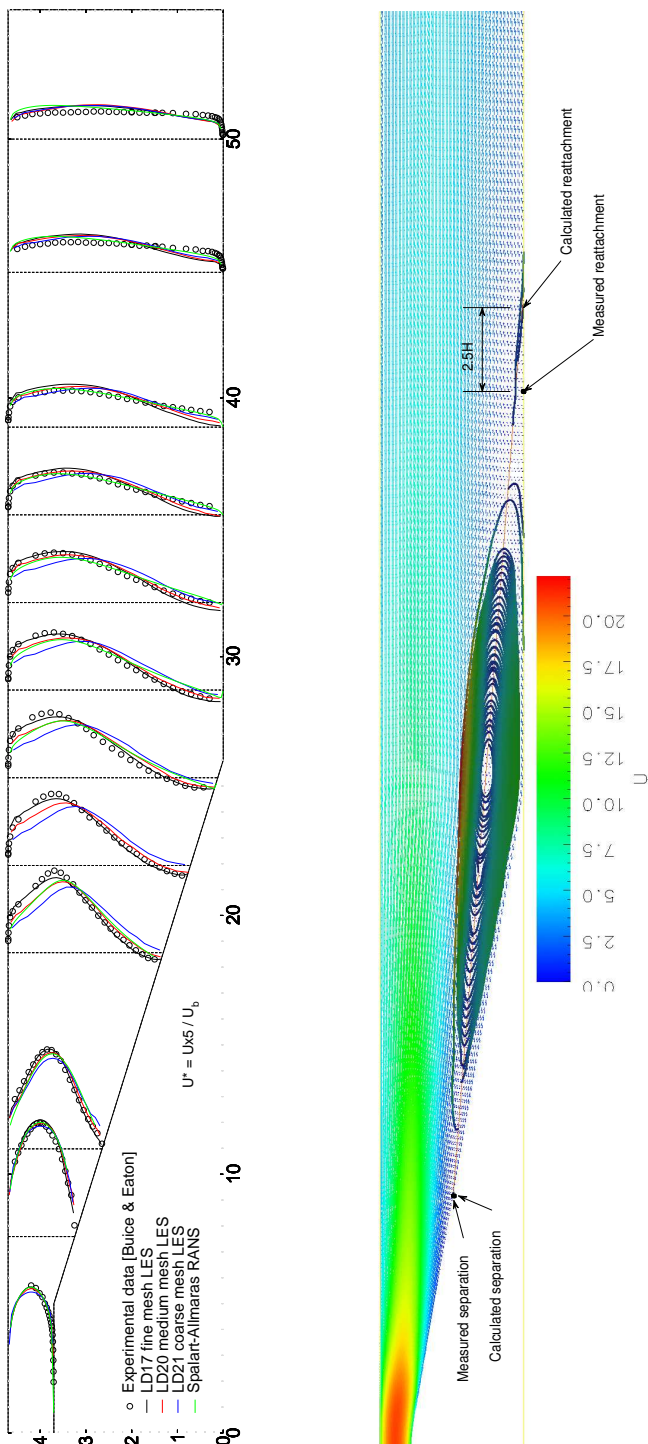


Figure 5.17: Velocity distribution for LES diffuser Streamwise velocity, U_x (left) and velocity vectors and recirculation streamlines (right) for fine mesh LES.

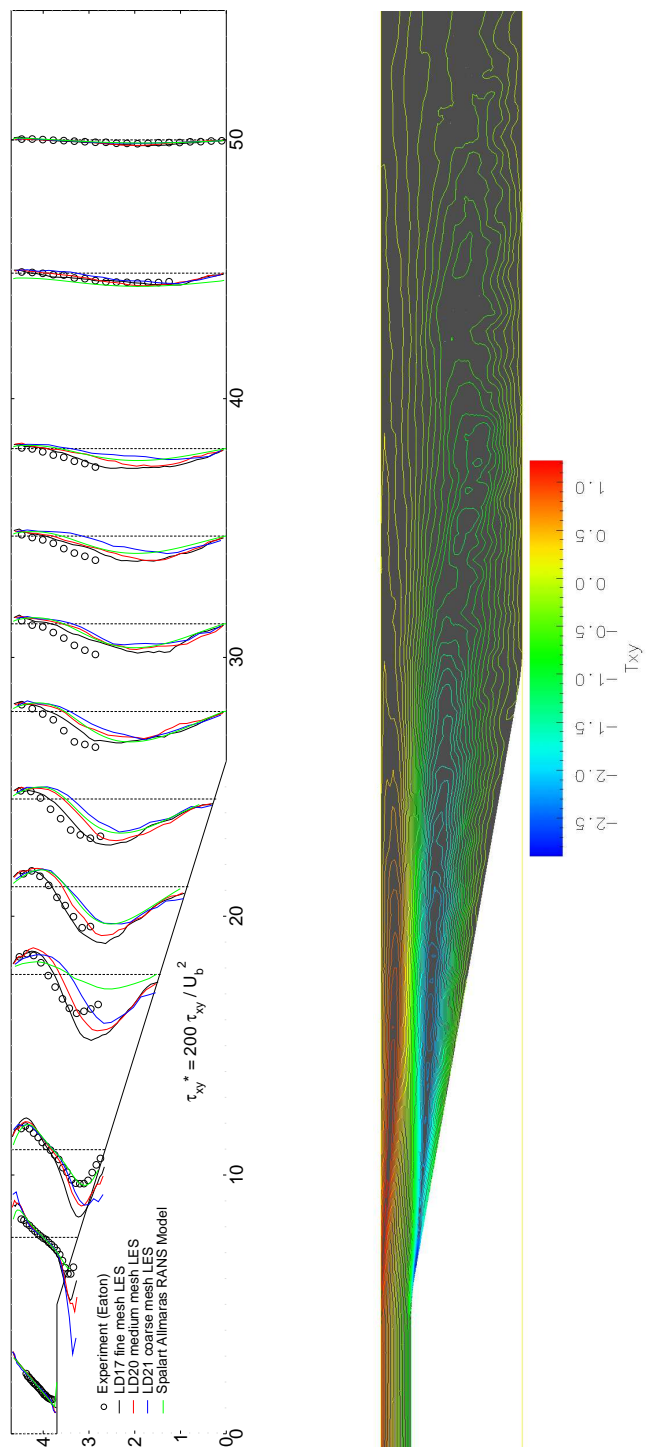


Figure 5.18: Total turbulent shear stress distribution for LES diffuser, T_{xy} wall normal profiles (left) and contours (right) for fine mesh LES.

5. Basic Test Cases

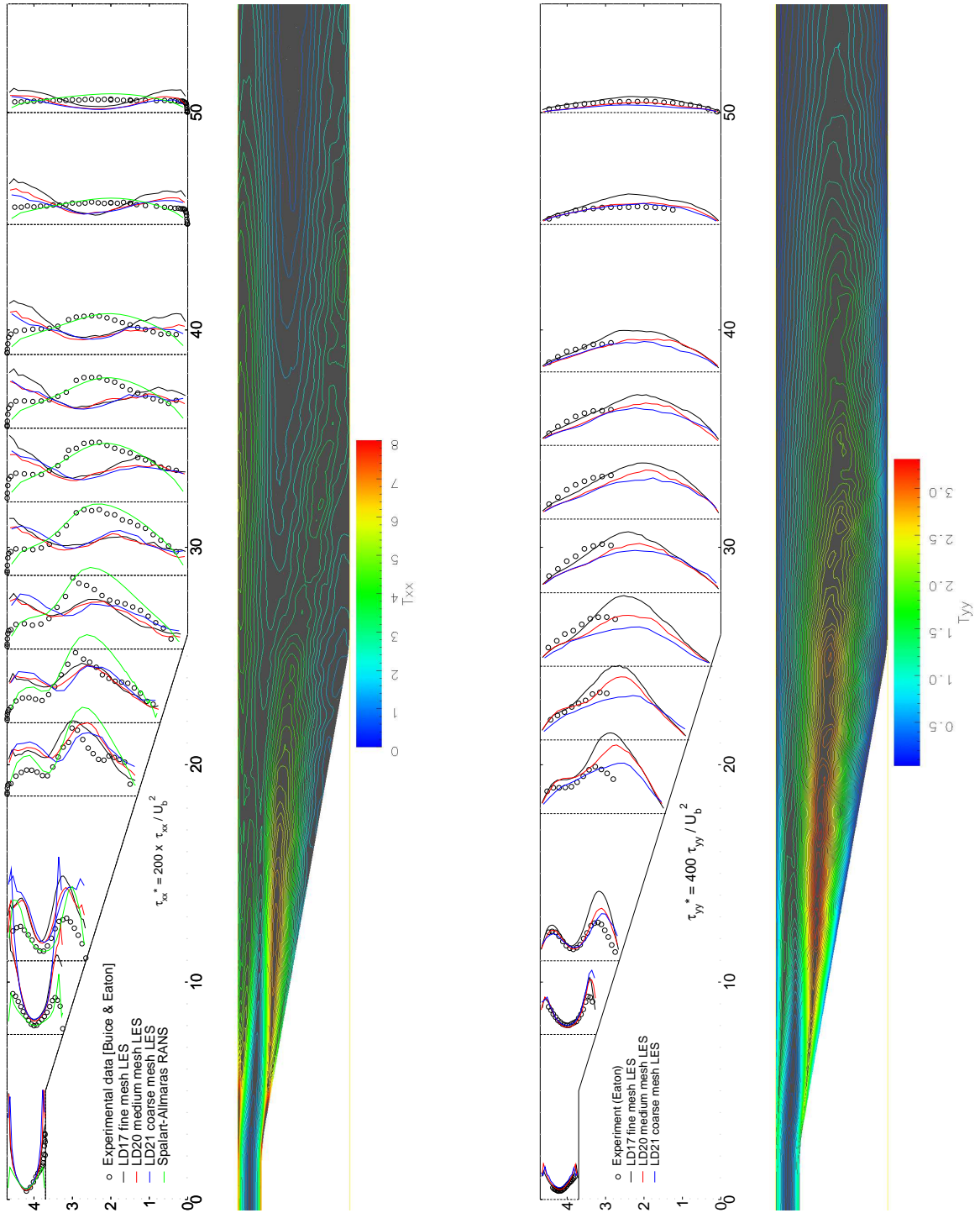


Figure 5.19: Total normal stress distribution for LES diffuser, Selected profiles of streamwise Reynolds stress, T_{xx} (far left); contours of T_{xx} (middle left) for the fine mesh LES; Profiles of wall normal Reynolds stress (middle right), T_{yy} ; and contours of T_{yy} (far right) for the fine mesh LES.

and wall-normal components coincide with the shear layer in the expanding section of the diffuser. The wall-normal component does not, however, exhibit the excessively large peak along the top wall that the streamwise one does, and neither does it display the shift of the shear layer peak toward the bottom wall. In fact, returning to the shear stress distribution in fig.5.18 left, it shows a rather good correlation between the peaks in wall-normal normal stress, T_{yy} and the shear, T_{xy} . Looking back at the resolution studies conducted for the plane channel flow (5.1.4), it can be seen that both the shear and wall-parallel stresses are over predicted at any given wall-normal displacement for the coarser meshes. This is not the case for the wall-normal normal stresses which are constrained by the presence of the solid boundary. For similar reasons, the coarse near-wall resolution in the recovery region, (which is not compatible with DES specifications), is contributing to the under prediction in wall stress which decreases retardation of flow in its vicinity and toward the boundary. Other inaccuracies, namely the excessive turbulent energies in the resolved scales near the separation point at $x/h \approx 10$ and along the line of the free shear layer, can be partially attributed to the coarse meshes acting on the flow according to the mechanism described in sec.5.1.4. In other words, the lack of adequate dissipation is causing a build up of energy in the large scales. The lack of dissipation can only be attributed to SGS model inaccuracies on a coarse mesh. This over-prediction combines with the coarse near-wall mesh to delay the point of reattachment.

Wall statistics for the LES diffuser are depicted in fig.5.20, again showing a marked improvement over the combined RANS results. The LES wall pressure distributions (fig.5.20 left), $C_p = 2\Delta p/U_b$, in contrast with the RANS, all include the conspicuous inflection point found in the experimental data around $x/h = 20$. The magnitude of fine mesh results also shows good agreement with experimental measurements. It should also be noted that the slight over prediction of this pressure drop was also encountered by Kaltenbach *et al.* [81] in their well resolved simulation of an identical diffuser. The superiority of the LES method is most apparent in the wall shear distribution, $C_f = 2\tau_w/U_b$ (see fig. 5.20 right). The separation point is almost exactly predicted for the fine mesh case, the shear distribution along the top wall is accurate to within a few percent (in contrast with the large errors found for the RANS calculations) and the total length

5. Basic Test Cases

of the mean separated region is only slightly over-predicted. In fact, the only significant discrepancy is the under-predicted wall shear stress found along the bottom wall, in the recovery region, after reattachment. Also very apparent in the wall statistics, is the improvement in mean results with increased mesh resolution. As mentioned before, the implication is that further refinement will produce a corresponding increase in accuracy.

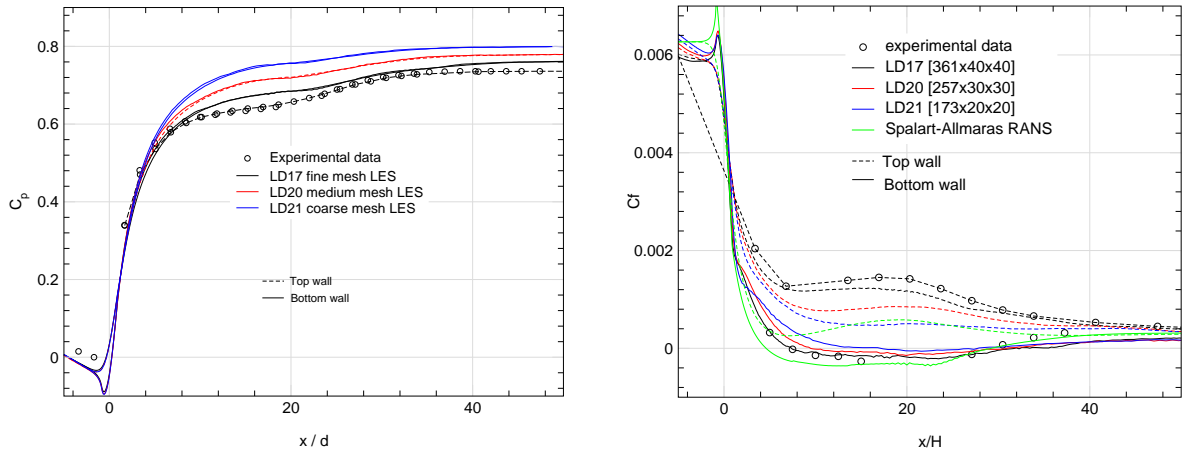


Figure 5.20: LES diffuser wall statistics: pressure coefficient (left), wall shear stress coefficient (right)

5.2.4 Spalart-Allmaras DES Model

As shown in the unpredictable results of the channel flow section and expounded in the summary of sec.3.3.3, the Spalart-Allmaras DES model is not really suited to flows that are dominated by boundary layer or “attached” eddies. The diffuser is such a case. It lacks a proper outer layer where the near-wall RANS-like turbulent viscosity portion of the DES model can be matched to the interior LES flow. More importantly, the eddies generated along the walls of the channel inlet section are a crucial trigger for large scale turbulence production in the free shear layer. The S-A model in DES mode is expected to apply excessive damping in the under-resolved, channel greatly reducing or even completely damping these eddies. Nevertheless, it was felt that diffuser simulations using this model would give some insight into the capabilities of S-A DES and also test its robustness

under unfavourable conditions. Since the RANS portion of DES is intrinsically a low Reynolds number model, it should perform better if the wall-normal mesh spacing is of the order of one near the surface. Starting from the fine mesh case used in previous calculations, several additional layers of cells were added normal to the wall, conforming to this condition. The resulting mesh has double the number of cells of the original. In addition to the standard DES implementation, some minor permutations of the model were also tested to ascertain whether improvements in the results for confined flows could be achieved. The first alteration changes the value of C_{DES} , the multiplicative constant used to calculate the LES length scale from the cell dimensions from 0.65 to 0.4. The motivation for doing so is related to a similar constant's (C_S) reduction employed when using the Smagorinsky SGS model in channel flows (as opposed to isotropic turbulence) to decrease dissipation effects on the highly anisotropic near-wall eddies [128]. Since the standard value of C_{DES} was also calculated from isotropic turbulence, it was felt that a comparable decrease might lead to similar improvements in DES results. The second modification simply changes the definition of the LES cell derived length scale from $\Delta = \max(\Delta x, \Delta y, \Delta z)$ to $\Delta = V^{1/3}$ as described in sec.4.4.2. As opposed to the more or less constant length scale produced in the LES region by the standard approach, the volume based length scale decreases toward the walls as the wall-normal mesh spacing becomes finer. This leads to a smoother interface between the near-wall and interior length scales, but only returns the “correct” DES length scale for cubic cells. The overall effect of the different modifications on the DES length scale in the inlet section of the diffuser can be seen in fig.5.21.

The mean streamwise velocity produced by the different versions of the DES model can be seen in fig.5.22 left. The inadequacy of the S-A DES model for these types of flows is clear. Both the models using the standard length scale eduction (SAD2 and SAD4) produce short intense recirculation zones that reattach before the end of the inclined plane (see fig.5.22 middle). In the recovery region, the peak velocity is shifted toward the bottom wall, producing profiles that appear inverted compared to the experimental data. Note that the calculation using the lower values for C_{DES} generally produces slightly better results than the standard approach, albeit still very inaccurate. The simulation

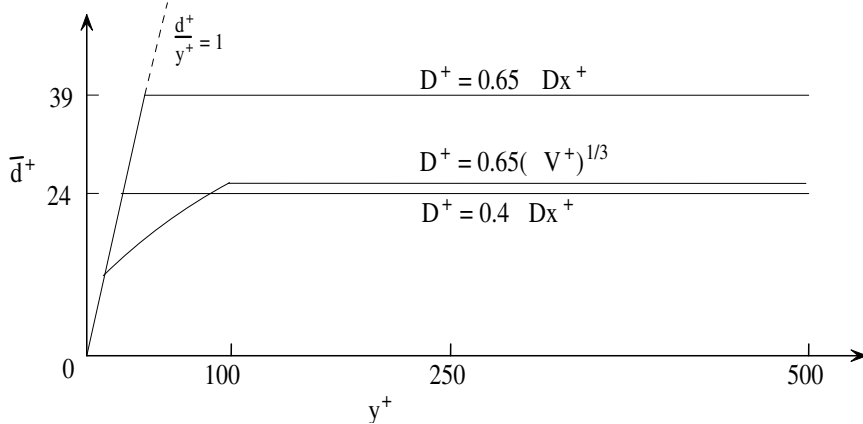


Figure 5.21: Effect of modifications on the DES length scale distribution in the diffuser.

using the volume-based length scale produces much better agreements, its velocity profiles showing similarity to some of the RANS results. A small recirculation zone is visible at the junction of the inclined and bottom outlet walls and profiles in the recovery region show fair agreement with experimental data. The fact that the length scale used for this variation is essentially identical to that used for the more accurate SGS turbulent energy model lends some credence to this approach. The shear stress distributions shown for the cell edge length scale examples in fig.5.22(right) again show large deviations from target values, but this time the standard variant provides slightly better agreement than that using the modified value of C_{DES} . The volume-based method produces shear stresses much smaller than those produced by either of the other two approaches and experiment. The fact that the length scales used in the central part of the calculation are approximately equal for cases SAD2 and SAD5, indicates that the difference must originate near the wall. A comparison of the mean SGS turbulent viscosity fields produced by the different modelling approaches shown in fig.5.23 presents a cause for the discrepancy in the DES results. The large difference in modeled viscosity is due to the DES approach, which places a larger burden on the turbulence model near the walls. More of the stress is thus accounted for by the model than the resolved scales when compared to the SGS energy model. In the case of the Spalart-Allmaras treatment the interaction of the elevated SGS viscosity and resolved turbulence produces earlier separation which produces increased stress resulting in the production and transport of more SGS turbulence into the free-

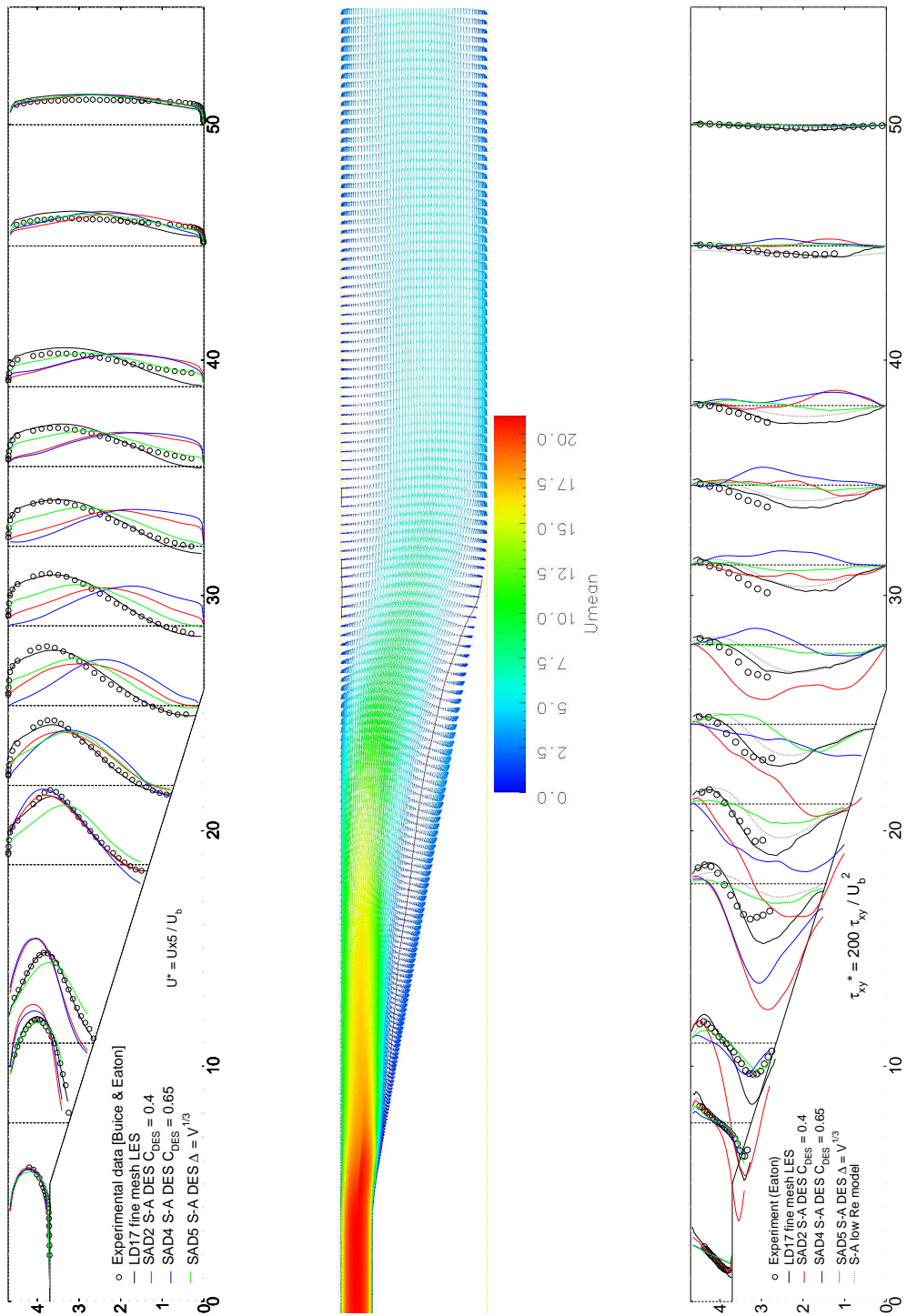


Figure 5.22: Result comparison for Spalart-Allmaras Detached Eddy Model: mean streamwise velocity, U_x (left), velocity vectors for standard S-A DES model (middle) and total shear stress distribution, T_{xy} (right).

5. Basic Test Cases

shear layer. The increased momentum transfer across the shear layer in turn produces quicker reattachment and gross flow distortion.

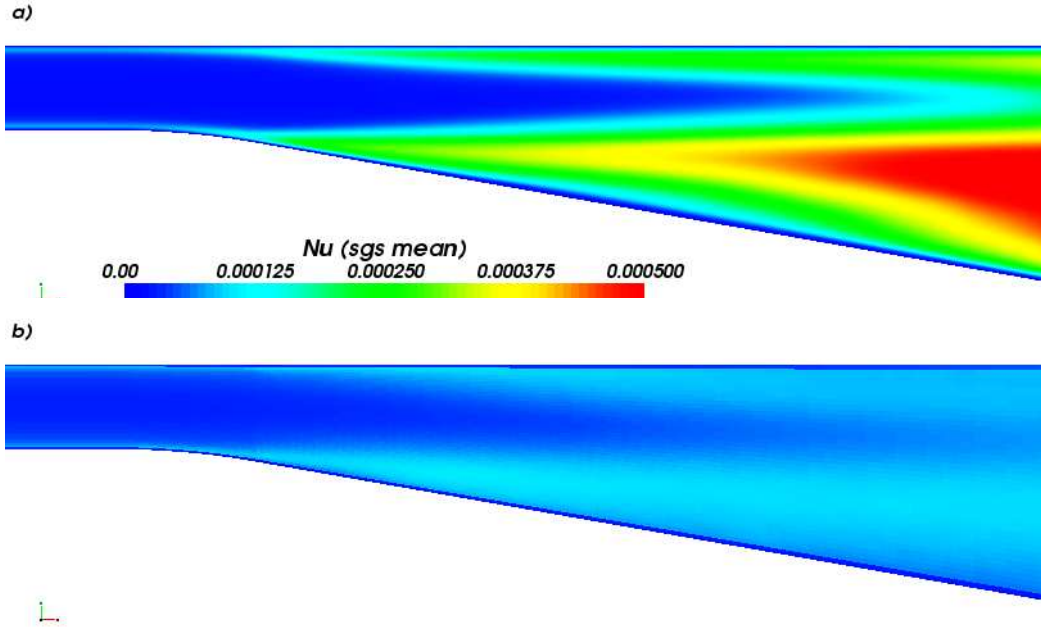


Figure 5.23: Diffuser SGS turbulent viscosity a) Spalart-Allmaras (SAD4) b) Turbulent energy transport (LD17).

The wall statistics shown in fig.5.24 only serve to accentuate the deficiencies of the S-A DES approach in these kinds of flows. The variations that use the edge length-based approaches to calculating \tilde{d} still show anomalous distributions for both the pressure drop and wall shear results, confirming previous conclusions. The volume based method shows at least qualitative, if not quantitative agreement with experimental data. Of some interest is the spike in wall shear observed for the SAD5 case, which is reminiscent of a similar feature observed in the diffuser calculation with a recorded inlet. As can be seen, the other two simulations display the same sudden drop in wall shear, but unlike the volume-based length scale approach, fail to reattach shortly after the short separation.

In summary, various DES simulations of the diffuser have confirmed the inapplicability of this method to boundary layer dominated flows. The standard model proved particularly ineffective and variation of the length scale constant C_{DES} failed to produce

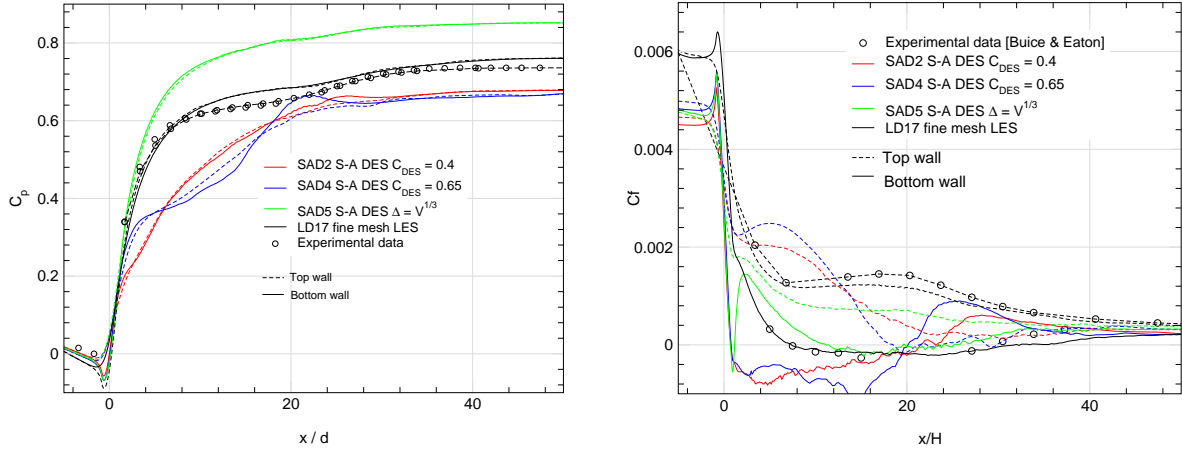


Figure 5.24: Spalart-Allmaras DES diffuser wall statistics: pressure coefficient (left), wall shear stress coefficient (right)

consistent improvement or deterioration of results, implying a lack of sensitivity to this quantity. The use of a volume-based turbulent length scale did result in somewhat better agreement with experiment, but ultimately produced results far inferior to those of the SGS energy model. This does not mean that this model will perform poorly as an outer layer matching method, only that it must be used with caution where intermediate matching is coupled to large scale unsteadiness or non-equilibrium flows. Finally, although the use of S-A DES as an inner layer matching model (matching height, $y^+ \lesssim 20$) is possible, this would require wall-parallel mesh spacings of 30 wall units or less, which is adequate for well-resolved LES, making such an implementation somewhat redundant. In this context it should be noted that the mesh employed for the DES calculations is not entirely suited to DES: wall-parallel spacings being $\Delta^+ \approx 80$ instead of $\Delta^+ > 200$ required for a representative implicit average of near-wall turbulent structures. Using a mesh of the latter resolution would however preclude resolution of turbulent structures in the shear layer, producing a RANS-like solution. There is thus a clear danger involved in employing the S-A DES approach: while accuracy on coarse and well-resolved meshes is comparatively good, the results on intermediate meshes is unpredictable. In terms of practical applications, this means the S-A DES model cannot be applied with confidence to flows of low to intermediate Reynolds number.

5.2.5 Local Mesh Refinement

Since the diffuser flow is only of moderate Reynolds number, even a well resolved simulation is within the bounds of possibility. Having a moderately well resolved solution and excellent experimental data provides the opportunity to test and validate methodologies to further reduce the computational cost through local mesh refinement. Following on the description of mesh refinement indicators in sec.4.5.2, a coarse mesh solution will be analysed and modified to test various approaches. Specifically, a mesh with only half the resolution of the fine mesh case (LD17) was constructed and a solution calculated using the SGS energy equation model and the same methodologies employed in sec.5.2.3. This solution is then analysed for mesh refinement indicators and a uniform ($2 \times 2 \times 2$) refinement applied to each hexahedral cell that meets the specified criteria.

Turbulence Indicator

The first indicator explored was the simple SGS turbulence ratio. Implicit in the LES approach is that only a small portion of the turbulence is modeled, which suggests that regions with high SGS to resolved scale turbulence ratios will be under-resolved. Eq.4.117 defines the time averaged indicator function as follows:

$$\langle M \rangle = \frac{\langle K_{sgs} \rangle}{\langle K_{resolved} + K_{sgs} \rangle}$$

A value of $\langle M \rangle = 0$ thus indicates no SGS turbulence while $\langle M \rangle = 1$ represents a region with zero resolved turbulence. The comparison of this field for the fine (LD17) and coarse (LD21) mesh cases is displayed in fig.5.25.

It can be seen that even for the coarse mesh the SGS turbulent fraction is everywhere below or close to 0.2, which would indicate that even the coarse mesh is adequately resolved. The predictions however show that the coarse mesh does not adequately resolve important turbulent features. The conclusion is thus that in the low to intermediate Reynolds number regime simulated here, even the comparatively small turbulent scales are anisotropic and crucial to the behaviour of the overall flow. There is also a lack of large relative differences between the two simulations, the slight elevation in the SGS turbulence

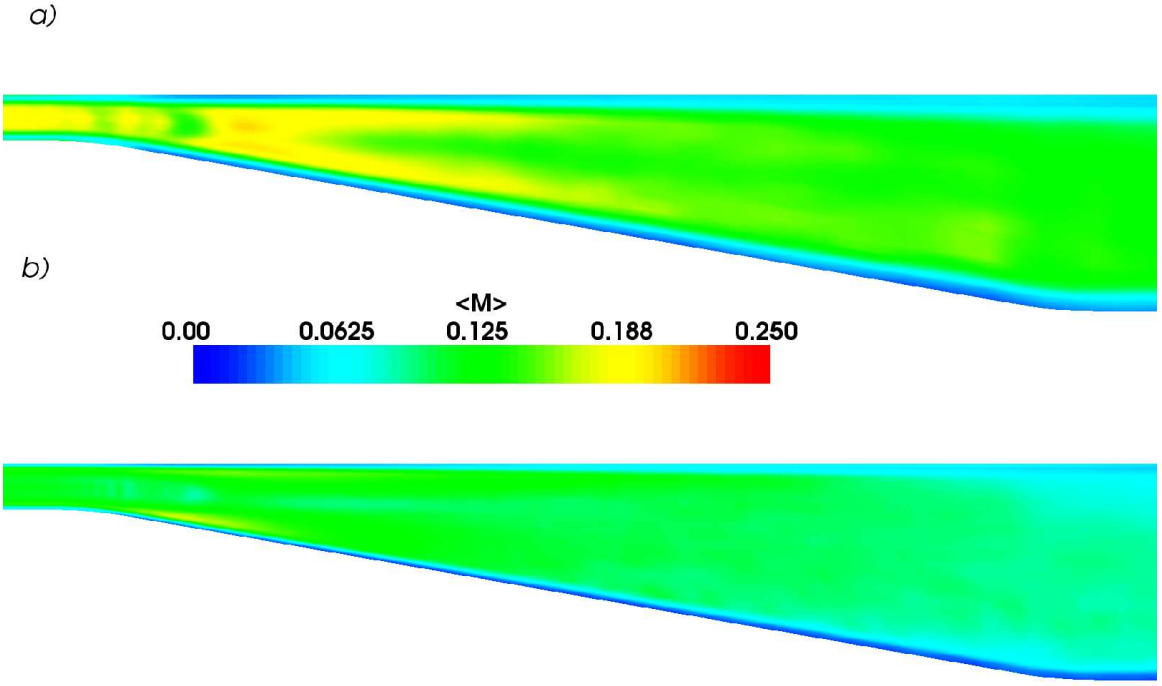


Figure 5.25: Ratio of SGS to total turbulent energy a) Fine mesh (LD17) b) Coarse mesh (LD21)

fraction being almost universal in the coarse mesh case. For this case $\langle M \rangle$ is not a very useful indicator for local mesh refinement purposes since it infers an almost universal increase of mesh density throughout the domain. As a result, no mesh refinement was employed in conjunction with this approach, the conclusion being that low to intermediate Re flows are not good candidates for this form of analysis. This does not invalidate the SGS turbulence ratio as a refinement indicator for more vigorous or less well resolved flows.

Residual Error Estimation

Residual error estimation provides another tool to locate regions of inadequate resolution in the solution domain by detecting local deviations from the assumed linear distribution of quantities across the control volume. By substituting time averaged values for the relevant quantities in eq.4.112 an error estimation for the average LES solution can be

5. Basic Test Cases

derived. It was found that error estimation for the transported SGS turbulent energy produced the most useful predictions. To produce this estimate, the following substitutions are effected to eq.4.112:

$$\mathbf{U} = \langle \bar{\mathbf{u}} \rangle \quad (5.2)$$

$$\phi = \langle K \rangle \quad (5.3)$$

$$\Gamma_\phi = \nu + \frac{C_\mu \langle K_{gs} + K_{sgs} \rangle^2}{\langle \epsilon \rangle} \quad (5.4)$$

where the approximation of the standard $K - \epsilon$ equation is used to derive the effective time-mean turbulent viscosity given the mean resolved and sub-grid scale turbulent energy and the mean dissipation rate. The resultant error estimate is now normalised using the volume weighted flux contributions of the terms in the error equation [66], to produce the error magnitude. The corresponding distribution is displayed in fig.5.26 for the fine (LD17) and coarse (LD21) mesh cases respectively.

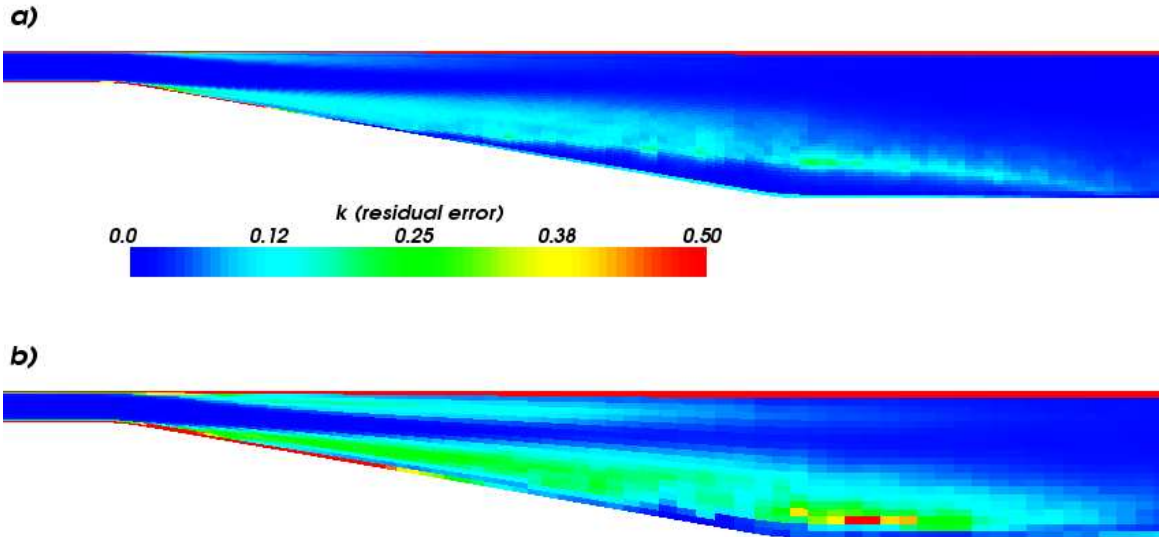


Figure 5.26: Normalised residual error in unrefined diffusers a) Fine mesh diffuser (LD17) b) Coarse mesh (LD21)

It is immediately clear that there is much greater contrast between the SGS turbulent energy error estimates for the different mesh densities than was observed for the SGS turbulent energy ratio indicator. The error estimate is thus expected to provide a much

more precise measure of grid quality than the latter method. Fig.5.26(b) shows zones of increased error correspond to the regions of higher shear, specifically in the free-shear layer and along the top and bottom walls of the expanding section. These are also regions of the highest SGS turbulence production and most vigorous resolved scale motion and it is therefore not surprising that the uniform density mesh resolves gradients here less well than in calmer portions of the flow. Interestingly, both the fine and coarse mesh estimations show a very high error level along the top wall. Under-resolution of this boundary layer could explain the inaccurate wall shear stress predictions along its extent.

To derive a mesh refinement strategy from the error estimate, cutoff values are chosen and all regions of the domain with residual errors in excess of these values are marked. For the purposes of the current investigation two threshold values are chosen at 60% and 115% of the volume weighted average error over the entire domain. The partitioning resulting from these threshold values is shown as red in fig.5.27. The indicated refinement regions are roughly similar: both prescribe refinement along the entire top wall, along the bottom wall before separation and in the vicinity of the shear layer. The distribution of the 60% cutoff (5.27(b)) extends over a somewhat larger area than the more conservative threshold. Cells falling within the demarcated regions are refined producing case *LD23* for the 115% cutoff and case *LD24* for the 60% cutoff.

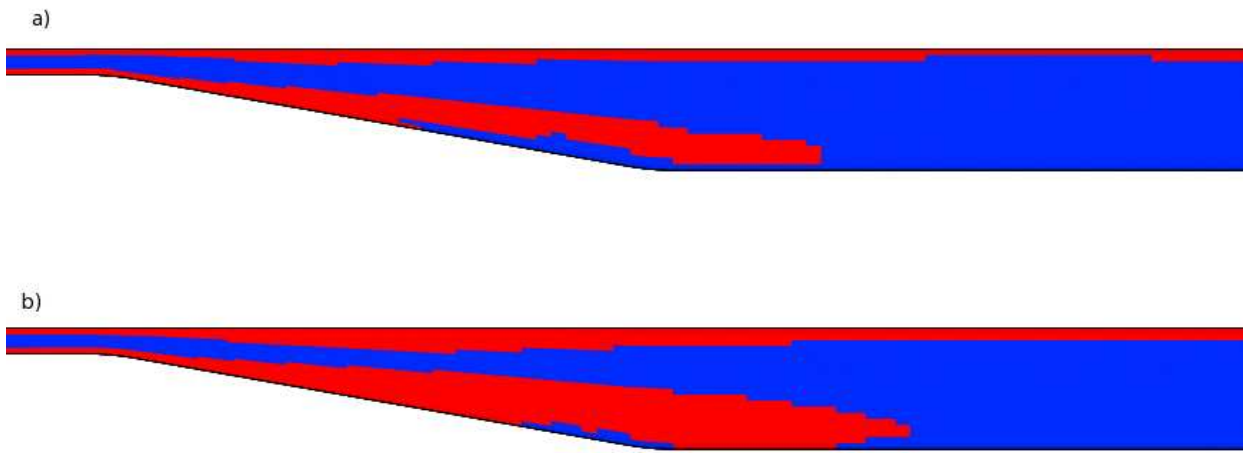


Figure 5.27: Zones selected for refinement shown as red regions a) Refinement for residual $k_{err} > 115\%$ of mean level throughout the domain (LD23) b) Refinement cutoff 60% of mean error (LD24)

5. Basic Test Cases

Solutions are mapped from the coarse mesh to the new meshes and simulations performed in accordance with the specifications set out in sec.5.2.3. Results from the new meshes are compared to the fine and coarse cases in fig.5.28. The results consist of the time and spanwise averaged total (resolved + SGS) turbulent energy distributions. This field very clearly shows the effect of the applied refinement on important turbulence producing features such as separation, free-shear and wall boundary layers. Comparing first the unrefined cases figs.5.28(a) and (b), it can be seen that the coarse mesh produces much higher turbulence at the start of the inclined wall and along the top wall at the same position. This is caused almost exclusively by resolved scale turbulent fluctuations. These elevated levels of turbulence are quickly damped out however, so that the turbulence intensity in the shear layer is lower than for the fine mesh. The position and extent of the shear layer is also distinctly different, being slightly lower and considerably shorter than for case *LD17*. The local refinement in case *LD23* reduces the oscillations at the start of the incline to near the level found in *LD17* and in addition the boundary layer along the top wall is much better resolved. Unfortunately, the refinement region in the recirculation zone is simply not large enough to cover the repositioning of the shear locus from its position nearer the wall in *LD21* to the higher location in *LD17*. The extent and position of this feature is more or less the same in *LD23* as in the coarse mesh solution. *LD24* shows a completely different picture. All major features of the fine mesh solution are accurately reproduced: macro boundary and shear layer characteristics are more or less identical. The only difference lies in smaller scale features which are partially due to reduced averaging times employed for the refined case and the influence of refinement boundaries.

Comparing the error estimates of the refined mesh solutions (figs.5.29(a) and (b)) with the uniform mesh residual errors (figs.5.26(a) and (b)) sheds a different light on the effects of local refinement. The reduction in predicted error is very good in both cases. The refinement boundary is visible as a sudden jump in error level and seems to indicate that the refinement extent is only barely adequate in the case of *LD24* and insufficient around the shear layer in *LD23* confirming observations of the turbulence results. Encouragingly, the refinement boundary does not seem to introduce additional

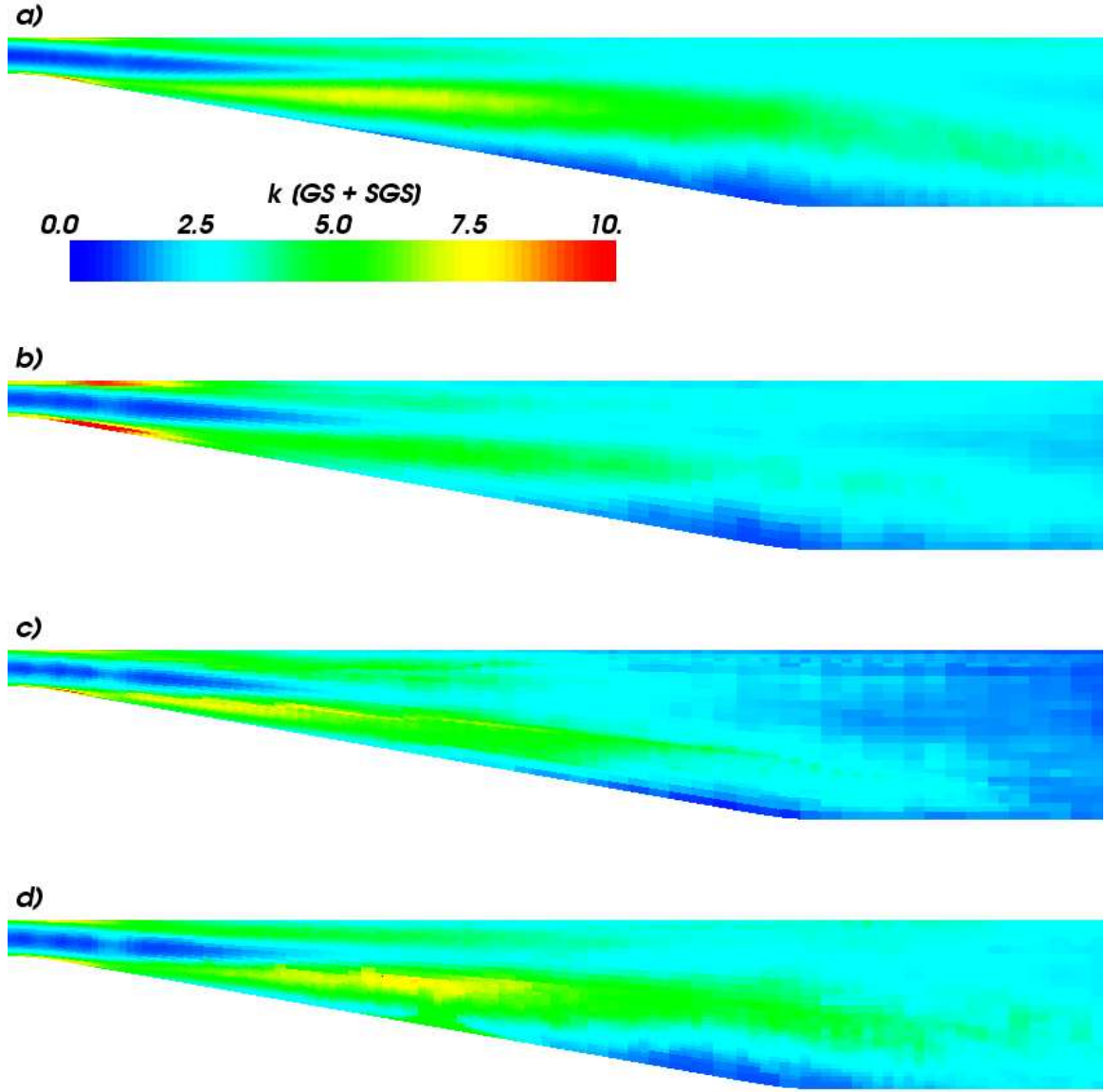


Figure 5.28: Effect of embedded mesh refinement on the turbulence distribution in the diffuser
 a) Fine mesh (LD17) b) Coarse mesh (LD21) c) Refinement cutoff 115% of mean K_{err} (LD23)
 d) Refinement cutoff 60% of mean K_{err} (LD24)

error in its vicinity. Another surprising aspect is the effect of the different refinement patterns on the error along the top wall: although the refinement extent along this surface is similar between the cases, the effect on the error distribution is markedly different. This suggests that the residual error here is closely tied to the position of the shear layer. The mechanism is unclear.

The wall statistics of the different cases are compared in fig.5.30. The results for the

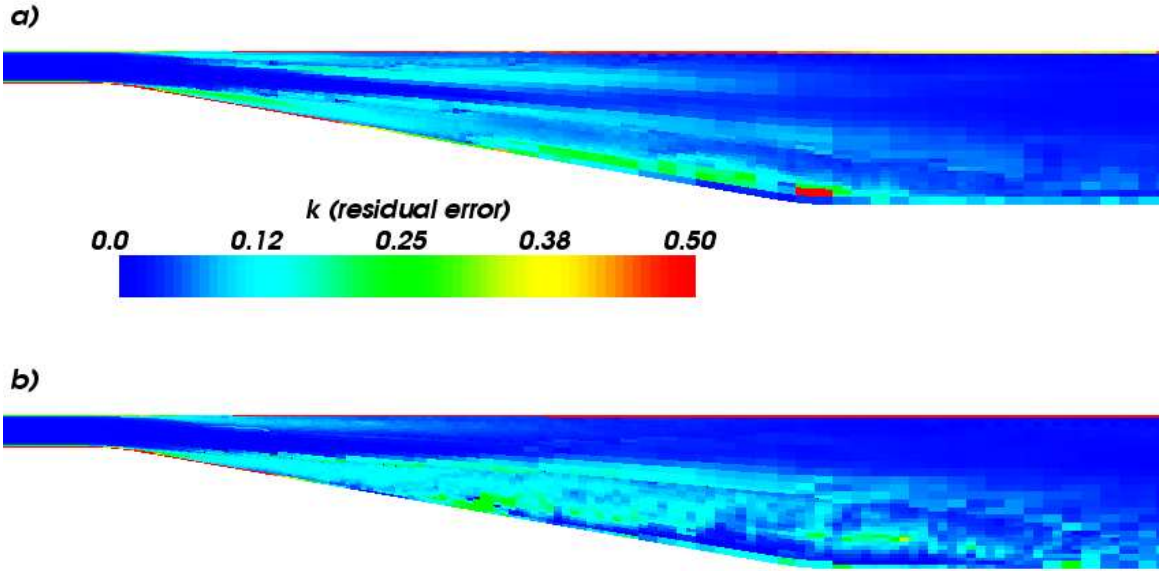


Figure 5.29: Normalised residual error in refined diffusers a) Refinement cutoff 115% of mean K_{err} (LD23) b) Refinement cutoff 60% of mean K_{err} (LD24)

lesser refined case (LD23) can be seen to be very similar to the coarse mesh values; the wall pressure for LD23 being more inaccurate than LD21 and the wall shear being near identical. The case with the greater refined region (LD24), on the other hand, shows results that agree exceedingly well with the fine mesh solution. Note that small high frequency deviations are due mostly to reduced averaging times. The large discrepancy between the accuracy of the locally refined meshes is somewhat surprising considering the modest difference in overall mesh size (200000 vs. 300000 cells). Also of note is the character of the difference: the results do not show a smooth progression from the coarse to the fine mesh, but instead evince a "jump" between cases LD23 and LD24. Since the walls are equally well resolved for both refined cases the discrepancy must lie in the increased shear layer resolution present in LD24. This deduction seems to be born out by the error estimates for these cases (fig.5.29), which clearly show the shift in maximum error from below (LD23) to above (LD24) the region of refinement.

In summary, it has been shown that local mesh refinement can produce simulations of comparable quality on meshes with much lower overall grid size than uniformly fine spacings, resulting in a 50% cost saving in the case of LD24. Using the residual error in the transported SGS turbulent energy as a refinement indicator proved particularly

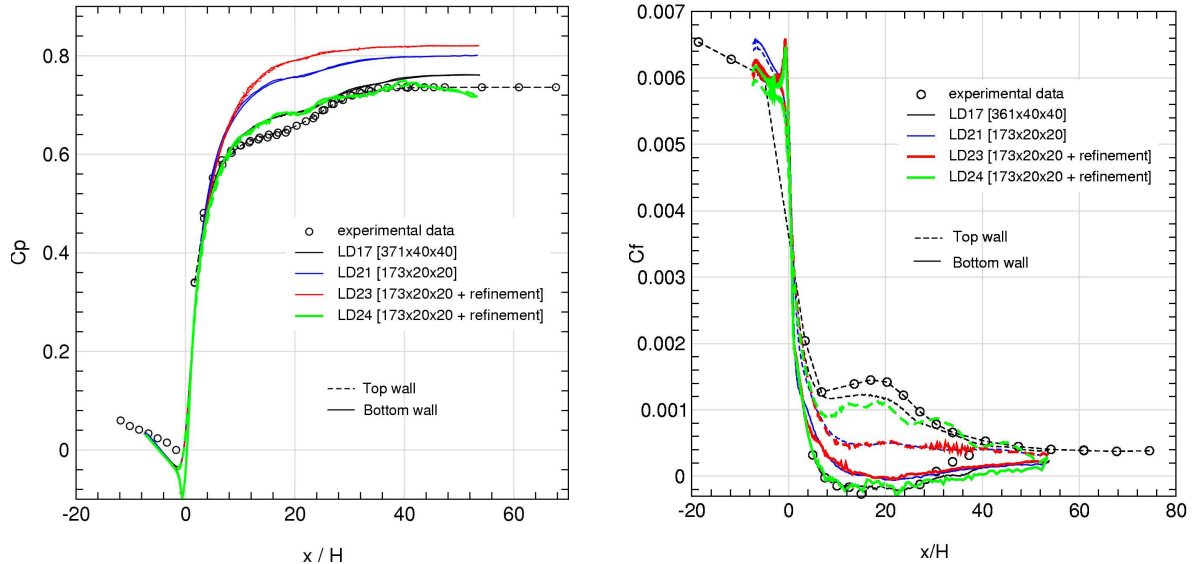


Figure 5.30: Diffuser with embedded refinement wall statistics: pressure coefficient (left), wall shear stress coefficient (right)

successful for the diffuser case, while the SGS turbulence ratio was found inadequate for this class of intermediate Re flows. The refinement test is far from conclusive, since the two variant locally refined meshes produced distinctly different results. Additionally, the line of maximum shear predicted by the coarse mesh case (*LD21*) was not in the right position. As a result, the residual error distribution and thus the region of mesh refinement prescribed by the coarse mesh solution does not coincide exactly with the well-resolved case's prediction of this feature. For case *LD24* the extent of the refinement region is large enough to capture the shear layer, producing very good results, but for case *LD23* the somewhat reduced refinement volume excludes some crucial feature resulting in dramatically poorer comparison with experiment. Mesh refinement for LES thus remains an unpredictable procedure, requiring an iterative approach and some measure of experience.

5.2.6 Summary

The calculations of the diffuser have produced four distinct conclusions:

- It has been shown that relatively coarse mesh LES simulations with simple wall

5. Basic Test Cases

treatments can produce very good results in weakly separating flows, at least as far as the first order velocity moments and wall shear are concerned.

- The LES results have in turn been shown to be superior to equivalent RANS calculations, encouraging the use of LES in similar flows.
- The standard Spalart-Allmaras detached eddy approach was found to be inapplicable to low-Re boundary layer dominated flows that incorporate weak pressure driven separation.
- Finally, embedded local refinement proved to be a viable if unpredictable methodology in LES.

Most importantly, the experience gained in performing the comparatively inexpensive diffuser calculations allowed for a much more measured approach to the main case of the investigation: the wall mounted side mirror.

Chapter 6

Side Mirror

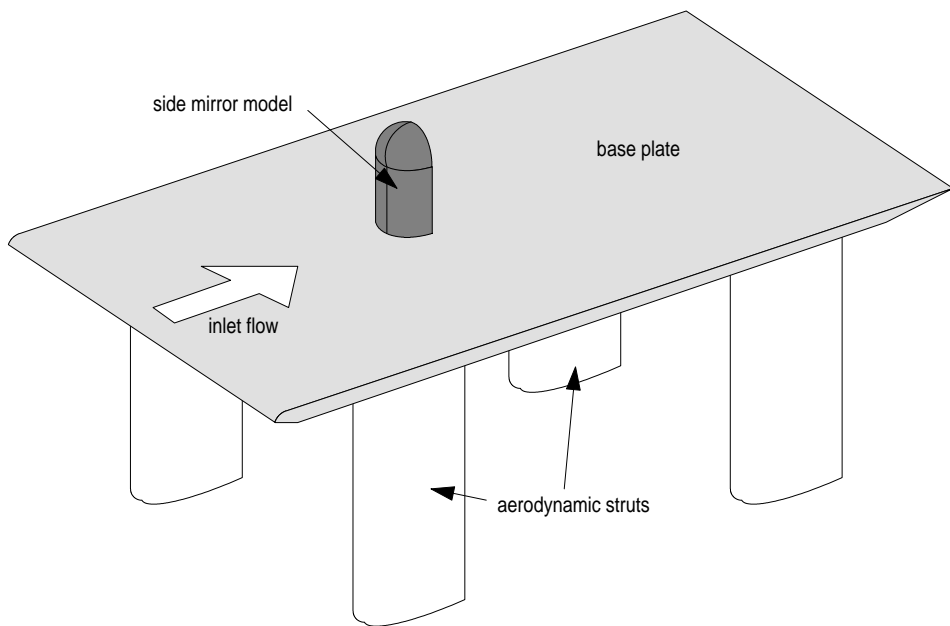


Figure 6.1: Side mirror: experimental setup Case A.

This chapter presents the study of the flow around side mirror-like bodies (which are presented as a reasonable facsimile of car side mirrors) at Reynolds numbers comparable to those encountered in real automotive applications. One of the purposes of these calculations is to ascertain the range of validity of the DES and other approximations inherent in the Spalart-Allmaras and modified SGS turbulent energy models as presented in Chapter 3. Equally important is validation of the LES/DES methodology as an aero-

6. Side Mirror

acoustic noise source predictor. In many cases, automobile side mirrors are believed to contribute significantly to cabin noise at high speed. A CFD tool which could reliably model this phenomenon would thus be of significant value. LES promises this capability and more: not only should it allow evaluation of specific mirror geometries, but its detailed representation of the flow field can also provide insight into the physics of the phenomenon, leading to an intelligent design process. Despite its apparent advantages, concerns of high computational cost and procedural robustness have limited the uptake of LES for this application. Addressing these concerns is one of the chief motivating factors for this investigation.

Two different experimental setups are available for comparison (hereafter referred to as Case A and Case B). In Case A [141] the mirror is mounted on a flat plate with an elliptic leading edge in a high velocity ‘open’ acoustic wind tunnel with a freestream velocity of 38.9 m/s (see fig.6.1). The Case B [31] assembly uses the same mirror model and base plate but is mounted in a closed windtunnel (see fig.6.2) which has a bulk velocity of approximately 26 m/s.

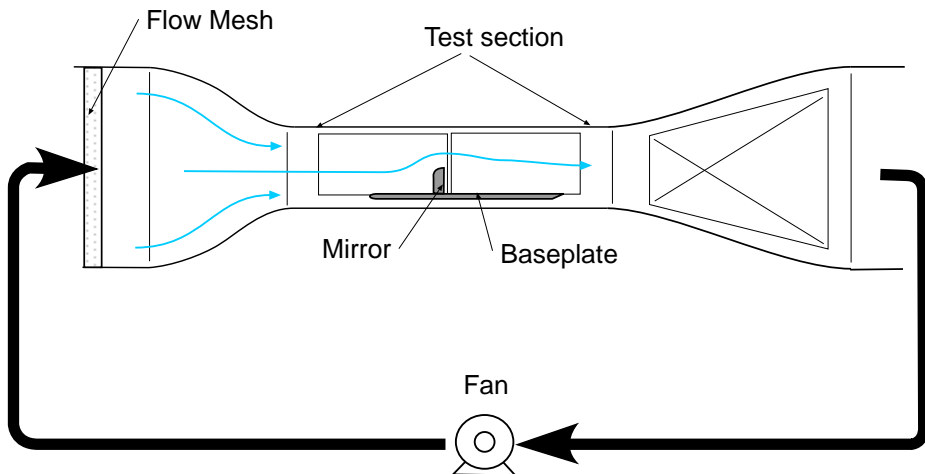


Figure 6.2: Side mirror: experimental setup Case B.

The experiments have several characteristics which make them ideal as test cases for LES and aero-acoustic noise source prediction:

- In both cases the local (shear-based) Reynolds number is of the same order as those

observed in full scale automobiles, guaranteeing the usefulness of the results.

- The inlet flow is reasonably well characterised: for Case A it is for all intents and purposes the oft-studied flat plate boundary layer developing in zero pressure-gradient. The same applies for Case B, but in conjunction with known properties of the wind-tunnel boundary layers. Judicious choice of the calculation domain inlet plane to coincide with the expected transition from laminar to turbulent boundary layer, provides a comparatively ‘easy’ inlet boundary for LES.
- Time averaged velocity and stress measurements were made for Case B using **Laser Doppler Anemometry** (LDA), allowing the comparison of large scale flow features.
- Crucially, both sets of experimental data include measurements of surface pressure spectra at several points on and around the mirror model. Surface pressure fluctuations provide the basis for the calculation of acoustic noise levels using the Lighthill [92] method of generation and propagation separation. Computational agreement with this data therefore represents a necessary condition for accurate noise prediction.
- The flow includes large scale unsteady separation and reattachment features connected by strong free-shear layers, all of which should be well captured by the DES treatment.

The case has some drawbacks as well. Chief among these is the lack of velocity and stress measurements for mirror A. This makes it difficult to examine Reynolds number effects on the flow structures. In addition, the front face of the mirror is known to exhibit laminar flow and transitional behaviour. While the resolved velocity field will tend to behave in the correct fashion under such conditions, the SGS models do not, producing unphysically high turbulent viscosities. The impact of this problem needs to be ascertained as no DES model is currently able to treat transition.

6.1 Side Mirror A

The first part of this chapter deals with the high speed mirror (Case A). The freestream velocity of 38.9 m/s is equivalent to a vehicle speed of nearly 140 km/h, which produces a Reynolds number of approximately 5×10^5 based on the mirror diameter. Such high vehicle speeds, are commonly encountered and present a challenging regime for automotive designers concerned with aero-acoustic noise levels. Available experimental data includes static and dynamic pressure measurements and limited oil film visualisations. It is the earliest available data set and as a result this particular mirror was the subject of most of the permutations with respect to setup, model implementation and numerics. Brief mention is made of this evolution of simulation methodology, with the focus resting on the wealth of data generated from the calculations.

6.1.1 Computational Setup and Reference Details

The experimental data was collected at FKFS aero-acoustic wind tunnel at the University of Stuttgart and published by Hoeld *et al.* [56]. A photograph of the experimental rig can be seen in fig.6.3. The raised aerodynamic struts, combined with the tunnel's comparatively low levels of free-stream turbulence produce very well-behaved boundary conditions. The main focus of the experiment was the measurement of aero-acoustic noise sources via high frequency surface pressure transducers and point noise levels using microphones. Dynamic pressure measurements were made at several points on and around the mirror, with particular emphasis on the region downstream of the mirror edge. The measurements were made at a frequency of 20 kHz, which is more than sufficient to capture all significant audible noise-producing frequencies [36]. Several test geometries and varying angles of attack were considered during the experiment, but the current setup was the one chosen as being the most representative of this class of flows and as a consequence was used for all LES comparisons.

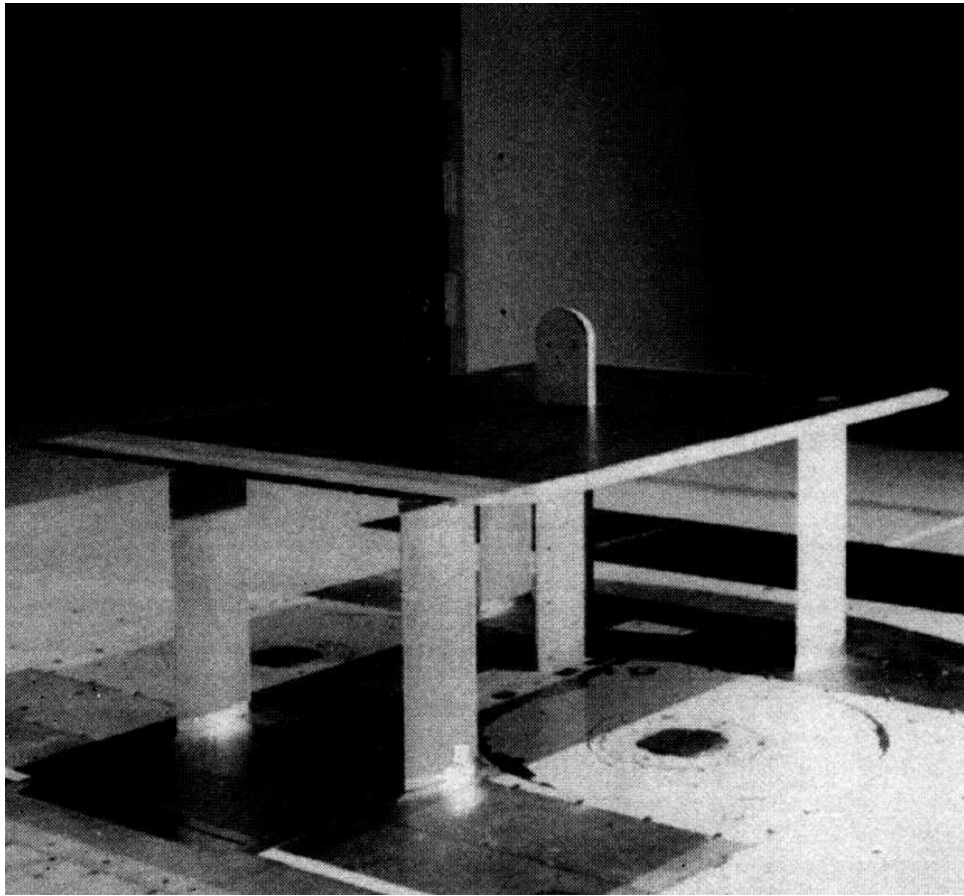


Figure 6.3: Mirror A experiment (reproduced from Siegert et al. [141]).

Solution Domain and Model Geometry

The simulation solution domain and applied boundary conditions are graphically represented by fig.6.4. As can be seen from the figure, the mirror consists of a half cylinder topped by a quarter sphere with a diameter of 20 cm. In the experimental setup, the mirror is placed 1m downstream of the leading edge of the base plate. In the simulation however, the mirror is only 80 cm from the inlet. This allows us to specify the inlet properties unambiguously, since the 20 cm between the leading edge and the start of the computational domain at the imposed free stream velocity is approximately the same length needed for a flat plate boundary layer at this Reynolds number to transition to the turbulent regime. Assume that the flow arriving at the leading edge of the base plate has

6. Side Mirror

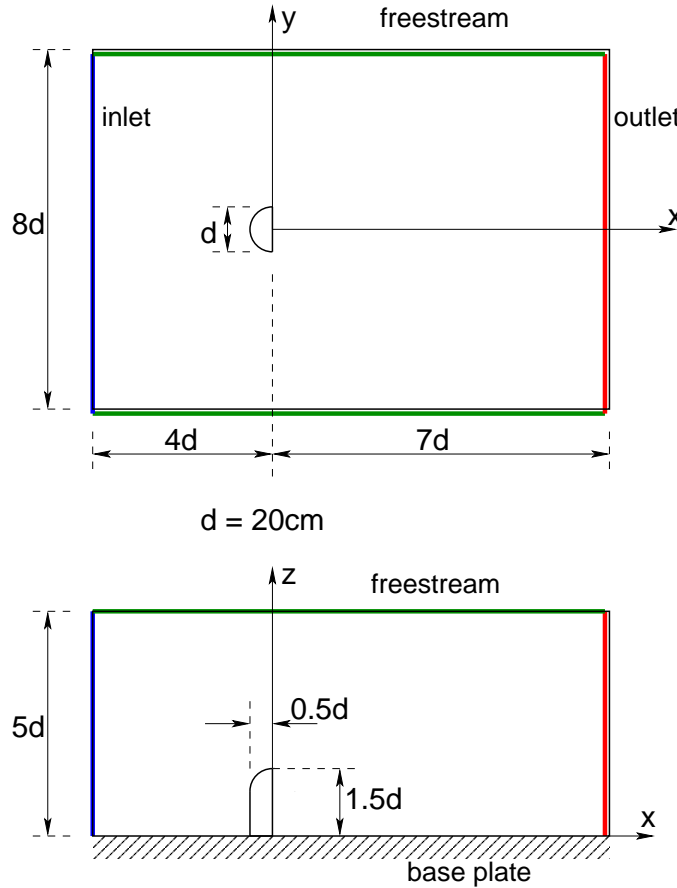


Figure 6.4: Problem domain and boundary conditions for side mirror A.

a uniform velocity and the laminar boundary layers growth follows the classical relation

$$\frac{\delta}{x} = \frac{4.910}{\sqrt{Re_x}} \quad (6.1)$$

$$Re_x = \frac{U_b x}{\nu} \quad (6.2)$$

where x is the distance from the leading edge, U_b is the free stream velocity and δ is the boundary layer thickness defined as

$$u|_{y=\delta} = 0.99U_b \quad (6.3)$$

The transition from laminar to turbulent boundary layer occurs at a streamwise Reynolds number of between 5×10^5 and 3×10^6 . For the current setup this corresponds to a distance from the leading edge of between 0.197 m and 1.982 m. We can thus plausibly assume that the flow entering the calculation domain is on the verge of transition. Thus the mean

velocity in the near-wall region can now be deduced from the displacement thickness, free stream velocity and a parabolic velocity profile. The near-wall SGS turbulence intensity under these conditions will be negligible, so we set it to a small constant value determined by the background freestream turbulence intensity (1 – 2%). Since the boundary layer entering the domain is assumed to be laminar and the DES approach with RANS treatment in the near-wall region is being employed, there is no point in trying to impose turbulent structures on the incoming flow. Additionally, the low levels of free stream turbulence (< 2%) allow all turbulence at the inlet to be modeled as a RANS or SGS viscosity.

The lateral and top boundaries are implemented as symmetry planes. While this is not a strictly accurate representation, their location is chosen far enough from the mirror body so that the effects of blockage (3.5%) will be minimal. The outlet is a standard convective boundary located at a position downstream where no reverse flow or zero-gradient assumptions will affect statistics in the measured region. The base plate and mirror surface are no-slip impermeable walls with instantaneous wall functions used to provide the tangential shear stress at the surface.

Numerical Grids

For the purposes of this project the only available grid generation method able to ensure meshes of sufficient quality for LES was a block type generator. In addition, a limited form of refinement could be employed to increase resolution in critical areas. The combination allows for very fine control of mesh density and quality, but makes it very difficult to simulate domains of more than elementary complexity, another reason why the side mirror was chosen as the primary test case.

As emphasised in chapter 4, grid generation is at best an iterative procedure and the construction of the side mirror mesh was no exception. The initial mesh had a graded body conforming structure composed of nearly 5 million cells. The solution of this problem took nearly 3 months on a 16 processor SGI Origin 2000 computer. Unfortunately, the results were marred by the curved (body fitted to the mirror front face) inlet surface and naive inlet property specification. The long time spans required by the calculation make such errors particularly costly and in response a more efficient mesh was developed using

6. Side Mirror

local mesh refinement. The coarse mesh version (700000 cells) of this grid is depicted in figs.6.5 and 6.6. The finer mesh which is used for the bulk of comparisons in this section, uses the same base mesh, but several layers of successive refinement in the region of the mirror surface and the wake put the final cell tally at approximately 3.3 million cells.

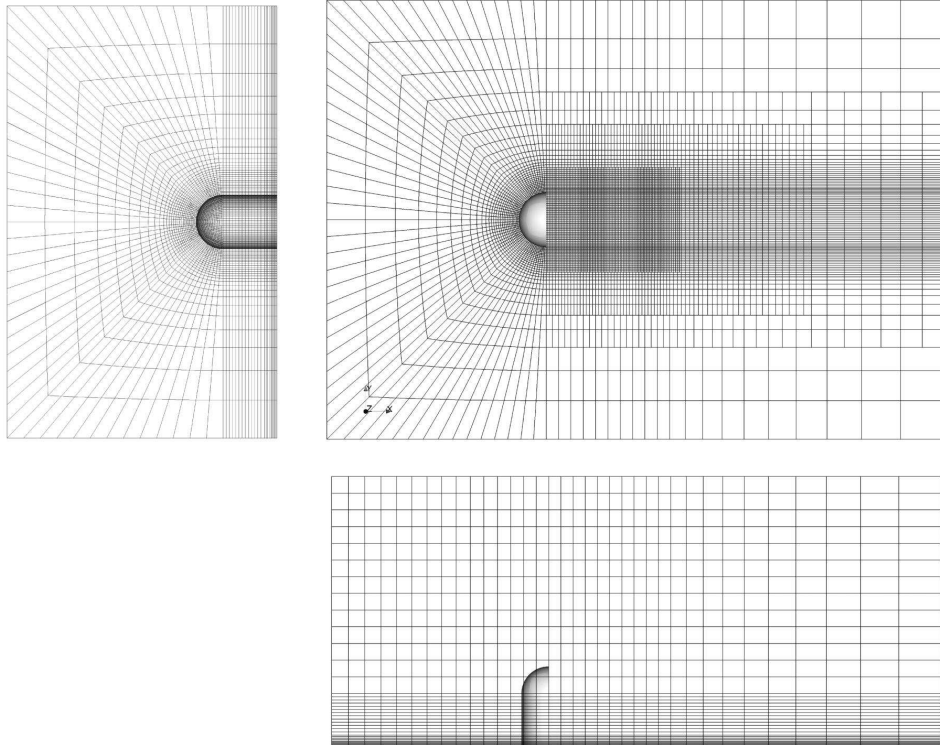


Figure 6.5: Coarse mesh for mirror Case A,

The main concerns influencing the shape and distribution of the mesh were:

- Capturing the dynamics of the free shear layer encapsulating the recirculation zone behind the mirror, a vital feature in terms of the overall simulation, but one ideally suited to LES. The bulk region corresponding to the mirror wake is meshed and refined to have cubic cells $2.5 \sim 5\text{mm}$ to a side.
- Aero-acoustic noise at sub-sonic velocities is for the most part generated when turbulent structures impact and pass over solid boundaries [43]. In addition, the strong shear above the base plate requires high wall normal resolution if its evolution is to be captured accurately. Since the regions of highest shear (and turbulence produc-

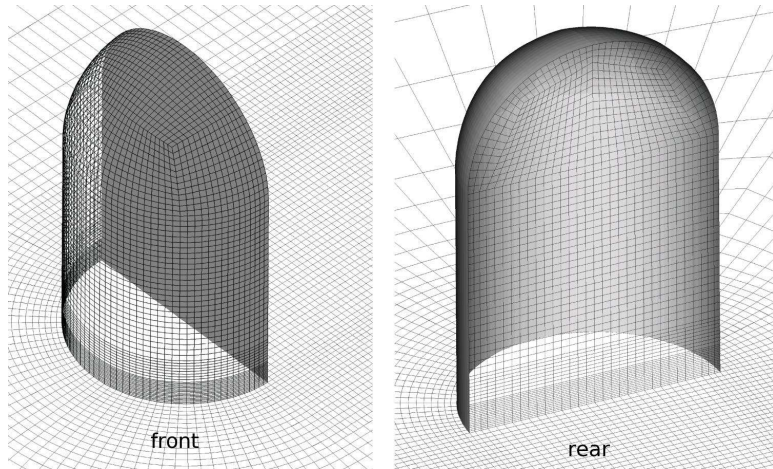


Figure 6.6: *Mirror A coarse surface mesh*

tion) will occur near the base of the mirror edges the mesh is contracted and refined normal to the base plate to produce cells with wall normal dimensions of between $y^+ = 5$ and $y^+ = 20$ adjacent to the surface. (Extra levels of embedded wall-normal refinement are not shown in fig.6.5.)

- Strong pressure gradients and changes in shear are also expected on the cylindrical front face. Repeated embedded refinement reduces the wall normal cell size in this region to $y^+ \approx 5$. The hope is that this resolution will be sufficient to capture the adverse-pressure-gradient induced laminar separation expected a short distance upstream of the edge. (Not shown in fig.6.5.)
- Away from regions of interest the cell count had to be kept to a minimum to reduce the overall cost of calculation. This is accomplished by stretching the mesh toward the inlet, outlet and lateral boundaries. Wall functions are employed for solid surfaces in these regions since typical wall normal cell spacings are of the order of $y^+ \gtrsim 100$.

The final mesh, while much better than the initial attempts, is far from optimal: a large number of cells are located in the middle of the recirculation zone where they are superfluous. High non-orthogonality caused by the body-fitted grids will introduce numerical inaccuracies and/or additional correction costs and despite some knowledge

6. Side Mirror

of the expected flow field the transient, highly coupled nature of the problem makes it difficult to guarantee that all important events will be resolved adequately. The results and experience so far show however, that LES as implemented here is surprisingly robust in the face of such concerns. Nevertheless, an attempt is made to more rigorously address these and other issues during the construction of the Case B grid in sec.6.2.

Model and Simulations Details

The setup described in the previous section is initialised using first a potential flow solution, followed by a steady-state RANS simulation of the geometry. LES simulations were performed on a coarse and a fine mesh, the former being used to initialise the latter. In all cases, accumulation of data for averaging purposes only commences after flushing of the calculation domain for at least one (or more for the first coarse mesh calculations) flow-through times, calculated as $t_{ft} \approx 0.06$ s based on the bulk inlet velocity. Averaging times are based on the largest scale motions produced by the mirror flow field: bulk periodic shedding. Assuming the Strouhal number is similar to that of a cylinder in a cross flow, $St = \frac{f_s d}{U} \approx 0.18$, the period of the phenomenon can be found as $t_s \approx 0.03$ s. Ideally, the averaging time should be large enough so that the mean data approaches symmetry to within a small degree of variance. In practice and especially for large unsteady three-dimensional motion, this can result in very costly simulations. Since the main focus of the investigation is the reproduction of aero-acoustic noise sources which occur on time and length scales much smaller than the main shedding frequency, an averaging time encompassing at least 10 realizations of the main shedding time scale is considered sufficient for our purposes. As will be seen, the resulting datasets although not perfectly symmetrical, tend sufficiently toward that state to engender confidence in the accuracy of the averaged quantities.

Owing partially to the use of the unbounded central differencing scheme for convection discretisation, the maximum Courant number in the domain has to be kept below one (typically in the range 0.5 - 0.8) to ensure stability. Coupled with the high velocities (> 50 m/s) and small cell sizes (~ 1 mm) necessary to resolve noise producing turbulence, this enforces the use of a very small timestep. For the fine mesh it is chosen as $\Delta t = 1 \times 10^{-5}$ s

and for the coarse mesh $\Delta t = 2 \times 10^{-5}$ s, which requires that the simulations be averaged for approximately 32000 and 16000 timesteps respectively.

Calculations on the meshes were performed using the turbulent energy and Spalart-Allmaras models to predict the SGS stresses as outlined in chapters 3 and 4. In addition, a calculation is performed with a variation of the turbulent energy model, where the influence of the damping function on the front face is increased to better approximate the laminar flow in that region. Results presented in the following sections include a general overview of the observed flow structures and dynamics, followed by comparative plots of the various simulations and the experimental data.

6.1.2 Flow Features and Dynamics

The first set of results show the flow around the mirror in a purely qualitative sense. Due to the lack of experimental data, no comparisons are attempted and unless stated otherwise, it should be assumed that all simulations in this section produce results that are broadly similar.

The flow is dominated by a large recirculation zone behind the body, bounded on all sides by free shear layers. Other features of note include a horse-shoe shaped vortex that wraps around the front and sides of the mirror and an extensive V-shaped wake region downstream of the recirculation zone. In figs.6.7 and 6.8 these features are clearly depicted by velocity magnitude contours and streaklines of both the time mean and instantaneous flow for the fine mesh case using the Spalart-Allmaras DES model. Figure 6.7 shows the distributions in the symmetry plane passing through the mirror, from which the extent and properties of the recirculation zone are readily apparent. Inspection indicates that reattachment is predicted at $x/d \approx 2.25$ downstream of the mirror edge, which compares favourably with the experimental value of $x/d \approx 2.5$. The contour plot (fig.6.7a) also portrays the growth of the top portion of the bounding shear layer that drives the recirculation. This image is mirrored by the streaklines in fig.6.7b, which show the initially thin layer slowly increasing in thickness until a point about 2 diameters downstream of the mirror edge is reached, after which a sudden divergence of fluid and a thickening of the shear layer occurs. From fig.6.7c, which shows the instantaneous velocity contours for

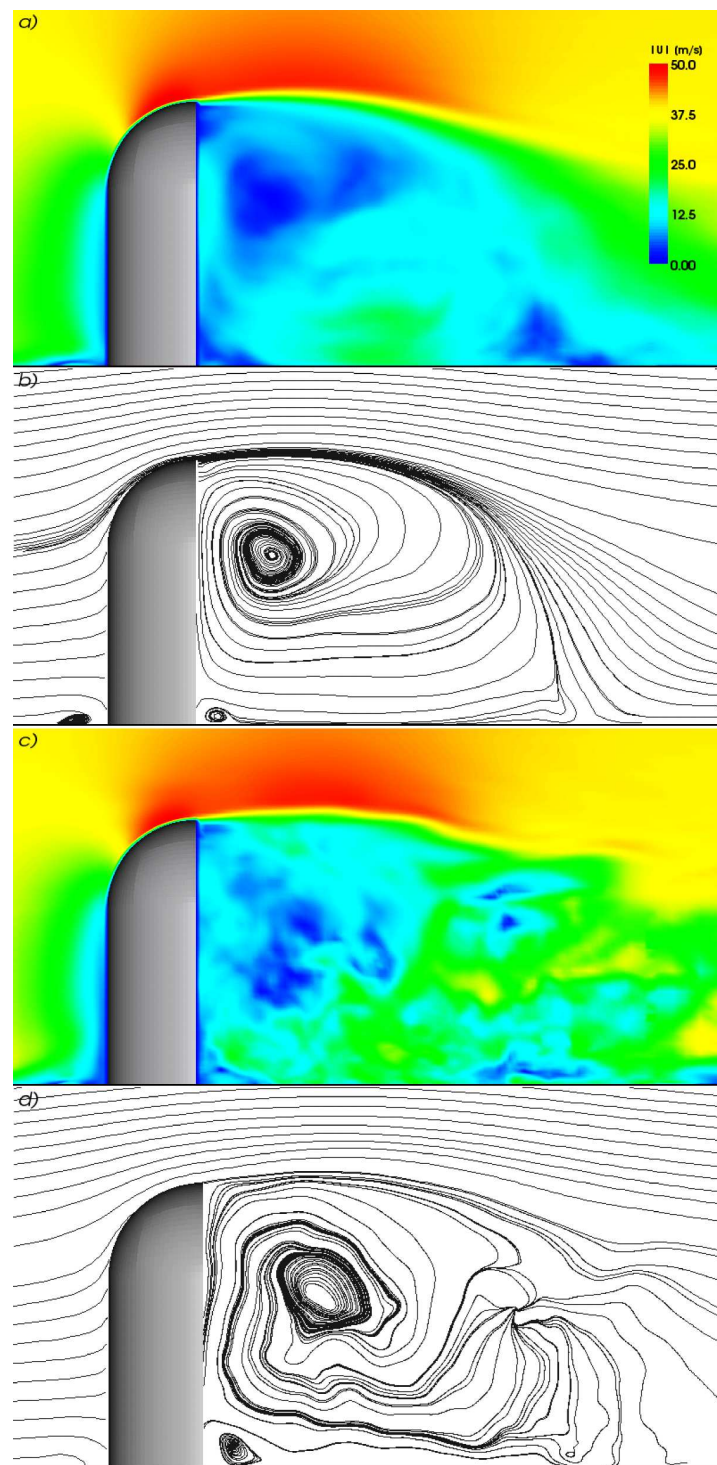


Figure 6.7: Centre-line velocity: a) mean velocity magnitude, b) mean streaklines, c) instantaneous velocity magnitude and d) instantaneous streaklines.

the section, this growth can be seen to correspond to a sudden increase in the scale of resolved turbulent motions, a non-linear growth regime. Because the momentum transfer characteristics of the shear layer largely determine the extent and strength of the recirculation zone, capturing its dynamics is crucial for predicting the gross properties of the flow around the mirror.

The streaklines in figs.6.7b and 6.7d also show some interesting secondary circulations: a counter-rotating vortex at the base of the recirculation zone (referred to from here on out as the base vortex) and a bow vortex in front of the mirror. The base vortex is similar to that observed in the backward-facing step problem and occupies a spanwise extent nearly as wide as the mirror itself. The bow vortex is more complex, being a mildly unsteady structure that wraps around the front of the mirror in the shape of a horse-shoe. The two vortices are of similar origin, and although their appearances differ markedly, their overall influence on the system is subjectively the same. Both are formed as a result of competing forces produced by the retarding influence of the base plate and the sharp curvature of the flow at the junction of the base and the mirror. The low pressure generated in the base vortex tends to “pull” fluid around the edge of the mirror and into the open ends of the vortex, creating small regions of higher velocity fluid directly behind the mirror edge than would otherwise be the case. The effect is intermittent and has a destabilising effect on the shear layer in its vicinity.

The bow vortex does not interact with the shear layer directly. The characteristic horse-shoe shape is the result of induction by the primary vortex formation mechanism and the acceleration of flow around the edges of the mirror. Its primary influence is to move fluid down and toward the base of the mirror and the wake, which because of its intermittent nature, will also tend to initialise instabilities in the near-base shear layer. This induction also tends to increase velocities at the junction of the edge and the base plate, intensifying the local shear and turbulence production, which in turn should have a positive effect on noise producing structures spawned in this region.

Figure 6.8 shows the same general overview of velocities and streaklines in a plane 1.5 cm above the base plate. From the asymmetry in fig.6.8b, it is clear that this time averaged solution has not yet reached a statistically steady state on the scale of the

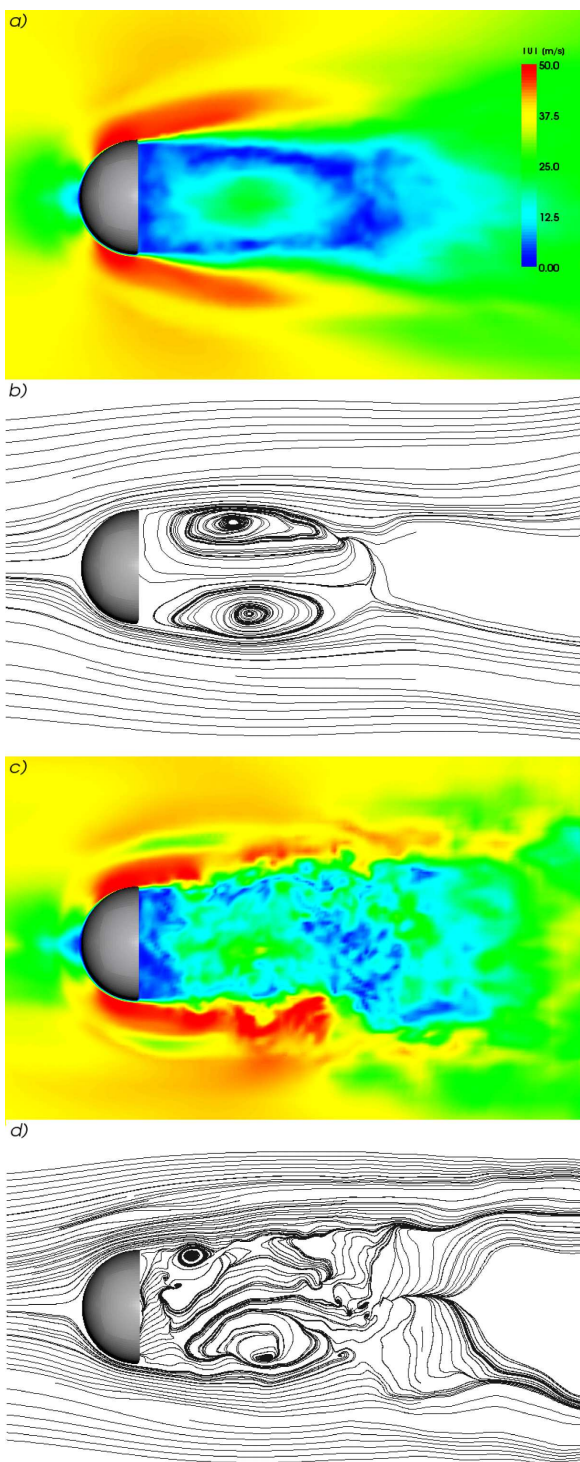


Figure 6.8: Base plate ($z = 1.5 \text{ cm}$) velocity: a) mean velocity magnitude, b) mean streaklines, c) instantaneous velocity magnitude and d) instantaneous streaklines.

main shedding cycle. When compared to the instantaneous realisation (fig.6.8d) however, it appears that the solution is converged enough to allow qualitative assessment of the averaged flow features. Figure 6.8a presents a good overview of the extent and strength of the recirculation zone in the vicinity of the base plate. The zone in which the mean flow reattaches is visible as a velocity minimum at the downstream end of the structure. The velocity maximum slightly to the left of this location coincides with the region of strongest backflow in the recirculation bubble. Also apparent is the V-shaped spreading of the entire wake complex, a feature typical of bluff body flows and a result of the continued growth and mixing produced by the free-shear layer. Less obvious is the effect of the bow vortex on the velocity field. Its influence can however be seen in the minima between the high velocity fluid extending from the mirror front face down the side of the wake and the far field. The vortex' circulation accelerates flow from its upstream side over itself and then down toward the base of the mirror, producing the twin high speed plumes that can be seen bounding the wake. The effect is especially pronounced in the instantaneous velocity field of fig.6.8c.

An interesting feature is revealed by the streaklines behind the mirror in fig.6.8b. The **mean** recirculation zone is seen to contain two counter-rotating vortices. Taken in combination with the mean streaklines on the mirror symmetry plane (fig.6.7b), these vortices are seen to form one large upside-down “U”-shaped circulating structure inclined toward the rear face of the mirror. Note that this configuration does not necessarily exist in the instantaneous flow (fig.6.8d), instead the wake is populated by spanwise alternating shedding type vortices that combine temporally to form the mean structure.

The dynamics of the mirror flow are more clearly depicted by a time series animation of the result fields. An animation of the deviatoric pressure on the base plate

$$\bar{p}' = \bar{p} - \bar{p}_{mean} \quad (6.4)$$

for the coarse mesh case using the turbulent viscosity SGS model is included in Appendix A (anim.A.1). The swirling circular low pressure (blue) regions in the animation represent upright vortex cores moving over the surface. The “upright” nature of the vortices being shed from the mirror edge can be more clearly seen from the -100 Pa isosurface animation also included in Appendix A (anim.A.2). Focussing in the vicinity of mirror edge, a

6. Side Mirror

relatively high frequency perturbation source is observed. The exact source of these perturbations is unclear - while they are more common near the base plate they occur around the entire periphery of the mirror edge. So while it is likely that the base and bow vortices contribute to the formation of instability, their limited extent mean they cannot be the only effectors. A probable candidate is self-induction via a natural periodic oscillation of the shear layer. This would also account for the regular nature of the edge vortices.

Moving downstream, we note that not all the eddies produced at the trailing edge develop into fully-fledged shedding vortices. Only around 30 – 50% of the initial perturbations enter a growth stage that result in the large swirling motions so characteristic of shedding flows. The main processes that prevent vortex growth are agglomeration, where one eddy is “swallowed” by another, and advection, which can cause a developing eddy to be ejected from the free-shear layer that normally supplies the energy fuelling its growth. As can be seen from the isosurface animation, the early stages of vortex growth in the free-shear layer is two-dimensional in that the eddies comprise of elongated structures roughly aligned with the edge of the mirror that spawned them. As these structures start to grow to sizes of the same order of magnitude as the recirculation zone, they begin to interact with each other and non-local portions of the shear-layer. In particular, as the larger agglomerated eddies move downstream, their tops encounter the downward flow at the rear of the recirculation bubble. The mean velocity distribution of the flow in this region (see figs.6.8a and 6.7a) causes the pillar-like vortices to be tilted toward the centre line. The spanwise velocity differential across the wake then induces stretching so that the main vortical structures in the far wake are nearly parallel to the base plate and diagonally aligned with respect to the free stream (see anim.A.3).

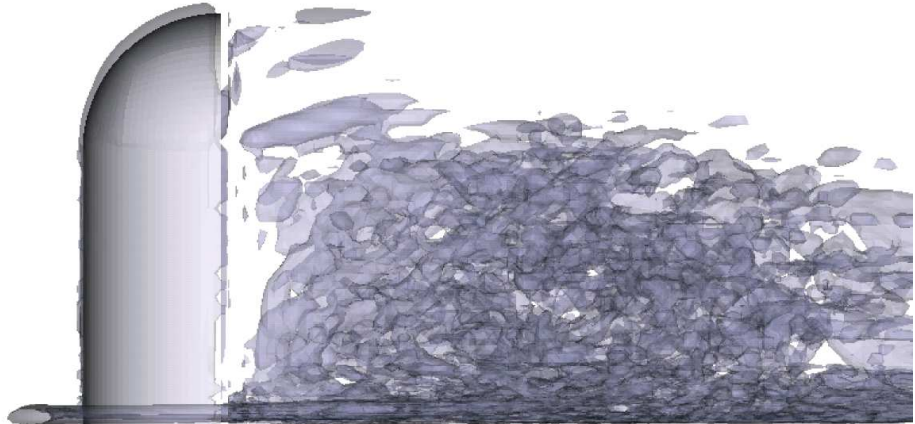
Even at this coarse resolution, the animations very clearly show the bow vortex both as a low-pressure isosurface and as a surface pressure minimum in front of the mirror base. The strongly intermittent character of the bow vortex may be an artefact of the low mesh resolution, as instantaneous realisations of finer mesh cases show a more stably fluctuating structure at this location. Figure 6.9 takes a more detailed look at the bow vortex, which is here visualised by the translucent isosurface of the time mean second invariant of the

velocity gradient, $Q_{\nabla \bar{U}} = 5 \times 10^5$ (see sec.2.2) for the finer mesh case using the Spalart-Allmaras DES model. From the side view (fig.6.9a) the bow vortex can be seen to reside very close to the base plate and has a flattened oval cross section. The shape of the vortex follows the bulk flow direction as it curves around the mirror. Although it is not clearly shown in fig.6.9b because of the limitations of the visualisation method, the vortex grows weaker and larger as it extends downstream. Since its rotation grows less intense further downstream, visualising the entirety of the structure is all but impossible as smaller, less well defined eddies start to obscure the vortex as the iso-surface value is decreased. It is thought likely that the downstream portions of the bow vortex extracts energy from the mean shear in the boundary layer similar to Townsend's "attached eddies" (fig.2.16), while the portion in front of the mirror acts like a two-dimensional roller. Interestingly, fig.6.9b seems to indicate that there is a second smaller bow vortex between the primary and the mirror. This structure does not occur in the coarser mesh cases or when using the turbulent energy SGS model, but as we shall see from the LDA measurements in sec.6.1.6 there is some evidence that it is present in the experimental flow. Its origins are thought to be a result of induction by the main vortex, employing a balance of forces similar to that giving rise to the larger structure. The fact that LES is accurate enough to capture both of these structures is very encouraging, since similar RANS calculations are unable to do so [56].

The strength and extent of the recirculation zone is largely determined by the properties of the free-shear layer that bounds it. In fig.6.10 several sections through the flow domain show the intensity of the shear layer via time averaged contours of the total (resolved and SGS) turbulent normal stresses. The results are for the finer mesh using the turbulent energy SGS model, all sections use the same scale with darker regions denote higher intensity. The plot has been rendered in grey-scale to highlight the shape of the feature. Development of the shear layer structures is seen to be a gradual process, thin plumes directly behind the mirror edge trace an approximately linear perturbation growth for the first half mirror diameter downstream. In the portion of the flow nearer the base plate more complex interactions like agglomeration and non-linear growth cause a sudden increase in the width of the shear layer after this distance. Behind the upper portion

6. Side Mirror

a)



b)

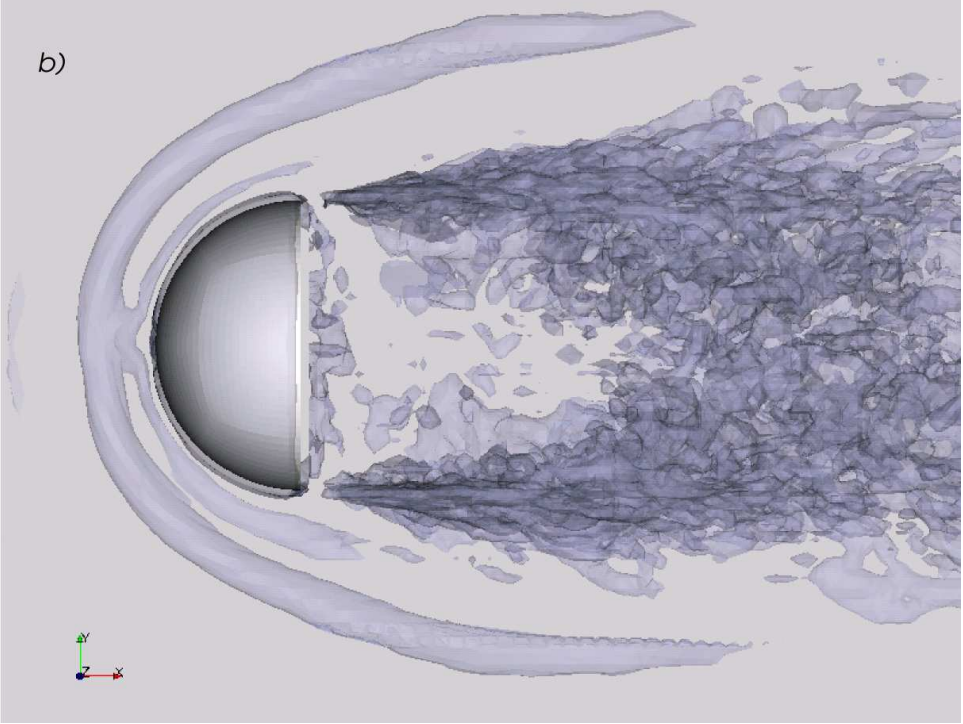


Figure 6.9: Bow vortex depicted by mean 2nd invariant of $(\nabla U)_{mean}$, $\mathbb{Q}_{\nabla \bar{U}} = 5 \times 10^5$ a) side and b) top view.

of the mirror, this accelerated growth is not observed, a stable rate persisting for a diameter or more downstream of the trailing edge. The difference in behaviour is tied to the velocity distribution of the recirculating flow: the maximum backflow occurs above the base plate, while the flow near the top of the mirror is more or less aligned with the bulk velocity. This results in much higher velocity gradients and thus shear stresses and turbulent growth rates in the regions adjacent to the reversed flow.

Positioned two diameters downstream of the obstacle and half a diameter above the base plate is a large region of very intense turbulent motion (figs.6.10a and 6.10c) where all but the lowest portion of the free-shear layer converges. This region also overlaps the reattachment line of the recirculation zone, which being unstable contributes significantly to the observed turbulence intensity. The majority of the fluctuations are however the result of rapidly growing shear-layer eddies that are convected through this region.

The structure of the shear layer while complex in its detail has relatively simple overall features. Observed from a mean flow perspective, it begins at the edge of the mirror as a thin region of high velocity gradients. Perturbations across the velocity gradient quickly grow into elongated two-dimensional vortices that either meld into other eddies or grow into the large shedding structures. The shear-layer's thickness grows along with these eddies and does so more rapidly near the base plate where stronger backflow sets up steeper velocity gradients to power this growth. As the flow progresses toward the reattachment line, it is pulled down and toward the symmetry plane by the low pressure behind the mirror, with the downward motion being more pronounced. Some fluid is pulled into the recirculation zone by the backflow, effectively splitting the shear layer. The remaining (greater) portion carries on downstream, but the upside-down "U"-shape of the shear-layer is deformed by the deflection. The top of the shear-layer moves much closer to the base plate (see fig.6.10a). The resulting continuity considerations now cause the "legs" near the base plate to spread further and further apart (fig.6.10b), producing a large "V"-shaped wake with a flattened cross-section downstream of the mirror. Travelling down-stream the slower moving wake is gradually eroded by the free-stream, giving it a tapered appearance. Since the far wake is known not to contribute significantly to the production of aero-acoustic noise, eddies in this region are generally not very well

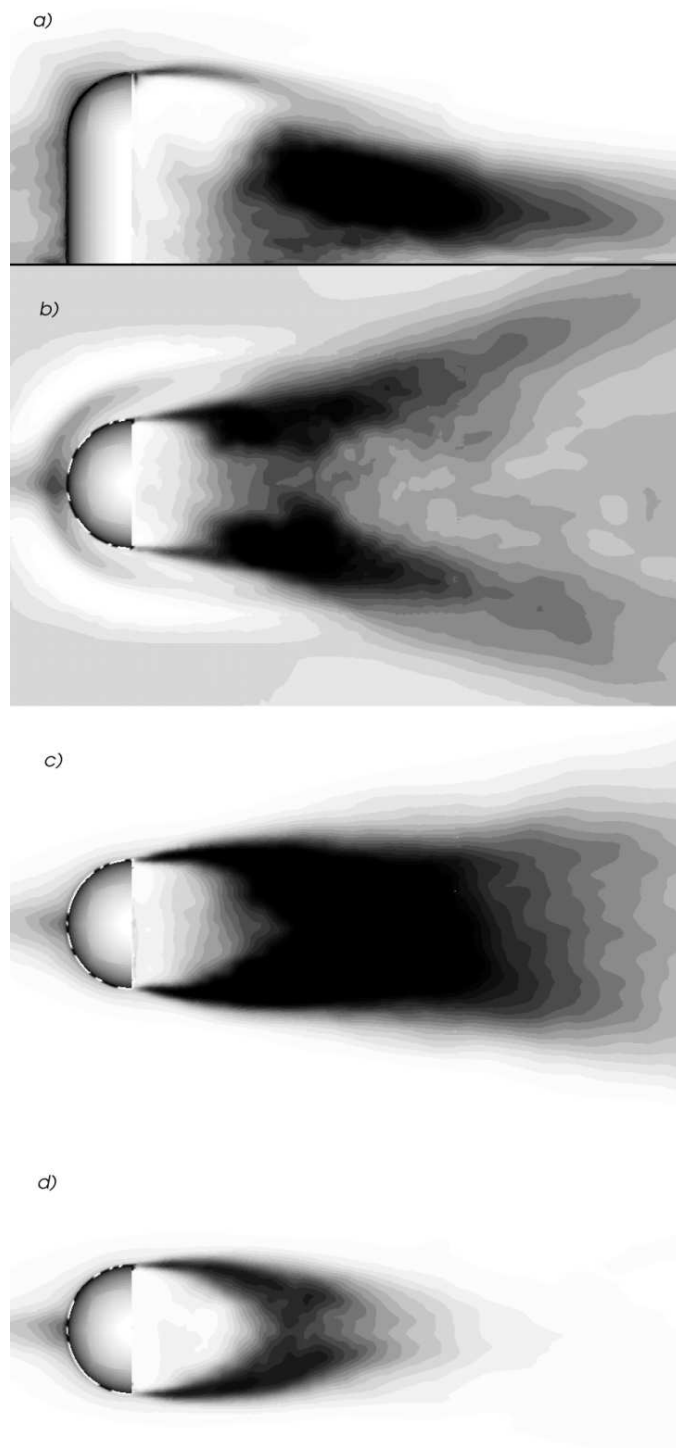


Figure 6.10: Mean total turbulence intensity (resolved + SGS) for a) centre plane and base parallel planes with b) $z = 0.5\text{cm}$, c) $z = 10\text{cm}$ and d) $z = 20\text{cm}$.

resolved. The dominant structures are however identified (see anim.A.3) as diagonally inclined spanwise rollers that are direct descendants of the shedding vortices produced in the free-shear layer around the recirculation zone.

6.1.3 Static Pressure

Having identified the salient features and dynamics of flow around the mirror, we can now turn to a quantitative comparison of selected properties with the experimental data to gauge the accuracy of the different LES calculations. For mirror Case A, the following representative simulations are chosen for this purpose:

- AK1: Coarse mesh (700k cells) + SGS turbulent energy transport model,
- AK3: Fine mesh (3.3M cells) + SGS turbulent energy transport model,
- ASA3: Fine mesh (3.3M cells) + Spalart-Allmaras DES model.

Comparing cases AK1 and AK3 allows us to examine the effects of grid density, while contrasting AK3 and ASA3 provides some insight into the influences of the different SGS model implementations on the solution.

The first result comparison is for the mean pressure at discrete locations on the mirror surface. This is a first order statistic. High accuracy is therefore expected and any deviations from experiment should highlight basic shortcomings of the LES/DES calculations. The overall surface pressure distribution on the mirror for case AK3 is shown in fig.6.11. Predictably, the pressure is highest on the front of the mirror where flow stagnation occurs. It then rapidly decreases toward the trailing edge as the impinging flow becomes more oblique and the flow parallel to the surface accelerates. A few centimetres upstream of the edge a minimum is reached, thereafter the tendency of the tangential flow to move liquid away from the surface causes the pressure to increase again. The flow will thus experience a favourable pressure gradient across most of the front face and an adverse pressure gradient near the mirror edge. This is somewhat similar to the case of the well documented cylinder in a cross-flow [13, 160, 164]. For the case of the cylinder flow separation will occur before 90° if the attached flow remains in the laminar regime ($Re_d < 10^7$)

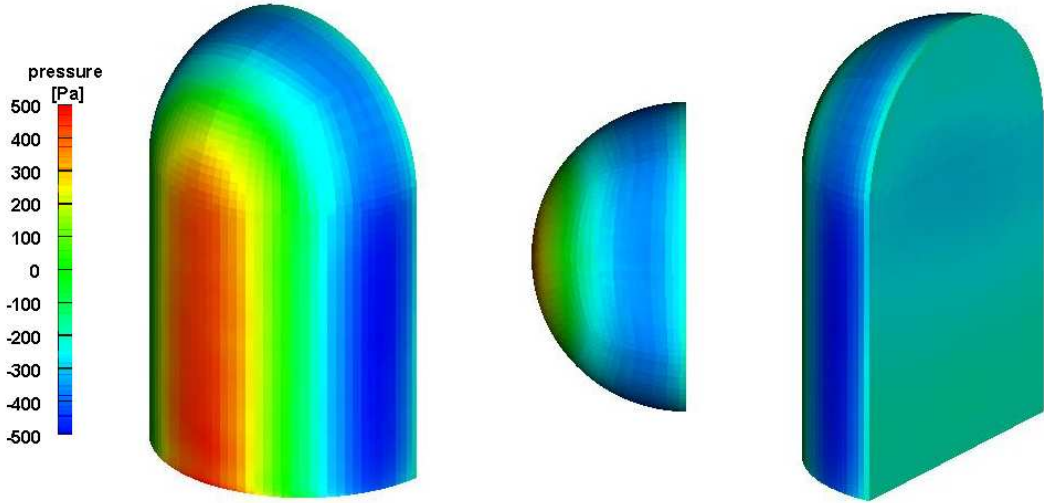


Figure 6.11: Mean pressure on the mirror surface for AK3.

and after 90° if the flow on the front half undergoes transition. While the half-cylinder of the mirror will not behave identically to the cylinder because of the backflow in the recirculation region, it is reasonable to assume that transition to turbulence on the front face will occur (or not occur) at similar Reynolds numbers. For Case A, the Reynolds number based on the mirror diameter is $Re_d \approx 5 \times 10^5$, which puts the attached flow firmly in the laminar regime. Any inaccuracies in the turbulence modelling or numerical noise in the resolved velocity could thus have important consequences. We will take a closer look at the implications of this problem in the context of the mirror case and the currently implemented modelling and numerics in sec.6.1.5.

On the rear face of the mirror the pressure distribution is more uniform. Slightly elevated levels are seen near the base where the recirculating flow impinges on the surface, lower pressure coincides with the upper portion of the recirculation zone where there is a movement of fluid away from the mirror. All the views of the mirror surface display a good approach to symmetry in the pressure field. This is not surprising since very large scale, low frequency fluctuations are not expected very close the mirror. Note also, that only the surface pressure contours for case AK3 are displayed since the distributions for the other representative cases are nearly identical.

The locations of the probe points where discrete pressure levels are compared is shown in fig.6.12. The left hand side of the figure contains the locations on the mirror front face, while the rear points are depicted on the right. The exact locations of these points can be found in Appendix B. Figure 6.13 shows the dimensionless pressure at each of these locations for all three LES cases, the experimental data and RANS RNG-k- ϵ calculation (from [141]). The X -axis represents the consecutively numbered probe locations, divided into different regions. The overall agreement for the LES simulation is clearly good, with the different SGS models and grid densities performing very similarly. The coarse mesh AK1 under predicts the pressure at the edge of the front face (probes 1-9) more than the fine mesh cases, but otherwise the discrepancy between the calculations is marginal. Scrutinising the different probe ranges (depicted in fig.6.13) from left to right, we see that along the front edge (probes 1-9) all the calculations under predict the pressure to some extent, with the Spalart-Allmaras DES calculation (ASA3) providing the best agreement with experiment. Over the centreline locations (probes 10-20) agreement is excellent for all the LES calculations. The only pressure that is not accurately predicted is probe 10, which is also near the edge. Note, that despite the zero gradient assumption on the pressure between the wall and the first grid point, stagnation pressures are very well predicted, not only in their level, but also in terms of distribution. The probes along the front curvature (21-25) show similar behaviour to 10-14. We can however see a much larger discrepancy between the calculated and measure values as the probe location approach the mirror edge. Again the simulations under predict the pressure in this region, but this time by a larger margin. Switching to the rear of the mirror we see very good agreement for both the rear edge region (probes 26-31) and the rear centre (32-34). Pressure levels on the mirror's rear are largely determined by the characteristics of the wake, e.g. stronger recirculation can increase the back pressure and *vice versa*. The accuracy of the simulations in predicting the levels and distribution in these regions is thus an indicator that at least the gross properties of the recirculation bubble have been recreated.

The question naturally arises as to why the pressure minimum near the mirror edge is under predicted. Recall that the flow on the front face of the mirror is almost certainly

6. Side Mirror

laminar. Neither of the currently-implemented SGS models incorporate a treatment for laminar shearing flow regimes (examples of such model modifications in the literature have shown limited improvement [160]) and as a result the production of SGS turbulence will continue irrespective of the actual flow behaviour. The expectation is thus that, even if there are no resolved scale motions, there will be significant levels of modeled SGS turbulence in the flow adjacent to the surface. Such turbulence will increase wall normal mixing, which counters the tangential movement of fluid away from the curving mirror surface, causing elevated near-wall velocities and the reduced surface pressure minimum.

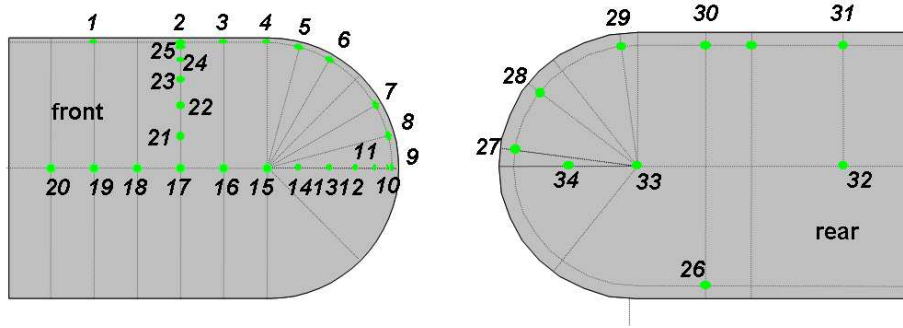


Figure 6.12: *Static pressure probe locations.*

Although no experimental data is available for the mean pressure distribution on the base plate, a brief comparison of the distributions produced by the different cases will highlight qualitative differences. Figure 6.14 shows from left to right the base plate pressure distribution for cases AK1, AK3 and ASA3. Some salient features common to all the results are the high pressure bow region; low pressures coincident with the accelerating flow near the mirror edges; and the large low pressure recirculation zone in the wake. All the frontal high pressure regions show (to a greater or lesser extent) the footprint of the bow vortex as slivers of low pressure penetrating the stagnation region. The wake low pressure regions for the different cases, although similar, differ in some details of the zone's extent. In particular, a comparatively low degree of symmetry is observed in the finer mesh cases due to insufficient averaging on the scale of the main shedding vortices. As noted before, this is not of great concern for the aero-acoustic portion of the investigation as the frequencies of the noise producing structures are much higher than the shedding

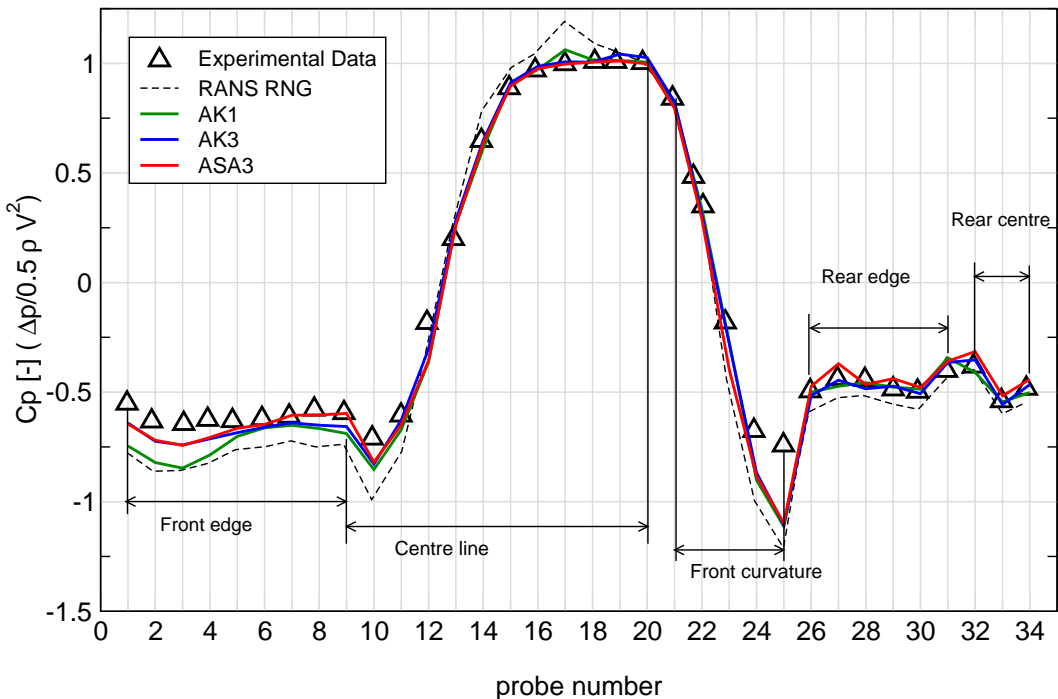


Figure 6.13: Comparison of mean pressure at selected probe locations on the mirror surface.

frequency.

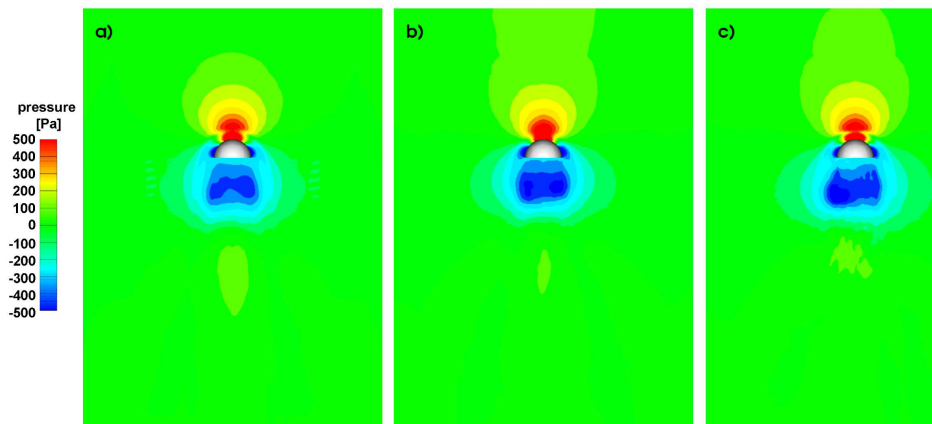


Figure 6.14: Mean pressure distribution on the base plate for cases a) AK1, b) AK3 and c) ASA3.

6. Side Mirror

Overall, agreement of the mean pressure results with experimental data is very good. Discrepancies are explained in terms of deficiencies in the current SGS model implementations. When comparing the mean pressure results for the fine and coarse mesh SGS energy model simulations (AK1 and AK3), we find very little difference in statistics, especially at the probe locations. On the front face of the mirror, increased length scales (and thus turbulent mixing) due to the coarser mesh exacerbate the problem of overshoot in the local pressure minima near the mirror edge. While this is not universally the case, we see some effect of this in the front edge region of the comparison. Comparing the probe results from the different SGS models (AK3 and ASA3) with experiment, fails to clearly distinguish a superior approach. The Spalart-Allmaras DES model performs slightly better on the front face, while the SGS turbulent energy model shows better average agreement on the rear of the mirror.

Without experimental pressure data on the base plate, it is difficult to evaluate the impact of the failure to replicate the laminar flow on the mirror front face on the wake flow. The expected behaviour is an overall reduction in the dimensions of the recirculation zone, as the lateral motion away from the mirror front surface is curtailed by turbulent mixing and increased wall shear. In the following sections special attention will be paid to deviations that might be indicative of the lack of laminar flow modelling, with the hope that its impact on this class of flows can be quantified.

6.1.4 Pressure Spectra

As stated earlier, one of the main purposes of this investigation is to evaluate the capabilities of LES as an aero-acoustic noise source predictor. Although the actual noise levels will not be calculated, a brief description of how the surface time-pressure data is transformed into point noise predictions is useful in illustrating the part LES can play within the study of aero-acoustics.

The basis for the simulation of the origin and propagation of sound in an acoustic medium is laid by Lighthill's well known acoustic analogy [92]. Equation 6.5 describes the motion of density waves in an acoustic medium at rest (l.h.s.), with turbulent and

thermo-acoustic stresses acting as source terms (r.h.s.).

$$\frac{\partial^2 \rho}{\partial t^2} - a_0^2 \nabla^2 \rho = \nabla^2 \mathbf{T}_{LH} \quad (6.5)$$

$$\mathbf{T}_{LH} = \rho \mathbf{u} \mathbf{u} + (p - a_0^2 \rho) \boldsymbol{\delta} - \boldsymbol{\tau}_v \quad (6.6)$$

Here a_0 is the speed of sound in the medium of density ρ and $\boldsymbol{\delta}$ is the Dirac delta. The Lighthill tensor \mathbf{T}_{LH} represents a combination of turbulent, thermal and viscous ($\boldsymbol{\tau}_v$) stresses. For the purposes of this class of problem it is convenient to work with pressure rather than density. Following Ffowcs-Williams and Hawkings [43], the inhomogeneous wave equation for radiated sound can be derived from the basic Navier-Stokes equations using generalised functions [80], giving eq.6.7 below. This also includes the effects of surface interactions on sound generation.

$$\frac{1}{a_0^2} \frac{\partial^2 p'}{\partial t^2} - \nabla^2 p' = \left(\frac{\partial \rho u_n}{\partial t} \right)_A - \nabla \cdot (\mathbf{n}_A p)_A + \nabla^2 \mathbf{T}_{LH} \quad (6.7)$$

Here p' is the sound pressure, u_n is the surface normal velocity and \mathbf{n}_A is the surface normal vector. The l.h.s. now describes the propagation of sound waves, while the source terms on the r.h.s. have the following physical connotations:

- $\left(\frac{\partial \rho u_n}{\partial t} \right)_A$ is a simple source of order zero known as a monopole and is generated by the displacement effect due to a moving body. A membrane of a loudspeaker is a typical example.
- $\nabla \cdot (\mathbf{n}_A p)_A$ comprises momentum sources (dipoles, order 1), describing the energy transformation of a fluctuating surface force into sound radiation. The impact of turbulent structures on a surface produces this kind of source.
- $\nabla^2 \mathbf{T}_{LH}$ describes turbulent stresses that produce quadropoles, sources of order 2, which are almost exclusively produced in energetic shear layers.

Even in a domain with stationary boundaries, sources of order 1 and 2 are both likely to be present if the flow is turbulent. In practice however, their dependence on Mach number

$$Ma = \frac{U}{a_0} \quad (6.8)$$

6. Side Mirror

where a_0 is the speed of sound, implies that one or the other will normally be dominant in any given flow. The acoustic efficiency η_a for three-dimensional sound radiation is related to the Mach number as follows [141]:

$$\begin{aligned} \text{monopole: } \eta_a &\propto Ma \\ \text{dipole: } \eta_a &\propto Ma^3 \\ \text{quadrupole: } \eta_a &\propto Ma^5[93] \end{aligned}$$

Since the Mach number for the mirror calculation will be in the range $Ma \approx 0.1$, it is clear that surface dipoles caused by unsteady loading will be the only significant source of sound radiation. Neglecting the zeroth and second order source terms from eq.6.7 and assuming small changes in Mach number, provides after some manipulation [141],

$$p'(\mathbf{x}, t) = \frac{1}{4\pi a_0} \int_S \left[\frac{\mathbf{r}}{|\mathbf{r}|^2 (1 - Ma_r)^2} \cdot \frac{\partial \mathbf{n}_A p(\mathbf{y}, t')}{\partial t} \right] dS \quad (6.9)$$

where \mathbf{x} is the observation location, \mathbf{y} is the centroid of the surface element dS , t is the observation time, t' is the radiation time, $\mathbf{r} = \mathbf{x} - \mathbf{y}$ is the acoustic distance and Ma_r is the relative Mach number. The radiated sound pressure at any location can thus be easily predicted by inserting the time derivative of the calculated temporal variation of surface pressure into eq.6.9 and integrating over the surface. The different times t and t' for the reception and emission times respectively, implies that the pressure term in the integral must be evaluated at retarded times. Once the acoustic pressure history at a point is available, it can be converted to sound pressure level (SPL),

$$SPL = 10 \times \log \left(\frac{p'^2}{p_0^2} \right) \quad (6.10)$$

where p_0 is the reference pressure, approximately equal to the smallest pressure difference discernable by the human ear, 2×10^{-5} Pa. Sound pressure level has units of decibel [dB], which is commonly used to categorise sound levels.

Recording surface pressure levels for each timestep in an LES calculation can be an expensive process and measuring the time-pressure trace for the entire surface in an experiment is neigh on impossible. Fortunately, the comparison of pressure spectra at discrete points is sufficient for the level of validation attempted here. Having a broader

overview of the acoustic source distribution is however desirable, if only for contextual reasons. The mean acoustic power density [W/m^2] of a surface noise source can be found from,

$$I_a = \frac{\langle \bar{p}'^2 \rangle}{\rho_0 a_0} \quad (6.11)$$

where the angled brackets represent long time averaging. The power density is easy to calculate for the domain boundary on a cell by cell basis, provided the mean pressure is known *a priori*. This provides a convenient way of locating surface regions that produce the largest contributions to the overall far field noise level and also gives a more complete (but less detailed) picture of the source distribution than discrete point measurements can supply.

To display the noise source intensity on the front face of the mirror, the acoustic power density is converted to sound pressure level so that it may be more easily compared with the point SPL spectra. Figure 6.15 shows the calculated distributions for cases AK1, AK3 and ASA3 respectively.

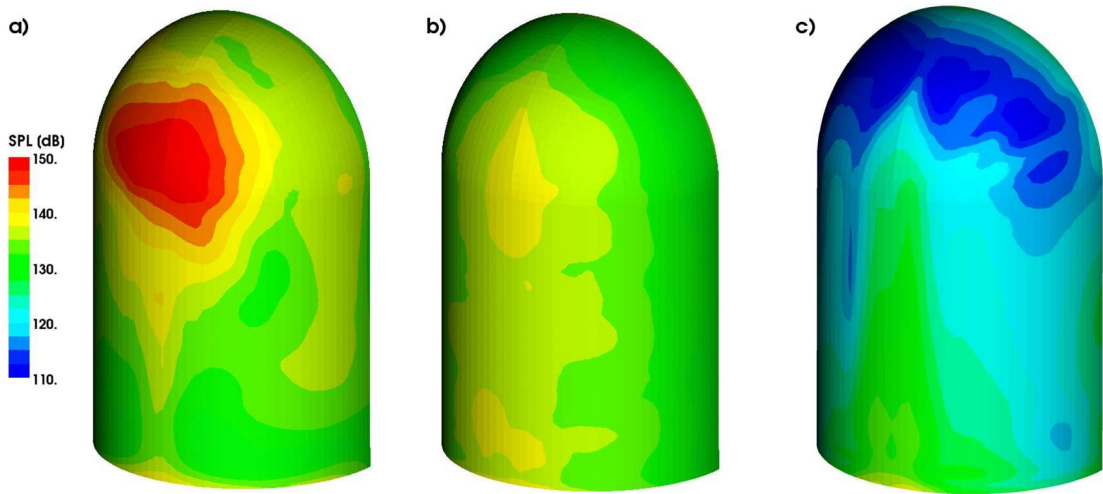


Figure 6.15: Mean sound pressure level ($10 \times \log_{10} \left(\langle \bar{p}'^2 \rangle / (2 \times 10^{-5})^2 \right)$) on the mirror front face for cases a) AK1, b) AK3 and c) ASA3.

The most noticeable aspect is the large differences in predicted sound sources between the three cases. In fact, with the approaching bulk flow being devoid of resolved eddies

6. Side Mirror

one would expect only a moderate amount of noise near the base plate (because of the impinging boundary layer) and edges (shedding). The discrepancy is entirely due to numerical noise. The central differencing scheme used for momentum convection, while being non-dissipative, tends to be dispersive when the mesh spacing is non-uniform [160]. With reference to fig.6.5, we can see the body-fitted mesh in front of the mirror has a rapidly decreasing cell size as it approaches the mirror. In addition, the distortion induced by the radial shape of the mesh produces skewness and non-orthogonality errors that further reduce the accuracy of the results. These error sources combine to create spurious flow fluctuations in front of the mirror that generate pressure fluctuations when they impact the mirror's front surface. The acoustic power density in fig.6.15 is thus to a large extent a reflection of the SGS model's capability to react to and damp out the grid generated numerical noise. Fortunately, the largest errors occur near the centre plane and are rapidly attenuated by the favourable pressure gradient on the front face (see sec.2.4.2, so that the accuracy of the downstream solution is not as negatively impacted as might otherwise be the case. Unfortunately, this numerical noise means the flow near the mirror front face is subject to two types of errors, resolved numerical noise and unphysical SGS turbulence. The accuracy of transient results is expected to be impacted negatively as a result.

In relative terms, case ASA3 (fig.6.15c) is seen to exhibit much lower levels of spurious noise than the cases which use the SGS turbulent energy transport equation. The reason for this can be traced back to the formulation of the source terms in the Spalart-Allmaras transport equation (eq.3.79). The production term (first on l.h.s. of eq.3.79) is proportional to a constant, the working turbulent viscosity, $\tilde{\nu}$ and a rate of strain equivalent \tilde{S} . The definition of this “rate of strain” is given by eq.3.80,

$$\tilde{S} \equiv \omega + \frac{\tilde{\nu}}{\kappa^2 \tilde{d}^2} f_{v2}$$

Although the vorticity magnitude ω goes to zero in the absence of shear, the second term on the r.h.s. has no such limiting behaviour. In fact, it is dependent only on the turbulent viscosity and the inverse square of the length scale \tilde{d} . In the LES portion of the flow \tilde{d} is proportional to the mesh spacing, not the wall distance as in the original formulation. Far from the wall, this term will thus not tend to zero, but instead to some finite value

determined only by the mesh spacing and the cell size. Unlike the turbulent energy SGS model, the S-A model can thus support a small but finite turbulent viscosity in the absence of mean shear. It is this small added diffusion which prevents the build-up of numerical noise upstream of the mirror. The result is a fortuitous cancelling of errors that, while not strictly accurate, is very useful in suppressing weak mesh-induced fluctuations in a low shear environment. More than anything, the presence of the numerically induced noise serves to highlight the sensitivity of the current LES methodology to mesh quality. Even comparatively slow changing cell sizes coupled to mesh skewness and face non-orthogonality can serve to produce unphysical phenomena provided there is no or little damping forthcoming from the SGS model. While this is not a concern in wall-dominated duct flows, it can tend to be problematic in flows that have laminar regions. Combating numerical noise while maintaining high formal accuracy is an ongoing pursuit in LES research.

The next figure (fig.6.16) shows a comparison of pressure spectra at three locations on the mirror front face shown in the accompanying diagram. The spectra are generated by calculating the Fourier transform of the square of the deviatoric pressure time history (i.e. power density),

$$\Phi_p(f) = \int_{-\infty}^{\infty} p'^2(\mathbf{x}, t') e^{-j2\pi f t'} dt' \quad (6.12)$$

For the purposes of the comparison power spectral densities are rendered into SPL using eq.6.10. All measurements were made close to the mirror edge to capture the noise generated by the shedding behind the mirror. The different simulations predict very similar spectra and are in reasonable agreement with experimental data at the two points closest to the trailing edge up to a frequency of $\sim 5\text{kHz}$ (the limit of mesh resolution). However, at point 103, some distance upstream, there is a large discrepancy between the measured and calculated values. It is easy to assume that the bad prediction is due to the numerical noise described above. Upon closer inspection, it is however clear that the shape of the spectral distribution at 103 is remarkably similar to that at points 101 and 102. In addition, reference to fig.6.15 shows a trend where noise levels reach a minimum, before they increase again as the flow moves toward the edge. It is thus probable that the elevated levels at point 103 are induced by the same mechanism that produces

6. Side Mirror

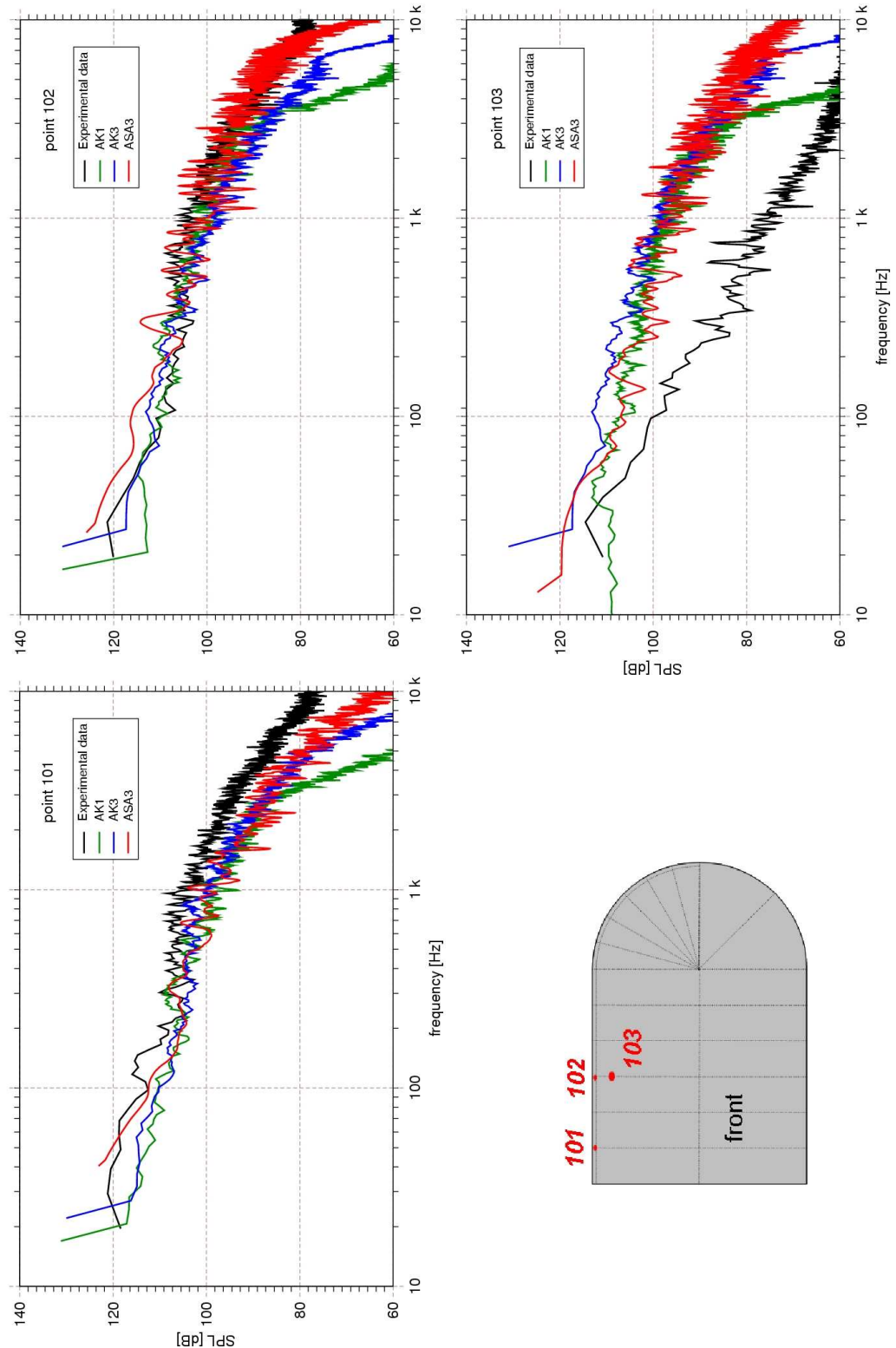


Figure 6.16: Spectra of SPL at selected points on the mirror front face.

the noise at points 101 and 102, and not the upstream numerical noise. The source of this high frequency noise at the front face probe positions is somewhat uncertain. Low frequency or narrow band acoustic spectra can be explained in terms local oscillations, but broadband noise requires a cascade mechanism or intrinsic temporal unsteadiness to spread energy across the frequency range. The predominantly laminar regime on the front face excludes the possibility of a turbulent cascade, leaving a highly variable unsteady shedding phenomenon as the primary candidate for noise production at the mirror edge. Since the experimental data exhibits broad spectrum noise and the calculated values correspond so well at point 102, it is likely that the similar distribution at 103 results from the same source displaced upstream. The cause of this displacement is unknown, but likely due to changes in flow character brought about by the elevated predicted turbulence on the front face.

Focussing on points 101 and 102, good agreement with experiment for all three calculations is apparent. While the slightly depressed high frequency levels at point 101 are probably due to higher turbulent viscosities from the RANS boundary layer, the correspondence at 102 is excellent. Of the three cases we see slightly better predictions from the Spalart-Allmaras DES model over the entire frequency range. Comparing the two mesh densities used in AK1 and AK3 reveals that the coarser mesh resolves significantly less high frequency content than the finer one, but produces equivalent predictions at the low end of the spectrum. This is not surprising since the limit of sound frequency resolution is proportional to the mesh spacing times the local convection velocity:

$$f_{max} \propto |\vec{u}_c| \Delta_c \quad (6.13)$$

In other words, the smaller the resolved noise producing turbulent structures and the faster they are convected across the surface, the higher the resulting sound source frequency. Provided the velocity fields are similar the mesh able to resolve smaller structures will thus capture higher frequency noise sources up the limit of the smallest resolvable structures. It is thus of some significance that the finer meshes resolve the acoustic spectrum up to 7-8 kHz. This range, somewhat higher than the 2-4 kHz aimed for during project planning, results from the fine mesh placed near the edge in an attempt to capture the separation dynamics that occur in its vicinity.

6. Side Mirror

Next the noise properties on the rear face of the mirror are compared, the mean SPL distributions for which are shown in fig.6.17. Note that the contours displayed in these surface plots are predominantly the product of a very narrow energetic frequency band. In the mirror case, the low frequency sub-audible noise is on average much stronger than the higher range content, so that the distribution of the SPL contours displayed throughout is mostly the result of low frequency phenomena. The lack of symmetry in the time averaged mean SPL fields displayed in figs.6.17, 6.15 and 6.19 can thus be explained by comparatively small overall averaging times when compared to these scales. The dominance of the large scales in the contour plots is supported by the SPL spectra

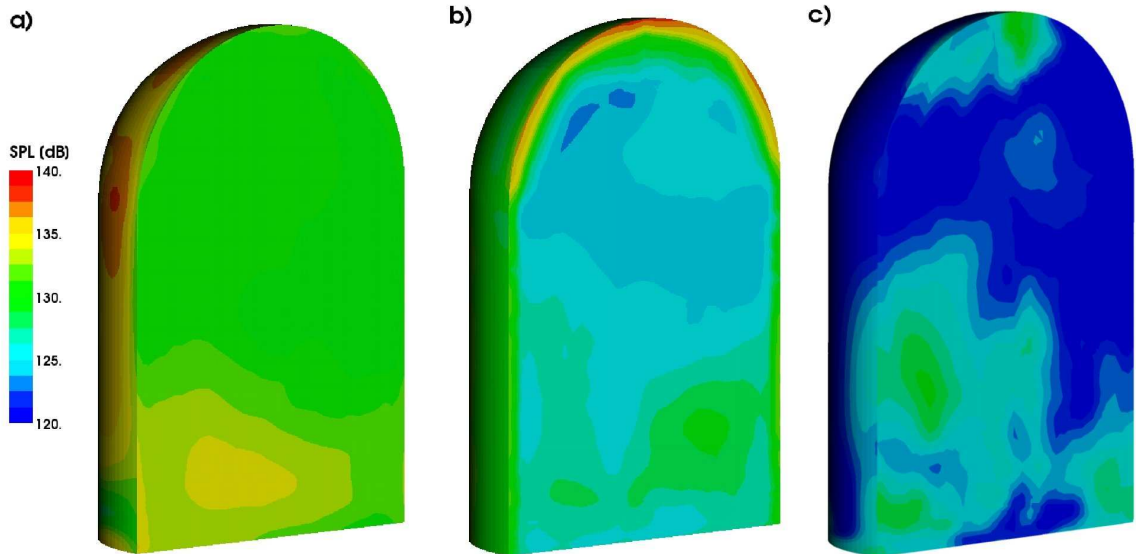


Figure 6.17: Mean sound pressure level on the mirror rear face for cases a) AK1, b) AK3 and c) ASA3.

for three locations on the rear face shown in fig.6.18. The spectral distributions do not show nearly as much variation between the cases as intimated by the mean distributions. Of the three points on the rear face, two are near the edge (113,114) and one in the centre (115). Although the mean SPL contours seem to suggest higher fluctuations near the trailing edges, the opposite is revealed by the experimental spectra. The levels at point 115 are higher than the edge points across the entire compared frequency range. The most likely explanation is that points 113 and 114 are simply too far from the edge (10

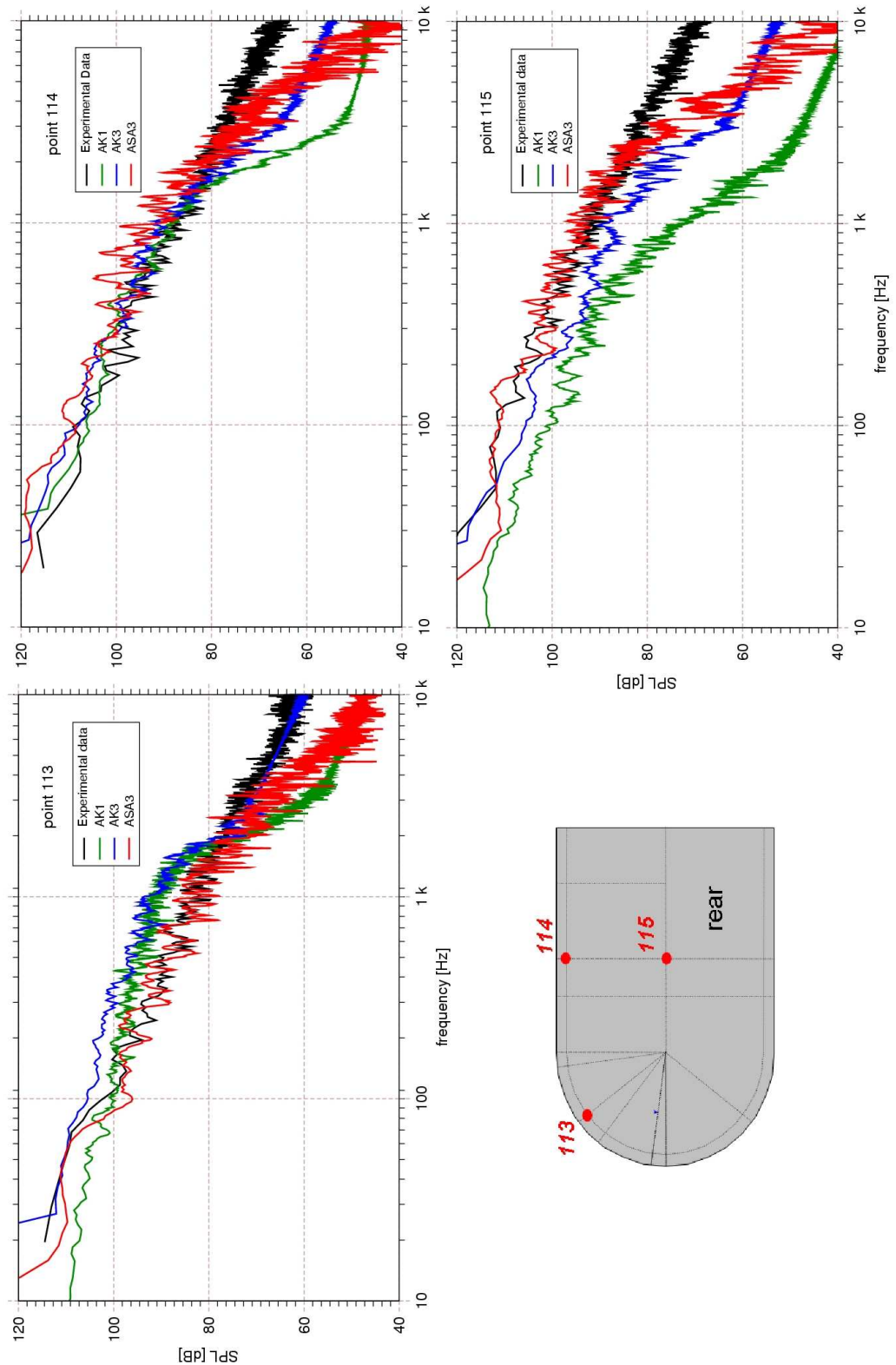


Figure 6.18: Spectra of SPL at selected points on the rear of the mirror.

6. Side Mirror

mm) to feel the brunt of the fluctuations occurring in its vicinity. This would imply that the majority of the noise-producing structures at these points are likely convected via the recirculation zone. Indeed, the streaklines and velocity contours in figs.6.7 and 6.8 show that the magnitude of the recirculating flow in the vicinity of point 115 is stronger than near 114, which in turn is higher than the levels around point 113. This primacy corresponds to the levels of the SPL spectra observed at the same locations.

Unlike the front face positions, the comparison with calculated values is fairly good for all probes on the rear face. As intimated, the properties of the recirculation zone probably play a big role in determining the character of the spectra. The accuracy of the prediction here thus reflects on the fitness of the respective DES models to capture the phenomena that produce this kind of flow, (just like the front face spectra relate to the LES performance in that region). Case ASA3 in particular shows very good agreement for all the points up to frequencies of 2-4 kHz. The mesh on the rear face is identical for AK1 and AK3, so all differences are due to transported effects. Thus, where the backflow is strongest (point 115) the difference in SPL spectra is largest, while at point 113 where the flow is comparatively weak, there is much less difference between the predictions. This is especially true for the higher-frequency content which has a much shorter lifespan than the lower portion of the spectrum. The differences between the two models on the fine mesh are much more marked. Case AK3 under and over predicts the noise levels at points 115 and 114 respectively. The various influences that might affect this discrepancy are simply too many and complex to hazard a causal explanation.

The final set of SPL spectra comparisons are on the base plate in the wake at four locations shown in figs.6.20 and 6.21. The wake and especially the intersection of the base plate with the free shear layer are the primary source of acoustic noise on and around the mirror assembly. This is clearly illustrated by the comparative mean SPL surface contours shown in fig.6.19. As with the front face SPL contours, a large amount of numerical noise is again evident upstream of the mirror for case AK3 and especially case AK1. The coarser mesh has higher cell based Reynolds numbers, larger cell size differences and skewness and, as a result, is more prone to unphysical instabilities. In the case of the Spalart-Allmaras calculation, the purpose-built near-wall RANS model again

prevents the build-up of numerical noise through a higher modeled turbulent viscosity. Since the mesh is relatively coarse upstream of the mirror, the perturbations generated here are of a similarly large scale that contribute very little to the audible noise spectrum.

Focussing on the region behind the mirror, we see very similar double-lobed patterns dominating the near-wake SPL distribution for all the cases. The perturbations that cause these features are the result of rapidly growing pillar-like vortices in the shear-layer behind the mirror's edge. The initial thickening can be explained in terms of non-linear perturbation growth and the oscillating character of the wake. After reaching maximum strength approximately 3 radii downstream of the mirror, the recirculation zone starts to reattach, producing an attendant decrease in shear strength because of the reduced backflow. Additionally, many of the large vortical structures start to break down into smaller less coherent structures reducing the energy available at the largest scales and increasing the dissipation of turbulence via the energy cascade.

Figures 6.20 and 6.21 show the spectra produced by the vortices as they grow and travel across the base plate. An overview of the plots shows a remarkably good correspondence between the calculated and experimental data. In the near wake (points 120 and 121) the fine mesh cases predict the spectra to around 4 kHz, while the further points (122 and 123) show good agreement to beyond 2 kHz. Although there are differences between the results for the SGS turbulent energy model and the S-A model, neither outperforms the other at all the comparison points. We can also see that the > 50 Hz noise-bearing range is particularly well predicted in almost all cases.

The effect of mesh density is much more noticeable and consistent in this region than on the mirror surface. The agreement between AK1 and AK3 is excellent until some way beyond 1 kHz, after which the former's reduced resolution fails to capture the smallest structures. We can see that the frequency resolution of the coarser mesh is on average half that of the finer. In the vicinity of the probe points the coarse mesh cells have typical spacings of $5 \times 5 \times 1.5$ mm, while the corresponding fine mesh dimensions are $2.5 \times 2.5 \times 0.375$ mm. The predominant flow direction along the probe points is at an angle of 6° away from the centreline parallel to the base plate. Combined with the upright

6. Side Mirror

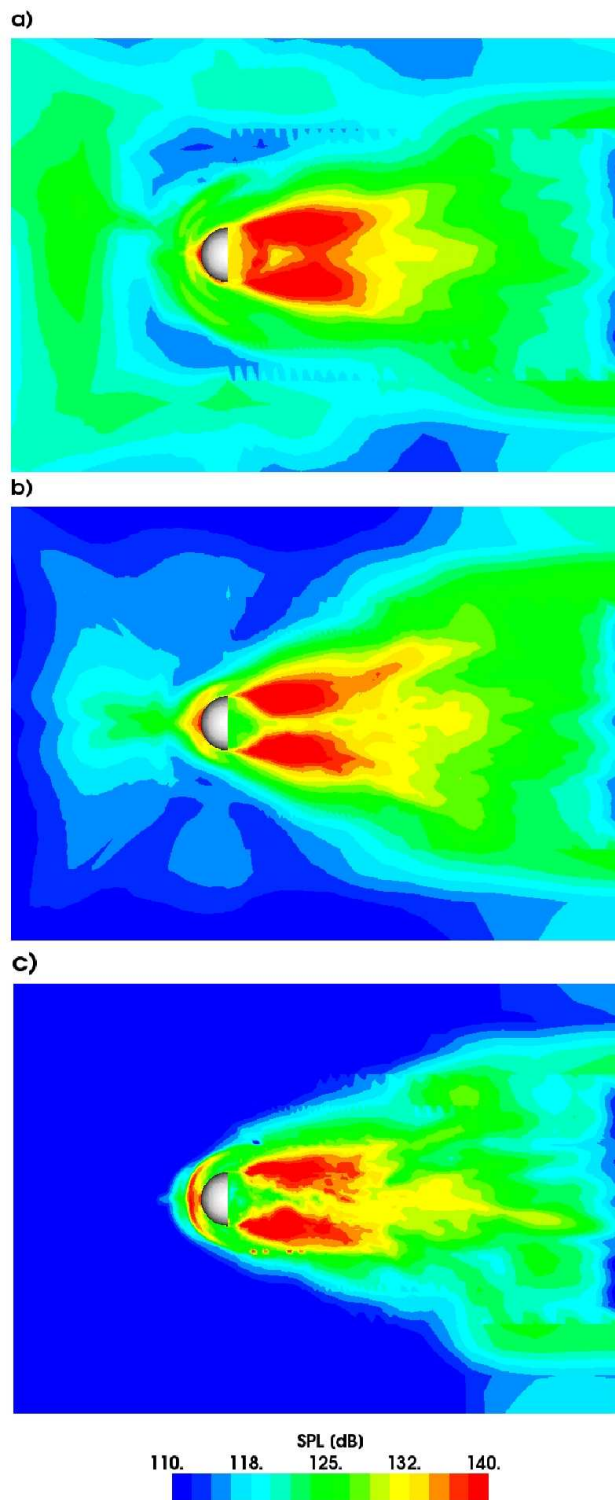


Figure 6.19: Mean sound pressure level in the mirror wake for cases a) AK1, b) AK3 and c) ASA3.

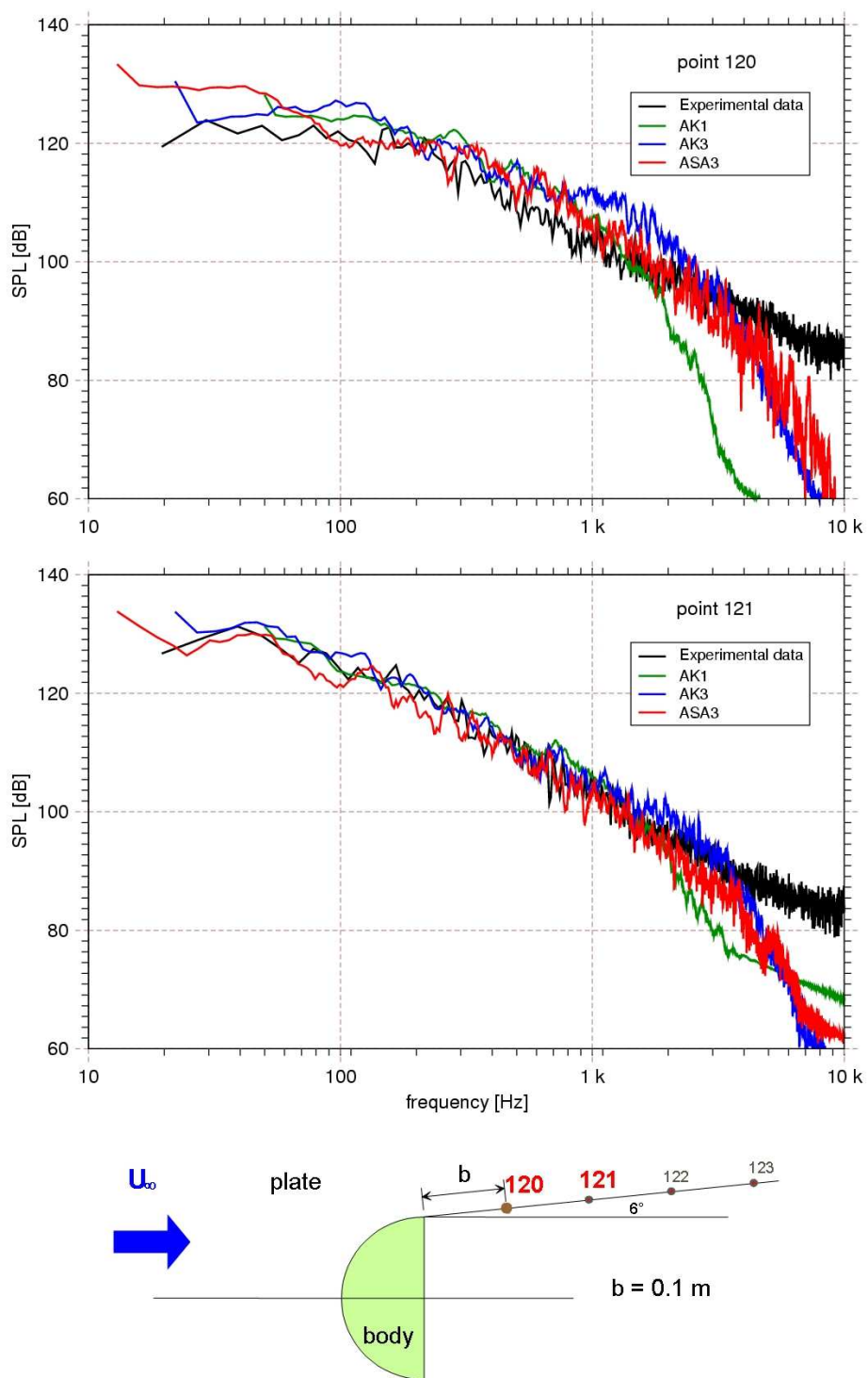


Figure 6.20: SPL spectra in the mirror wake.

6. Side Mirror

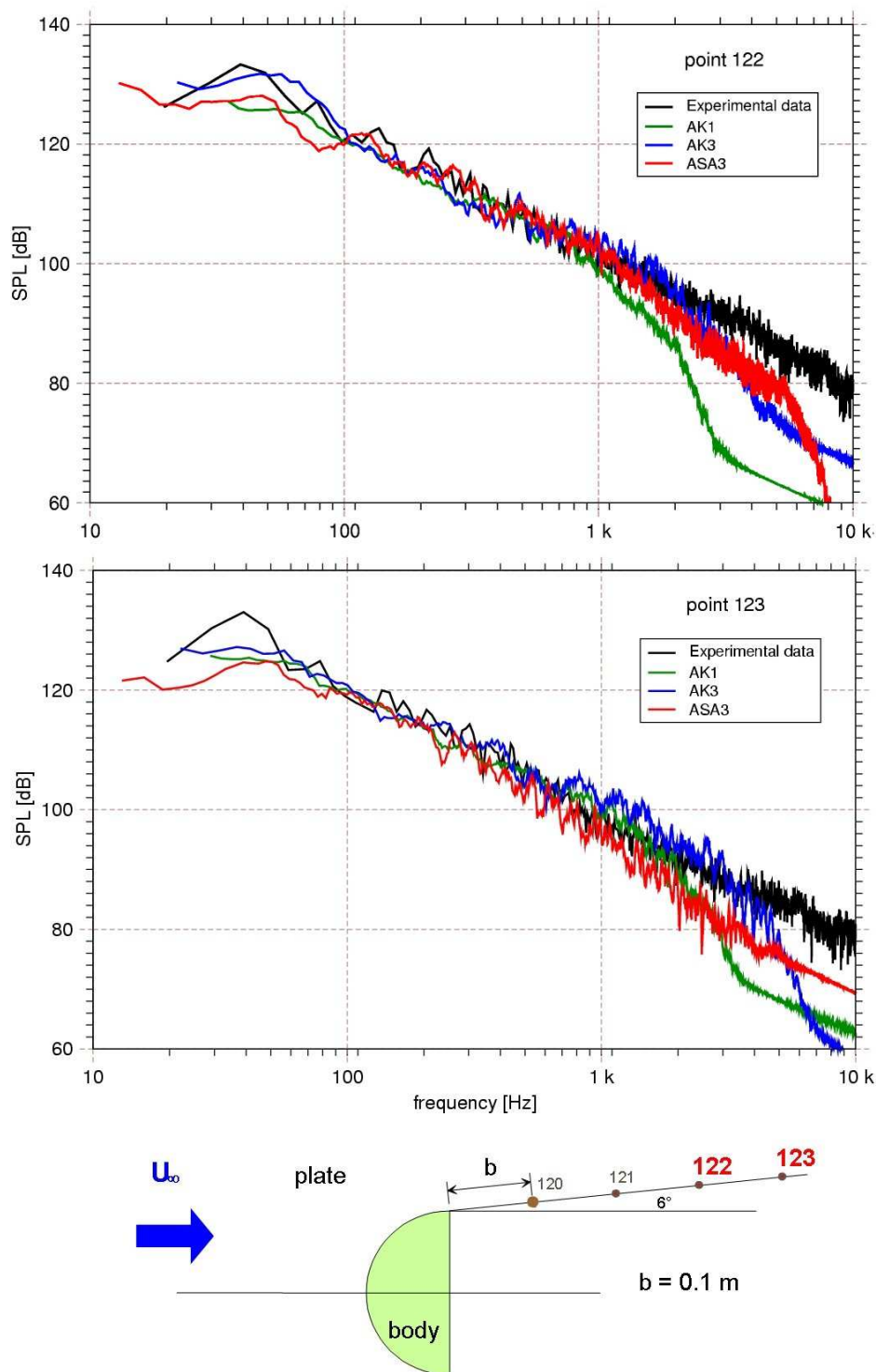


Figure 6.21: SPL spectra in the mirror wake.

character of the vortices in this region, this means that the x and y dimensions of the cells will be dominant in determining the minimum dimensions of the structures that can be advected across them. Thus, since these two components of the mesh differ with a factor of two, this implies a linear scaling of the resolved frequency range with mesh resolution. The expectation is thus that continued mesh refinement will deliver similar extensions in the resolvable spectrum. Knowledge of the convection velocity, cell size and maximum resolved frequency can also provide more information about SPL frequency resolution requirements in absolute if approximate terms. Given the maximum resolvable frequency, f_{max} and the approximate convection velocity u_c , we can employ the wave equation (eq.6.14) to find the minimum resolvable wavelength λ_{min} for cases AK3 and ASA3:

$$\begin{aligned}\lambda_{min} &= \frac{u_c}{f_{max}} \\ &= \frac{40 \text{ m/s}}{4 \text{ kHz}} = 10 \text{ mm}\end{aligned}\tag{6.14}$$

Given a characteristic cell dimension of 2.5 mm, this implies a resolution of at least 4 cells to capture any given wavelength. It must be stated again that this parameter is very approximate. It is difficult to determine the mean advection velocity of the noise producing structures with any certainty (the stated value was found via inspection) and the characteristic cell dimension relies on the assumption that the turbulent structures are predominantly two-dimensional. Also, the normal assumption of “frozen” advecting turbulence is not entirely accurate in the midst of a strong shear layer. Still, this relation provides another guide to meshing requirements and holds true for the coarser grid case as well.

Overall, the calculated wake SPL spectra provide significantly better predictions than the other probe locations. The reasons for this are two-fold: firstly, the mesh in the shear layer was made particularly fine to properly capture the regions of maximum noise generation (see fig.6.5), allowing the simulation to resolve nearly all the energetic motion. Secondly, and most importantly, the turbulence that produces the wake noise is generated by the free shear layer surrounding the recirculation zone. Unlike near-wall turbulence which is confined by the solid surface and results in subsets of very small energetic scales,

6. Side Mirror

free-shear turbulence's growth is limited only by the rate of momentum transfer, resulting in large easy to resolve eddies. Since most of the eddies will be resolved, there is very little reliance on the comparatively less accurate SGS models, making the predictions more precise. The shear layer and the noise it produces is also found to have limited dependence on the upstream conditions. The damping effect of the accelerating flow around the front face combined with the strong natural oscillatory behaviour of the near shear layer means that upstream perturbations do not directly affect the wake spectra in a significant way. Admittedly, the lack of proper laminar modelling on the front face and numerically induced noise can be expected to distort mean flow characteristics, which in turn produce alterations in the spectral character of the wake. Specifically, sec.6.2 shows the effect of turbulent flow on the front face is to decrease the width and length of the recirculation zone because of the delayed separation. Even in this relatively sensitive case however, the deviation is found to be small compared to the overall dimensions of the main flow features.

The surface noise sources in the wake are also seen to be a good 10-20 dB louder than the other probe locations across most of the spectrum. Because of the logarithmic nature of the decibel scale and the large area occupied by the wake sound sources, their influence will tend to dominate the compound noise signature of the assembly. Thus LES noise prediction in the wake of high Reynolds number bluff body flows is expected to be highly accurate, as long as the DES assumptions hold (boundary layer eddies are much weaker than shedding vortices).

6.1.5 Length Scale Reduction

Before moving on to the the second mirror case, a brief detour is made to investigate the effect of the turbulent length scale on the front face flow. Note this is not an attempt to provide a laminar sub-model, but rather a sensitivity study designed to shed some light on the effect of the erroneous turbulence modelling in this region.

As mentioned previously, we know from a plethora of experiments that flow on the upstream side of a cylinder in a cross flow is almost exclusively laminar up to Reynolds numbers of tens of millions. The front face of the mirror is expected to show similar

behaviour and with low freestream turbulence and a Reynolds number of only 5×10^5 should almost certainly be laminar. One of the most obvious features of laminar cross flow around a cylinder is separation of the boundary layer before it has travelled 90° around the circumference. The mirror is no exception and the oil film visualisation in fig.6.22a clearly displays such a separation line approximately 1.5 cm upstream of the edge.

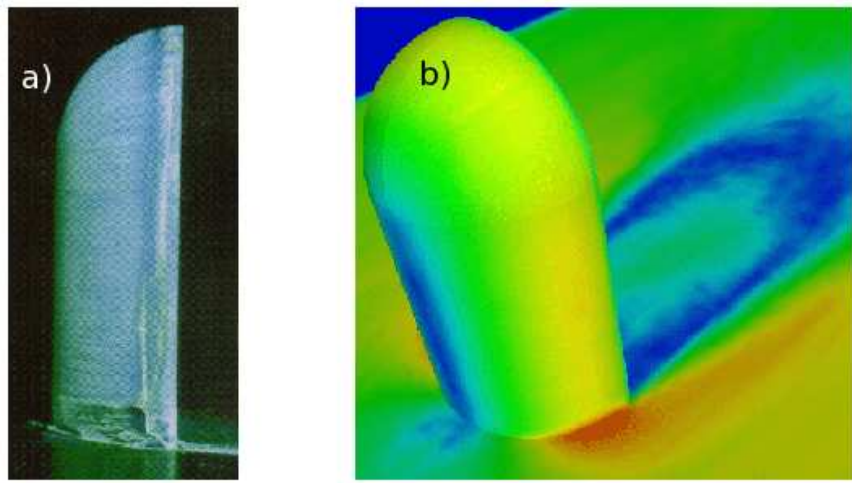


Figure 6.22: Flow features on the mirror front face, a) oil film visualisation and b) mean wall shear magnitude AK3.

Although a post-processor with the ability to draw streaklines on curved surfaces was not available to provide a direct comparison, the lack of a line of zero wall shear stress magnitude in fig.6.22b clearly shows that there is no front face separation in the AK3 results. The cause of this lack of separation was outlined in sec. 6.1.3. Simply put, the RANS/SGS turbulence models used in the DES approach do not have the ability to sense laminar flow regions and as a result predicts turbulence in the presence of laminar shear where there should in fact be none (or very little). In addition, sec.6.1.4 clearly showed there is a significant amount of numerically-induced noise in this region, which might increase the apparent turbulence levels (although case ASA3 which had significantly less numerical noise did not show market differences from the other cases). The extra mixing induced by all the non-physical turbulence then causes the boundary layer to stay attached all the way to the edge of the mirror.

6. Side Mirror

Better mesh construction and/or tailored numerics could conceivably reduce the error-induced motions, but the cost and possible complexity of these options place them outside the scope of this project. Instead, the effect of reducing modeled turbulence will be investigated with an eye on measuring the impact of this assumption. This is done via an *ad hoc* reduction of the turbulent length scale in the vicinity of the front face by increasing the effect of the Van Driest damping function tenfold. Recall the near-wall turbulent length scale for the SGS turbulent energy model is given by eq.4.65 as,

$$l_t = \min \left(\kappa y_w \left[1 - e^{-y^+/A_k} \right] / C_S, V^{1/3} \right)$$

The Van Driest damping function is supposed to suppress turbulence in the laminar sub-region ($y^+ \lesssim 5$) near the wall by reducing the length scale. It is a simple matter to reduce the length produced by this relation even further by multiplying it with some constant value $c_l < 1$ as illustrated in fig.6.23.

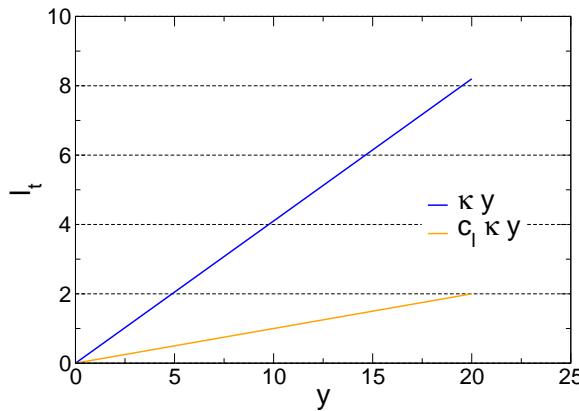


Figure 6.23: Reducing the turbulent length scale on the mirror front face.

For the front face, $c_l = 0.1$ is chosen to produce turbulent length scales an order of magnitude smaller than would otherwise be the case. Simulations were performed on a fine mesh and boundary conditions identical to that employed for case AK3. This calculation is henceforth referred to as AK3RL to indicate the reduced length scales near the front face.

Figure 6.24 shows the effect of this adjustment on the predicted turbulent viscosity near the surface. The maximum value has decreased from 5.3×10^{-3} to $3.4 \times 10^{-3} \text{ m}^2/\text{s}$. Although this is a significant reduction, it is not nearly as much as the order of magnitude decline in the length scale. Also, consider that the laminar viscosity of the air is $1.56 \times 10^{-5} \text{ m}^2/\text{s}$, nearly 200 times smaller than the reduced length scale predicted viscosity. A further decrease in the turbulent length scale using the same methodology is not viable, since the effect would start to influence adjacent boundary regions. Analysing even minor changes should however, give an general indication of the trends that would be introduced by an accurate laminar treatment.

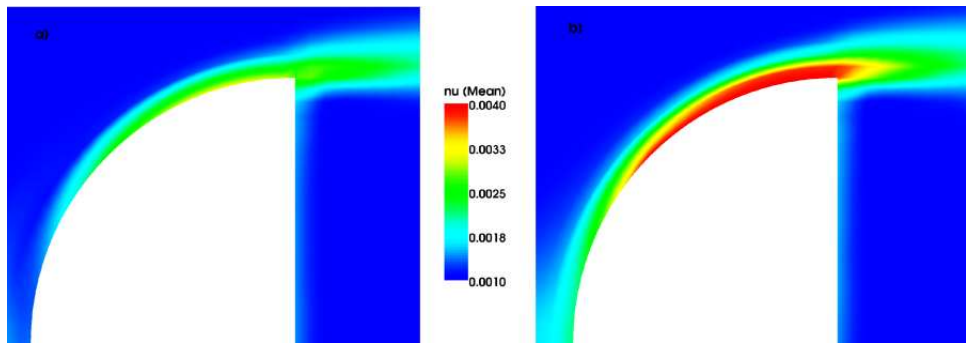


Figure 6.24: Mean subgrid-scale viscosity adjacent to the mirror front surface, case a) AK3RL and b) AK3.

The front face flow in terms of the near-wall velocity is depicted in fig.6.25. Although there is no radical change in the flow patterns, such as separation, comparison of the contours for the cases AK3 and AK3RL, show small but noticeable differences between the reduced length scale and reference cases. Firstly, the maximum near-surface velocity for case AK3RL is lower, which is indicative of less turbulent mixing and more motion of fluid away from the front face. Secondly, a larger deceleration of near-wall flow can be seen near the trailing edge, a product of the same phenomenon.

Comparison of selected SPL spectra also show incremental benefits of reducing the front face turbulence modelling error (fig.6.26). (See sec.6.1.4 for exact positions.) At point 102, the reduced turbulent viscosity on the front face translates directly into less damping of the small scales, producing a more accurate prediction of the high frequency

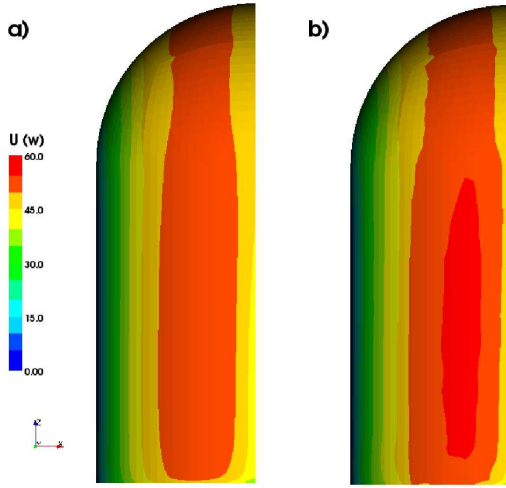


Figure 6.25: Velocity magnitude in surface adjacent cells on the front face of mirror, case a) AK3RL and b) AK3.

range. The changes in the spectral distribution at the other locations are more difficult to relate to the length scale reduction. A general decrease in the over prediction of noise sources around the 1 kHz range is however apparent at all the locations and especially on the base plate near the edge (point 120). Possible explanations include shifts in global flow patterns and more accurate vortex growth in the initial stages of the shear-layer.

The changes produced by decreasing the modeled turbulence near the front face are modest, but the trends are in line with expectations. Unfortunately, numerical noise is also present in case AK3RL. The resolved fluctuations occur upstream of and on the front face, almost certainly reducing the impact of the length scale reduction. Despite these problems, a scheme which can account for laminar flow regimes is clearly desirable as even the effects of modest corrections are positive. Admittedly, the dynamic procedure (sec.3.2) in the absence of error induced fluctuations, fulfills such a role in pure LES. To date an extension of this methodology for the URANS portion of the DES methodology has not been forthcoming. Some hope of a transitional DES approach is offered by intermittency and turbulence potential type models currently being developed for RANS applications (see for example Wang and Perot [165] and Steelant and Dick [152]). Again interaction with numerically generated resolved motions might hamper these approaches,

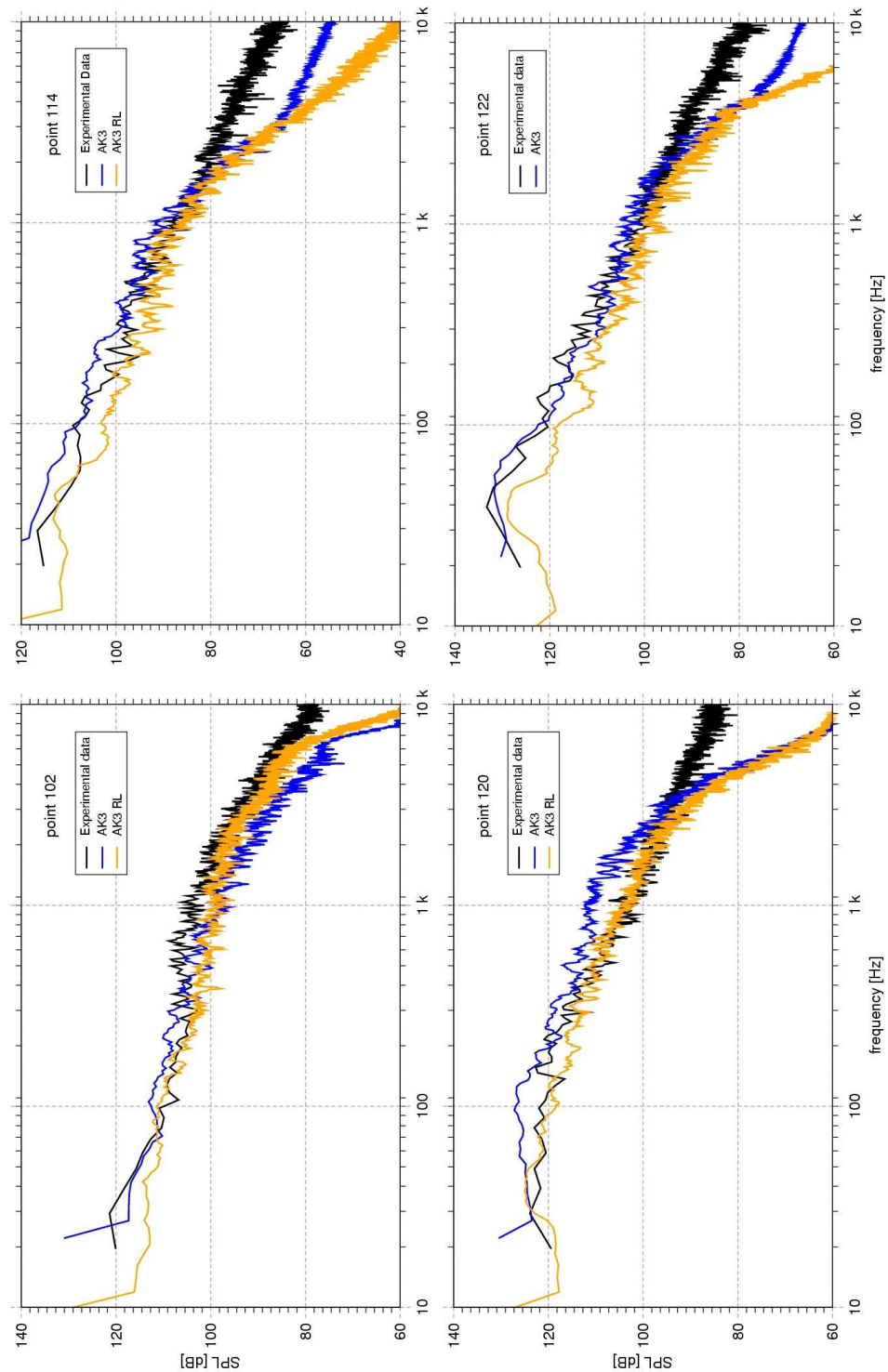


Figure 6.26: Comparison of SPL spectra for reduced front face length scale calculations.

so combating spurious noise production becomes a real concern in future development of LES applications.

6.1.6 Summary

Overall simulation results for mirror Case A were very encouraging. The majority of comparisons showed excellent agreement with experimental data. Static pressure distributions showed particularly good agreement for all simulated cases, with only small regions near the edge of the mirror front face exhibiting significant deviations. The same kind of picture is revealed by the SPL comparisons: results on most of the mirror surface agree well with experiments, the exception being the over prediction of noise in what should be a very low perturbation region on the laminar front face of the mirror. The probe spectra on the base plate in the wake on the other hand, are very well predicted for all calculations and probe locations. DES seems to be well suited to simulating wakes and shedding flows.

Conversely, the DES approach used in this study cannot predict laminar flow regimes. The lack of laminar modelling on the front face combined with numerically induced upstream perturbations are the main causes of deviation from the experimental data sets. For mirror B (sec.6.2), the mesh is constructed to minimise numerical inaccuracies, but no elegant method was found to correct the laminar treatment deficiency. Although improving this treatment would translate to better predictions on the front face, indications are that this modelling error has a small influence on the sites of largest noise production; the wake shear-layers.

Comparing the results from the different mesh resolutions, very little grid dependence is observed for the first order statistics (mean pressure). The influence of grid spacing on the maximum resolvable SPL frequency is very apparent though and a linear relation between cell dimensions and this frequency is observed in the wake.

On identical meshes, the differences between the Spalart-Allmaras and SGS turbulent energy cases is comparatively small. This small deviation is however consistently expressed as an improved prediction for the S-A model (case ASA3), making it the preferable turbulence model for external aerodynamic flows. This advantage is probably due to a

better near-wall length scale specification compared to the Van Driest damping function.

Rounding off the section on mirror A, it should be mentioned again that the cases displayed here by no means constitute the entirety of the simulation conducted. Additional cases included intermediate mesh densities for all the models and application of the pressure sensitised wall functions (sec.3.3.1). None of these results however contributed significantly to the conclusions outlined above and as a result were omitted from the discussion.

6.2 Side Mirror B

The second part of this chapter examines the flow around the mirror in the enclosed wind tunnel, Case B. The case provides more experimental data in the form of LDA measurements, extensive surface flow visualisations and dynamic pressure traces, making more a complete comparison between it and the LES simulations possible. Since the experiment was performed toward the end of this CFD investigation only a limited number of calculations could be performed. These calculations however employ all the best practices developed during earlier simulations, resulting in very good general agreement between them and the experimental data. To keep the discussion concise, only the simulated results for the best setup are presented.

6.2.1 Experimental Data

The experiments for mirror B were conducted during the course of the project at Imperial College and were sponsored by DaimlerChrysler AG and Computational Dynamics Ltd. The data sets are as yet unpublished and references are confined to personal communications from Chronopoulos and Taylor [31].

A diagram of the windtunnel used for the experiments is displayed in fig.6.27 and a photograph of the experimental rig is shown in fig.6.28. The tunnel is a closed loop configuration with a maximum test section bulk velocity of 25.8 m/s. A series of flow straighteners and fine grids ensure that the flow in the test section is steady with a minimal amount of free-stream turbulence (<2%). The Reynolds number achieved with this setup,

6. Side Mirror

$Re \approx 3.3 \times 10^5$, is somewhat lower than that employed for the Case A experiments, but still similar enough to keep Re dependant variations to a minimum. A contraction and bleeder slots ensure that the flow entering the test section has very thin boundary layers. All these factors combine to produce very well characterised boundary conditions for the LES calculations.

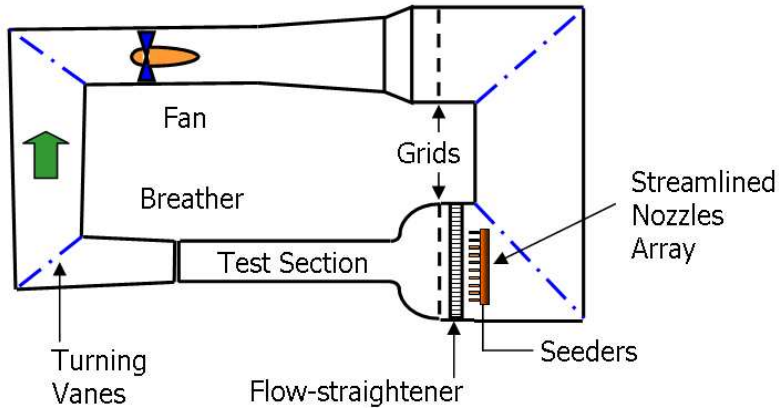


Figure 6.27: Diagram of Imperial College closed windtunnel (courtesy of [31]).

The same mirror model and a virtually identical base plate to that used by Hoeld *et al.* [56] for Case A are employed for these experiments. Figure 6.28 shows a frontal view of the mirror and base plate assembly inside the windtunnel. The raised base plate with a shaped leading edge allows for a well characterised boundary layer free from tunnel induced flow defects in the critical region upstream of the mirror. Also note the Perspex side panels that allow access for the Laser Doppler Anemometry. The seeding equipment to allow proper functioning of the laser probes is positioned upstream of the flow straighteners and grids, resulting in evenly distributed seed particles. Positioning of the LDA emitter and receiver on either side of the tunnel and lack of a top access panel allows only the velocity components in the streamwise and base plate normal directions to be measured.

Access limitations complicated the measurement of pressure spectra on the mirror surface itself. Instead a wider number of probe locations were employed in front of and behind the mirror on the base plate. The tapings are mounted flush with the surface and



Figure 6.28: Frontal view of Imperial College experimental rig [31].

the pressure is sampled at ~ 65 kHz (which is far in excess of the audible range) using the same pressure transducers employed in the previous experiment.

Further, surface flow visualisations were made by spreading a mixture of silicon oil and powdered aluminium oxide on and around the mirror and allowing the mixture to be distributed by the flow over the course of several hours. These visualisations present a very convenient and intuitive way of comparing large scale time-averaged flow features like the wake extent and horse-shoe vortex positioning.

No static pressure measurements were made for mirror B. These and the SPL spectra on the mirror surface can still be compared in an approximate fashion by using appropriately scaled data from mirror A. At some locations the two experimental sets are also directly compared without scaling to highlight the influence of Reynolds number.

6.2.2 Computational Setup and Reference Details

A detailed depiction of the calculation domain for mirror B is presented in fig.6.29. The main difference from the previous case is the lateral wall boundaries, which are less than half a meter from the mirror symmetry plane. The smaller cross-sectional area of the tunnel and the retarding influence of the far walls will cause a some acceleration of the

6. Side Mirror

flow around the mirror. However, since the mirror blockage is only 8% of the overall area and the side wall boundary layer thickness is estimated to be less than 4cm it can be assumed that this effect will be comparatively small. Wall functions are used to calculate the shear stresses at the side walls and on the base plate away from the mirror. Close to and on the mirror, the mesh is refined normal to the surface so that no-slip boundaries may be employed. The outlet is chosen the same distance downstream from the mirror as in Case A, to ensure recirculation and outflow effects do not influence the measurement region. Pressure at the outlet is fixed and zero gradient is imposed on all other properties.

The location of the inlet plane is not chosen as before with an eye on easing the approximate inlet specification. Instead LDA measurements of the streamwise component on the symmetry plane were made at the furthest upstream location allowed by the side access windows. This velocity profile is used to provide a near-exact mean distribution above the base plate as shown in fig.6.30. The measured profile is blended into the bulk velocity some distance above the base plate where the two become equal. At the side wall boundaries a similar method to Case A is employed to calculate the boundary layer thickness. Growth of the lateral and top wall boundary layers is assumed to begin at the contraction in the tunnel about 1.5 m upstream of the computational section. In contrast with Case A, the top and side boundary layers are almost certainly turbulent from inception due to upstream effects. A turbulent version of eq.6.1 is used to calculate the position of $U = 0.99U_b$:

$$\delta = \frac{0.385x}{Re_x^0.2} \quad (6.15)$$

Given the velocity at a distance δ from the wall, it is a simple matter, assuming equilibrium boundary layer conditions, to derive the velocities in the boundary layer from the logarithmic law of the wall. For the present case the boundary layer thickness at the inlet was found to be $\delta \approx 3$ cm. For the SGS turbulence properties at the inlet, a small amount of turbulence equal to the background level in the base plate boundary layer is assumed. For the fully turbulent side and top walls, a constant turbulence intensity proportional to the wall shear is applied at all inlet faces within the boundary layer. Compared to Case A in the open windtunnel, the boundary specifications, especially at the inlet and sides, are much more accurate.

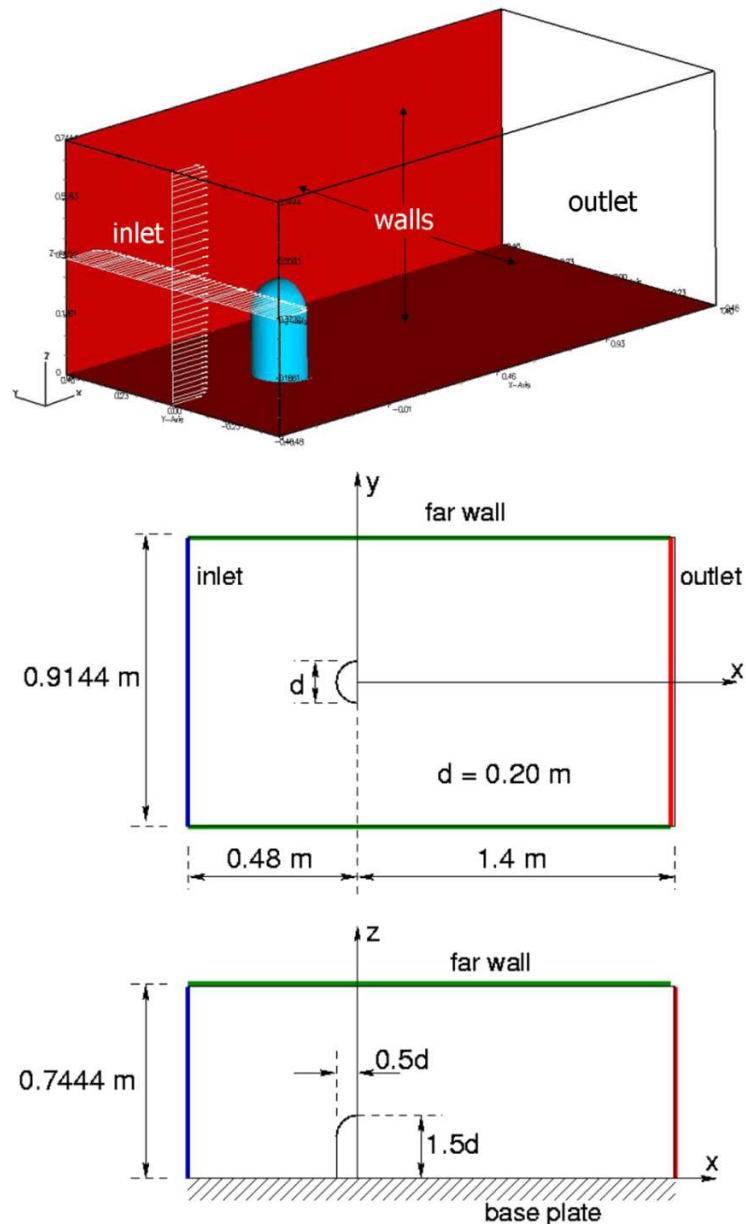


Figure 6.29: Case B calculation domain.

6. Side Mirror

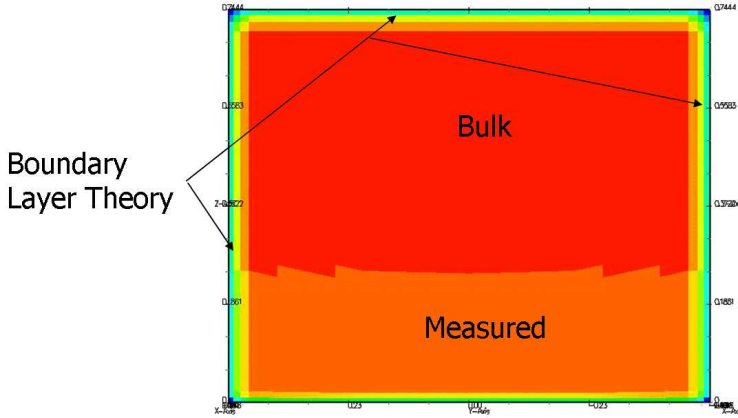


Figure 6.30: Inlet velocity distribution for case B.

As mentioned previously, the mesh for Case B was constructed so as to reduce the numerical errors encountered in the Case A calculations. To this end, a different block structure is employed in the region upstream of the mirror as depicted in fig.6.31. When compared to fig.6.5, the grid is seen to contain far less non-orthogonality and cell faces are predominantly parallel or at right angles to the oncoming flow. Changes in mesh size are also generally much more gradual, which will reduce commutation errors.

Mesh B uses a lot more embedded refinement and grading to put resolution where it is needed while reducing the overall mesh size. Specifically, the cells on the front face, in the shear layer region and on the base plate around the mirror are repeatedly refined and squeezed to produce very good resolutions in these regions. The reduction in Re number also places a lesser requirement on wall normal spacings to achieve reasonable y^+ values. In addition, a choice was made to resolve the SPL spectra only up to the 1-2 kHz range since the noise production levels beyond this point are small compared to those in the 100 Hz - 1 kHz section. All these modifications combine to produce a mesh tailor-made to the problem at hand, yet with a total cell count below 1.2 million. The smaller mesh is much more manageable in terms of calculation times and post-processing requirements, the only drawback being the time required to actually create such a complicated grid using the tools available.

Initially, two simulations of mirror B were performed; one with the Spalart-Allmaras

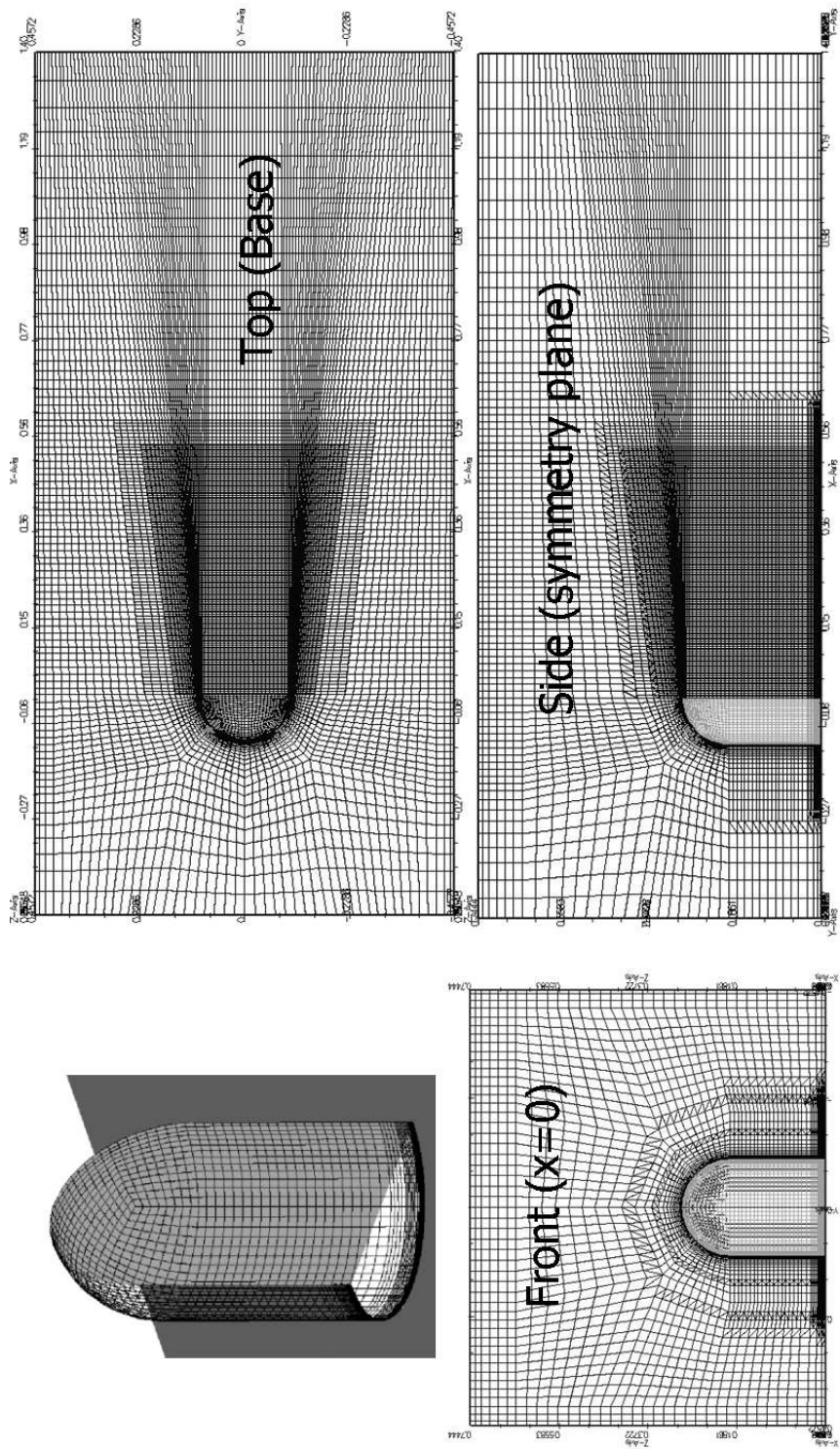


Figure 6.31: Computational mesh for case B.

6. Side Mirror

DES model and the other using the SGS turbulent energy model. After calculating a limited number of flowthrough times and comparing the results, it was however felt that in light of the availability of experimental velocity and stress measurements, a longer time averaged solution for one of the cases would better serve the purposes of this investigation than two poorly converged ones. Based on the results of the intermediate calculations and the experience gained from the previous case, the Spalart-Allmaras model was chosen for further simulation. This case is henceforth referred to as BSA3 to denote its equivalence to ASA3. It should be mentioned in passing that the intermediate results of the turbulent energy model, while marginally less accurate than the S-A model, were by no means poor.

The time scale of the largest periodic motion based on the Strouhal number for a cylinder in a cross-flow, $St = \frac{f_s d}{U} = 0.23$ [41] is found to be $t_s = 0.0545$ s. The Courant number restriction of $CFL \approx 0.5 - 0.8$ combined with a very fine grid in some regions, necessitates a timestep of only 5×10^{-6} s. To improve the quality of the time averaged results it is necessary to increase the averaging times significantly beyond the 10 characteristic times previously employed. Calculations were therefore performed for a period of 1.2 s, or approximately 23 shedding cycles. Of these, a period of 3 characteristic times were devoted to flushing the effects of the initial conditions from the system before averaging is started. The short flushing time is motivated by the use of appropriately scaled and mapped LES flow fields from mirror A, instead of RANS results, for initial conditions. Still, the simulation requires 200000 timesteps to achieve this target, which translates into a approximately 2 months of calculation time on the available hardware (8×1.8 GHz P4 Beowulf cluster). The high cost is the prime motivation for restricting the calculations to a single setup.

6.2.3 Flow Features and Dynamics

In a qualitative sense, the major flow features for mirror B are more or less the same as those encountered in Case A. Figure 6.32 shows mean streaklines and velocity magnitude on the symmetry pane and a base parallel plane at $z = 0.1$ m. The recirculation zone with its upside down “U” shaped arch vortex is again the most obvious feature. Animations A.5 and A.6, provide a more detailed picture of the mean flow patterns via a moving

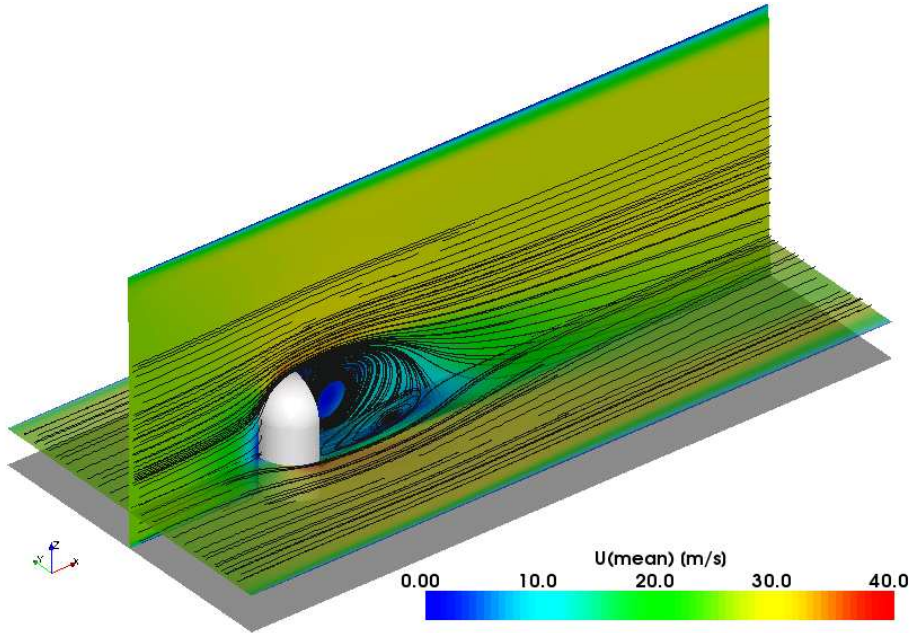


Figure 6.32: Overview of mean flow features, streaklines and velocity magnitude.

cutting plane of velocity contours and vectors.

A direct like-for-like comparison of predicted normalised velocity contours for ASA3 and BSA3 is shown in fig.6.33. Some subtle differences between the cases can be observed in this depiction. The most obvious of these is probably the larger high velocity plumes beside the mirror in fig.6.33b, that are due to the enhanced blockage effect of the mirror in the smaller cross-section tunnel. Also apparent is a much higher degree of lateral symmetry in case BSA3, which implies that the increased averaging time achieved its stated goal. The boundary layers on the side walls are obviously only present for mirror B, but other than this most remaining features appear to have the same extent and general

6. Side Mirror

and shape. Specifically, the recirculation zone which has much smoother contours because of the lengthier averaging time, still has approximately the same size in case BSA3 as it did in mirror A's DES calculations.

A different view of the smaller scale structure of the flow is presented by instantaneous isosurfaces of the second invariant of the velocity gradient, $\mathbb{Q}_{\nabla \bar{u}} = 5 \times 10^5$. Figure 6.34 compares these structures for the case ASA3 and BSA3. It should be noted that these surfaces are not really equivalent in that no velocity related scaling is applied to establish dimensionless forms. Although the same kind of structures are present in the bow vortex and shear layer eddies, they differ quite a bit in their fine scale details. We can see a lot more "noise" and irregularity in BSA3 contrasted with the much smoother features in ASA3. Part of this, like the increased shedding from the top of the mirror, may be due to acceleration and increased shear caused by the blockage effect. The increased small scale structures around the base of and behind mirror B are more difficult to explain though. Although the enclosed mirror Re is lower, the mean cell size is slightly larger to compensate: it is thus not likely to be a purely modelling related phenomenon. If these small scale vortices at the junction of the mirror and base plate are real, it has interesting implications for the view that the near shear layer is dominated by upright rollers (sec.6.1.2). Conversely, we see a large amount of incipient perturbations all over the front face where the flow should be laminar. If the same phenomenon is responsible for triggering the small vortices around the base, then this is yet another numerical inaccuracy. One significant difference between the meshes used for Case A and B, is the wall-normal dimensions of the cells on the front face. In an attempt to resolve flow in the adverse pressure gradient near the mirror edge, the wall-normal dimensions of the first off-the-wall cells on the front face was reduced to 0.06 mm. Unfortunately this small size combined with wall parallel spacings of approximately 8 mm on the curved surface introduce significant skewness errors at precisely the location where greater accuracy is desired. So counter to expectations, this modification appears to exacerbate the problem of excessive mixing on the front face and also introduces additional inaccuracies in the form of error-induced fine scale structures. The impact of this phenomenon will be gauged during the rest of this section.

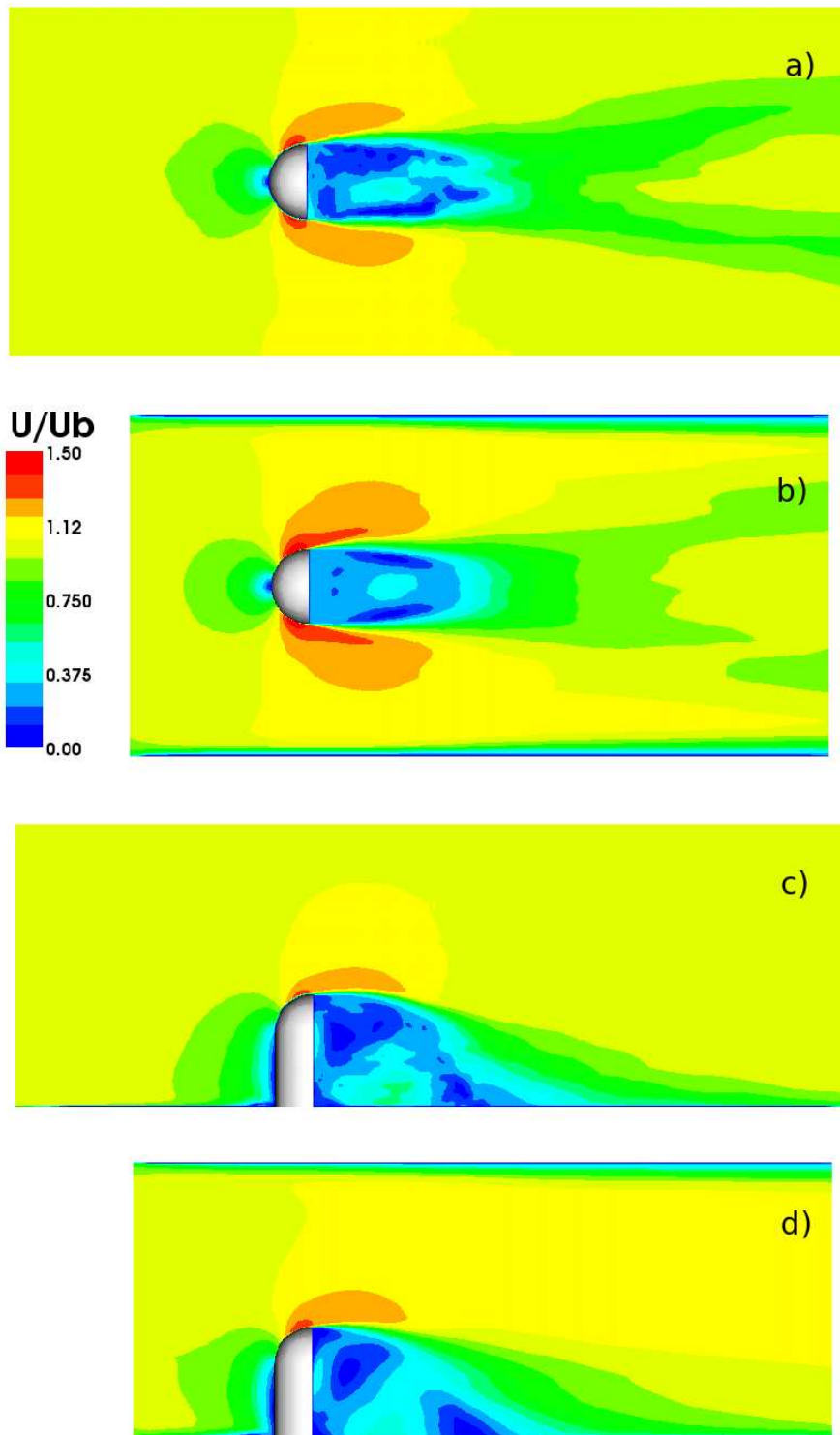


Figure 6.33: Comparison of scaled velocity magnitudes U/U_b ; Top view ($z=10 \text{ cm}$) a) ASA3, b) BSA3 and side view ($y=0$) c) ASA3, d) BSA3.

6. Side Mirror

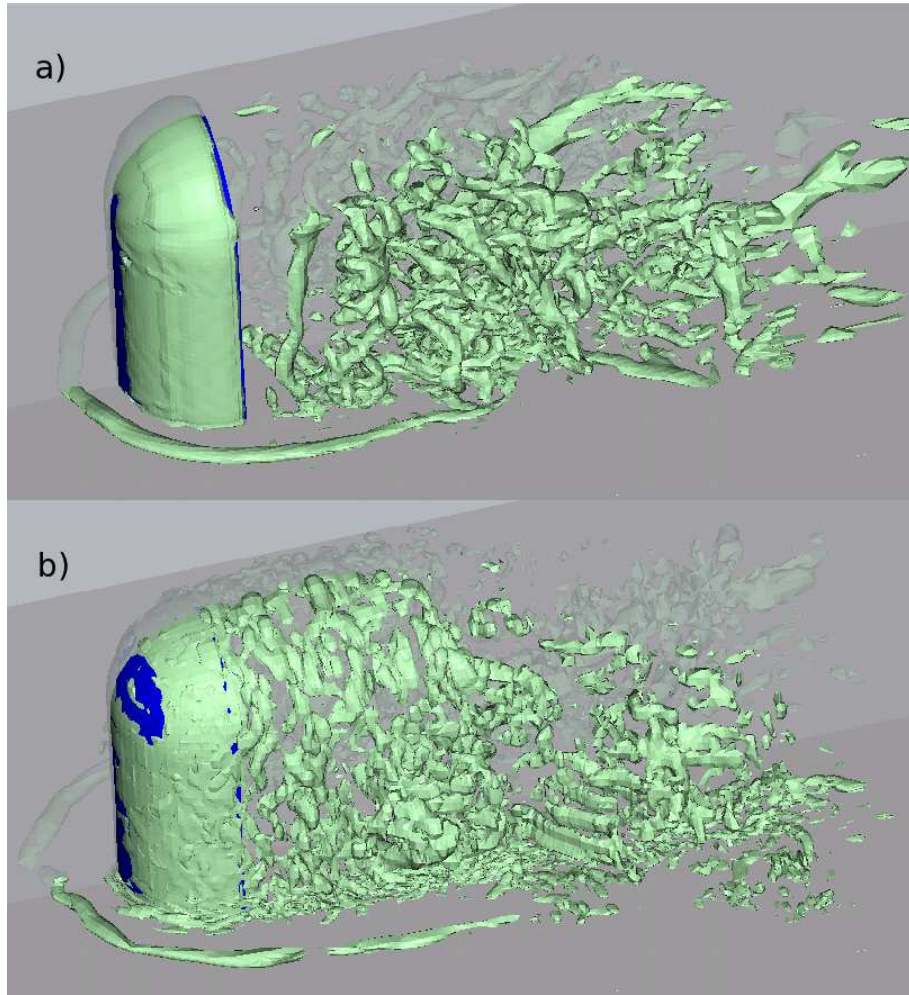


Figure 6.34: Comparison of instantaneous vortex cores visualised as isosurfaces of $Q_{\nabla \bar{u}} = 5 \times 10^5$, a) ASA3, b) BSA3.

The more complicated solution-adapted mesh used for mirror B has proven very beneficial in terms of reducing computational overheads while maintaining overall accuracy. Unfortunately, excessively fine wall-normal cell dimensions on the front face have introduced skewness errors that nullify precisely the effect they were designed to counter. Additionally, the rapid change in cell size necessary to reach the fine near-wall resolution will introduce commutation errors, further complicating the picture. The smaller mesh size has however allowed much longer averaging times which will provide more stable distributions for comparison with the LDA measurements and low frequency SPL spectra.

6.2.4 Surface Flow Patterns

The oil film visualisations are the result of a carefully applied viscous aluminium oxide suspension. The streaks produced when the flow redistributes the mixture over a long time period reflects the surface-parallel path of the near-wall fluid. Comparing these images with surface streak lines thus provides a comprehensive and intuitive overview of the the LES simulation's ability to reproduce these features.

In fig.6.35 we see a comparison of the entire wake surface flow. Note that the oil film method aggregates matter in regions of high flow curvature (white regions), a feature that is not reflected by the streaklines. Observing the line formations in the oil film and equating strong curvature in the streaklines to heavy oil depositions, reveals good correspondence between the two representations. Progressing from the outermost features, we first see very similar curves described by the oil film and the streamline in the lateral wake region. The flow curves outward around the bow vortex region and then back in parallel to the reattachment region, before spreading out in the far wake. The flow passing between the bow vortex an the recirculation zone is also well represented, but the prominent compression of this flow region seen in the oil film toward the right hand side of the image is not reproduced. This is probably due to a lack of laminar separation which results in a shorter more compact recirculation zone. Near the rear-mirror base we see very similar secondary recirculation features indicated by strong curvature of the surface streaks. There is some indication that the counter-rotating vortex in the experiment is marginally stronger than that produced by the simulation. Moving downstream, the simulation's main recirculation region appears fairly consistent with that produced by the experiment, with any differences probably owing to a somewhat thinner wake. Toward the reattachment region however, we see more obvious discrepancies appearing: notably the experimental wake spreads out considerably faster than predicted. The simulation's recirculation zone appears a bit more compact as the flow turns toward the centreline before the position indicated by the experimental data. The reattachment length, although consistent in terms of its general placement, does seem a bit shorter when compared to the centre of the large white patch that indicates the same in the oil film. The biggest difference appears after reattachment though. The streaklines seem to straighten out after

6. Side Mirror

an initial deflection, while the oil streaks continue to curve outward. Initial indications are that the lack of laminar treatment on the front face reproduces the trends seen in mirror A, where the additional mixing prevents early separation resulting in a narrower and shorter recirculation zone. Without the straighter, non-separating flow bounding the recirculation zone, the flow in the experiment is free to expand faster than is the case in the experiment.

Focussing on the region right behind the mirror (fig.6.36), we see very similar fine details in the surface streaks. In particular, we see the hornlike features toward the lateral margins of the wake that indicate very strong curvature of the flow from the interior and exterior toward the shear layer. Again, however, the recirculation zone appears marginally thicker in the experimental image when using the mirror base for reference, and the inward curvature of the simulated streakline right behind the trailing edge appears stronger than expected.

The structure of the flow in front of the mirror shown in fig.6.37 is not as easy to discern as the deposition of the oil film material is very dense in this region. Curvature of the streaks away from the stagnation region is however consistent and there is some indication of a bow vortex footprint in both images. The difference in perspective between figs.6.37a and 6.37b makes detailed comparison difficult.

Figure 6.38 displays the results of the oil film visualisation on the mirror front face. The simulation is presented in terms of the near-wall velocity magnitude in lieu of the ability to plot streaklines on a curved surface. The lack of a velocity minimum in fig.6.38b is a clear indication that no separation is produced on the front face. The fact that this occurs in the experiment is clearly indicated by a heavy line of oil material deposition between 1 and 2 cm upstream of the edge. The extremely high mesh resolution employed in this region and the lack of strong resolved scale mixing, implies that the discrepancy is purely down to modelling inaccuracies.

The surface visualisations confirm that the DES methodology is capable of reproducing all major flow features in external aerodynamic flows to a good degree of accuracy. The impact of erroneous laminar modelling on the front face remains a concern and is probably the cause of the limited quantitative discrepancies that were observed.

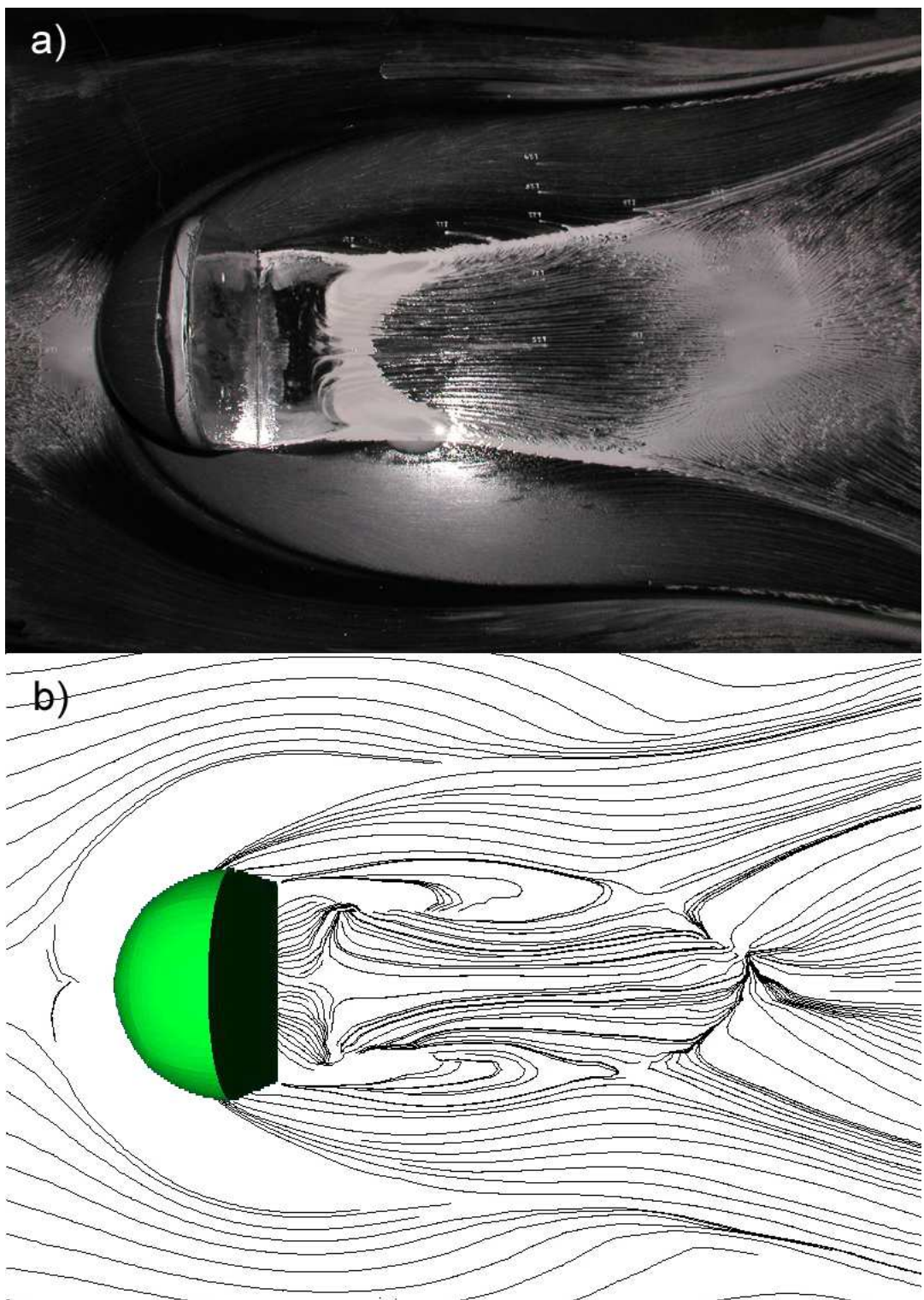


Figure 6.35: Surface flow features on the mirror base plate a) experimental oil film, b) BSA3 near-surface streaklines.

6. Side Mirror

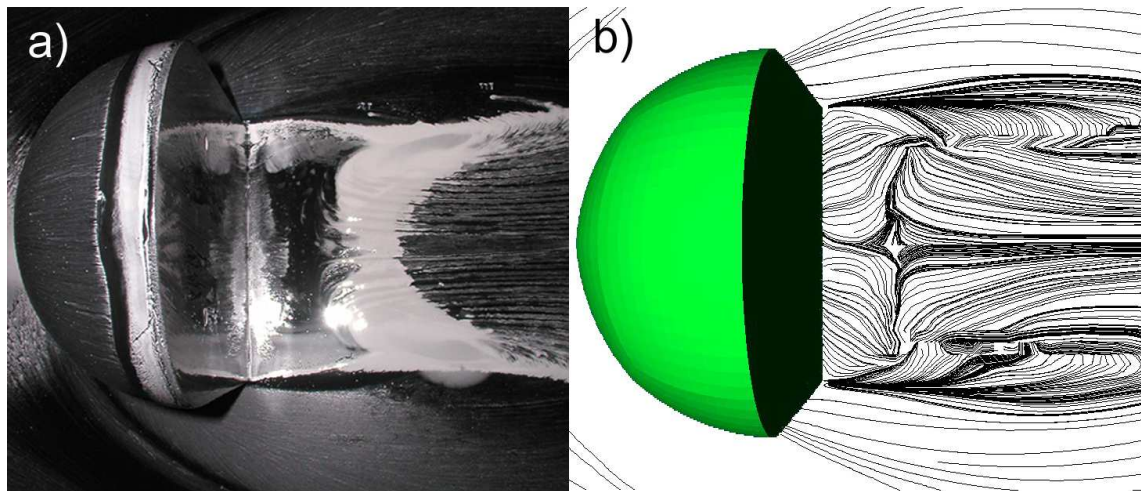


Figure 6.36: Surface flow features in the mirror recirculation zone a) experiment, b) BSA3.

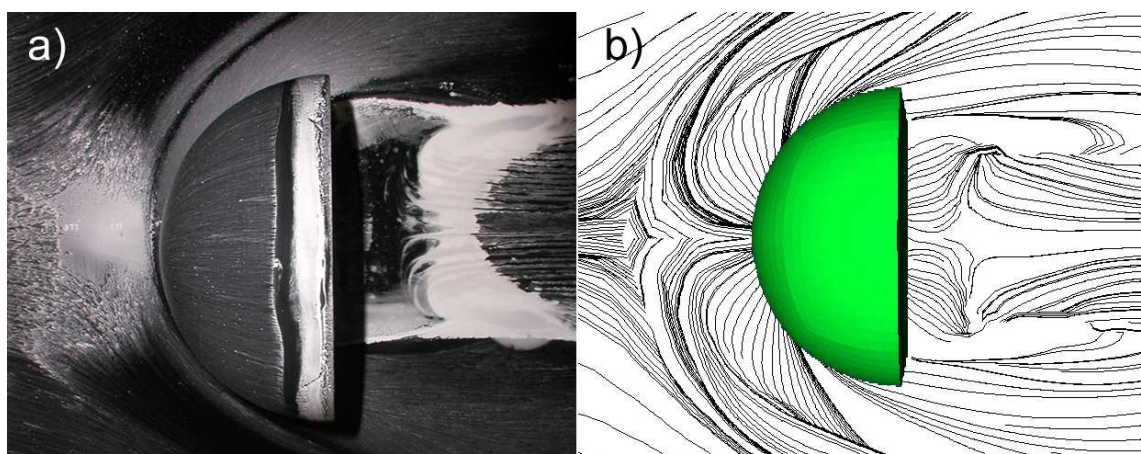


Figure 6.37: Surface flow features in front of the mirror a) experiment, b) BSA3.

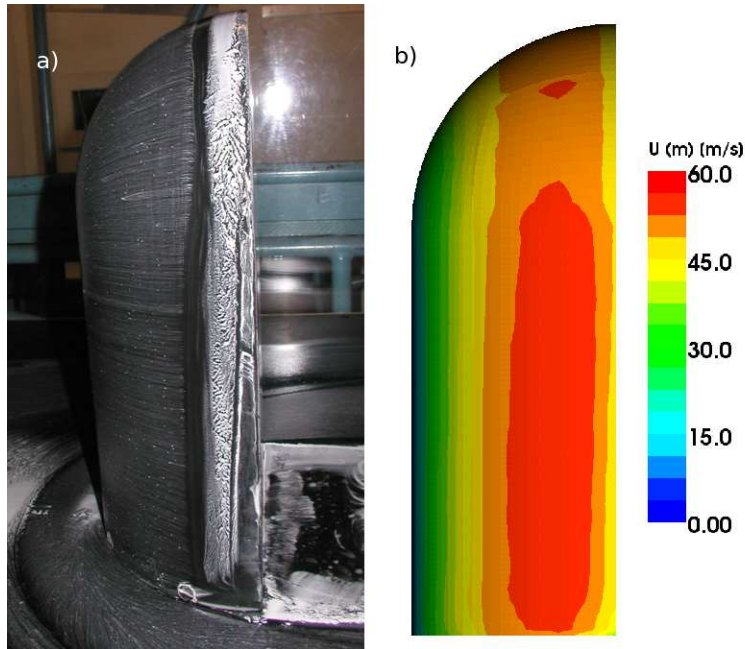


Figure 6.38: Surface flow features on the mirror front face a) experimental oil film visualisation, b) near-surface velocity magnitude for case BSA3.

6.2.5 Static Pressure

As mentioned in sec.6.2.1, no static pressure measurements were made during the closed windtunnel experiments. Assuming the Reynolds number effects are not very large, we can however compare the simulated pressure levels on the mirror to the non-dimensionalised equivalents obtained during the experiments of mirror A.

Figure 6.39 shows various views of the pressure distributions on the mirror and the base plate. The contours on the mirror are very similar to those encountered for Case A, the obvious difference of course being the maximum and minimum levels, which are somewhat less extreme in the current case. The pressure on the front face again decreases from the stagnation maximum toward a minimum after which the flow encounters an adverse pressure gradient. On the rear face the present choice of contour levels paints a somewhat distorted picture. The rear face maximum is near the base where the recirculating flow impinges as shown, but the levels in the higher pressure region at the top are in fact somewhat lower than the image would suggest.

While the relative distributions on the mirror show little change, the base plate pres-

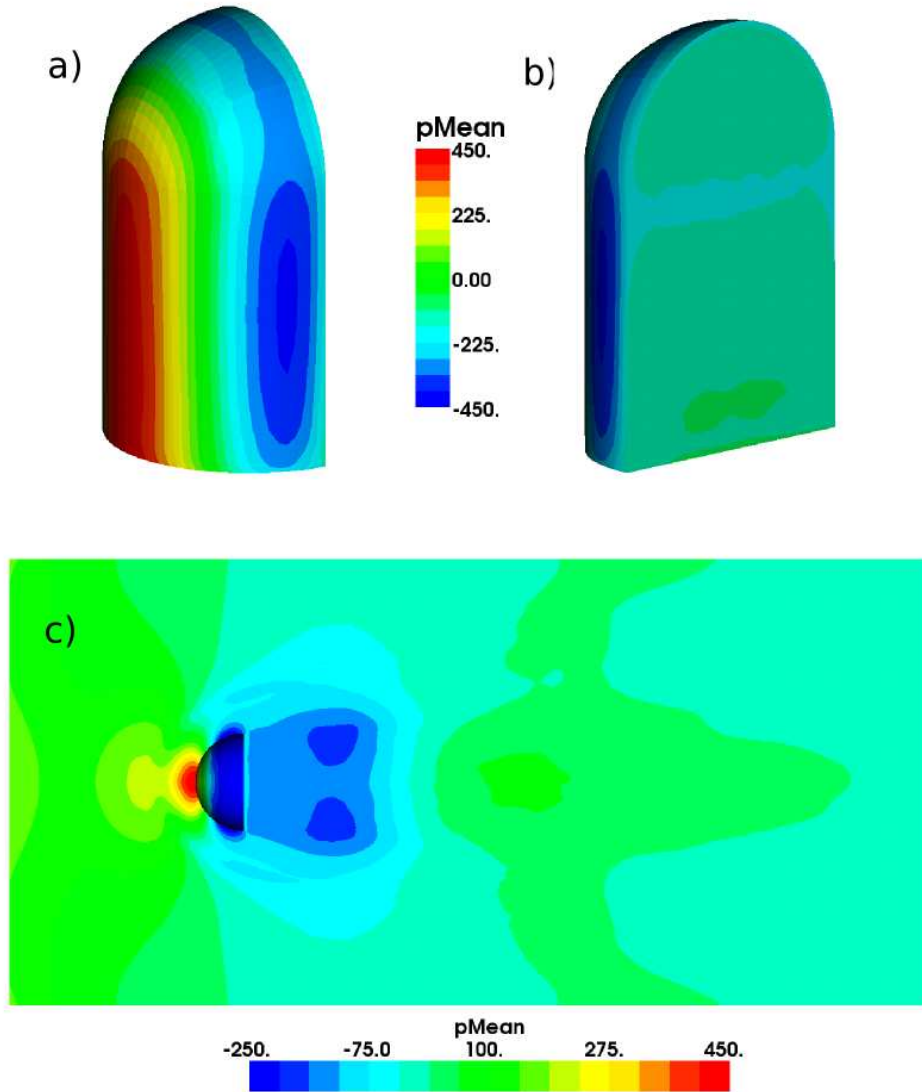


Figure 6.39: Mean surface pressure for case BSA3 a) mirror front face, b) rear and c) base plate.

sure contours (fig.6.39c) have several features which distinguish them from fig.6.14, the equivalent for Case A. Firstly, the blockage effect of the mirror combined with the side walls and the resulting acceleration of the flow produces a lower pressure region at the sides of the recirculation zone. Secondly, the long averaging times show much better symmetry, which is especially apparent in the wake and recirculation zone. The high pressure caused by reattachment is more apparent in fig.6.39 because of the relatively lower pressure in the surroundings.

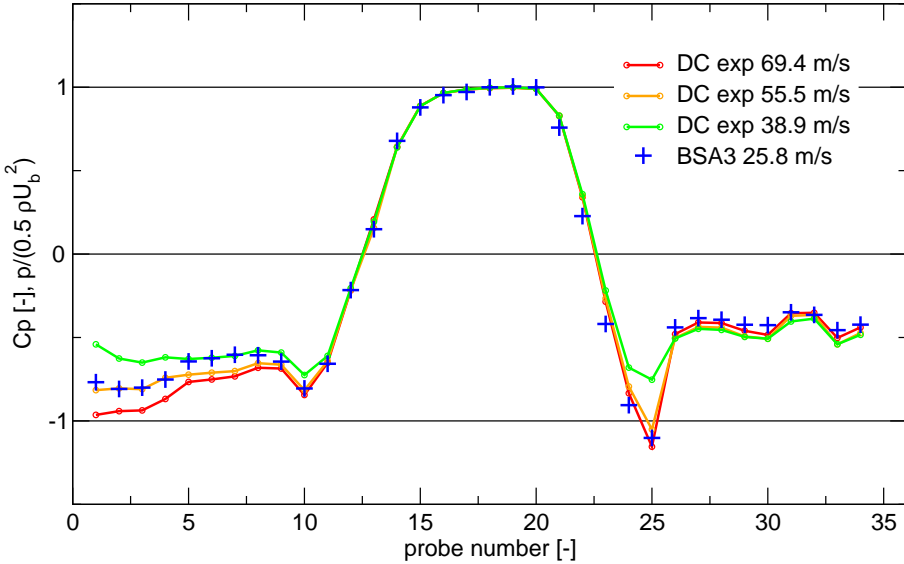


Figure 6.40: Static pressure probes on the mirror surface.

Some unpublished static pressure measurements are available from the Hoeld *et al.* [56] experiments for higher freestream velocities than investigated to date. Combining the higher velocity data with the measurements for Case A highlights the Reynolds number dependence of the flow around the mirror (fig.6.40).

The probe locations are identical to those shown in fig.6.12 and all pressures are scaled with the bulk velocity. Focussing first on the experimental data sets, a tendency of the higher Re flows to produce lower pressures near the mirror edge (locations 1-10, 24, 25) is readily apparent. This lower pressure is thought to be associated with weaker or delayed separation of the flow approaching the mirror edge. On the back face (26-34) and toward the stagnation region on the front face (11-23) there is virtually no difference between the experiments. A degree of Reynolds number dependence thus seems to hold near the edge regions where separation occurs, while the pressure at the rest of the measurement point is virtually Re independent.

Although three speeds are not enough to establish a good trend, it is to be expected that the 25.8 m/s Case B should produce edge pressures closer to the 38.9 m/s experiment than the higher velocity variants. The pressure distribution for BSA3 is however much

closer to the higher Re experiments. This inaccuracy despite the fine resolution on the front face is almost certainly the result of an over prediction of the turbulent viscosity in the boundary layer by the DES model discussed earlier (lack of laminar treatment). Apart from the edge discrepancies, the simulation produces very good overall agreement with the scaled experimental data for mirror A.

6.2.6 Pressure Spectra

As mentioned in sec.6.2.1 no pressure traces were recorded for points on the mirror surface during the Imperial College experiments. It was however felt that some form of comparison, even approximate, with the Case A data would be useful in judging the relative merits of the two calculations. To this end, scaled versions of mirror A experimental spectra were used where available. This scaling while generally valid, does not account for Reynolds number effects and comparisons that contain only scaled data should be viewed with this in mind. Scaling is performed as follows:

$$p'_B = \frac{U_{bB}^2}{U_{bA}^2} p'_A f_B = \frac{U_{bB}}{U_{bA}} f_A \quad (6.16)$$

where U_{bA} and U_{bB} are the bulk velocity for Cases A and B respectively. The deviatoric pressures are then converted to sound pressure level spectra as described in sec.6.1.4.

Mean surface SPL for the mirror and the base plate are displayed in the composite image, fig.6.41. The improved symmetry of the better converged solution is apparent when compared to figs.6.15, 6.17 and 6.19. Despite improved meshing practices, the effects of numerical noise are still apparent on the front face (fig.6.41a). To obtain a better idea of where this noise originates and what the volumetric structure of the intense pressure fluctuations are, the moving cutting plane of this property displayed in anim.A.4 should be viewed. The double-lobed feature in the middle of the front face is clearly a local phenomenon, i.e. fluctuations are not convected from upstream as is generally the case in the simulations for mirror A. A probable cause for these error-induced fluctuations is the skewness of the high aspect ratio near-surface cells in a high velocity/pressure gradient flow. In addition, there is a fairly rapid change in the cell sizes in this region, which could induce commutation errors. For the most part however, the error levels are considerably

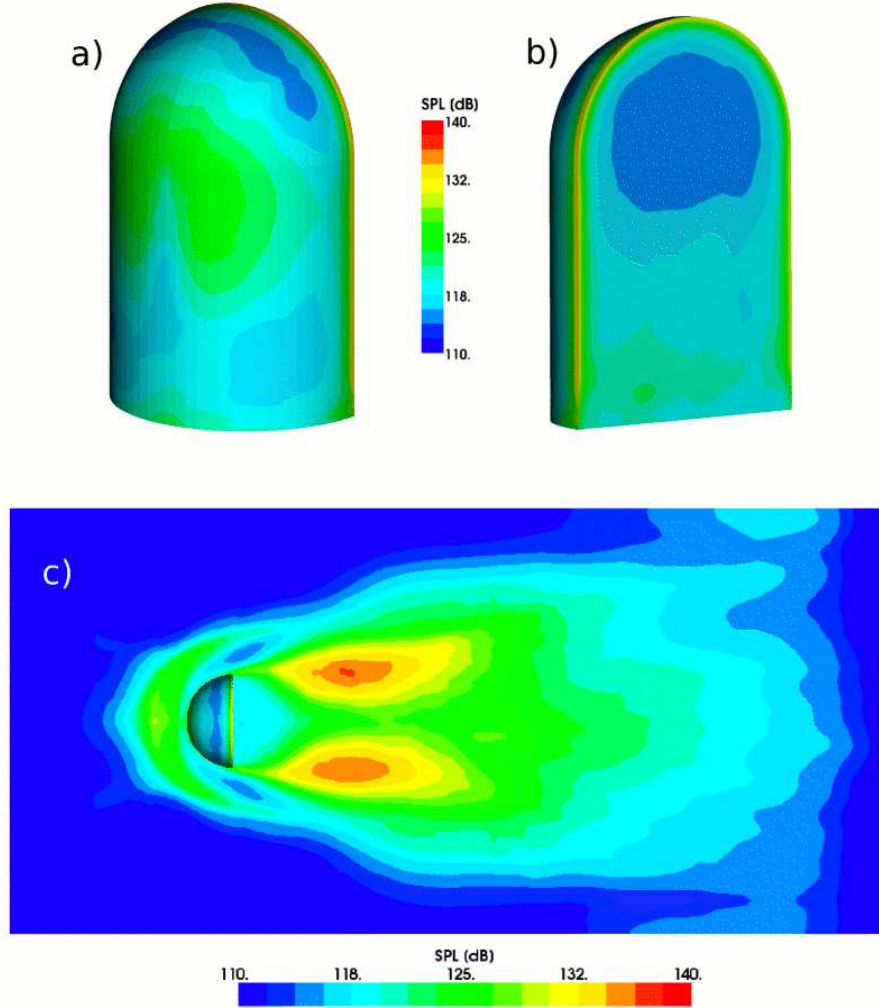


Figure 6.41: Sound pressure level for surface sources on mirror B, a) Mirror front face, b) Rear face and c) Base plate.

lower than in Case A.

The rear face of the mirror, fig.6.41, shows a SPL distribution consistent with expectation; high values around the periphery where unsteady separation is taking place; intermediate strength noise sources near the junction with the base plate caused by the impinging recirculating flow; and very low level perturbations on the upper central part where bulk flow is convecting away from the surface. The base plate is however where the most acoustic sources reside and this is reflected by the mean SPL contours (fig.6.41). The noise levels are of course lower than for mirror A, but the distribution, especially

6. Side Mirror

in the wake, is very similar. A big improvement in symmetry is apparent due to the prolonged averaging times. There appears to be no numerical noise upstream of the mirror, but the bow vortex footprint is much larger in size than was recorded for ASA3. Returning to anim.A.4, some columnar artefacts are visible in the flow to the sides and slightly upstream of the mirror. These features correspond to a joining line where 5 cell blocks meet. We thus expect some non-orthogonality and/or skewness error at this location. Fortunately, the fluctuations induced here do not appear to convect very far before being damped out. The base of the columns do however overlap with the position of the sickle shaped bow vortex footprint, and so might be inducing some variability in what was previously a fairly stable structure.

Apart from the probes located on the mirror at positions 102, 103, 114 and 115, which can be found in figs.6.16 and 6.18, all the point positions on the base plate are shown in fig.6.42. In addition to the old comparison locations on the shear layer base (120-123), there are a plethora of new points upstream of the mirror (116-118), along the wake centreline (130-133) and across the shear layer (125-129).

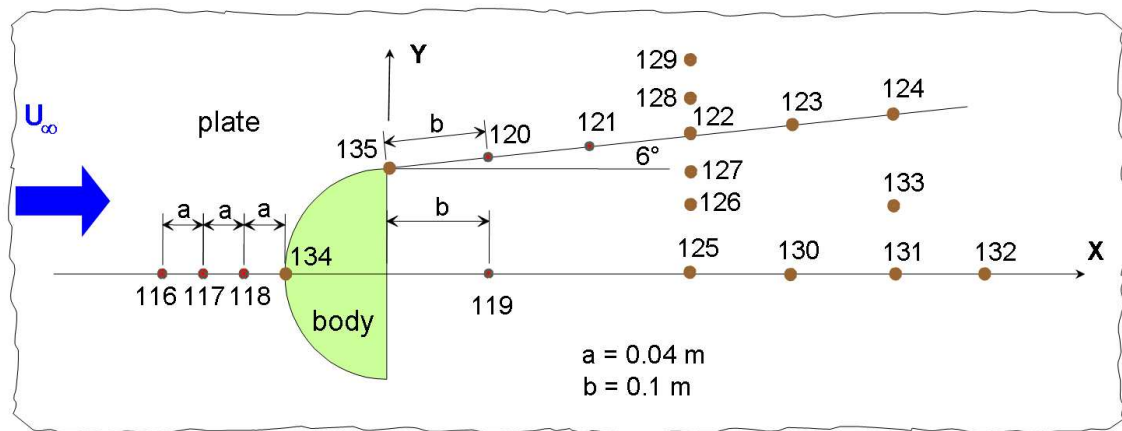


Figure 6.42: Probe locations on the mirror base plate, Case B.

Figure 6.43 shows the spectra on and upstream of the mirror. As mentioned previously, there were no pressure spectra measurements on mirror B, so the comparisons for these points use the scaled data from the mirror A experiments, which means they are not exactly equivalent. In all cases “DC experiment” refers to the experiments by Hoeld *et*

al. , while “IC experiment” indicated measurements made by Chronopoulos and Taylor at Imperial College. At points 102 and 103 very much the same trends as in fig.6.16 are seen. Near the mirror edge (102) the levels, while not very accurate, show at least the right approximate values up to 2 kHz. At point 103 where the experiment indicates mostly laminar flow, the calculated spectra show over prediction of the noise content just like for mirror A. Unlike Case A, the over prediction for case BSA3 occurs only at higher frequencies between 200 Hz and 2 kHz, with those below 100 Hz actually comparing passingly well with the scaled data. The BSA3 spectra on the front face clearly have different modes of noise production from those observed in ASA3. For example, the new results show a maximum in the 200-500 Hz range that has no analogue in the older calculations. Overall levels, even when scaled also appear lower than those predicted by ASA3. Whether this is the result of Reynolds number dependencies or simply less numerically induced instability is difficult to ascertain.

Looking at the points on the rear surface (114 and 115) we see somewhat better agreement with the scaled data, especially near the trailing edge (114). The BSA3 results however buck the trend by predicting lower noise levels in the middle of the back surface (115) than at the edge. Looking at fig.6.41b, this appears to be largely an edge effect which is more pronounced than before and is consistent with predicted levels displayed in the mean surface SPL. Also very prominent are spikes in the rear face spectra at 500 Hz. Since this phenomenon is extremely prominent near the edge, it is likely associated with a regular small scale shedding cycle at this location. Again, the lack of this feature in the scaled data places some doubt on its accuracy.

Points 116, 117 and 118 on the base plate in front of the mirror produce the first comparisons with the SPL spectra from the Imperial College experiments. Scaled data from mirror A are included for reference and to allow examination of Re effects and sensitivities. Taking the comparisons at the three locations as a whole, we see a range of result qualities going from very good 12 cm upstream of the mirror, to poor at 8 and 4 cm. Looking at the mesh upstream of the mirror (fig.6.31), we see a very rapid reduction in resolution. The radial nature of the local grid and the previously discussed focused meshing methodology combine to produce cells that have approximate wall parallel spacings of

6. Side Mirror

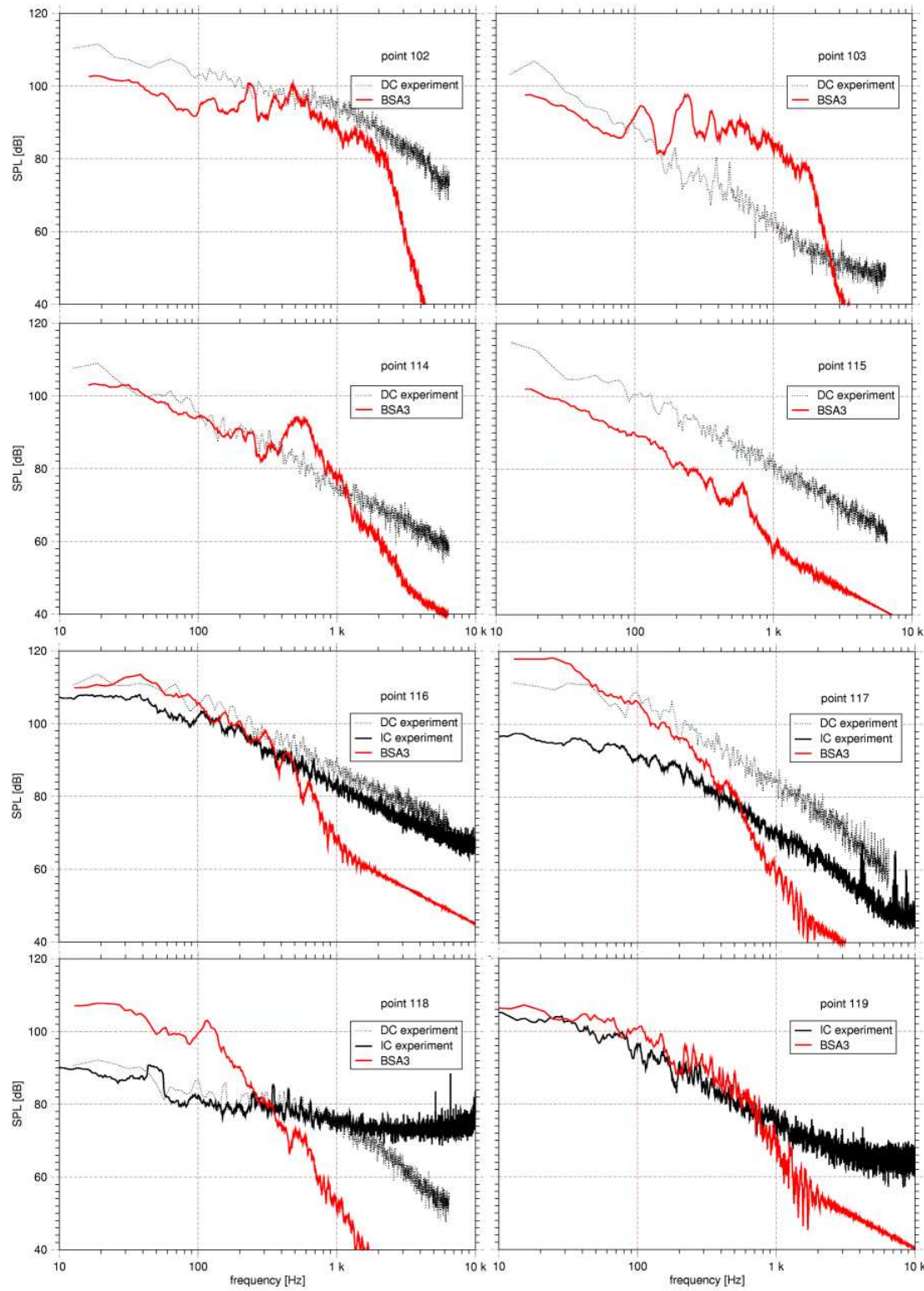


Figure 6.43: Point SPL spectra on and around the mirror.

11, 14 and 16 mm at points 118, 117 and 116 respectively. Compared to the wall-normal spacing of 0.4 mm, these dimensions are fairly coarse and in retrospect should be somewhat finer to properly resolve the relatively fine bow vortex. Strangely enough, the best agreement with experiment is at point 116, which also has the coarsest mesh, but still supports a frequency of above 500 Hz. At the other two locations the low frequency noise is completely over predicted. When comparing the fine scale and irregular shape of the bow vortex in fig.6.34 with the large footprint shown in fig.6.41 it seems likely that the over prediction of low frequency sources at 117 and 118 is due to big oscillations in the position of the vortex between these locations. Large cells and non-orthogonality errors from the pillar-like source highlighted in the animation probably contribute to this problem. The erratic agreement of the two experimental sets at these locations also points toward rapid, hard to predict spatial variation in the acoustic sources.

The final plot in fig.6.43 for point 119 is actually in the mirror wake near the middle of the recirculation zone. Much better agreement is achieved at this position, with only slight over prediction in SPL between 10 and 900 Hz, the limit of resolution. Since the spectra beyond 1 kHz have a SPL well below 80 dB, they will not contribute significantly to the effective noise level. The favourable comparison indicates that the noise bearing structures and the mechanisms that produce them in the recirculation zone have been well represented by BSA3.

The next set of plots (fig.6.44) show spectra on the base plate below the shear layer and close to the mirror, including point 135 which is right at the base of the mirror edge. Of the three plots only point 135 shows significant deviation from experiment. While the low frequency noise at this position agrees with experiment, the band between 100 and 2000 Hz is significantly over predicted with a peak at 500 Hz. Going back to fig.6.34, we see the small scale structures that were speculatively attributed to skewness errors on the front face correspond with this position at the junction of the base and mirror edge. We also see peaks at similar frequencies for the spectra at points 114 and 115 on the rear face. Taken together, these features point toward an excitation of strong high frequency fluctuations in the near shear layer by skewness-induced perturbations from the front face near the trailing edge. Fortunately, this high frequency noise appears to be localised and

6. Side Mirror

short lived as indicated by a lack of similar deviation at positions 120 and 121 downstream of the corner. Animation A.4 confirms this deduction, showing small intense regions of pressure fluctuation right behind the edge, that rapidly decrease in strength as the flow moves downstream.

Focussing on the shear-layer points 120, 121 and 122-124 in fig.6.45 near-perfect prediction of the experimental spectra is observed. In contrast with the same comparisons for mirror A, the longer averaging time results in low frequency content between 10 and 50 Hz being well predicted. This is particularly evident at the characteristic shedding frequency (25 – 30 Hz), whose position and drift is very well reproduced by the simulation. Note however, that 20 Hz is at the lower limit of the human audible range, so that this peak will in fact not contribute as much to the perceived noise level as the content between 100 and 1000 Hz. The higher end of the shear-layer spectrum is only resolved to about 1-2 kHz, somewhat less than for the fine meshes used for the mirror A calculations. This is intentional, as the SPL beyond this frequency rapidly drops below 80 dB, it is unlikely to contribute significantly to the overall perceived noise levels. Also recall that in sec.6.1.4 the resolution requirement for a specific frequency was shown to be directly proportional to the local convection velocity. This implies that to resolve the same frequency for the lower velocity case the resolution would have to be improved from 2.5 mm to nearly 1 mm. This kind of resolution throughout the wake is clearly not compatible with an objective of performing long time averages, as it would cause the overall cell count and computational cost to skyrocket. Using a target frequency of 1500 Hz and a projected convection velocity of 23 m/s, produces a wavelength of around 15 mm. Following the results from sec.6.1.4 this scale is resolved by at least 4 grid points producing the final cell size of 3.75 mm for BSA3, an acceptable compromise.

Interestingly, the relative SPL at points 120-124 exactly match the trend in the mean surface contours of the same quantity in fig.6.41. This is most prominent in the peak values around 25 Hz, which start out well below 120 dB at point 120 and then rapidly increase to a maximum of 124 dB at point 122, as the large vortices in the shear layer develop, before decreasing again toward the rear of the wake. It is clear from the quality of the comparisons at the larger scales that the resolution used is more than adequate to

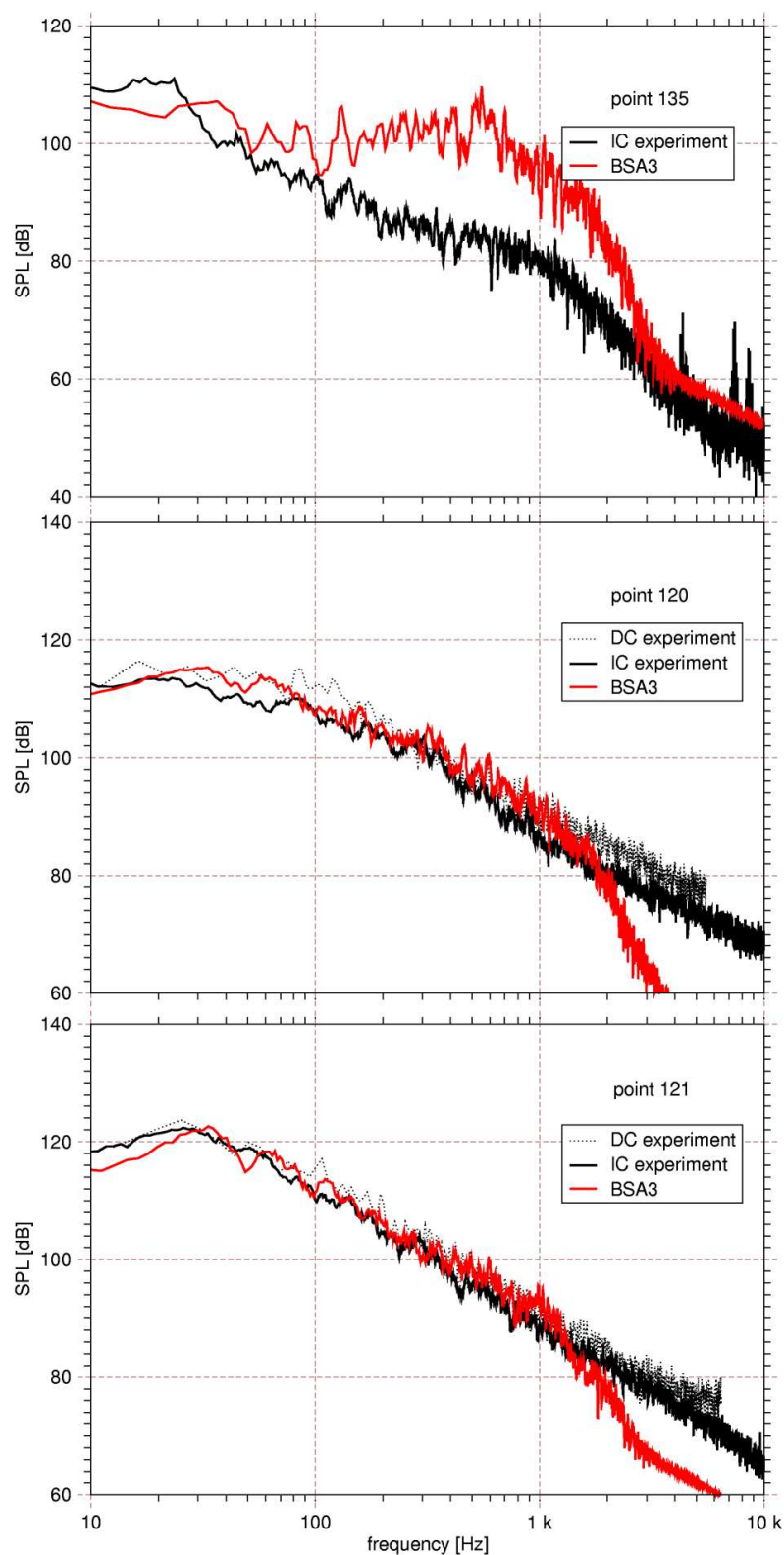


Figure 6.44: Point spectra in the near shear layer.

6. Side Mirror

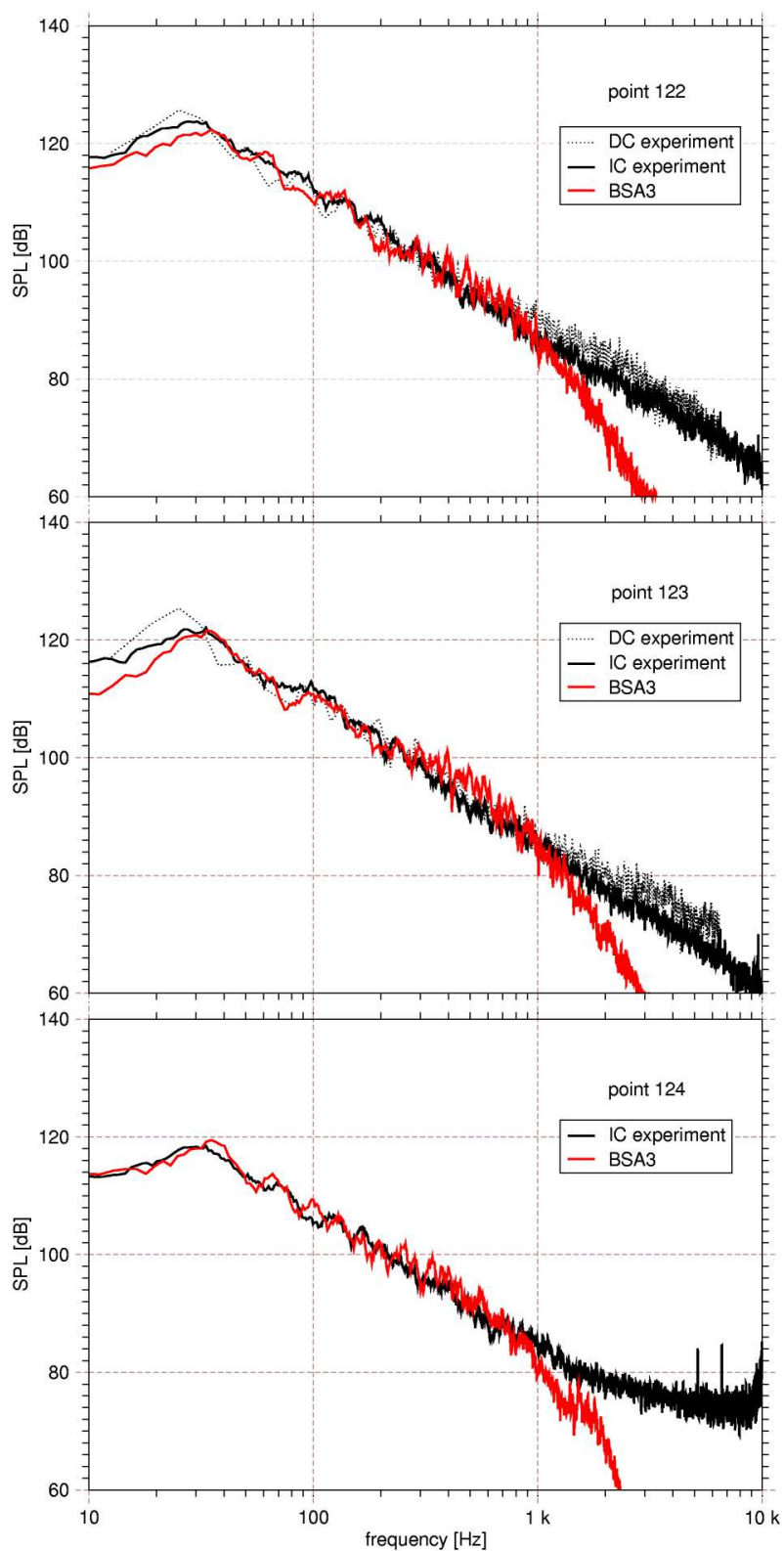


Figure 6.45: Point spectra in the far shear layer.

capture the energy-bearing scales necessary for accurate flow prediction. Comparing the available experimental spectra for mirror A and B in the wake also shows very limited Reynolds number dependence in this region of the flow.

Many new locations were included in the spectral measurements made by Chronopoulos and Taylor, and fig.6.46 shows four of these that traverse the shear layer from the centreline 125 to the other side of the shear layer 129 (fig.6.47). The increase in relative SPL from the centreline toward the far side of the shear layer is clearly visible. The comparisons between the measured and calculated spectra are less exact than along the shear layer and the maximum resolved frequency is only around 1 kHz. The cause is apparent when fig.6.31 is examined: the mesh resolution away from the shear layer decreases rapidly to conserve resources, so that the typical mesh spacing at the centreline is more than twice the finest value. The worst predictions are at the points on the inside of the shear layer (126, 127) where the experimental data is over predicted by about 5 dB, while those on the outside (128 and 129) and the centreline (125) show quite acceptable results. The exact cause of this deviation is not known, but mean flow deflection due to the lack of laminar treatment on the front face is a possible candidate. Also, the mesh becomes coarser quicker on the inside of the shear-layer than the outside, which might be causing anti-aliasing errors due to insufficient resolution of the energy-bearing turbulent structures and/or a lack of turbulent damping.

The last set of spectra at locations 130-132, 2-3 mirror diameters downstream from the base along the centreline in the mirror far wake, are shown in fig.6.47. The trend of the simulation to over predict the measurements continues (generally by less than 5 dB) and the spectra are only resolved to around 800 Hz on the coarser mesh in this region.

Given that the spectra in regions and frequencies of highest noise production, which will dominate the overall sound production, are well reproduced, it is probable that the results are more than adequate for aero-acoustic predictive purposes. The fact that the strongest noise sources along the shear layer wake are so well reproduced across a large part of the spectrum is very encouraging. Indications are that the predictions could everywhere be improved to this level by simply increasing mesh resolution, reducing computational uncertainty to an arbitrary error level limited only by cost.

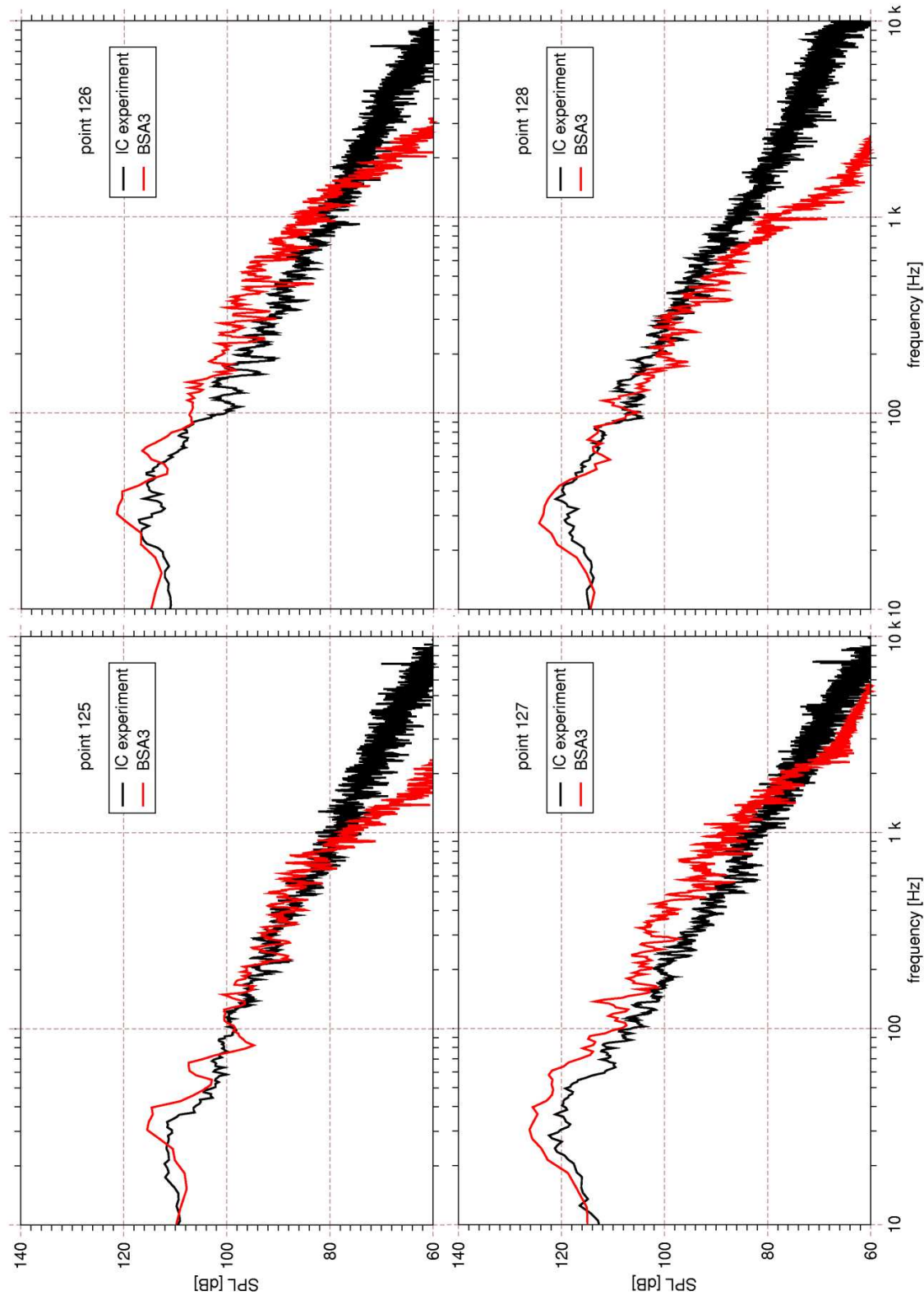


Figure 6.46: Point spectra across the shear layer.

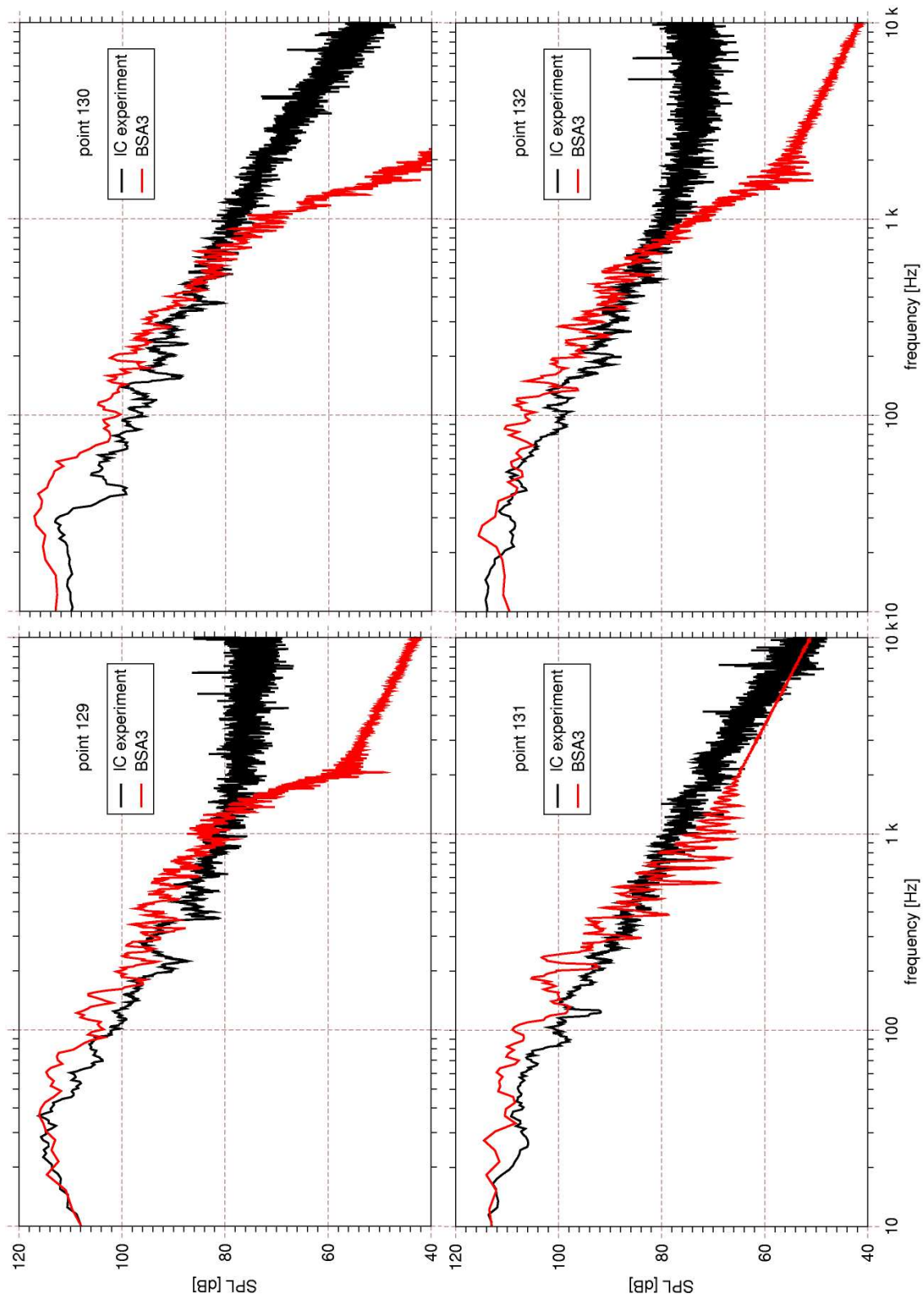


Figure 6.47: Point spectra on the wake centreline.

6.2.7 Mean Velocity and Reynolds Stress

In the mirror experiments at Imperial College, five sets of LDA measurements were made of the flow around the mirror, focussing on characterising the bow vortex and the recirculation zone. This data allows us to judge the capability of the LES calculation to accurately reproduce these prominent mean flow features. Combined with the well characterised boundary conditions and the pressure spectra, these measurements provide a very comprehensive validation case for any CFD methodology, and especially LES.

The five measurement locations include:

- The symmetry plane at the base of the mirror's front face; this section characterises the location and strength of the bow vortex.
- A lateral section of the bow vortex displays the properties of this feature in a plane parallel and near the rear face of the mirror.
- The recirculation zone's maximum extent, which is measured via the streamwise velocity component on the symmetry plane 1 cm above the base plate.
- Cross wake profiles, which show the velocity distribution between the symmetry plane and the far side of the shear layer at two streamwise positions.
- Numerous probe locations on the wake symmetry plane, which give a detailed picture of the recirculation zone, its extent, strength and the positioning of its most prominent features.

Figure 6.48 shows the position of the front measuring plane as a red rectangle at the mirror base. Measurements are made along 7 lines from 0.1 m upstream to the mirror and between 5 mm and 60 mm above the base plate. Both the streamwise and base normal velocity components are measured, except at the lowest line, the position of which made it inaccessible to the LDA equipment's vertical measuring configuration.

Various comparisons between measurements and predictions are shown in fig.6.49. Figure 6.49a displays the predicted velocity vectors and magnitudes for case BSA3 in the plane of the measurements for reference. A very strong recirculation reaching right up

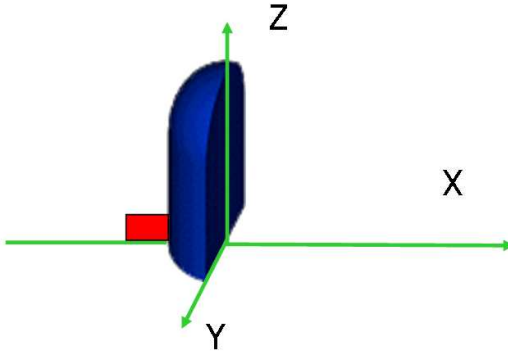


Figure 6.48: LDA measurement plane in front of the mirror.

to the base of the mirror is evident in this image. Below this, in fig.6.49b, an attempt is made to directly compare the velocity vectors from the experiment with those from the calculation. The measured vectors are coloured by U/U_b , while the calculated ones are left black. The agreement between the data sets is fairly good. Magnitudes and directions match over a large portion of the field and the position of the bow vortex appears quite similar. This is confirmed by fig.6.49c, which contrasts the vortex centre pinpointed via the \mathbb{Q} with the experimentally determined vortex core found via interpolation. It is clear in both cases that the mean position of this feature differs by less than 1 cm, i.e. less than 10% on the scale of the mirror.

A more detailed comparison of the velocity components is presented in fig.6.50. For most part the two data sets agree very well, the exception being the positions closest to the base plate. These lines actually pass through the bow vortex and also show the calculated vortex positioned slightly closer to the mirror than the experiment indicates. Comparison of the base normal velocities at $Z/R = 0.1$ and 0.2 reveals a qualitative difference between the distributions. The calculations do not show the same inflection and rapid increase in velocity near the front face exhibited by the experimental U_z values. Something similar is revealed by the bottom-most comparison of the U_x component at $Z/R = 0.05$. The experiment shows the flow along the base plate reversing underneath the bow vortex, but the vortex does not extend to the front face of the mirror. The flow in the simulation reverses, but it does not show the second inflection to become positive again, so that the

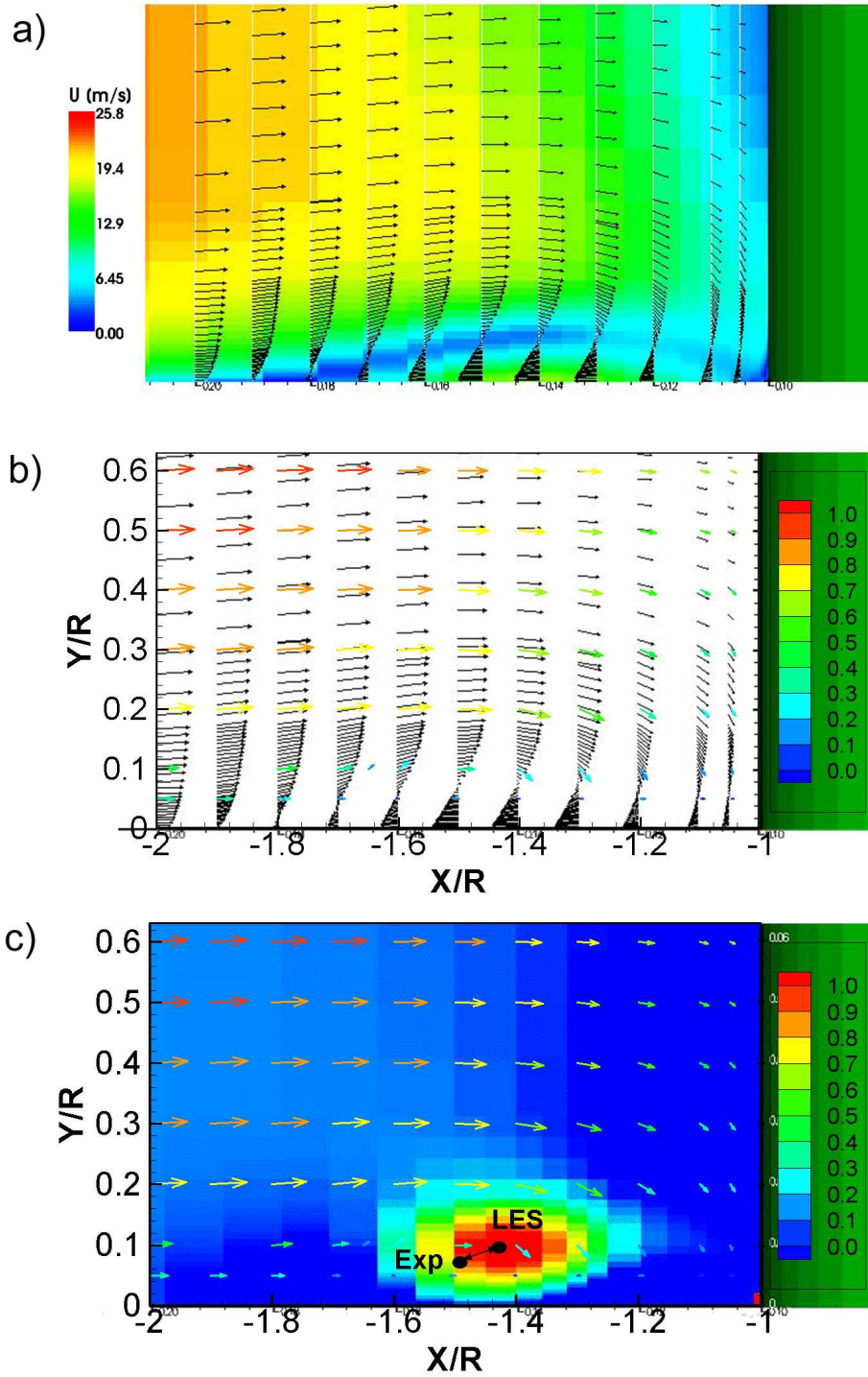


Figure 6.49: Comparison of calculated bow vortex with LDA vectors, a) BSA3 velocity magnitude and vectors, b) BSA3 velocity vectors (black) and LDA vectors (coloured by U/U_b) c) Location of bow vortex core, experimental LDA vectors, positive contours $Q_{\nabla \mathbf{U}}$ for BSA3.

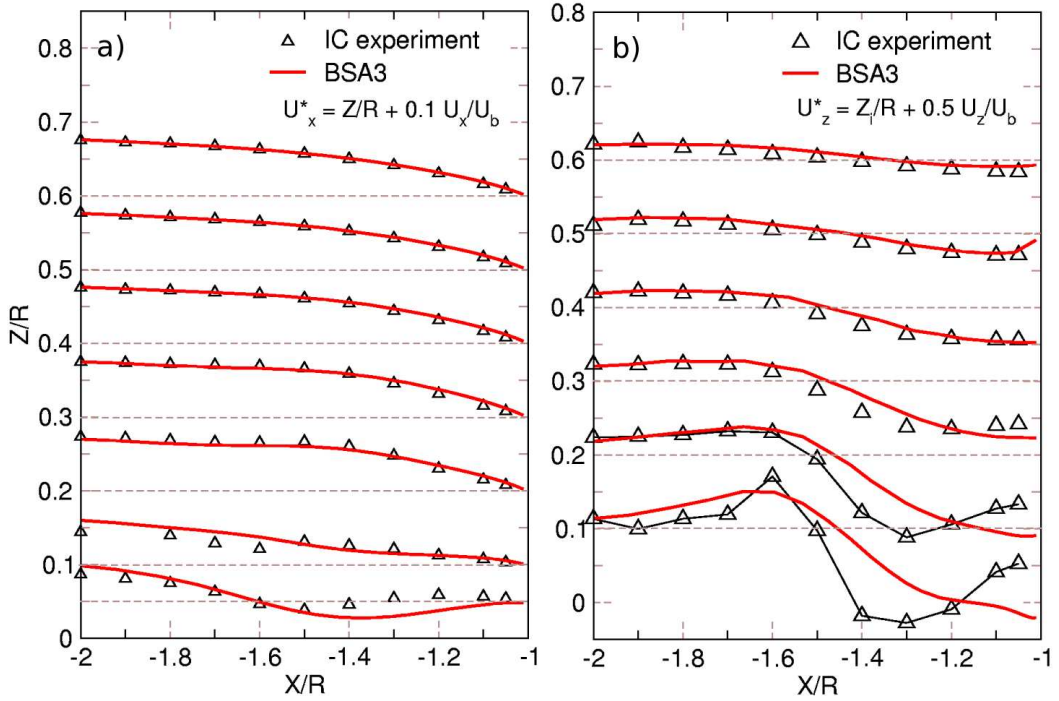


Figure 6.50: Comparison of experimental and calculated velocity components in front of the mirror a) Streamwise component, U_x b) Base plate normal component, U_z

vortex nestles up against the mirror. It thus seems that the small dislocation in vortex core position is not the only difference between experiment and calculation, the vortex itself appears to extend much further toward the mirror in the calculation producing much more downward flow close to the mirror base. The deficiencies of the mesh upstream of the mirror have been noted before and the possibility that the simulated vortex is oscillating more than it should is almost certain. It must be noted that the bow vortex is by nature a very sensitive structure. The flow, being balanced between the back pressure from the streamwise and downward impinging flux, the upstream velocity profile generated through turbulent forces and the shear layer above the small recirculation, is sensitive to changes in any of these features and will respond in an unstable fashion if any of them feed perturbations into the system. One possible perturbation source has already been identified at the junction of five block structured mesh components that introduce non-orthogonality into the mesh at a position contiguous with the bow vortex' location. The vortex being so close to the base plate, will also be very susceptible to deviations in the

6. Side Mirror

boundary layer profile due to errors in the RANS portion of the DES model. Alternatively the transition between the RANS zone and regions that derive their length scales from the LES assumptions might be introducing excessive turbulent viscosity into the bow vortex system. The precise cause of these comparatively small discrepancies is clearly difficult to isolate and might even be a combination or none of the above mentioned possibilities. The net effect though is a slightly larger, but weaker bow vortex situated a bit closer to the front face on the symmetry plane.

The position of the next measuring plane to the side of the mirror is shown in fig.6.51. The data includes 5 profiles of the streamwise and base-normal velocity components between 1 cm and 7 cm above the base plate.

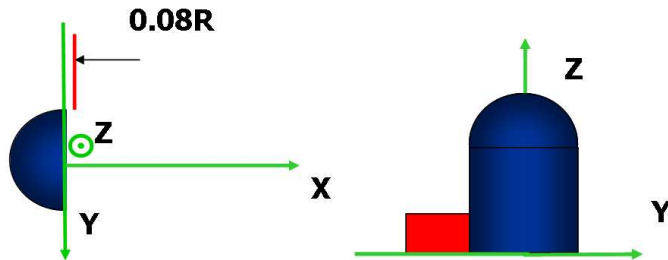


Figure 6.51: LDA measurement plane beside the mirror.

Figure 6.52 shows a selection of vectors streaklines and velocity component magnitudes from the BSA3 simulation on this plane. Individually and in combination these images clearly show the bow vortex as it wraps around the side of the mirror.

The profiles of U_x and U_z on the mirror's side plane are presented in figs.6.53a and 6.53b respectively. Two problems are immediately apparent: firstly, the bow vortex is about 1 cm further from the mirror than it should be; and secondly, the flow in close proximity to the mirror front face is completely misrepresented. The bulk of the flow on the other hand is very well reproduced.

Without trying to deduce a complex causality, it is noted that the bow vortex to the side of the mirror edge is subject to more or less the same uncertainties that plague the structure in front of the mirror. The difference in the predicted and measured location of

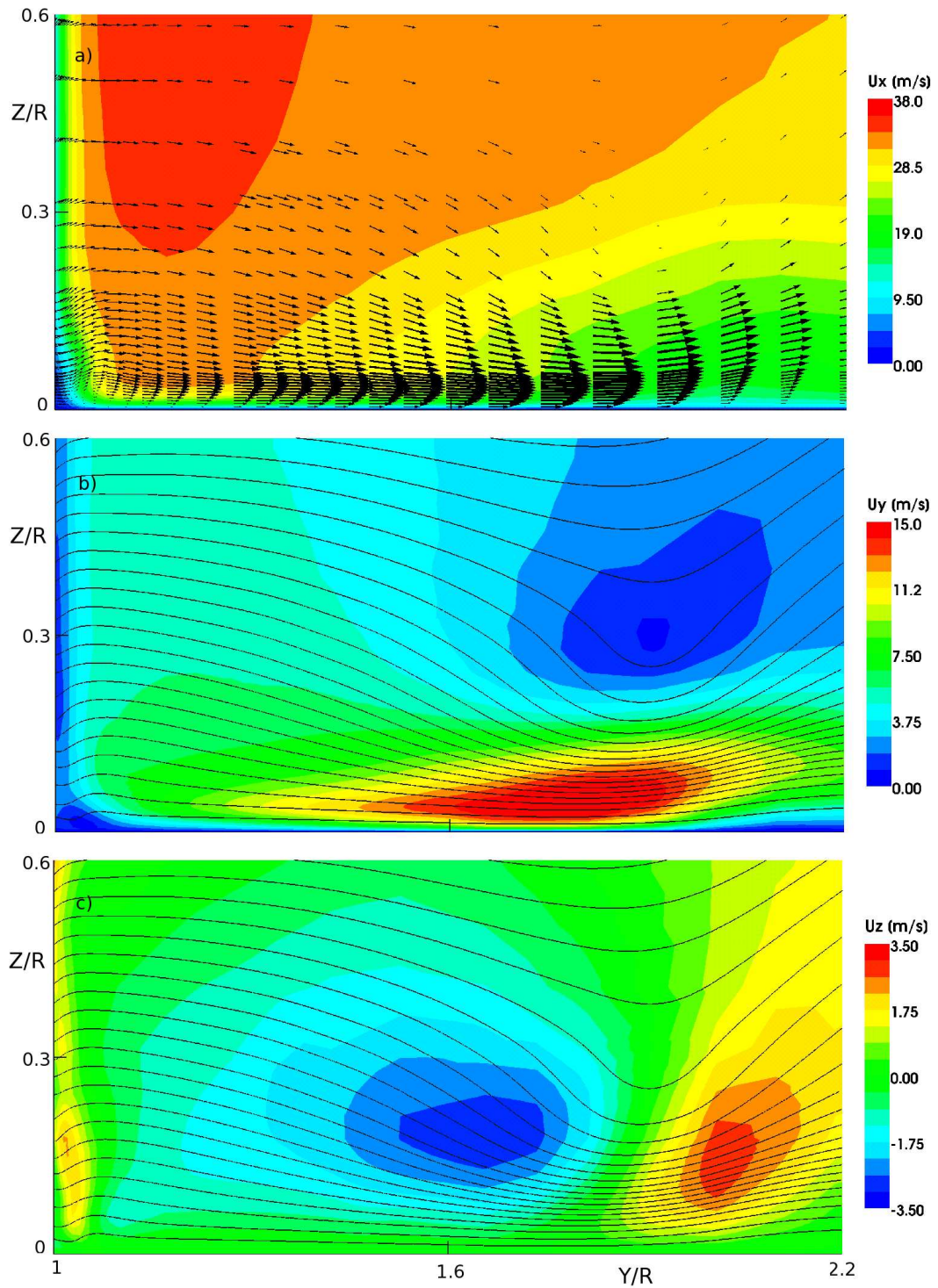


Figure 6.52: Calculated velocity distribution on the side measurement plane, a) velocity vectors and contours of U_x , b) streaklines on the plane and contours of U_y c) U_z .

6. Side Mirror

the vortex core is however comparatively small.

This is not the case near the mirror edge. Although line-of-site issues prevent LDA measurements very near the edge, the influence of the erroneous turbulence modelling on the laminar front face is non-the-less very apparent in the comparison of experimental and simulated flow 8 mm behind the trailing edge.

The measured profiles all show shallower gradients or inflected distributions induced by adverse pressure gradients and laminar flow near $X/R = 1$. These are particularly noticeable 2 and 3 cm above the base where the front face recirculation is known to be at its strongest. The error at the same locations in the base normal component of velocity is even more extreme, with some of the distributions being oppositely signed to the measured values. It is less clear what causes this deviation, but it is more than likely tied in some way to the same lack of laminar treatment on the front face. Interestingly, it appears from the inflection in the experimental data that a small but intense vortex exists at the base of the mirror. A similar structure was observed for the ASA3 simulation, but was not reproduced during the current simulation, which suggests that a lack of adequate resolution of some flow feature might be the cause of the discrepancy.

The approximate side location of the vortex core can be derived from the experimental velocity data using the first and second derivatives of the velocity components. When the experimental location is compared with the predicted vortex location shown in fig.6.54 as contours of $\mathcal{Q}_{\nabla \bar{u}} > 0$ the difference is found to be comparatively small, supporting the general accuracy of the method.

The line shown in fig.6.55 indicates the traverse used to measure the streamwise extent of the recirculation zone 1 cm above the base plate. The streamwise velocity is recorded at 8 locations from 20 cm to 60 cm downstream of the mirror. Figure 6.56 shows the extent of the predicted recirculation zone in the plane at the same height, as indicated by contours of the streamwise velocity, with the thin solid black line representing $U_x = 0$. Figure 6.57 compares the measured and predicted streamwise velocities along the traverse. The predicted recirculation length of 4.5 mirror radii is shown to be some 10% longer than the measured value of 5.1 radii. Some of the deviation is almost certainly due to the narrower wake which might be caused by the lack of laminar separation on the front face. Just how

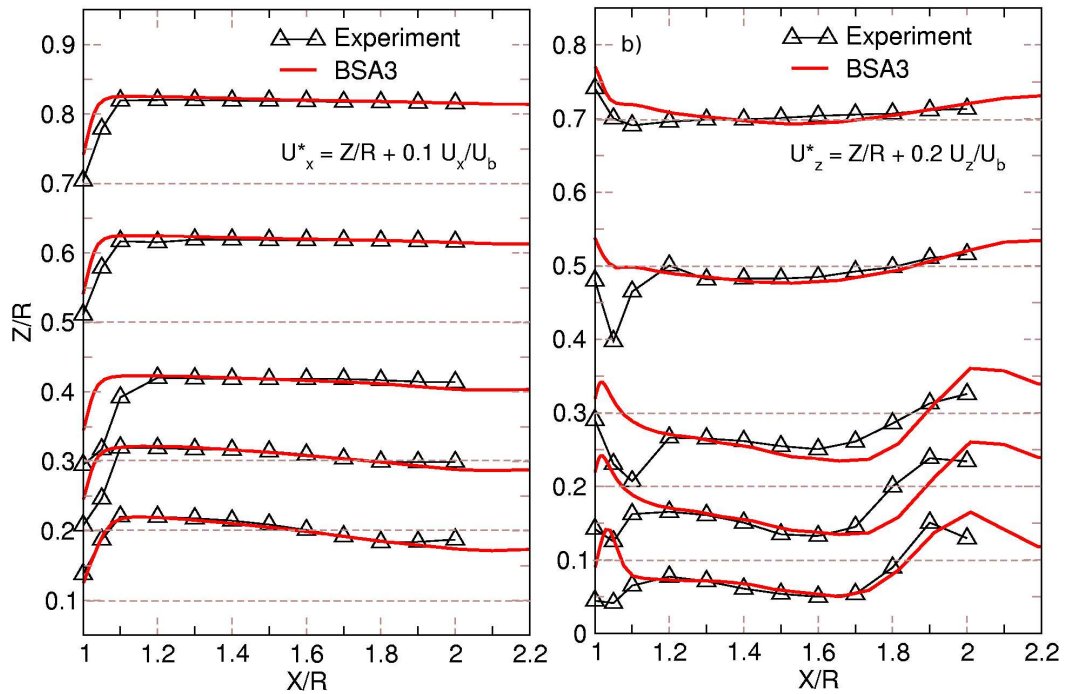


Figure 6.53: Comparison of experimental and calculated velocity components beside the mirror
 a) Streamwise component, U_x b) Base plate normal component, U_z

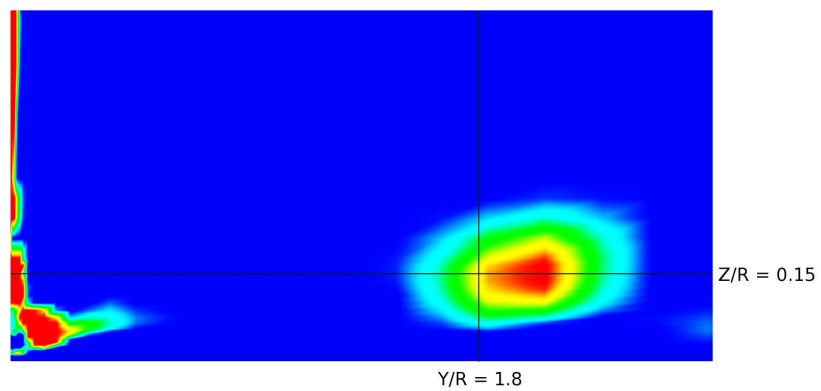


Figure 6.54: Side plane location of the bow vortex core, measured (black lines) and positive contours of $Q_{\nabla U}$ for BSA3.

6. Side Mirror

strong this effect is relative to other possible causes is impossible to say.

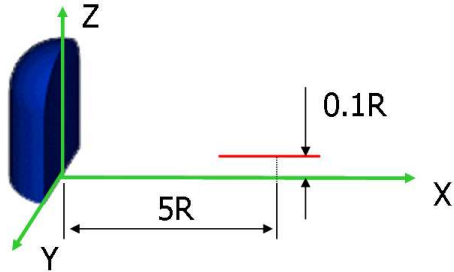


Figure 6.55: Measurement line for LDA of the recirculation extent.

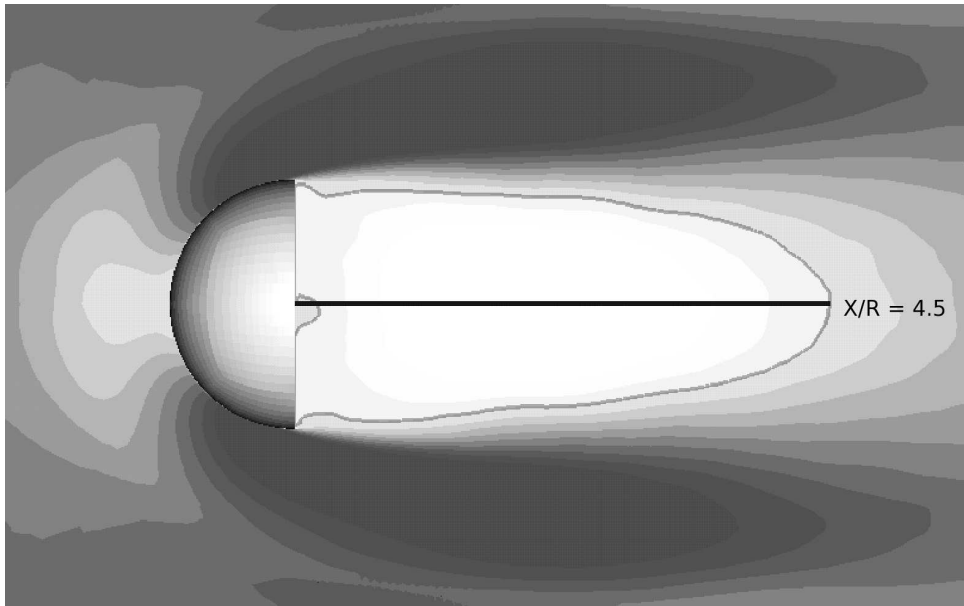


Figure 6.56: Extent of the predicted recirculation zone on the plane $X/R = 0.1$.

Another set of LDA measurements are available across the wake and shear-layer as indicated in fig.6.58. They provide an indication of the lateral extent of the shear layer and allow judgement on the effectiveness of the prediction in capturing this feature.

Figure 6.59 also shows the traverse locations, along with a general overview of the calculated flow patterns at the same elevation above the base plate. The measurement lines pass through one of the branches of the “U”-shaped vortex, the region with the highest spanwise velocity differential in the wake.

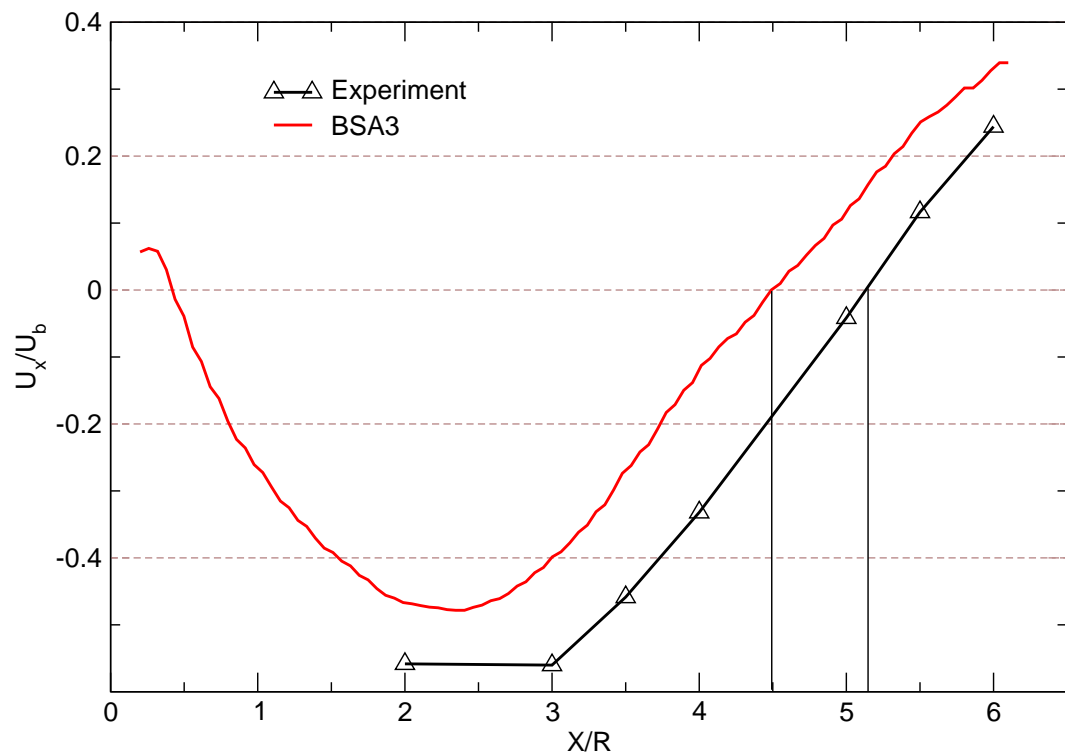


Figure 6.57: Streamwise velocity component in the recirculation zone.

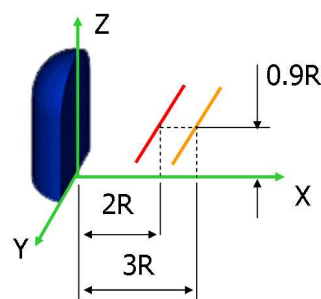


Figure 6.58: LDA measurement locations across the wake.

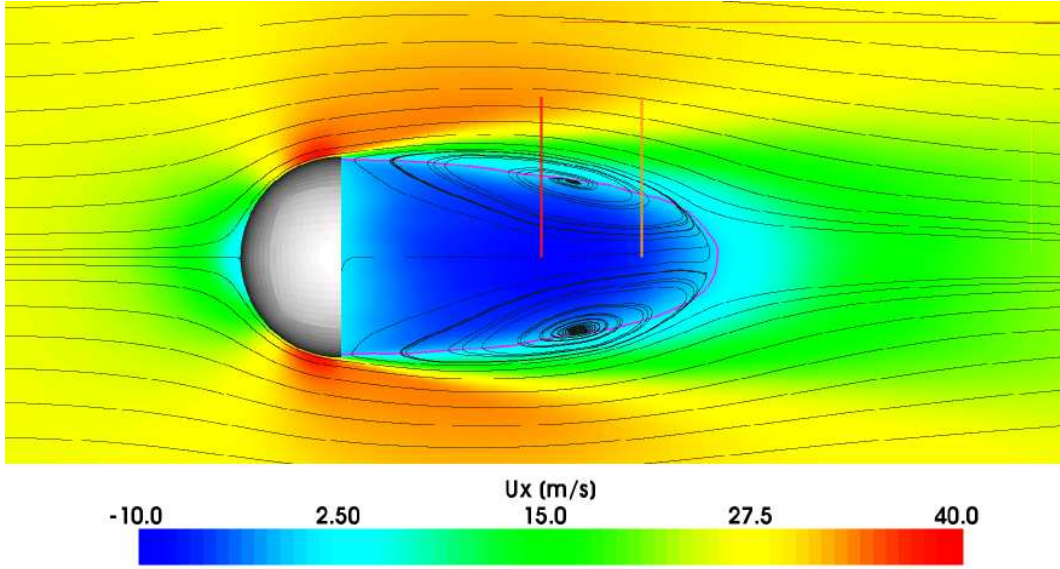


Figure 6.59: Streaklines and streamwise velocity magnitude in the $Z/R = 0.9$ plane.

The comparison for streamwise velocity in fig.6.60 is not as good across the wake, as has generally been the case at previous measurement locations. Qualitatively, the curves still compare very well, but there is a clear contraction of the recirculation zone as evidenced by the 1.5 cm difference in the centre of the shear layer indicated by the zero intercept. It is likely that this deviation is also partially due to the lack of front face separation, which would otherwise increase the lateral deflection of the oncoming flow. There is however a growth in the difference beyond the shear-layer, which suggests that other forces might be aiding and/or exacerbating the observed drift. Further, a clear under prediction in the magnitude of the recirculating flow can be seen. Coupled with the smaller overall size of this feature, the weaker recirculation indicates reduced momentum transfer via the shear layer to the recirculating flow. Why the momentum transfer and thus the mixing in the simulated shear layer is less intense than in the experiment is uncertain.

The last LDA measurement plane, located on the symmetry axis of the mirror and extending through the recirculation zone, is shown in fig.6.61. The comparisons in this region are especially important in terms of judging the performance of the DES approach,

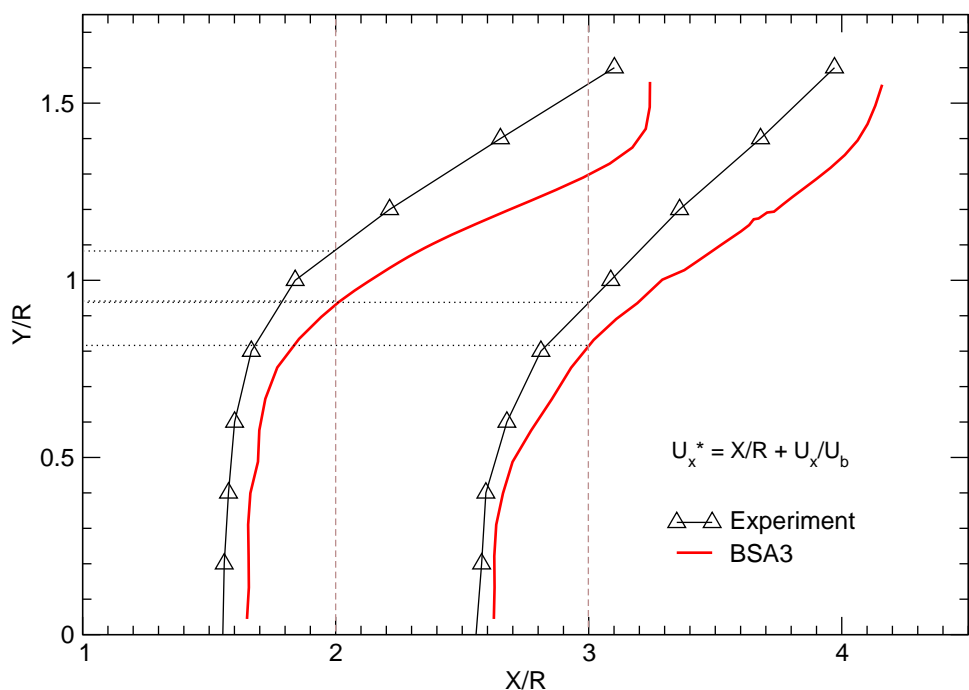


Figure 6.60: Comparison of streamwise velocity component for LDA and case BSA3 across the recirculation zone.

6. Side Mirror

as the detached eddies that abound here are exactly what the model is supposed to be best at predicting.

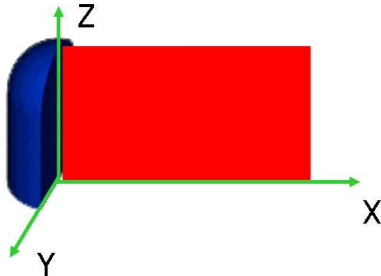


Figure 6.61: LDA measurement position in the wake symmetry plane.

Figure 6.62 presents an overview of the measurements and predictions on the plane. The top image (fig.6.62a) shows calculated streaklines and velocity magnitude which conveniently outline the shape of the recirculation zone. The coincidence of low velocity magnitudes with regions of high flow curvature explain the pattern of heavy oil film depositions seen in fig.6.35. Figure 6.62b shows a direct comparison of the measured and calculated velocity vectors along the 4 probe lines. The coloured vectors represent the experimental values and the black the simulation results. Note that the relative vector scalings are approximate. There are evidently some rather large discrepancies between the data sets. The interpolated locus of the calculated recirculation is displaced some 2 cm toward the mirror and the wake described by the experimental vectors is clearly longer and higher than the simulated equivalent.

The velocity component distributions in fig.6.63 show that the disagreement is not as extreme as the vectors would suggest. Although the differences at locations $X/R = 3$ and 4 are certainly larger, the discrepancy is akin to a constant displacement, so that the velocity gradients at equivalent Z/R positions are approximately equal. This displacement, which is larger at $X/R = 4$, is evidently tied to the shorter recirculating zone, yet the calculated results still mirror some details of the measurements such as extrema and inflections. So even though the exact proportions of this feature are not accurately predicted, the results do suggest that the majority of the dynamics are reproduced.

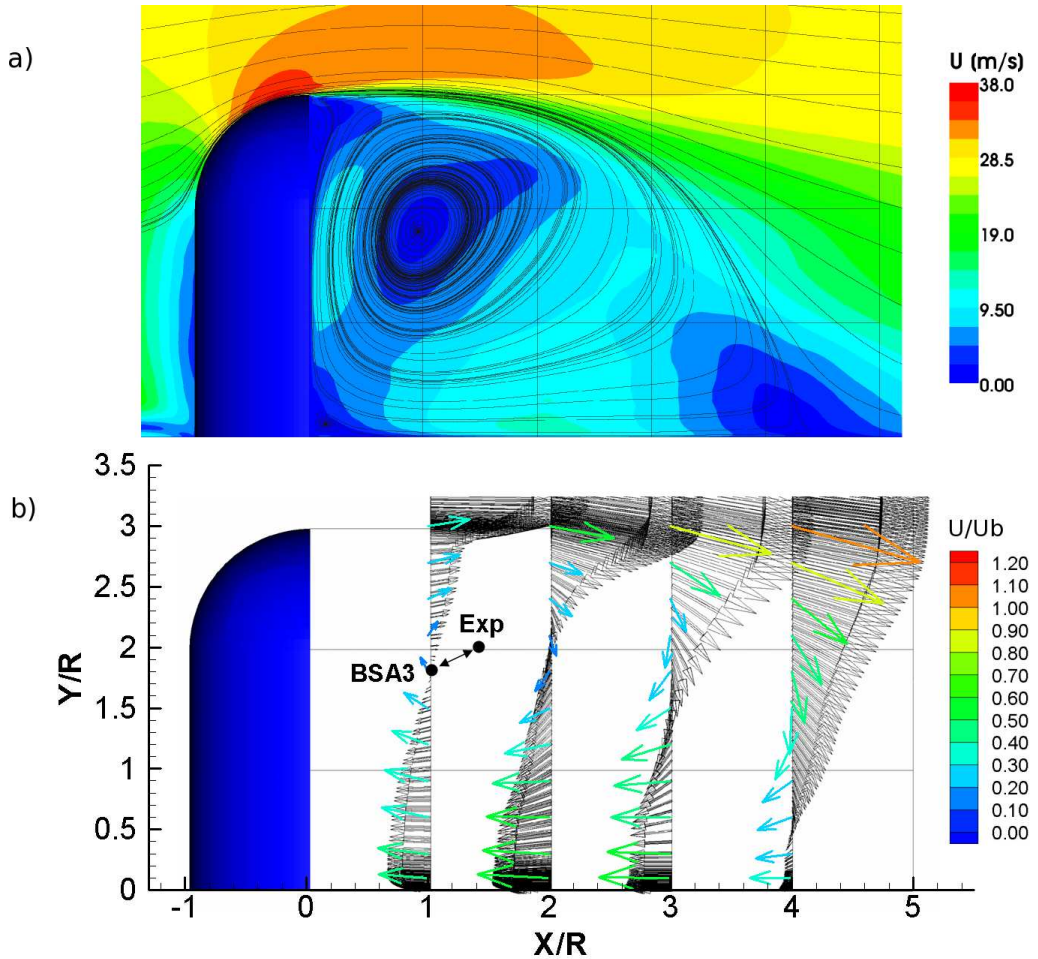


Figure 6.62: Velocity on the symmetry plane, a) Streamlines and velocity magnitude for BSA3, b) Measured velocity vectors (coloured) and calculated BSA3 (black).

Unlike the rightmost graphs, the distributions at $X/R = 1$ and 2 agree quite well with the experiment over most of their vertical extent. This is not surprising, considering the trend of increasing inaccuracy in the downstream distributions. What is noteworthy however is the large over prediction of velocity near the top of the graphs. Although fig.6.60 showed a similar trend, these results are a lot closer to the mirror edge and so show the immediate impact of the errors in the front face turbulence modelling on the recirculation zone much more clearly. The lack of early separation on the mirror face and the increased mixing that contributes to it causes the edge velocity profile to look like a turbulent boundary layer (with its attendant severe gradients and high shear stresses,

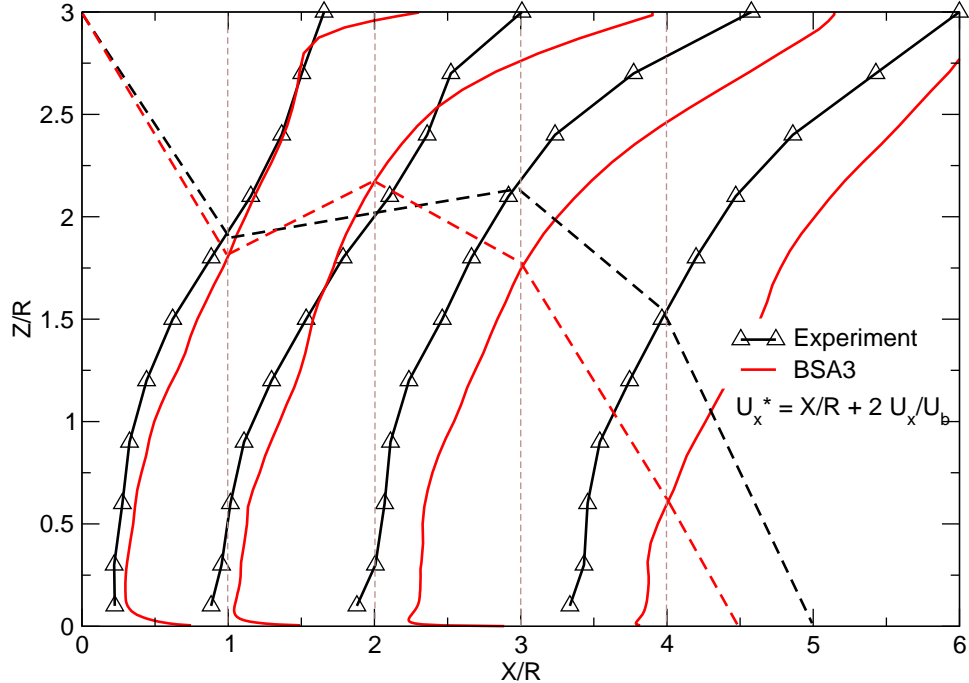


Figure 6.63: Streamwise velocity in the mirror symmetry plane.

see fig.6.53a). Thus, instead of being deflected away from the mirror surface with a mild inflected velocity gradient separating it from the recirculation bubble, the flow hugs the wall like a jet, resulting in very high shear just behind the mirror edge. Beside the impact of the narrower flow direction on the shape and proportions of the wake, the high shear has a secondary consequence that can affect the aero-acoustic prediction. As highlighted by the elevated small scale noise levels at point 134 in fig.6.44 and confirmed by the SPL maximum a short distance downstream of the edge in anim.A.4, this high shear causes the small perturbations behind the trailing edge to develop faster and become more energetic than would normally be the case. Fortunately, the small size of these eddies causes most of them to dissipate before they can carry this additional turbulent energy far downstream. Increased noise sources are thus limited to a narrow region very close to the edge. What secondary effects these oscillations might have on the larger system dynamics via changes in the transported SGS property is unknown.

In addition to the mean velocity, LDA measurements were made of the fluctuating velocity components, which allows comparison of the turbulent stresses. Figure 6.64 shows the calculated distribution of the streamwise normal stress T_{xx} , which includes the effects of resolved and SGS turbulence and the mean of:

$$T_{xx} = (\bar{u}_x^2 - U_x^2) + \frac{2}{3}K_{SGS} \quad (6.17)$$

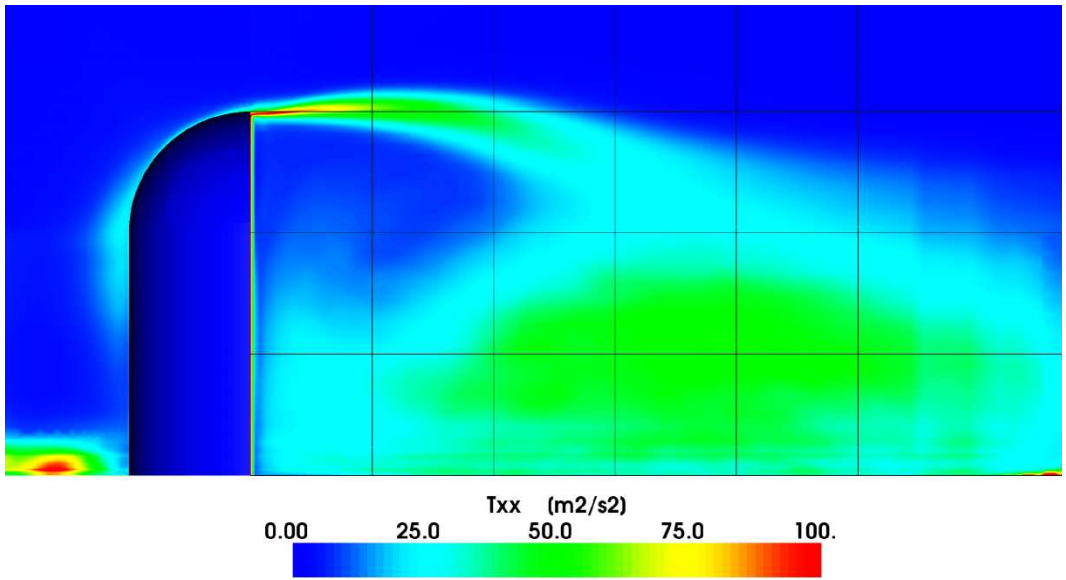


Figure 6.64: Streamwise normal stress component, T_{xx} .

For the most part, the contours are as expected. There is a strong maximum near the mirror edge due to the elevated velocities coming off the front face that expand into the shear layer. A large region of medium strength turbulence is also apparent around the reattachment zone, since the volume is traversed by many eddies and is subject to bulk oscillations of the reattachment. What is somewhat surprising is the intensity of the normal stresses in the core of the front bow vortex. It is clear from the vortex core visualisation in fig.6.34 that there are no small scales of turbulence in the same vicinity as the bow vortex, and although SGS energy levels are slightly elevated at this locality, they are not nearly large enough to account for the observed maximum. The only remaining source of normal stresses is thus large scale oscillations in the position and strength of the vortex itself. This hypothesis is supported by the calculated SPL spectrum at point

6. Side Mirror

118 in fig.6.43, but not with the experimental spectrum at the same point. It thus seems likely that the predicted fluctuations in the bow vortex position are erroneous. The bow vortex is the result of several carefully balanced competing phenomena, including back pressure from stagnation on the front face, the shape of the oncoming velocity profile and turbulent shear stresses between the recirculating flow and the free stream. Perturbations introduced through any of these would almost certainly cause the vortex to oscillate and a likely candidate was already identified (sec.6.2.6) as non-orthogonality errors resulting from local distortions in the mesh.

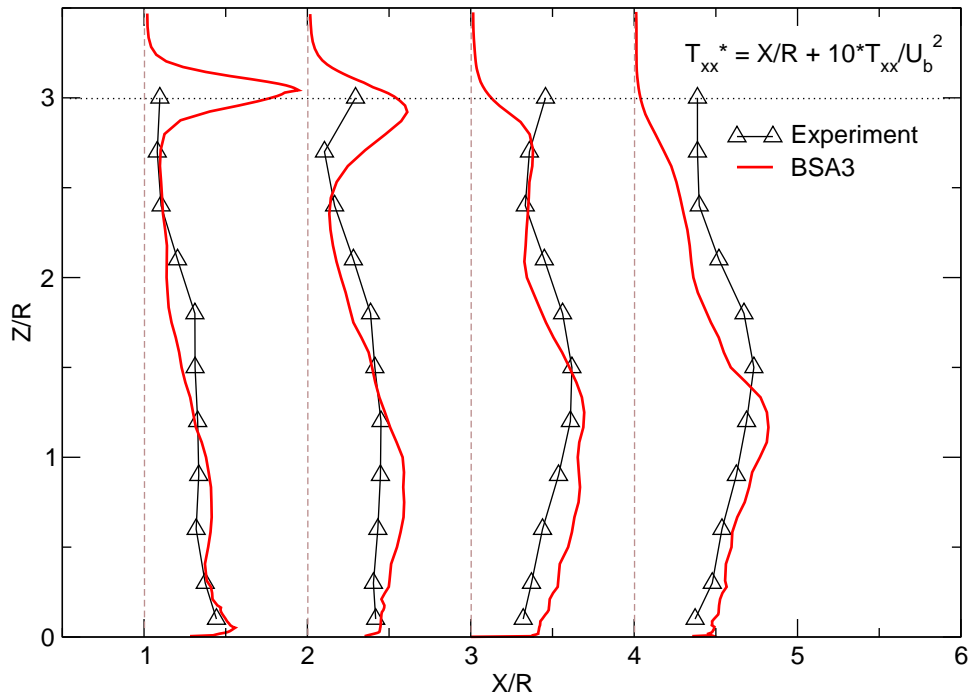


Figure 6.65: Comparison of streamwise normal stresses in the mirror symmetry plane.

As the normal stresses are a second-order property of the flow, less accuracy is expected than with first-order properties like velocity and pressure. Figure 6.65 shows surprisingly good agreement between the data sets. Along the top of the graphs the tell-tale signs of the downward displaced shear layer are visible again. The free-stream fluid is visibly moving downward from left to right on the graphs in the vicinity of $Z/R = 3$ and the

maxima nearer the mirror edge are clearly lower than those that must be present in the experimental flow beyond the extent of the measurements. Unfortunately the normal stress maxima in the shear layer were not measured during the experiment. Comparisons of these magnitudes with calculated values would have provided valuable insight into the quality of the DES shear layer simulation.

6.2.8 Summary

The results obtained for mirror B have confirmed all the conclusions drawn during the mirror A calculations. DES is very good at predicting noise in flows dominated by detached eddies and the simulations are robust in spite of modelling and numerical errors upstream of the measurement locations. Pressure spectra again show good agreement, especially in regions of highest SPL at the base of the shear-layer. A direct link between mesh resolution and highest resolvable frequency is confirmed and the approximate relationship is successfully used to specify cell sizes in the wake. All the major flow features observed using LDA are reproduced and their position and strength predicted to a good degree of accuracy. Surface visualisations confirm these findings and extend the comparisons to the far wake and lateral boundaries.

In addition, case BSA3 has highlighted the importance of good meshing practices. Numerical errors, while still present, were much less severe on the improved mesh and the use of local refinement allowed large reductions in mesh size and savings in computational time without sacrificing accuracy. Of course, such an iterative meshing process is expensive and relies heavily on past experience to guide the process, which is far from ideal if a reproducible cost-effective solution is being sought.

The inaccuracies resulting from the turbulence modelling on the front face were much more evident due to the nature of the experimental data. The error was quantified and the effect it has on various structures and dynamics explored. While an improved mesh all but removed numerical errors upstream of the mirror, wall-normal refinement of the cells of the front face introduced skewness and commutation errors which manifest as small resolved perturbations. These are thought to combine with the strong shear layer behind the mirror edge to excite more intense high frequency oscillations than would normally

6. Side Mirror

be the case. A final inaccuracy was noted in the overly high SPL spectra below the front portion of the bow vortex. The bow vortex intersects a compact region of the mesh that contains non-orthogonal regions. Errors introduced by these are found to produce small localised fluctuations in the resolved fields. Since the bow vortex coincides with these locations and is thought to be unstable to such perturbations, its oscillations will introduce moderately intense low frequency noise into the system.

The numerous and often detailed discussions of the flaws in the calculation should not detract from the fact that for the most part its predictions are excellent. In general quantities are calculated correctly to within 10% of their experimental equivalents and where larger or consistent discrepancies arise plausible explanations have been advanced.

Chapter 7

Conclusions and Suggestions

The main goal of this thesis was to determine the applicability and practicality the LES methodology for the prediction of aerodynamic properties and aero-acoustic noise production in an automotive environment. The answer to this question of fitness was found to be an emphatic “yes” in both cases. To reach this conclusion a variety of numerical experiments and validations were conducted, each providing particular contributions to this thesis.

7.1 Summary of Primary Results

In the early part of this thesis, investigation of the turbulent dynamics near the wall revealed that wall treatments can be categorized according to the regions of the flow they excise from the LES portion of the calculation. The proposed categories correspond to fully resolved (i.e. DNS of the near-wall boundary layer); inner layer matching, where only perturbations in the viscous sub-layer are not directly simulated; outer layer matching, which models all the turbulent structures in the boundary layer; and intermediate matching, falling between the last two extremes, but requiring some form of structural synthesis to account for the lack of resolved vortices in the modeled region. While there can be some cross-over between the categories, they do provide a framework within which to evaluate and compare wall treatments.

Two groups of validation cases were investigated. The first set, consisting of the

7. Conclusions and Suggestions

periodic turbulent channel flow and the asymmetric plane diffuser, were mainly used to assess the physical models and numerics implemented for this investigation. The second, consisting of the two mirror experiments, were used to test the approach at operating conditions similar to those encountered in real automotive aero-dynamic and aero-acoustic applications.

The periodic channel calculations served not only to validate the methodologies including several variations of the SGS turbulent energy and Spalart-Allmaras models in a canonical test case, but also to study the effects of mesh resolution. The main findings of these studies are:

- Wall normal cell dimensions should be no less than $y^+ = 40$ if the near-wall turbulent cycle is to be captured with any degree of accuracy. Failure to reproduce the turbulent cycle in at least an approximate sense results in a sudden and large decrease in the accuracy of the wall shear prediction. Additionally, turbulent structures near the wall are considerably disturbed at larger resolutions, leading to unpredictable results.
- The Spalart-Allmaras DES model is unsuited to boundary layer dominated flows, because it excessively damps the resolved turbulence near the wall. Resolution studies show however, that its wall shear prediction, although less accurate, is fairly insensitive to resolution, which implies that it will be the more robust model when applied to engineering quality meshes.

The asymmetric plane diffuser represents a more challenging case, with incipient separation and reattachment along the lower wall requiring a greater degree of accuracy to reproduce. Simulations of this problem produced the following findings:

- A novel LES inlet condition is proposed for fully developed channel flows, which maps flow results from the interior of the domain onto the inlet. This methodology is shown to be more flexible and accurate than the conventional method of interpolating a library of pre-computed turbulent flow.
- LES simulations using the SGS turbulent energy model with inner layer matching are considerably more accurate than the equivalent RANS simulations at predicting

separation and the resulting recirculation along an inclined surface. The use of the inner layer matching approximation decreases the required mesh size enough to make the added expenditure relative to outer layer matching a viable proposition when the enhanced accuracy of the LES methodology is paramount.

- The Spalart-Allmaras DES methodology performs poorly in the diffuser environment in which representing the influence of pressure gradient on boundary layer eddies is crucial to the accuracy of the simulation. Since these eddies feed into and eventually become the vortices that dominate mixing in the free-shear layer, they have to be resolved if the shear-layer is to be represented accurately. The S-A DES methodology is by definition an outer layer matching approach with RANS-type modelling being used near the surface, which explains its deficiency in this context. This has the implication that, at least for weakly separating flows, outer-layer matching methods may not be applicable. For DES of more vigorously separating flows however, it is likely that separation accuracy will be dictated by the capabilities of the RANS model.
- Local embedded refinement for LES provides attractive cost-saving characteristics, while maintaining the overall accuracy of a finer mesh. Refinement experiments using the diffuser and residual error guided refinement show a twofold decrease in total mesh size without significant loss of accuracy. Choosing the right property to determine refinement regions is however non-trivial and as such requires further investigation.

Simulation of the two mirror test cases produced some very good comparisons with the experimental pressure and velocity data. In addition several strengths and weaknesses of the current implementation and the general DES approach were identified.

- Both the SGS turbulent energy model used in the outer layer matching mode and the Spalart-Allmaras DES model provide good prediction of mean flow and noise source properties for problems which are not dominated by boundary layer eddies, such as the mirror. Free shear layers, where the energetic eddies are directly resolved and the SGS model plays a secondary role, are particularly well represented.

7. Conclusions and Suggestions

- Where inlet boundary layers are thin and the eddies they contain constitute a small portion of the total turbulent energy of the system, representing the inlet via mean velocities and SGS properties is an acceptable compromise in light of the DES approximation. In other words, omitting turbulent structures at inlets which fulfil these specifications does not compromise the overall accuracy of the DES simulation.
- Different mesh resolutions for Case A indicate that capturing a specific noise generation frequency is closely tied to the local cell size relative to its wavelength and a minimum of 4 cells are necessary to capture a given wave length. Pressure spectra results in the wake of mirror B confirm this hypothesis, with pre-planned mesh densities reproducing the expected frequency range. Although use of such requirements as mesh construction guidelines can only be approximate due to uncertainties inherent in predicting the local advection velocity, it does provide a useful tool when planning mesh density distributions.
- Lack of proper transitional behaviour in the SGS turbulent model can lead to significant inaccuracies in bluff body flows application. Experimental comparisons of static pressures, mean velocity profiles and pressure spectra on and around the mirror confirm that the excessive predicted turbulence on the front face of the mirror causes several distinct deviations from the predicted behaviour.
- Errors in LES were categorised in sec.4.5 as owing to discretisation, modelling or filter related inaccuracies. Of these, discretisation and filtering errors were found to produce a significant destabilising effect on the flow upstream of the front face of the mirror, especially in the coarser mesh Case A calculations. Comparison of the error-induced noise from the meshes for Cases A and B indicate that mesh non-orthogonality in combination with large cells is the primary source of unphysical perturbations. Local error sources were also found to correspond to regions of mesh skewness as evinced by the SPL distribution for mirror B. In addition, commutation errors are apparent near the front face, where the mesh is aggressively graded to better resolve the velocity profile. All these errors can be minimised through careful mesh construction, but the added cost may be prohibitive.

- Despite the modelling and numerical errors on and upstream of the mirror front face, pressure spectra in the wake (which is the dominant noise source) are extremely well predicted up to the frequency limit of the local mesh resolution. This is testament to the LES methodology's accuracy when dealing with resolved-scale turbulence such as that found in the shear layer and highlights the robustness of the DES approach to inaccuracies in the RANS portion of the flow.
- Long time-averaged calculations show LES' capability to accurately predict not only high-frequency noise sources, but also large scale unsteady phenomena such as the main shedding cycle of the mirror. This opens the door for the use of LES to predict unsteady aerodynamic loading, which is not always accurately represented by unsteady RANS type calculations.
- The calculated mean flow morphology around the mirror corresponds well with experiment. The flow is characterized by a flattened arch vortex in the recirculation zone, a bow vortex which wraps around the front of the mirror to bound both sides of the wake and a smaller roller at the base of the rear face.
- Mean velocity components and even Reynolds stresses in the wake are predicted to a fair degree of accuracy. The reduction in recirculation length, thought to be due primarily to inaccuracies in the front face modelling, is the main source of difference between experiment and calculation.
- Comparison of experiments from Case B with simulations using the Spalart-Allmaras model on a highly refined and graded mesh, show that not only can LES reliably predict aerodynamic and aero-acoustic properties with less than a 10% margin of error, it can also do so in a cost-effective manner. The low cell count of 1.2 million cells used for this simulation indicates that engineering scale LES calculations of portions and even whole vehicles are a distinct possibility, especially if more effective error-minimising mesh generation tools become available.

The results for the different test cases indicate that the SGS turbulent energy model is the preferred methodology where resolution of boundary layer structures is important.

7. Conclusions and Suggestions

Conversely, the Spalart-Allmaras DES model shows several advantages for flows where boundary layer eddies are weak compared to other sources of turbulence. Mirror calculations with the turbulent energy model are however accurate enough to warrant the use of this approach where both types of boundary treatment are required in a single domain. In addition, the use of supplementary instantaneous wall functions to predict the wall shear in regions where the wall normal mesh is too coarse to apply the classical no-slip condition, was found to improved results in conjunction with both inner and outer matching wall treatments. Overall, the validations and other investigations showed many positive aspects associated with LES as a predictive tool for both internal and external flows.

7.2 Proposals for Future Work

Another valuable result of this investigation is the insight it provided into the limitations of the current set of approaches and how they might be extended and improved. In addition, many possible avenues for advancement were touched upon during the project, but not pursued due to lack of resources. If LES is to become a reliable and cost-effective engineering tool some of these issues will have to be addressed and the overall use of the methodology and its constituent components has to be automated to a degree which requires much less specialised knowledge from the end-user. While a lot of these concerns have been addressed in recent times by commercial and other researcher organisations the following suggestions for future research resulting from this work are still relevant:

- The DES method largely alleviates the high cost of meshing the near-wall region for external flows and is quite accurate provided the assumptions inherent in the modelling are met. Unfortunately, no equivalent methodology is yet available for the large subset of boundary layer dominated flows, making the tractability of these problems strongly Reynolds number dependent. It is proposed that continued work on wall treatments should focus on alleviating this dependence through a combination of structural support models and more advanced wall shear predictions. Some success has recently been achieved in specifying artificial inlet conditions for

turbulent boundary layers and RANS to LES transitions ([65][37]). Applying this technology as forcing functions to wall treatments with intermediate matching holds some promise.

- As demonstrated throughout Chapter 6 the lack of correct laminar treatment of the flow on the mirror front face is directly and indirectly responsible for many of the inaccuracies encountered in the simulated results. Since this type of transitional behaviour occurs in a large subset of bluff body, turbo-machinery and other flows, its importance cannot be underestimated. Several approaches attempt to address this issue in the RANS framework ([165][152]) and extending these methods to DES seems like a logical progression.
- Dynamic models, while proven to be quite successful in moderate to well resolved flows have not been translated to the DES approach. While the gain in accuracy from applying dynamic methods in the bulk LES away from the RANS boundary layers (where the existing models are known to perform well) is uncertain, calculations which include both modeled and resolved boundary layers would certainly benefit from such a methodology. As mentioned in sec.3.2.4, the dynamic procedure has some shortcomings with regards to its choice of averaging volume to damp local unphysical oscillations in the dynamic model coefficients. This can be remedied through the use of a Lagrangian averaged dynamic model [106]. A successful combination of the dynamic Lagrangian approach with a DES model promises the cost-saving features of DES on the majority of the domain boundaries while introducing greater accuracy in the bulk and around critical well resolved boundary regions.
- Full Reynolds stress closure of the SGS stresses should be investigated further. Recent channel flow calculations for this approach are very promising [44]. The removal of the SGS isotropy assumption reduces the modelling uncertainty (especially near walls) and allows more flexible modification of the tensorial SGS stresses resulting from the application of wall treatments. At the same time the added cost of multiple SGS transport equations is relatively modest when compared to the cost of solving

7. Conclusions and Suggestions

pressure equation.

- Discretisation and commutation errors were found to have a destabilising effect on the flow around the mirror. While these errors can be reduced through careful mesh construction, a numerical method which is inherently resistant to their effects without compromising accuracy would be a great boon. Explicit filtering and stabilising discretisation schemes are possible avenues of approach.
- One of the most important factors in setting up a successful LES calculation is meshing. Since LES results can be much more sensitive to discretisation and other errors induced by poor quality cells and rapid changes in resolution, such occurrences should be avoided where possible. LES also has very specific requirements in terms of near-wall resolution and Courant number allowances. Experience has shown, that when coupled with the unbounded (but non-dissipative) central differencing convection scheme, the degenerate tetrahedral cells typically produced by some commercial meshing tools can produce instabilities that lead not only to inaccuracies, but in extreme cases can cause divergence of the solution. Overall, these factors place some demanding requirements on LES meshes. For simple geometries crafting such meshes by hand is possible, if time consuming. For domains of engineering complexity a tailored meshing approach that caters to the dictates of LES is required.
- Despite the cost savings elicited by wall treatments and local refinement, long calculation times are still the main obstacle to widespread adoption of LES. Any and all possible methods to reduce the cost therefore warrant investigation. Two related aspects of the current approach contribute significantly to the high cost: 1) the strong Courant number limit imposed via stability concerns by the combination of the PISO solver and central differencing scheme and 2) the large number of inner loops the pressure solver must perform to reach convergence at each iteration of the pressure solution. Numerical methods such as SIMPLE based pressure solvers can potentially relieve the Courant number restriction. This is significant, since any increase in the Courant number limit will directly translate into equivalently

larger timesteps and from there to reduced calculation times. Much more research is however necessary to establish what practices will provide numerical stability at high Courant numbers without adversely affecting the accuracy of the result.

Since the pressure solver can easily account for 80% of the cost of an LES calculation, methodologies that reduce this expense are very desirable. Promising approaches such as multi-grid methods are already in wide use and continued development in this area will could provide further benefit. Additionally, there are indications that solving the LES equations for a compressible system even at low Mach numbers, might be less costly under certain circumstances because the pressure equation is no longer elliptic. Whether this saving can offset the cost of more complicated boundary conditions and the additional differential equation necessary to close the system is uncertain.

- Another avenue to reduced LES calculations times is of course more powerful computational hardware. Although computational resources have been growing rapidly, there has been a recent slowdown in the rate at which serial computing capabilities have been increasing. At the same time however there has been a large decrease in cost and increase in performance of massively parallel systems, a trend which is set to continue with the introduction of multi-core processing units. The parallel efficiency of the LES solver, especially when large numbers of nodes are employed, therefore plays a critical role in determining the duration of the calculation. Such parallelization has already moved LES calculations to the periphery of main-stream adoption. Continued improvement of parallel algorithms and domain decomposition methodologies therefore promise to be a very fruitful area of investigation in the near future.

7.3 Closing Comments

What we require from a simulation tool is a solution of a specified accuracy at the lowest possible cost. While the accuracy of LES is undoubtedly better than that of equivalent RANS simulations in most cases, the cost is at least an order of magnitude higher. In

7. Conclusions and Suggestions

an industry where calculation turn around times have to be measured in at most a few days, the current weeks typically required by LES make it unfeasible for commercial CFD applications unless RANS simulations simply cannot produce acceptable results. As has been demonstrated in this thesis however, LES has some unique capabilities that are not reproduced by steady or unsteady RANS simulations. The prediction of broad spectrum aero-acoustic sources, successfully demonstrated herein, is but one of a range of problems that can only be addressed computationally via LES or DNS. Other such problems include atmospheric and oceanographic simulations, the calculation of free surface breakup in sprays, some unsteady loading problems and many accuracy critical applications. These growing niche markets ensure a future for the methodology, while its uptake in the mainstream of commercial CFD is being hastened by methodological advances and increased computational resources.

Appendix A

Mirror Animations

The images presented in this Appendix are extracts from animations which can be found on the CD-ROM disk accompanying this thesis.

Animation 1: Deviatoric surface pressure

Figure A.1 shows an extract of animation 1 depicting the deviatoric surface pressure, \bar{p}' , on the base plate of simulation AK1 (Case A). The animation clearly shows the presence of a horse-shoe vortex in front of the mirror and the “footprints” of pillar vortices being shed from the mirror edges.

Animation 2: Side view isosurface of local pressure minima

The animation represented by fig.A.2 shows a sidelong view of the isosurface of the deviatoric pressure, $\bar{p}' = -100$ for simulation AK1. The isosurfaces inclose local pressure minima which correspond to vertex cores. In this case the pressure minimum criterion was found to highlight the larger and more strongly circulating vortices, producing a clearer overview of the 3D vortex dynamics than the $Q_{\nabla U}$ criterion with its multitudes of smaller vortices could provide.

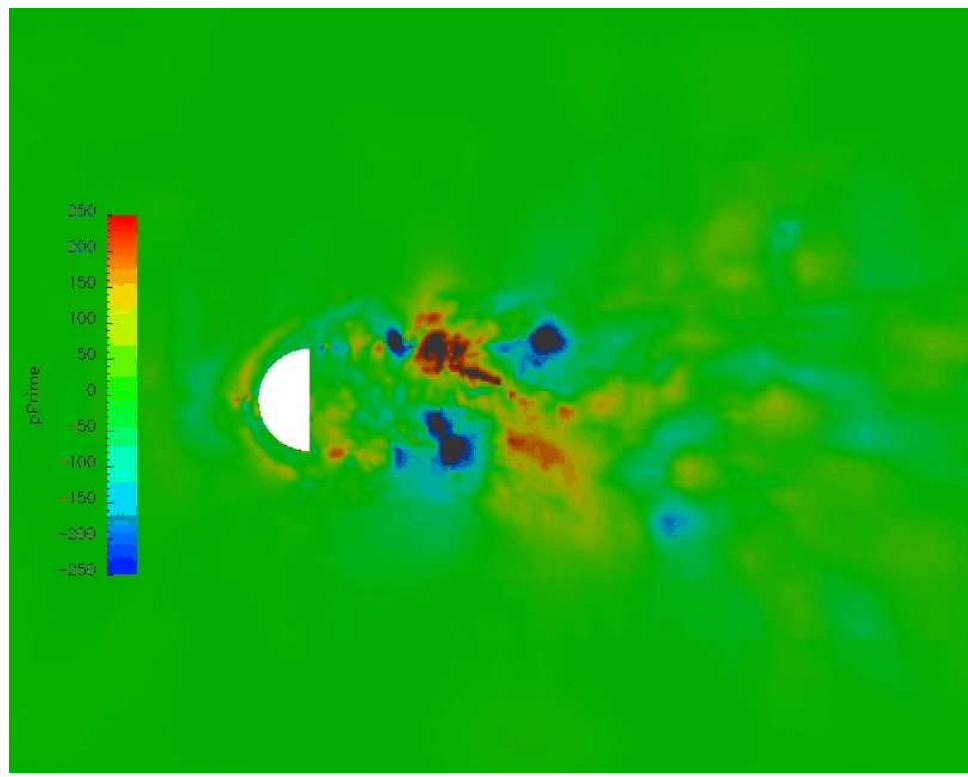


Figure A.1: Deviatoric surface pressure on the mirror base plate

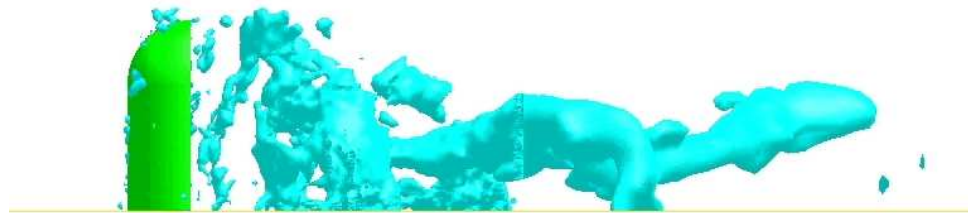


Figure A.2: Isosurface of deviatoric pressure $p' = 100$, side view.

Animation 3: Top view isosurface of local pressure minima

Animation 3 (fig.A.3) is a top down view of the same vortex structures depicted in animation 2.

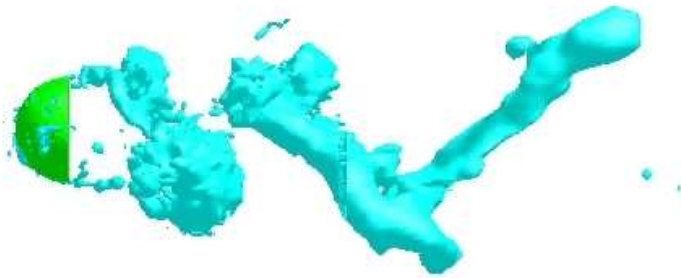


Figure A.3: Isosurface of deviatoric pressure $p' = 100$, top view.

Animation 4: Sound pressure level

Figure A.4 shows the first frame of animation 4, which consists of a cutting plane coloured with contours of sound pressure level in deciBels. The plane traverses the mirror domain from top to bottom and depicts time averaged results for simulation BSA3, a Case **B** calculation.

Animation 5: Velocity magnitude

Animation 5 shows a cutting plane similar to animation 4, but coloured by mean velocity magnitude. An extract of the animation is shown in fig.A.5. The simulation depicted is again BSA3.

A. Mirror Animations

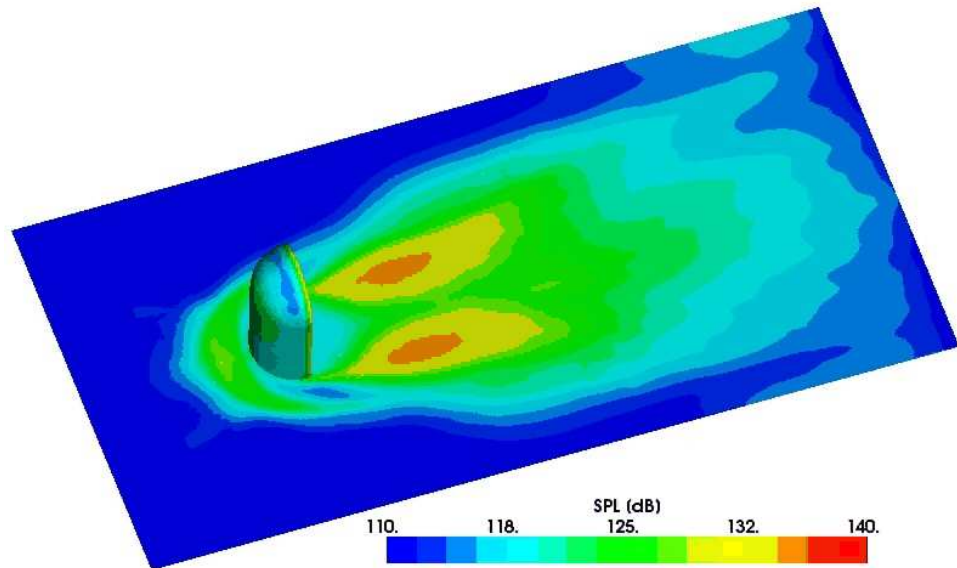


Figure A.4: SPL contours on a moving cutting plane

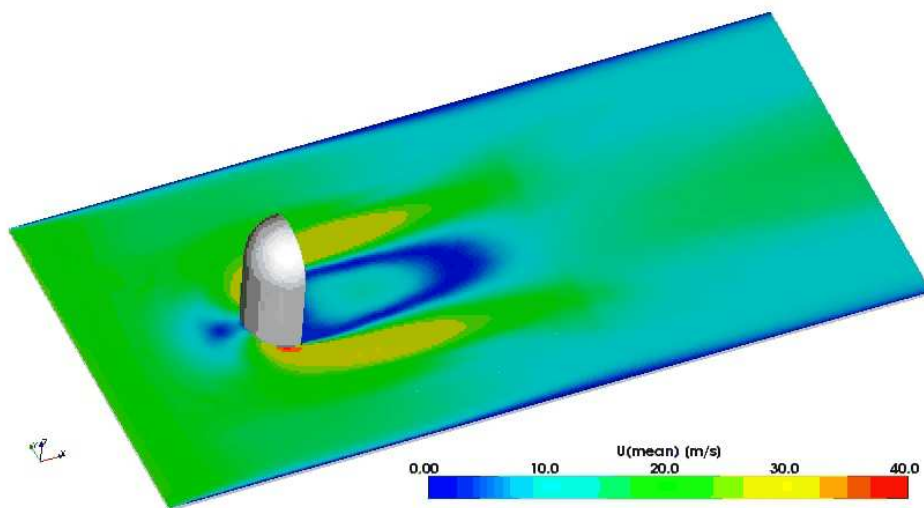


Figure A.5: Velocity contours on a moving baseplate-normal cutting plane

Animation 6: Velocity vectors

The vertical cutting plane of simulation BSA3 shown in fig.A.6 depicts both mean velocity contours and vectors. For animation 6 the plane traverses the mirror domain in a spanwise direction.

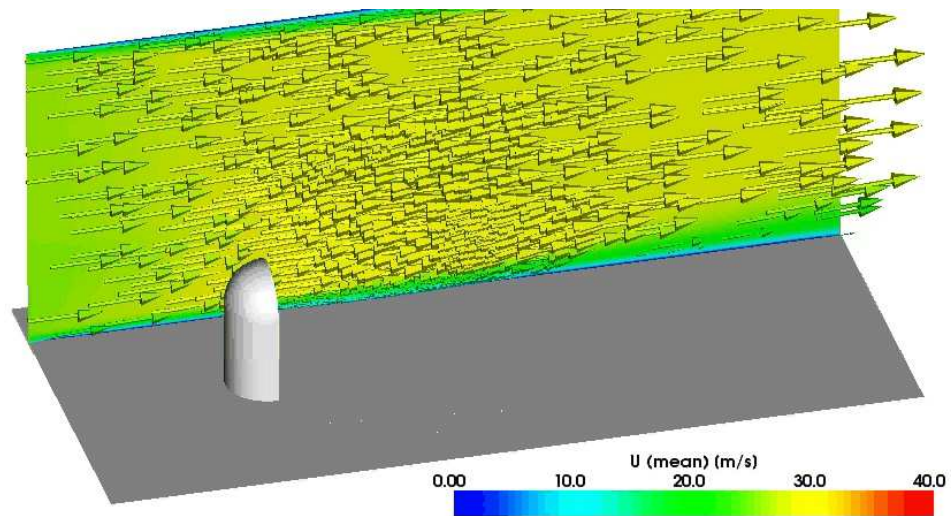


Figure A.6: Velocity contours and vectors on a cutting plane moving across the mirror

A. Mirror Animations

Appendix B

Probe locations

The following table gives the locations of the static and dynamic pressure probes employed during the experiments for mirrors A and B. All measurements are in meters and the coordinate origin is on the symmetry plane at the base of the mirrors rear face.

B. Probe locations

Probe number	x	y	z	Probe number	x	y	z
1	-0.006	0.09981	0.0666	25	-0.02588	0.096599	0.1332
2	-0.006	0.09981	0.1332	26	0.0	-0.085	0.1499
3	-0.006	0.09981	0.1665	27	0.0	0.01109	0.28427
4	-0.006	0.09981	0.1998	28	0.0	0.05174	0.26743
5	-0.006	0.09641	0.22583	29	0.0	0.08427	0.21109
6	-0.006	0.08644	0.24991	30	0.0	0.085	0.1499
7	-0.006	0.04951	0.28644	31	0.0	0.085	0.05
8	-0.006	0.02583	0.29641	32	0.0	0.0001	0.05
9	-0.006	0.0	0.29981	33	0.0	0.0001	0.20
10	-0.02588	0.0	0.29659	34	0.0	0.0001	0.25
11	-0.05	0.0001	0.2866				
12	-0.0708	0.0001	0.2708				
13	-0.0866	0.0001	0.25				
14	-0.09659	0.0001	0.22588				
15	-0.101	0.0001	0.1998				
16	-0.101	0.0001	0.1665				
17	-0.101	0.0001	0.1332				
18	-0.101	0.0001	0.0999				
19	-0.101	0.0001	0.0666				
20	-0.101	0.0001	0.0333				
21	-0.0966	0.02593	0.1337				
22	-0.0867	0.0507	0.1337				
23	-0.07075	0.07077	0.1337				
24	-0.0505	0.08665	0.1337				

Table B.1: *Static pressure probe locations*

Probe number	x	y	z		Probe number	x	y	z
101	-0.006	0.09981	0.0333		126	0.298	0.163	0.0
102	-0.006	0.09981	0.0999		127	0.298	0.1	0.0
103	-0.050	0.0866	0.0999		128	0.298	0.069	0.0
104	-0.006	0.0706	0.2706		129	0.497	0.069	0.0
105	-0.050	0.0612	0.2612		130	0.298	0.0	0.0
106	-0.006	-0.0706	0.2706		131	0.398	0.0	0.0
107	-0.050	-0.0612	0.2612		132	0.497	0.0	0.0
108	-0.006	-0.0998	0.100		133	0.597	0.0	0.0
109	-0.050	-0.0866	0.100		134	-0.1	0.0	0.0
110	-0.006	-0.0998	0.0333		135	0.0	0.1	0.0
111	0.0	-0.085	0.1167					
112	0.0	-0.0674	0.2517					
113	0.0	0.0674	0.2517					
114	0.0	0.085	0.1167					
115	0.0	0.0	0.15					
116	-0.14	0.0	0.0					
117	-0.18	0.0	0.0					
118	-0.22	0.0	0.0					
119	0.1	0.0	0.0					
120	0.0995	0.1105	0.0					
121	0.1989	0.1205	0.0					
122	0.2984	0.1314	0.0					
123	0.3978	0.1418	0.0					
124	0.4973	0.1523	0.0					
125	0.298	0.194	0.0					

Table B.2: *Dynamic probe locations*

B. Probe locations

References

- [1] Gibson M.M. and Dafa'Alla A.D. *Two-equation model for turbulent wall flow*. AIAA Journal, Vol. 33, No. 8, pp. 1514–1518, 1995.
- [2] Gibson M.M. and Launder B.E. *Ground effects on pressure fluctuations in the atmospheric boundary layer*. J. Fluid Mechanics, Vol. 86, p. 491, 1978.
- [3] Lien F.S. and Leschziner M.A. *Modelling 2D separation from a high lift airfoil with a non-linear eddy viscosity model and second moment closure*. Aeronautical Journal, pp. 125–144, 1995.
- [4] Lien F.S., Chen W.L. and Leschziner M.A. *Low-Reynolds-number eddy-viscosity modelling based on non-linear stress-strain-vorticity relations*. In Proc. 3rd Symp. on Engineering Turbulence Modelling and Measurements, Crete, Greece, May, 1996.
- [5] Ahmed S.R., Ramm G. and Faltin G. *Some salient features of the time-averaged ground vehicle wake*. SAE Technical Paper Series, 1984.
- [6] Bagget J.S. *Annual research briefs*. Center for Turbulence Research, Stanford Univ., 1997, Ch. Some modelling requirements for wall models in large eddy simulation., p. 51.
- [7] Bagget J.S., Jimenez J. and Kravchenko A.G. *Resolution requirements in large eddy simulation of shear flows*. CTR Annual Research Briefs., pp. 51–66, 1997.
- [8] Bagget J.S. *On the feasibility of merging LES with RANS for the near-wall region of attached turbulent flows*. In Annual Research Briefs. CTR, Stanford University, 1998, pp. 267–277.

References

- [9] Bailly C., Lafon P. and Candel S. *A stochastic approach to compute noise generation and radiation of free turbulent flows.* In Proc. 16th CEAS/AIAA Aeroacoustics Conf., Munich, Germany, 1995.
- [10] Balaras E., Benocci C. and Piomelli U. *Two-layer approximate boundary conditions for large eddy simulation.* J. AIAA, Vol. 34, No. 6, p. 1111, 1996.
- [11] Bardina J., Ferziger J.H. and Reynolds W.C. *Improved subgrid models for large eddy simulation.* Journal of AAIA, Vol. 80, p. 1357, 1980.
- [12] Berselli L.C. and John V. *On the comparison of a commutation error and the Reynolds stress tensor for flows obeying the law of the wall.* Technical Report 18, Universita di Pisa, 2004.
- [13] Bisset D.K., Antonia R.A. and Browne L.W.B. *Spatial organization of large structures in the turbulent far wake of a cylinder.* J. of Fluid Mechanics, Vol. 218, p. 439, 1990.
- [14] Blackburn H.M., Mansour N.N. and Cantwell B.J. *Topology of fine-scale motions in turbulent channel flow.* Journal of Fluid Mechanics, Vol. 310, pp. 269–292, 1996.
- [15] Bogard D.G. and Tiederman W.G. *Characteristics of ejections in turbulent channel flow.* Journal of Fluid Mechanics, Vol. 179, p. 1, 1987.
- [16] Bradshaw P. *The turbulent structure of equilibrium boundary layers.* N.P.L. Aero report, p. 1184, 1966.
- [17] Brown G.L. and Roshko A. *On density effects and large structure in turbulent mixing layers.* Journal of Fluid Dynamics, Vol. 64, pp. 775–816, 1974.
- [18] Brooke J.W. and Hanratty T.J. *Origin of turbulence producing eddies in a channel flow.* Physics of Fluids A, Vol. 5, pp. 1011–1021, 1993.
- [19] Buice C.U. and Eaton J.K. *Annual research briefs.* Center for Turbulence Research, Stanford Univ., 1997, Ch. Experimental investigation of flow through an asymmetric plane diffuser., p. 243.

- [20] Cabot W. *Annual research briefs*. Center for Turbulence Research, Stanford Univ., 1995, Ch. Large eddy simulation with wall models., p. 41.
- [21] Cabot W. *Annual research briefs*. Center for Turbulence Research, Stanford Univ., 1996, Ch. Near-wall models in large eddy simulations of flow behind a backward facing step., p. 199.
- [22] Cabot W. *Annual research briefs*. Center for Turbulence Research, Stanford Univ., 1997, Ch. Wall models in large eddy simulation of separated flow., pp. 97–106.
- [23] Cabot W., Jimenez J. and Bagget J.S. *On wakes and near-wall behavior in coarse large-eddy simulation of channel flow with wall models and second-order finite-difference methods*. In Annual Research Briefs. CTR, Stanford University, 1999, pp. 343–354.
- [24] Cabot W. and Moin P. *Approximate wall boundary conditions in the large eddy simulation of high Reynolds number flow*. Flow Trub. Combust., Vol. 63, pp. 269–291, 2000.
- [25] Cebeci T. and Smith A.M.O. *Analysis of turbulent boundary layers*. Academic, 1974.
- [26] Campagne F.H., Friehe C.A., LaRue J.C. and Wyngaard J.C. *Flux measurements, flux estimation techniques and fine-scale turbulence measurements in the unstable surface layer over land*. Journal of Atmospheric Science, Vol. 34, pp. 515–530, 1977.
- [27] Chandrusuda C. and Braadshaw P. *Turbulent structure of reattaching mixing layers*. Journal of Fluid Mechanics, Vol. 110, pp. 171–194, 1981.
- [28] Chen H. C. and Patel V. C. *Near-wall turbulence models for complex flows including separation*. AIAA Journal, Vol. 26, No. 6, pp. 641–648, 1988.
- [29] Chong M.S., Perry A.E. and Cantwell B.J. *A general classification of three-dimensional flow field*. Physics of Fluids A, Vol. 2, p. 765, 1990.

References

- [30] Chong M.S., Soria J., Perry A.E., Chacin J., Cantwell B.J. and Na Y. *Turbulent structure of wall-bounded shear flows found using DNS data.* Journal of Fluid Mechanics, Vol. 357, pp. 225–247, 1998.
- [31] Chronopoulos E. and Taylor A.M. *Measurement of flow around a wall mounted side mirror in a closed windtunnel.* Personal communications.
- [32] Chung Y.M. and Sung H.J. *Comparative study of inflow conditions for spatially evolving simulation.* AIAA J., Vol. 35, No. 2, pp. 269–274, 1997.
- [33] Clauser F.H. *Turbulent boundary layers in adverse pressure gradients.* Journal of Aero. Sci., Vol. 21, pp. 91–108, 1954.
- [34] Cook A.W. *A consistent approach to large eddy simulation using adaptive mesh refinement.* Journal of Computational Physics, Vol. 154, pp. 117–133, 1999.
- [35] Curle N. *The influence of solid boundaries upon aerodynamic sound.* In Proc. of the Royal Society of London, Vol. 231 of A, pp. 505–514, 1955.
- [36] Cutnell J. D. and Kenneth W. J. *Physics*, 4 ed. Wiley, New York, 1998. 466.
- [37] Davidson L. *Hybrid LES-RANS: Inlet boundary conditions.* In 3rd National Conf. Comp. Mech., Trondheim, Norway, B. Skallerud and H. Andersson, editors, pp. 7–22, May, 2005.
- [38] Deardorff J.W. *A numerical study of three-dimensional turbulent channel flow at large Reynolds number.* J. Fluid Mechanics, Vol. 41, p. 452, 1970.
- [39] Deardorff J.W. *The use of subgrid transport equations in a three-dimensional model of atmospheric turbulence.* ASME J. Fluids Eng., Vol. 95, p. 429, 1973.
- [40] DeGraaff D.B., Webster D.R. and Eaton J.K. *The effect of Reynolds number on boundary layer turbulence.* Experimental Thermal and Fluid Science, Vol. 18, pp. 341–346, 1999.

- [41] de Sampaio P.A.B. and A.L.G.A. Coutinho. *Simulating vortex shedding at high Reynolds numbers.* Proc. 10th Int. Offshore and Polar Eng. Conf., Vol. 3, pp. 461–466, May, 2000. Seattle.
- [42] Ferziger J.H. and Peric M. *Computational methods for fluid dynamics.* Springer-Verlag, Berlin-New York, 1995.
- [43] Ffowcs-Williams J.E. and Hawkings D.L. *Sound generated by turbulence and surfaces in arbitrary motion.* Phil. Transactions of the Royal Society of London, Vol. 264, pp. 321–342, 1969.
- [44] Fureby C, Gosman A.D., Tabor G., Weller H.G, N. Sandham and Wolfshtein M. *Large eddy simulation of turbulent channel flows.* Turbulent shear flows, Vol. 11, 1997.
- [45] Fureby C., Tabor G., Weller H.G and Gosman A.D. *Differential subgrid stress models in large eddy simulations.* Phys. Fluids, Vol. 6, No. 11, 1997.
- [46] Germano M., Piomelli U., Moin P. and Cabot W.H. *A dynamic subgrid scale eddy viscosity model.* In Proceedings of the Summer Workshop, Stanford, CA., Center for Turbulence Research, 1990.
- [47] Germano M., Piomelli U., Moin P. and Cabot W.H. *A dynamic subgrid-scale eddy viscosity model.* Phys. Fluids A, Vol. 3, p. 1760, 1991.
- [48] Ghosal S., Lund T.S., Moin P. and Akselvoll K. *A dynamic localization model for large eddy simulation of turbulent flows.* Journal of Fluid Mechanics, Vol. 286, p. 229, 1995.
- [49] Ghosal S. *Analysis of discretization errors in LES.* CTR Annual Research Briefs, 1995.
- [50] Ghosal S. *An analysis of numerical errors in Large Eddy Simulation of turbulence.* J. Comp. Phys., Vol. 125, No. 1, pp. 187–206, 1996.

References

- [51] Giger M., Jarika G.H. and Dracos Th. *Meandering jets in a shallow fluid layer*. In Turbulent shear flows V, J. Lumley, editor. Cornell University, 1985.
- [52] Grotzbach G. *Encyclopedia of Fluid Mechanics*. Gulf Publishing, 1987, Ch. Direct numerical and large eddy simulation of turbulent channel flows., p. 1337. ed. N.P. Cheremisinoff.
- [53] Gullbrand J. *Explicit filtering and sub-grid scale models in turbulent channel flow*. CTR Annual Research Briefs, pp. 31–42, 2001.
- [54] Hamilton J.M., Kim J. and Waleffe F. *Regeneration cycle of near-wall turbulent structures*. Journal of Fluid Mechanics, Vol. 287, pp. 317–348, 1995.
- [55] Hinze J.O. *Turbulence*. McGraw-Hill series in mechanical engineering. McGraw-Hill Book Company, 1959.
- [56] Hoeld R., Brenneis A., Eberle A., Schwarz V. and Siegert R. *Numerical simulation of aeroacoustic sound generated by generic bodies placed on a plate: Part 1 - Prediction of aeroacoustic noise sources*. AIAA Paper 99-1896, 1999.
- [57] Huang P.G., Bradshaw P. and Coakley T.J. *Skin friction and velocity profile family for compressible turbulent boundary layers*. AIAA Journal, Vol. 31, pp. 1600–1604, 1993.
- [58] Hunt J.C.R., Wray A.A and Moin P. *Eddies, stream and convergence zones in turbulent flows*. In Center for turbulence research report S88. CTR, 1988, p. 193.
- [59] Hunt J.C.R and Morrison J.F. *Eddy structure in turbulent boundary layers*. Journal of Fluid Mechanics, Vol. 19, pp. 673–694, 2000.
- [60] Hussain A.K.M.F. and Hayakawa M. *Eduction of large scale orginized structure in a turbulent plane wake*. J. of Fluid Mechanics, Vol. 180, p. 193, 1987.
- [61] Hwang R.R. and Jaw S.-Y. *Second order closure turbulence models, there achievements and limitations*. Proc. Natl. Sci. Counc., Vol. 22, No. 6, pp. 703–722, 1998. ROC(A).

-
- [62] Issa R. I. *Solution of the implicitly discretized fluid flow equations by operator splitting.* J. Computational Physics, Vol. 62, pp. 40–65, 1986.
 - [63] Jacobs D.A.H. *Preconditioned conjugate gradient methods for solving systems of algebraic equation.* Technical report, Central Electric Research Laboratory Report, 1980. RD/L/N193/80.
 - [64] Jameson A., Schmidt W. and Turkel E. *Numerical Simulations of the Euler Equations by Finite Volume Methods using Runge-Kutta time-stepping.* AIAA, 1981. 81-1259, Palo Alto.
 - [65] Jarrin N., Benhamadouche S. and Laurence D. *Inlet conditions for large-eddy simulation using a new vortex method.* In The Fourth Int. Symp. on turbulence and Shear Flow Phenomena, Williamsburg, Virginia, J. Humphrey, J. eaton, R. Frederick, N. Kasagi, M. Leschziner, and T. Gatski, editors, 2005.
 - [66] Jasak Hrvoje. *Error analysis and estimation for the finite volume method with application to fluid flows.* Ph.D. thesis, Imperial College London, 1996.
 - [67] Jasak H., Weller H.G. and Gosman A.D. *High resolution NVD differencing scheme for arbitrarily unstructured meshes.* Int. J. Numer. Meth. Fluids, Vol. 31, pp. 431–449, 1999.
 - [68] Jasak H. and Gosman A.D. *Residual error estimate for the finite volume method.* Numerical Heat Transfer, Part B, Vol. 39, pp. 1–19, 2001.
 - [69] Jasak H., Weller H.G. and Nordin N. *In-Cylinder CFD Simulation Using a C++ Object-Oriented Toolkit.* In SAE World Congress, Detroit, No. 2004-01-0110, 2004.
 - [70] Jeong J. and Hussain F. *On the identification of a vortex.* J. Fluid Mechanics, Vol. 285, pp. 69–94, 1995.
 - [71] Jeong J., Hussain F., Schoppa W. and Kim J. *Coherent structures near the wall in a turbulent channel flow.* J. Fluid Mechanics, Vol. 332, pp. 185–214, 1997.

References

- [72] Jiminez J., Moin P., Mozer R. and Keefe L. *Ejection mechanisms in the sublayer of a turbulent channel.* Physics of Fluids, Vol. 31, p. 1311, 1988.
- [73] Jiménez J., Wray A.A., Saffman P.G. and R.S. Rogallo. *The Structure of Intense Vorticity in Homogeneous Isotropic Turbulence.* Proc. 1992 Summer Program, CTR, Stanford, 1992.
- [74] Jiminez J. and Orlandi P. *The rollup of a vortex layer near a wall.* J. of Fluid Mechanics, Vol. 248, p. 297, 1993.
- [75] Jimenez J. *The physics of near-wall turbulence.* Physics A, Vol. 263, pp. 252–262, 1999.
- [76] Jimenez J. and Pinelli A. *The autonomous cycle of near-wall turbulence.* J. Fluid Mechanics, Vol. 389, pp. 335–359, 1999.
- [77] Jimenez J., Flores O. and Garcia-Villalba M. *The large-scale organization of autonomous turbulent wall regions.* In Annual Research Briefs - 2001. CTR, 2001, pp. 317–327.
- [78] Johnson D.A. and King L.S. *A mathematically simple turbulence closure model for attached and separated turbulent boundary layers.* AIAA, Vol. 23, pp. 1684–1692, 1985.
- [79] Johansson A.V., Alfredsson P.H. and Kim J. *Evolution and dynamics of shear layer structures in near-wall turbulence.* Journal of Fluid Mechanics, Vol. 224, p. 579, 1991.
- [80] Jones D.S. *Generalized Functions.* McGraw-Hill Inc., London, 1966.
- [81] Kaltenbach H.-J., Fatica M., Mittal R., Lund T.S. and Moin P. *Study of flow in a planar asymmetric diffuser using large eddy simulation.* J. Fluid Mechanics, Vol. 390, p. 151, 1999.
- [82] Kim J., Moin P. and Moser R. *Turbulence statistics in fully developed channel flow at low Reynolds number.* Journal of Fluid Mechanics, Vol. 177, pp. 133–166, 1987.

-
- [83] Kolmogorov A. N. *The local structure of turbulence in incompressible viscous fluid for very large Reynolds numbers.* Dokl. Akad. Nauk., Vol. 30, pp. 301 – 305, 1941. Reprinted Proc. Royal Soc. London; 434; 9; 1991.
 - [84] Kravchenko A.G., Moin P. and Moser R. *Zonal embedded grids for numerical simulations of wall-bounded turbulent flows.* Journal of Computational Physics, Vol. 127, pp. 412–423, 1996.
 - [85] Kravchenko A.G., Moin P. and Shariff K. *B-Spline method and zonal grids for simulations of complex turbulent flows.* Journal of Computational Physics, Vol. 151, pp. 757–789, 1999.
 - [86] Lamb H. *Hydrodynamics.* Dover, 1945.
 - [87] Launder B.E. and Spalding D.B. *The numerical computation of turbulent flows.* Computer methods in applied mechanics and Engineering, Vol. 3, pp. 269–289, 1974.
 - [88] Le A., Coleman G.N. and Kim J. *Near-wall turbulence structures in three-dimensional boundary layers.* Int. Journal of Heat and Fluid Flow, Vol. 21, pp. 480–488, 2000.
 - [89] Leslie D.C. *Theories of turbulence.* Oxford University Press, 1973.
 - [90] Lesieur M. *Turbulence in fluids*, third ed., Vol. 40 of Fluid Mechanics and its Applications. Kluwer Academic Publishers, 1997.
 - [91] Lesieur M., Begou P., Briand E., Danet A., Delcayre F. and Aider J.L. *Coherent vortex dynamics in large eddy simulation of turbulence.* Journal of Turbulence, Vol. 4, No. 016, 2003.
 - [92] Lighthill M.J. *On sound generated aerodynamically - I. General theory.* In Proc. of the Royal Society of London, Vol. 211 of A, pp. 564–587, 1952.
 - [93] Lighthill M.J. *On sound generated aerodynamically - II. Turbulence as a source of sound.* In Proc. of the Royal Society of London, Vol. 222 of A, pp. 1–32, 1954.
-

References

- [94] Lilly D.K. *On the computational stability of numerical solutions of time-dependent, non-linear, geophysical fluid dynamic problems.* Mon. Weather Rev., Vol. 93, p. 11, 1965.
- [95] Lilly D.K., editor. Proceedings of the IBM Scientific Computing Symposium on Environmental Sciences., Yorktown Heights, N.Y., No. 195.
- [96] Lilly D.K. *A proposed modification of the Germano subgrid scale model.* Physics of Fluids A, Vol. 4, p. 633, 1992.
- [97] Lugt H.J. *The dilemma of defining a vortex.* In Recent Developments in Theoretical and Experimental Fluid Mechanics, U. Müller, K. Roesner, and B. Schmidt, editors. Springer, 1979, pp. 309–321.
- [98] Liu S., Meneveau C. and Katz J. *On the properties of similarity subgrid-scale models as deduced from measurements in a turbulent jet.* Journal of Fluid Mechanics, Vol. 275, pp. 83–119, 1994.
- [99] Mansour N.N., Moser R.D. and Kim J. *Data set PCH10.* In A Selection of Test Cases for Validation of Large-Eddy Simulation of Turbulent Flow, J. Jimenez, editor, AR-345. AGARD, 1998.
- [100] Marusic I. and Perry A.E. *A wall-wake model for turbulent structure of boundary layers. Part 2. Further experimental support.* Journal of Fluid Mechanics, Vol. 298, pp. 389–407, 1995.
- [101] Mason P.J. and Callen N.S. *On the magnitude of the subgrid-scale eddy coefficient in large eddy simulation of turbulent channel flow.* Journal of Fluid Mechanics, Vol. 162, pp. 439–462, 1986.
- [102] Mason P.J. and Thomson D.J. *Stochastic backscatter in large-eddy simulations of boundary layers.* Journal of Fluid Mechanics, Vol. 242, pp. 51–78, 1992.
- [103] McDonald H. *The effect of pressure gradient on the law of the wall in turbulent flow.* Journal of Fluid Mechanics, Vol. 35, pp. 311–336, 1969.

-
- [104] Melander M.V. and Hussain F. *Polarized vorticity dynamics on a vortex column.* Physics of Fluids A, Vol. 5, p. 1992, 1993.
 - [105] Meneveau C., Lund T.S and Cabot W. *A Lagrangian dynamic subgrid-scale model of turbulence.* CTR Proceedings of the Summer Program, p. 271, 1994.
 - [106] Meneveau C., Lund T. and Cabot W. *A lagrangian dynamic subgrid-scale model of turbulence.* J. Fluid Mech., Vol. 319, p. 353, 1996.
 - [107] Metcalfe R.W., Hussain F., Menon S. and Hayakawa M. *Coherent structures in a turbulent mixing layer: a comparison between numerical simulations and experiments.* In Turbulent Shear Flows, F. Durst, B. Launder, J. Lumley, F. Schmidt, and J. Whitelaw, editors, Vol. 5. Springer, 1985, p. 110.
 - [108] Na Y. and Moin P. *Direct numerical simulation of separated turbulent boundary layer.* Journal of Fluid Mechanics, Vol. 370, pp. 175–201, 1998.
 - [109] Na Y. and Moin P. *The structure of wall-pressure fluctuations in turbulent boundary layers with adverse pressure gradient and separation.* Journal of Fluid Mechanics, Vol. 377, pp. 347–373, 1998.
 - [110] Naguib A.M. and Wark C.E. *An investigation of wall-layer dynamics using a combined temporal filtering and correlation technique.* J. Fluid Mechanics, Vol. 243, p. 541, 1992.
 - [111] Nagano Y., Tsuji T. and Houra T. *Structure of turbulent boundary layer subjected to adverse pressure gradient.* Int. J. of Heat and Fluid flow, Vol. 19, pp. 563–572, 1998.
 - [112] Nicoud F., Winckelmans G., Carati D., Bagget J. and Cabot W. *Boundary conditions for LES away from the wall.* Annual research briefs, p. 413, 1998. Center for Turbulence Research, Stanford Univ.
 - [113] Nicoud F. and Bagget J. *On the use of the optimal control theory for deriving wall models for LES.* In Annual Research Briefs. CTR, Stanford University, 1999, pp. 329–341.
-

References

- [114] Nickels T.B. and Marusic I. *On the different contributions of coherent structures to the spectra of a turbulent round jet and a turbulent boundary layer.* Journal of Fluid Mechanics, Vol. 448, pp. 367–385, 2001.
- [115] Bojan Niceno. *An Unstructured Parallel Algorithm for Large Eddy and Conjugate Heat Transfer Simulations.* Ph.D. thesis, Technical University Delft, 2001.
- [116] Nikitin N.V., Nicoud F., Wasistho B., Squires K.D. and Spalart P.R. *An approach to wall modelling in large-eddy simulation.* Physics of Fluids, Vol. 12, No. 7, pp. 1629 – 1632, July, 2000.
- [117] Obi S., Aoki K. and Masuda S. *Experimental and computational study of turbulent separating flow in an asymmetric plane diffuser.* In Ninth Symposium on Turbulent Shear Flows, Kyoto, Japan, p. 305, 1993.
- [118] Panton R.L., editor. *Self-sustaining mechanisms of wall turbulence*, Vol. 15 of Advances in Fluid Mechanics. WIT Press, Southampton, UK, 1997.
- [119] Park N., Yoo J.Y. and Choi H. *Discretization errors in large eddy simulation: on the suitability of centered and upwind biased compact differencing schemes.* J. Comp. Physics, Vol. 198, pp. 580–616, 2004.
- [120] Pascarelli A., Piomelli U. and Candler G.V. *Multi-block large-eddy simulations of turbulent boundary layers.* Journal of Computational Physics, Vol. 157, pp. 256–279, 2000.
- [121] Patankar S.V. *Numerical heat transfer and fluid flow.* Hemisphere Publishing Corp., 1981.
- [122] Perry A.E. and Chong M.S. *On the mechanism of wall turbulence.* Journal of Fluid Mechanics, Vol. 119, pp. 173–217, 1982.
- [123] Perry A.E., Henbest S. and Chong M.S. *A theoretical and experimental study of wall turbulence.* J. of Fluid Mechanics, Vol. 165, pp. 163–199, 1986.

- [124] Perot B. and Moin P. *Shear-free turbulent boundary layers. Part 1. Physical insights into near-wall turbulence.* Journal of Fluid Mechanics, Vol. 295, pp. 199–227, 1995.
- [125] Perry A.E. and Marusic I. *A wall-wake model for the turbulent structure of boundary layers. Part 1. Extension of the attached eddy hypothesis.* Journal of Fluid Mechanics, Vol. 298, pp. 361–388, 1995.
- [126] Piomelli U., Ferziger J.H and Moin P. *New approximate boundary conditions for large eddy simulations of wall-bounded flows.* Physics of Fluids A, Vol. 6, p. 1061, 1989.
- [127] Piomelli U. *Local space-time averaging in the dynamic subgrid scale model.* American Phys. Soc., Vol. 35, No. 10, 1991.
- [128] Piomelli U. *Large-eddy simulation: achievements and challenges.* Progress in Aerospace Sciences, Vol. 35, pp. 335–362, 1999.
- [129] Prandtl L. *Über ein neues formelsystem fur die ausgebildete turbulenz (On a new formation for the fully developed turbulence).* Technical report, Academy of Sciences, 1945.
- [130] Rajagopalan S. and Antonia R.A. *Some properties of the large structure in a fully developed turbulent duct flow.* Physics of Fluids, Vol. 22, p. 614, 1979.
- [131] Reynolds O. *An experimental investigation of the circumstances which determine whether the motion of water shall be direct and sinuous, and the law of resistance in parallel channel.* Phil. Trans. Royal Soc., pp. 51 – 105, 1883.
- [132] Reynolds W.C. *The potential and limitations of direct and large eddy simulation.* In Whither turbulence? Turbulence at the crossroads., J. Lumley, editor, No. 357 in Lecture notes in physics, Springer-Verlag, p. 313, 1990.
- [133] Robinson S.K. *Coherent motions in the turbulent boundary layer.* Annual Review Fluid Mechanics, Vol. 23, pp. 601–639, 1991.

References

- [134] Rodi W. and Mansour N.N. *Low Reynolds number k- modelling with the aid of direct simulation data.* Journal of Fluid Mechanics, Vol. 250, p. 509, 1993.
- [135] Saddoughi S.G. and Veervalli S.V. *Local isotropy in turbulent boundary layers at high Reynolds number.* Journal of Fluid Mechanics, Vol. 268, pp. 333–372, 1994.
- [136] Schumann U. *Subgrid scale model for finite difference simulations of turbulent flows in plane channels and annuli.* J. Computational Physics, Vol. 18, pp. 376–404, 1975.
- [137] Schoppa W. and Hussain F. *Coherent structure dynamics in near-wall turbulence.* Fluid Dynamics Research, Vol. 26, pp. 119–139, 2000.
- [138] Shih T.-H., Povinelli L.A., Liu N.-S. and Potapczuk M.G. *Turbulent surface flow and wall functions.* AIAA 99-2392, 1999. 20-24 June, AIAA-JPCE, Los Angeles, California.
- [139] Shi S. *Large-eddy simulation of ship wakes.* Ph.D. thesis, Dept. Mech. and Aerospace Eng., West Virginia University, 2001.
- [140] Shur M., Spalart P.R., Strelets M. and Travin A. *Detached eddy simulation of an airfoil at high angle of attack.* In Fourth International Symposium on Engineering Turbulence Modelling and Experiment, Corsica, W. Rodi and D. Laurence, editors, Elsevier, May, 1999.
- [141] Siegert R., Schwarz V. and Reichenberger J. *Numerical simulation of aeroacoustic sound generated by generic bodies placed on a plate: Part 2 - Prediction of radiated sound pressure.* AIAA Paper 99-1895, 1999.
- [142] Smagorinski J. *General circulation experiments with the primitive equations.* Mon. Weather Rev., Vol. 91, p. 99, 1963.
- [143] Smith C.R. and Metzler S.P. *The characteristics of low speed streaks in the near-wall region of a turbulent boundary layer.* J. of Fluid Mechanics, Vol. 129, pp. 27–54, 1983.

-
- [144] Smirnov A., Shi S. and Celik I. *Random flow generation technique for large eddy simulations and particle-dynamics modelling.* J. Fluid Engineering, Vol. 123, pp. 359–371, 2001.
 - [145] Soria J., Sondergaard R., Cantwell B.J., Chong M.S. and Perry A.E. *A study of fine scale motions of incompressible time developing mixing layers.* Physics of Fluids, Vol. 6, No. 2, pp. 871–884, 1994.
 - [146] Spalding D.B. *A single formula for the law of the wall.* Journal of Applied Mechanics, Trans. ASME, Series E, Vol. 28, pp. 455–458, 1961.
 - [147] Spalart P.R. and Allmaras S.R. *One-equation turbulence model for aerodynamic flows.* In Proc. AIAA ASM, Reno, NV, 1992.
 - [148] Spalart P.R. and Watmuff J.H. *Experimental and numerical study of a turbulent boundary layer with pressure gradients.* Journal of Fluid Mechanics, Vol. 249, pp. 337–371, 1993.
 - [149] Spalart, P.R. and Jou W.-H., Strelets M. and Allmaras S.R. *Comments on the feasibility of LES for wings, and on a hybrid RANS/LES approach.* In Advances in DNS/LES, Columbus, OH, C. Lui and Z. Liu, editors, Greyden, 1997. First AFOSR International conference on DNS/LES.
 - [150] Spalart P.R. *Strategies for turbulence modelling and simulations.* Int. J. of Heat and Fluid Flow, Vol. 21, pp. 252–263, 2000.
 - [151] Sendstad O. and Moin P. *The near-wall mechanisms of three dimensional turbulent boundary layers.* Technical report, Stanford University, 1992. Report TF-57.
 - [152] Steelant J. and Dick E. *Modeling of bypass transition with conditioned Navier-Stokes equations coupled to an intermittency transport equation.* Int. J. Num. Meth. Fluids, Vol. 23, pp. 193–220, 1996.
 - [153] De Stefano G. and Vasilyev O.V. *Sharp cutoff versus smooth filtering in large eddy simulation.* Physics of Fluids, Vol. 14, No. 1, pp. 362–369, 2002.
-

References

- [154] Stratford B.S. *An experimental flow with zero skin friction throughout its region of pressure rise.* Journal of Fluid Mechanics, Vol. 5, p. 17, 1959.
- [155] Tabor G.R., Baba-Ahmadi M.H., De Villiers E. and Weller H.G. *Construction of inlet conditions for LES of turbulent channel flow.* ECCOMAS, 2004.
- [156] Tennekes H. and Lumley J.L. *A first course in turbulence.* The MIT Press, 1972.
- [157] Townsend A.A. *Equilibrium layers and wall turbulence.* Journal of Fluid Mechanics, Vol. 11, pp. 97–120, 1961.
- [158] Townsend A.A. *The behaviour of a turbulent boundary layer near separation.* Journal of Fluid Mechanics, Vol. 12, pp. 536–554, 1962.
- [159] Townsend A.A. *The structure of turbulent shear flow*, 2nd ed. Cambridge University Press, 1976.
- [160] Travin A., Shur M., Strelets M. and Spalart P.R. *Detached eddy simulations past a circular cylinder.* Flow, Turbulence and Combustion, Vol. 63, pp. 293–313, 1999.
- [161] Vasillyev V., Lund T.S. and Moin P. *A General class of commutative filters for LES in complex geometries.* J. Comp. Physics, Vol. 146, pp. 82–104, 1998.
- [162] Van der Vorst H.A. *Bi-CGSTAB: A fast and smoothly converging variant of Bi-CG for the solution of non-symmetric linear systems.* SIAM J. Scientific Computing, Vol. 13, No. 2, pp. 631–644, 1992.
- [163] Wang M. *Annual research briefs.* Center for Turbulence Research, Stanford Univ., 2000, Ch. Dynamic wall modelling for LES of complex turbulent flows., pp. 241–250.
- [164] Wang M., Catalano P. and Iaccarino G. *Annual research briefs.* Center for Turbulence Research, Stanford Univ., 2001, Ch. Prediction of high Reynolds number flow over a circular cylinder using LES with wall modelling., pp. 45–50.
- [165] Wang C. and Perot B. *Prediction of turbulent transition in boundary layers using the turbulent potential model.* J. Turbulence, Vol. 3, pp. 22–36, 2002.

- [166] Warming R.F. and Beam R.M. *Upwind second order differencing schemes and applications in aerodynamic flows.* AIAA J., Vol. 14, pp. 1241–1249, 1976.
- [167] Watmuff J.H. *An experimental investigation of a low Reynolds number turbulent boundary layer subject to an adverse pressure gradient.* CTR Annual Research Briefs, pp. 37–49, 1989.
- [168] Williams J., Quinlan W.J., Hackett J.E., Thompson S.A., Marinaccio T. and Robertson A. *A CFD calibration study for automotive shapes.* In 18th AIAA Aerospace Ground Testing Conference, Colorado Springs, CO, June, 1994. AIAA 94-2607.
- [169] Wolfshtein M. *The velocity and temperature distribution in one-dimensional flow with turbulence augmentation and pressure gradient.* International Journal of Heat and Mass Transfer, Vol. 12, pp. 301–318, 1969.
- [170] Yakot V., Orzag S.A., Thangam S., Gatski T.B. and Speziale C.G. *Developement of turbulence models for shear flows by double expansion technique.* Physics of Fluids A, Vol. 4, No. 7, pp. 1510–1520, 1992.
- [171] Yoshizawa A. *A statistically-derived subgrid-scale kinetic energy model for the large-eddy simulation of turbulent flows.* Journal of the Physical Society of Japan, Vol. 54, No. 8, pp. 2834–2839, 1985.
- [172] Zhou J., Adrian R.J., Balachandar S. and Kendall T.M. *Mechanisms for generating coherent packets of heirpin vortices in channel flow.* Journal of Fluid Mechanics, Vol. 387, pp. 353–396, 1999.
- [173] Bayly B.J., Orszag S.A. and Herbert T. *Instability mechanism iin shear-flow transition.* In Anual Review in Fluid Mechanics, Vol. 20. January, 1988, pp. 359–391.
- [174] Simand C., Chilla F. and Pinton J.-F. *Inhomogeneous turbulence in the vicinity of a large scale coherent vortex.* Europhysics Letters, Vol. 49, No. 3, pp. 336–342, 2000.
- [175] Von Kármán T. Proc. Natl. Acad. Sci. U.S., Vol. 34, p. 530, 1948.